



THE HONG KONG
POLYTECHNIC UNIVERSITY

香港理工大學

Pao Yue-kong Library

包玉剛圖書館

Copyright Undertaking

This thesis is protected by copyright, with all rights reserved.

By reading and using the thesis, the reader understands and agrees to the following terms:

1. The reader will abide by the rules and legal ordinances governing copyright regarding the use of the thesis.
2. The reader will use the thesis for the purpose of research or private study only and not for distribution or further reproduction or any other purpose.
3. The reader agrees to indemnify and hold the University harmless from and against any loss, damage, cost, liability or expenses arising from copyright infringement or unauthorized usage.

IMPORTANT

If you have reasons to believe that any materials in this thesis are deemed not suitable to be distributed in this form, or a copyright owner having difficulty with the material being included in our database, please contact lbsys@polyu.edu.hk providing details. The Library will look into your claim and consider taking remedial action upon receipt of the written requests.

**MICRO-MACRO MECHANISMS OF COHESIONLESS
GRANULAR MEDIA—PARTICLE SHAPE, FABRIC,
CRUSHING AND LOADING PATHS**

YANG YI

Ph.D

The Hong Kong Polytechnic University

2015



The Hong Kong Polytechnic University

Department of Civil and Environmental Engineering

**MICRO-MACRO MECHANISMS OF COHESIONLESS
GRANULAR MEDIA — PARTICLE SHAPE, FABRIC,
CRUSHING AND LOADING PATHS**

YANG YI

**A Thesis Submitted in Partial Fulfilment of the Requirements for the
Degree of Doctor of Philosophy**

May 2015

CERTIFICATE OF ORIGINALITY

I hereby declare that this dissertation entitled “**Micro-macro mechanisms of cohesionless granular media — particle shape, fabric, crushing and loading paths**” is my own work and that, to the best of my knowledge and belief, it reproduces no material previously published or written, nor material that has been accepted for the award of any other degree or diploma, except where due acknowledgement has been made in the text.

(Signed)

Yang Yi

(Name of student)

Abstract of thesis entitled

**MICRO-MACRO MECHANISMS OF COHESIONLESS
GRANULAR MEDIA — PARTICLE SHAPE; FABRIC; CRUSHING;
AND LOADING PATHS**

submitted by **Yi Yang**

for the degree of Doctor of Philosophy

at The Hong Kong Polytechnic University in Aug 2014

Granular materials are applied in many fields, such as pharmaceuticals, agriculture, mining industry, geotechnical engineering and others. They are unusual media that cannot be directly categorized as solid, liquid or gas. The mechanical responses of a granular material are notoriously complicated to describe or predict. Although many previous researchers have attempted to explore the granular medium through different directions, the mechanisms of these materials under various conditions are still far from well understood. The nature of granular materials is composited by discrete grains and surrounded voids, which crucially determine the macroscopic mechanical behavior of granular media. Hence, it is extremely important to know the variation of particle contact information at the micro-scale. This study aims to deeply explore the variation of microscopic contact information with many new insights under different loading and boundary conditions, including biaxial drained, “undrained”, and one dimensional compression. In the current thesis, the discrete element method (DEM) is adopted as a robust tool to carry out a series of numerical tests, which can be considered to explain the relationships between the microscopic information and the macroscopic response.

Particle shape plays an important role in both the microscopic and macroscopic responses of a granular assembly. A more suitable shape descriptor SF is suggested for the quantitative analysis of the macro-scale strength indexes and contact parameters

for non-convex grains. The critical state friction angle increases linearly with the SF value. It is found that particle shape can directly influence the strain localization pattern, micro-scale fabric distribution, micro-scale mobilization indexes and probability density function (PDF) of the normalized contact normal force. Additionally, the accuracy of the stress-force-fabric (SFF) relationship can be overestimated or underestimated by the average normal force and the distribution of contact vectors.

A series of numerical tests on the quasi-static deformation of dense granular media are performed to investigate the characteristics of mixtures of shapes that are composed of round and non-convex (Elongate) particles. Four respective contact types, which are divided into circle-circle contacts (CC), circle-elongate contacts (CE), simple elongate-elongate contacts (EE1) and multiple elongate-elongate contacts (EE_m), are applied to interpret the macro granular mechanical response from the information of the effective contacts on a deeper micro-scale. The contact force ratio (K) of these four contacts can also be considered to explain the variation of the steady friction angle, particularly at the decreasing ranges of (0.2, 0.3) and (0.6, 0.7). Another interesting finding is that the PDF of friction mobilization (I_m) for the CE contacts nearly overlaps at the mixture of 30%~60% Elongated particles. For the end of the strong force chains, the probability of the CC contacts is approximately the same. However, the pdf curves of the normalised contact forces of EE1 and EE_m show a nearly linear increasing relationship with the increased percentage of Elongated particles. It should be point out that the variation of contact normal anisotropic coefficient is insensitive with the contact portions of EE1 and EE_m.

A traditional rolling resistance model has been implemented to compare with the simplified irregular clumps under the “undrained” shearing conditions. The numerical results indicate that the effects of rolling resistance model are limited to achieve the critical shear strength of irregular assemblages even when the rolling resistance coefficient $\alpha > 0.5$. Moreover, the artificial rolling resistance effect cannot easily

generate an apparent liquefaction as the loose packing of irregular particle. Furthermore, the main weights of anisotropic parameters for “undrained” Elongate medium sample (UEM) and Triangular medium sample (UTM) are related to contact normal. However, for the rolling resistance samples, the anisotropy of contact normal force dominates the macro shear strength. In addition, it should be noted that the patterns of the probability distribution of friction mobilization as well as the combined with the force class for the rolling resistance samples and irregular assemblages at the quasi-static or the critical state are obviously different.

The contact forces and coordination number distribution for crushable granular materials during one-dimensional compression are investigated using the DEM. A simple method is developed to reveal the fractal distribution of contact forces in comminuted granular materials. When the contact force distribution shows a log-normal relation, a fractal pattern of contact forces will emerge. The fractal contact force distribution can be considered to explain the evaluation of particle size distribution with a fractal feature. Moreover, systematically parametric studies show that the size ratio of the initial maximum size and the minimum crushable size, Weibull modulus, inter-particle frictional coefficient and permitted tensile stress of the initial largest particle can influence the patterns of contact force distribution at the ultimate state. Furthermore, the coordination number distribution for each particle displays a unified distribution within the fractal size distribution of granular assemblages at the ultimate state.

The effects of initial particle size distribution (PSD) for the crushable granular materials are investigated under one dimensional compression within the loading-unloading-reloading procedure. The numerical macro results can qualitatively match with previous experimental tests for the initial uniform, bimodal and fractal packings. Many interesting post-processing results have been investigated to explore the variation of the macro responses. It is noticeable that the contact force distribution would gradually decrease with the reloading procedure, which would also increase the

fractal dimension of the particle size distribution. However, the variation of the coordination number distribution is insensitive to the repetitive loading as well as the initial particle size distribution.

LIST OF PUBLICATIONS

Journal Papers

Yang, Y., Wang J.F., and Cheng, Y. M. (2015). Quantified evaluation of particle shape effects from micro-to-macro scales for non-convex grains. *Particuology*, (Accepted)

Yang, Y., and Cheng, Y. M. (2015). A fractal model of contact force distribution and the unified coordination distribution for crushable granular materials under confined compression. *Powder Technology*, 279, 1-9.

Xiao, B., **Yang, Y.**, and Chen, L. (2013). Developing a novel form of thermal conductivity of nanofluids with Brownian motion effect by means of fractal geometry. *Powder Technology*, 239, 409-414.

Conference Papers

Yang, Y. and Cheng, Y.M. (2014). The fractal features of contact force chains for crushable granular materials under confined compression. Proceedings of ASCE Engineering Mechanics Institute International Conference (Hong Kong, 7-9, Jan. 2015).

Yang, Y., Li, N., Yin, P. and Cheng, Y.M. (2013). Flow pattern for multi-size silos. Proceedings of Third International Conference on Geotechnique, Construction Materials and Environment (Nagoya, Japan, 13-15 Nov. 2013), 317-321.---*Special issue of International Journal of GEOMATE: Geotechnique, construction materials and environment*, 5(1), 712-716.

Yang, Y., Huang, R. Q., Cheng, Y. M., and Wang, J. F. (2013). Investigation of the Deformable Behavior of Loose and Dense Sand through DEM. Proceedings of International Conference on Applied Mechanics, Fluid and Solid Mechanics (Singapore, 15-16, Nov. 2013), 124-128.

ACKNOWLEDGEMENTS

I wish to express my great gratitude and sincere thanks to my supervisor, Dr. Y.M. Cheng, for his continuous inspiration and support throughout my research. Without his patient guidance and consistent encouragement, this thesis would not be near possible. It is a fruitful experience to work with Dr. Y.M. Cheng, who offered me a certain extent freedom to pursue my own ideas. I also appreciate him with many benefited conversations about my future career and life.

I am very grateful to Professor J.A. Wang from University of Science and Technology Beijing for introducing me to the field of geotechnical engineering. Many thanks are also due to Professor H.G. Ji for his kind support and encouragement.

I would like to express my gratitude to Professor J.H. Yin and Dr. Robina Wong for teaching me advanced soil mechanics and rock mechanics, which enhanced my understanding of geotechnical engineering. I am also benefit from many enjoyable and valuable discussions with Professor K.T. Chau. Many thanks extend to Mr. Raymond K.H. Leung and Ms. Fion P.F. Cheng for their assistance to my granular flume tests. In addition, the financial support from The Hong Kong Polytechnic University for this research work is acknowledged.

I would like to express my thanks to my defense examiners Dr. Z.Y. Yin from Ecole Centrale de Nantes and Dr. J. Yang from the University of Hong Kong for their valuable suggestions and comments.

I would like to express my thanks to Dr. J.F. Wang from City University of Hong Kong for his invaluable suggestions on my research. It is fortunate to join his research team meeting for several times, which I benefited a lot in using the discrete element method. Many thanks are also extended to Dr. B. Zhou, Mr. B.D. Zhao and Mr. S. Liu for the interesting and impressive discussions at City University of Hong Kong.

I would like to express my thanks to Dr. Gordon G.D. Zhou from the Institute of Mountain Hazards and Environment for the collaborative research on large scale granular mass flow tests at Dongchuan Debris Flow Observation and Research Station, Yun Nan Province, where I carried out nearly 100 group tests during two months. Although these materials aren't including in this dissertation, this experience inspires my deeper understanding about the nature of granular materials. Thanks are also extended to Mr. Y. Hong, Dr. H.Y. Chen, Dr. X.P. Leng, Mr. D.L. Liu and Mr. K. Li at Dongchuan for their assistances to my flume tests, as well as my daily life. It is a good memory there.

I would like to express my gratitude to Professor S.H. Lo and Professor K.Y. Sze from the University of Hong Kong, for teaching me advanced finite elements (CIVL6002) which I know many original concepts of FEM. Through deep discussion on the development of FEM, I fortunately find ways to improve my research direction into other immature regions. I am also grateful to Professor L.G. Tham and Dr. C.Y. Kwok who taught me advanced numerical modelling in geomechanics (CIVL8013) where I have learned a lot to enhance my research. Many thanks are due to my classmates from HKU.

I would like to express my thanks to Dr. J.D. Zhao and Dr. N. Guo from the Hong Kong University of Science and Technology for kindly sharing their research experiences which are beneficial for my research.

I also own my gratitude to all my friends and colleagues: Dr. W.B. Wei, Dr. L. Li, Dr. D.Z. Li, Dr. Y.J. Sun, Dr. D.S. Xu, Dr. H.X. Wang, Dr. G.S. Zhao, Dr. B.Q. Xiao, Ms. N. Li, Mr. W.Q. Feng, Mr. L.L. Liu, Dr. P. Yin and others from PolyU.

Finally, I am deeply indebted to my parents for their endless encouragement and selfless support. I would like to express my special thanks to my wife, Aki, for her unwavering love and continuous encouragement over these years.

TABLE OF CONTENTS

CERTIFICATE OF ORIGINALITY	I
ABSTRACT	II
LIST OF PUBLICATIONS	VI
ACKNOWLEDGEMENTS	VII
TABLE OF CONTENTS	IX
LIST OF FIGURES	XII
LIST OF TABLES	XV
CHAPTER 1 Introduction	1
1.1 General Background	1
1.2 Objectives and scope of the study	1
1.3 Thesis outline	2
CHAPTER 2 Literature review	6
2.1 Introduction.....	6
2.2 Macromechanics background of granular sands	6
2.2.1 Shear strength and dilatancy	6
2.2.2 Anisotropy.....	11
2.3 Micromechanical description of granular sands.....	12
2.3.1 Stress and strain tensors	13
2.3.2 Fabric structure.....	17
2.3.2.1 Void ratio.....	17
2.3.2.2 Coordination number	17
2.3.2.3 Contact normal orientation distribution	18
2.3.2.4 Contact force distribution	19
2.3.2.5 Contact vector distribution.....	21
2.3.3 Stress-force-fabric relationship	22
2.4 Particle shape effect of granular sands	25
2.4.1 Macro and micro responses.....	25
2.4.2 Particle shape descriptor	26
2.4.3 Particle shape modelling	28
2.5 Crushable granular materials.....	29
2.5.1 One dimensional compression	29
2.5.2 Particle crushing modelling.....	32
2.6 Discrete element method (DEM)	35
2.6.1 Brief description of DEM.....	35
2.6.2 Governing principles.....	37
2.6.3 DEM boundary conditions and load paths	40
2.6.3.1 Boundary types.....	41
2.6.3.2 Controlling boundaries	42

2.6.3.3 Implementation of different loading conditions.....	44
CHAPTER 3 Analysis of non-convex grains from micro to macro scales.....	54
3.1 Introduction.....	54
3.2 Investigation scheme.....	56
3.2.1 The compared particle shape descriptors	56
3.2.2 DEM simulation details.....	57
3.3 Numerical findings and discussions.....	59
3.3.1 Strength and deformation for the prior shape descriptor.....	59
3.3.2 Micro anisotropic parameters and SFF	60
3.3.3 Friction mobilization and force chain distribution	62
3.3.4 Confining pressure effect	63
3.4 Conclusions.....	63
CHAPTER 4 The development of contact types within different mixtures of shapes	77
4.1 Introduction.....	77
4.2 Investigation scheme.....	79
4.2.1 Particle shape mixtures and contact types.....	79
4.2.2 DEM simulation details.....	80
4.3 Numerical findings and discussions.....	80
4.3.1 Macroscopic results for the contact types	80
4.3.2 Microscopic results for the contact types	82
4.4 Conclusions.....	85
CHAPTER 5 Study of rolling resistance model and irregular particle shape during the	
“undrained” tests	99
5.1 Introduction.....	100
5.2 Investigation scheme.....	102
5.2.1 Rolling resistance model.....	102
5.2.2 DEM simulation details.....	104
5.3 Numerical findings and discussions.....	107
5.3.1 Macroscopic mechanical responses	107
5.3.2 Microscopic behavior.....	109
5.4 Conclusions.....	113
CHAPTER 6 A fractal model of contact force distribution and the unified coordination	
distribution for crushable granular materials under confined compression	133
6.1 Introduction.....	133
6.2 Investigation scheme.....	136
6.2.1 Grain breakage criteria.....	136
6.2.2 DEM simulation details.....	137
6.3 Numerical findings and discussions.....	138
6.3.1 Typical typology.....	138
6.3.2 Contact force and coordination number distribution.....	139
6.3.3 Parameter sensitive study.....	140
6.4 Conclusions.....	142
CHAPTER 7 Different particle size distribution of the crushable granular material within	
the confined compression throughout the repetitive loading	151

7.1 Introduction.....	151
7.2 DEM simulation procedures	153
7.3 Numerical findings and discussions	154
7.3.1 Macroscopic mechanical responses	154
7.3.2 Microscopic findings.....	156
7.4 Conclusions.....	159
CHAPTER 8 Conclusions and future work.....	170
8.1 Conclusions.....	170
8.2 Recommendations for the future work.....	172
REFERENCES.....	174

LIST OF FIGURES

Figure 2.1: Illustration of direct shear test on dense and loose sands.....	46
Figure 2.2: Schematic of saw-tooth model for dilatancy from Houlsby (1991).	46
Figure 2.3: Illustration of the associated contacts, contact normal (\mathbf{n}), contact force vector (\mathbf{f}), and contact vector (\mathbf{l}).....	46
Figure 2.4: Illustration of the strain calculation method from Wang et al. (2007a).	47
Figure 2.5: Schematic of measurement circle (a) from Bardet and Proubet (1991); (b) current calculated version.....	47
Figure 2.6: Illustrated of particle shape determination: (a) from Cho et al. (2006); (b) from Mitchell and Soga (2005).	47
Figure 2.7: Illustrated of Fourier descriptors from Mollon and Zhao (2012).	48
Figure 2.8: Schematic illustration of one dimensional compression behavior of sands: (a) idealized illustration; (b) experimental data from Yamamuro et al. (1996).	48
Figure 2.9: Experimental data of one dimensional compression from Nakata (2001a).....	49
Figure 2.10: Schematics of failure criterion of a broken particle and the related post-crushing replacing manners: (a) from Tsoungui et al. (1999); (b) from Lobo-Guerreo and his co-workers (2005, 2006); from Ben-Nun and Einav (2010).....	50
Figure 2.11: Illustration of calculation cycle in PFC^{2D} (Itasca, 2005).	50
Figure 2.12: Diagram of contact c between two entities.	50
Figure 2.13: Illustration of the contact law for both ball-to-ball and ball-to-wall contacts. ...	51
Figure 2.14: Schematic of the three boundary types within the DEM program.....	51
Figure 2.15: A schematic of specimen boundary.	52
Figure 2.16: The detailed procedure for isotropic consolidation.....	52
Figure 2.17: Schematic illustration of isotropic consolidation.....	53
Figure 3.1: (a) Schematic of the particle shapes; (b) illustration of different particle shape indexes.	66
Figure 3.2: Schematic of the numerical specimen and particle size distribution.....	67
Figure 3.3: Macroscopic behaviour of the numerical results (a) relationship between the principal stress ratio and the axial strain; (b) relationship between the volumetric strain and the axial strain; (c) error bars of the stress ratio in the critical state.	68
Figure 3.4: Peak friction angle (a), critical friction angle (b), and peak dilation angle (c) versus different shape quantitative indexes.....	70
Figure 3.5: Macroscale granular deformation observations and microscale rose diagrams at the critical state (15% axial strain) (a) painted grid distribution, (b) accumulated shear strain distribution, (c) statistical particle contact orientation and the related contact normal force, and (d) effect of the SF value on the orientation of shear band.	71
Figure 3.6: Illustration of the accuracy of the SFF relationship with collected data for different average contact normal forces (Eq. 3.2(a)) (a), relationship between respective anisotropic coefficients of contact normal (b), contact normal force (c), contact tangential force (d) and SF.....	72
Figure 3.7: Contact normal vector anisotropy coefficient (a) and contact tangential vector anisotropy coefficient (b) versus axial strain (polar distribution of Elongated5 at critical state).	72

Figure 3.8: Comparison of the relationship between the stress force and the fabric evaluation from the general SFF relationship with the simplified forms.	73
Figure 3.9: The probabilistic distribution of the friction mobilisation: (a) the mobilisation index I_m at the peak state and critical state and (b) the average value of I_m correlated with SF at the peak state and critical state.	74
Figure 3.10: (a) Probability distribution function of normalised normal force at the critical state (15% axial strain); (b) relationship between the strong force exponent and SF.	75
Figure 3.11: Strength indexes and PDF of normalised normal force under different confining pressures: (a) peak friction angle, (b) critical state friction angle, (c) peak dilation angle, (d) macro-responses of Circle, and (e) Elongated5 at the critical state (15 % axial strain).	76
Figure 4.1: The two shapes used for the mixture analysis.	87
Figure 4.2: Schematic of the PSD and the four contact types within the shape mixtures.	87
Figure 4.3: Snapshots of normal force chains for the two shape mixtures: (a) $\eta m = 0.3$; (b) $\eta m = 0.7$	88
Figure 4.4: Macro strength curves for different shape mixtures (a) the variation of sine value of internal friction angle along the axial strain, (b) peak friction/dilation angle, (c) error bars of friction angle at the steady state.	89
Figure 4.5: Void ratio as a function of the various shape mixtures at different axial strain level from isotropic state to critical state.	90
Figure 4.6: (a) error bars of the four contact types propagate at the critical state; (b) error bars of the normalised contact forces at the critical state.	91
Figure 4.7: Friction mobilisation for different ηm at the critical state (a) the variation of I_{gm} ; (b) the variation of I_{cm}	92
Figure 4.8: Probability distribution of the mobilisation I_m for different ηm at the critical state (a) global mobility distribution; (b) CC contact distribution; (c) CE contact distribution; (d) EE1 contact distribution; (e) EEm contact distribution.	94
Figure 4.9: Probability distribution of normalised contact normal force at the steady state for different ηm (a) all contact types distribution; (b) CC contacts distribution; (c) CE contacts distribution; (d) EE1 contacts distribution; (e) EEm contacts distribution.	96
Figure 4.10: Average friction mobilisation I_{fm} with the associated normalised contact normal force at the steady state for the ηm (a) all contact types distribution; (b) CC contacts distribution; (c) CE contacts distribution; (d) EE1 contacts distribution; (e) EEm contacts distribution.	98
Figure 4.11: Error bars of anisotropic coefficients at the critical state: (a) coefficients of contact normal for the four contact types; (b) coefficients of contact normal force for the four contact types; (c) coefficients of contact tangential force for the four contact types.	99
Figure 5.1: (a) The illustration of contact rolling resistance model proposed by Iwashita and Oda (1998, 2000); (b) mechanical responses at contact points.	116
Figure 5.2: Verified the rolling resistance model (a) pure rolling test; (b) pure shearing test.	117
Figure 5.3: Schematic of PSD and particle morphology.	117
Figure 5.4: Schematic of typical monotonic undrained behavior of granular materials (Gu et	

al., 2014; Yimsiri and Soga, 2010).	118
Figure 5.5: Undrained macro responses of biaxial shear tests with different rolling resistance coefficients: (a) (b) stress paths; (c) (d) deviatoric stress versus axial strain; (e) (f) pseudo excess pore water pressure versus axial strain; (g) (h) effective mean stress versus axial strain; (i) (j) the mobilized friction angle versus axial strain.	120
Figure 5.6: Evaluation of stress paths for the granular assemblies with various initial densities and shapes.	120
Figure 5.7: Evolution of deviatoric stress with different initial densities: (a) Disk; (b) Elongate; (c) Triangular.	121
Figure 5.8: Evolution of pseudo excess pore water pressure with different initial densities: (a) Circle; (b) Elongate; (c) Triangular.	121
Figure 5.9: Illustration of the SFF relationship in Eq. (2.59) with the collected DEM data: (a) the medium packing for the three shapes; (b) two rolling resistance samples.	122
Figure 5.10: Evolution of average coordination number and mobilization index.	122
Figure 5.11: Contributing percentages of the three anisotropic coefficients to the undrained shear strength of samples.	123
Figure 5.12: Evolution of the anisotropic coefficient of contact normal α	124
Figure 5.13: Polar distribution of contact normal at quasi-steady state and critical state for the five samples.	126
Figure 5.14: Probability distribution of normalized contact normal force at the quasi-steady state and the critical state (30%) for the six samples.	127
Figure 5.15: Probability distribution of the friction mobilization index I_m at the quasi-steady state and the critical state (30%).	128
Figure 5.16: Average friction mobilization I_{mf} with the associated normalised contact normal force at the quasi-steady state (UR5 PTS) and the critical state (30%).	129
Figure 5. 17: Spatial distribution of accumulated rotation for rolling resistance samples and irregular assemblages.	131
Figure 6.1: Configuration of the crushable granular assemblage: (a) initial DEM sample; (b) final grains topology (vertical stress 100 MPa); (c) final contact force network (vertical stress 100 MPa).	143
Figure 6.2: (a) Evolution of the PSD in the entire assembly by number; (b) evolution of the PSD within the broken particles by number; (c) probability distribution function of the normalized normal contact force by the average normal contact force in log-linear scale; (d) Comparison of previous physical models with the present crushable DEM simulations at the ultimate state. (e) Comparison with the q model at the ultimate state.	145
Figure 6.3: Evolution of the contact force magnitudes: (a) normal contact force by number; (b) shear contact force by number; (c) total contact force by number.	146
Figure 6.4: Probability distribution function of the coordination number in the (a) log-log scale and (b) log-linear scale.	147
Figure 6.5: Effect of the size of the minimum permitted crushing particle (a) normal contact force by number; (b) shear contact force by number; (c) total contact force by number.	147
Figure 6.6: Sensitivity analysis of the Weibull modulus, inter-particle frictional coefficient,	

and tensile strength of the largest particle for the contact forces (a) normal contact force by number; (b) shear contact force by number; (c) total contact force by number.	148
Figure 6.7: Sensitivity analysis of the Weibull modulus, inter-particle frictional coefficient, and tensile strength of the largest particle for the PDE of the coordination number in (a) log-log scale and (b) log-linear scale.	149
Figure 6.8: Evolution of PSD of the broken particles by number and visualization of the ultimate contact force network (vertical stress 100 MPa).	150
Figure 7.1: The three initial PSDs.	161
Figure 7.2: One dimensional compression for three PSDs under cyclic loading (a) compression curves; (b) stress-strain curves.	162
Figure 7.3: The variation of K_0 for the three PSDs during 1st cyclic loading condition (a) Loading stage; (b) Unloading and Reloading stages.	163
Figure 7.4: Evaluation of PSD for the three samples at the final state (a) the uniformly graded packing; (b) the binary mixture packing; (c) the fractal graded packing.	164
Figure 7.5: (a) the variations of crushing mass ratio during loading and reloading stages; (b) the visualization of force chain at the initial stage.	165
Figure 7.6: Evolution of PSDs in the whole assembly by number (a) the uniform graded packing; (b) the bimodal graded packing; (c) the fractal graded packing.	166
Figure 7.7: Probability distribution of normalized contact normal force (a) uniform graded 10 MPa; (b) uniform graded 50 MPa; (c) uniform graded 100 MPa; (d) three PSDs 100 MPa (Loading stage); (e) three PSDs 50MPa (Unloading stage); (f) three PSDs 100 MPa (Reloading stage); (g) visualization of contact force chain in unloading stage 10 MPa.	167
Figure 7.8: Probability distribution of coordination number (a) uniform graded 10 MPa; (b) uniform graded 50 MPa; (c) three PSDs at loading stage; (d) three PSDs at reloading stage.	168
Figure 7.9: evaluation of the <i>CFC</i> during the 1st cyclic loading (a) uniform graded 10 MPa; (b) uniform graded 50 MPa; (c) uniform graded 100 MPa; (d) bimodal graded 10 MPa; (e) bimodal graded 50 MPa; (f) bimodal graded 100 MPa; (g) fractal graded 10 MPa; (h) fractal graded 50 MPa; (i) fractal graded 100 MPa.	169

LIST OF TABLES

Table 3.1: Quantitative value of the shape indexes.	65
Table 3.2: Input microscale parameters in DEM simulations.	65
Table 4.1: Sample shape mixtures for DEM simulations.	86
Table 4.2: Input micro parameters in DEM simulations.	86
Table 5.1: Samples to be sheared for the rolling resistance model under undrained condition.	115
Table 5.2: Samples for disks and irregular clumps from loose to dense.	115
Table 5.3: Model parameter values used in the DEM simulations.	115

CHAPTER 1

Introduction

1.1 General Background

Granular materials, such as gravel, sand, rock and asphalt are quite common media in geotechnical engineering. A special feature of granular materials is the uncertain phase, which cannot be directly categorized as an absolute solid, liquid or gas (Jaeger et al., 1996). The mechanical responses of these materials are rather complicated as a result of inherent discontinuous and heterogeneous nature. Due to these uncertainty or unclear situations, many researchers have been attracted in this region to explore the mechanics of granular materials. Although many valuable contributions have been published in the past decades, we are still far from achieving a general theory to predict the mechanical behavior of a granular material under various conditions, which can be influenced by many factors, e.g., the initial relative density, the loading history, the drainage condition, the initial anisotropy, the interparticle properties, the particle shape and other factors.

The main challenge for the granular media is how to reasonably predict the mechanical responses. There are two main theoretical directions to determine the mechanism of granular materials, the phenomenological or structural approach (Fedda, 1982). In addition, laboratory tests are considered to validate the existed model or to construct new relationship for the above two distinct views. The phenomenological approach is developed by the traditional continuum theory to construct related constitutive models (Been and Jefferies, 1985; Dafalias and Popov, 1975; Schofield and Worth, 1968). These models can efficiently predict the macroscopic behavior of some engineering problems through a simplified or practical formulation. However, due to the discrete feature of granular materials, there still exist many fundamental questions which cannot be quantitatively predicted satisfactorily by the constitutive models, such as the anisotropy, strain localization, crushability, liquefaction and

others. As the granular mass is discrete in nature, the structure approach based on the microscopic grain interaction is much more approximate than the physical basis of granular medium. Moreover, laboratory tests considering the microscopic physical variables have been significantly developed in the past four decades (Drescher and De Jong, 1972; Oda et al., 1985). In recent years, some advanced high-resolution x-ray micro-tomography and diffraction techniques have been considered to characterize the individual particle (Andò et al., 2012; Jia et al., 2007; Moreno et al., 2010). Some researchers have attempted to represent the inter-particle contact forces through the inter-particle strain fields and spatial contact distribution (Andrade and Avila, 2012; Hall et al., 2011; Hurley et al., 2014). However, it remains unavailable to directly describe the accurate inter-particle contact forces within the natural sands, particularly when particle shape and crushing effects are considered. As an alternative numerical structural approach, the discrete element method (DEM), which was originally developed by Cundall and Strack (1979), can be used to reproduce the macroscopic mechanical behavior and simultaneously obtain detailed contact information for each grain, including contact force and energy transmission. These internal indexes cannot be easily captured by the laboratory tests. The numerical DEM has been verified in many fundamental geotechnical problems. Many element tests have been carried out to pursue the mechanism of granular materials, such as shear banding (Iwashita and Oda, 1998; Jiang et al., 2011; Wang et al., 2007b), anisotropy evaluation (Guo and Zhao, 2013; Rothenburg and Bathurst, 1989; Thornton, 2000; Yang and Dai, 2010; Yang et al., 2013; Yin et al., 2010a), crushability (Åström and Herrmann, 1998; Jensen et al., 2001; McDowell and Harireche, 2002; Tsoungui et al., 1999), etc. Moreover, various complicated boundaries conditions can be applied in DEM. Furthermore, the microscopic mechanical findings by DEM can assist the continuum approach to construct effective constitutive model. In addition, with the highly developed computer technology, DEM has a potential to analyze the large scale engineering problems in the future.

1.2 Objectives and scope of the study

Particle shape can significantly influence both the microscopic and macroscopic mechanical behavior of a granular soil. Especially for the consideration within the geotechnical discipline,

the shear strength and dilation effect are highly depended on the irregular particle shape. However, for the non-convex particle shape assembles the results remain a qualitative feature, which is induced by the complicated and inaccurate shape descriptors. The main objective of this thesis report is to deeply explore and interpret the particle shape effect. In addition, comminution is an another key controller for many physical phenomenon in many fields, such as mineral processing, fault gouge metamorphism, powder technology, and so on (Ben-Nun, 2011). However, the knowledge of the mechanism of the comminution is rather limited. An effective fractal approach is proposed to investigate the confined granular comminution at the microscopic through DEM simulations. Hence, another core objective of this thesis is to explore the mechanical process of crushable granular materials under one-dimensional compression. DEM is a robust research tool, which can provide detailed information on an individual particle and its contact interaction. These contact data within a granular assembly can be used to explore the microstructure during loading transfer. Meanwhile, the variations of these statistical data can be considered to explain the macroscopic behavior. Hence many new techniques are developed to visualize the microscopic contact information for interpreting particle shape and crushing effects. This thesis is focused on exploring the particle shape effect and the crushing effect of granular sands under the quasi-static condition, where the rate-dependent deformation can be ignored. It should also be pointed out that only the induced anisotropy is considered in this thesis. In addition, due to the restriction of computation efficiency, the particle number is relatively smaller than the realistic sample.

Based on the two-dimensional (2D) numerical DEM simulations (*PFC^{2D}*), a systematic series of biaxial shear tests would be performed to quantitatively interpret the shape effects of non-convex granular assemblies. The characteristics of mixtures of shapes are composed of round and non-convex particles are explored by four internal contact types, which are presented on a deeper micro-scale. Furthermore, a traditional rolling resistance model would be implemented to compare with the simplified irregular granular assemblies under the undrained shearing condition.

2D DEM is adopted to investigate the micromechanics for crushable granular materials under

one-dimensional compression. In addition, the initial particle size distribution (PSD) and unloading-reloading condition will be investigated within these numerical comminution tests.

1.3 Thesis outline

This thesis is organized as follow:

Chapter 1 presents the general background of the research subject, research objectives and scope, as well as the thesis organization.

Chapter 2 firstly gives a summary of the macromechanics of granular materials. The framework of microscopic descriptors are then discussed to provide a background of the micromechanics. In addition, the development of particle shape, particle crushing, and related DEM modelling techniques are also briefly reviewed in this chapter. At the end of this chapter, the methodology of DEM including the governing principles, contact models, the codes development as well as the servo-control schemes for various boundary conditions are introduced.

Chapter 3 describes a simple quantitative framework for investigating the particle shape effect. A systematic series of biaxial shear tests are performed to obtain a suitable shape index. In addition, the accuracy of the stress-force-fabric (*SFF*) relationship is also investigated for these non-convex granular assemblies.

Chapter 4 investigates the characteristics of mixtures of shapes that are composed of round and non-convex (Elongate) particles. Four internal contact types are applied on a deeper micro scale to explore the correlations from the information of effective contacts within the granular assemblages. The variation of macroscopic mechanical behavior will then be explored by the microscopic information of the respective contact types.

Chapter 5 compares the traditional rolling resistance model with the simplified irregular granular assemblages under the “undrained” shearing condition, which is different from the

above two chapters. It is also concentrated to clarify the feasibility of artificial rolling resistance effect.

Chapter 6 studies the mechanical process of crushable granular materials during one-dimensional compression. Detailed parametric studies have been performed to identify the sensitivity of contact force distribution, coordination number distribution, and PSD within the granular assemblies. Moreover, a simple method is developed in the current study to reveal the fractal distribution of contact forces in comminuted granular materials.

Chapter 7 extends the investigation performed in chapter 6 to consider the initial PSD within the unloading-reloading procedure. The initial uniform, bimodal and fractal granular packings are simulated to compare with the experimental tests.

Chapter 8 summarizes the major findings of this dissertation and recommends an outlook necessary for further studies.

CHAPTER 2

Literature review

2.1 Introduction

In this chapter, the shear strength, dilatancy and anisotropy of granular materials are firstly presented to give a simplified background on the associated macromechanics.

Afterwards, an introduction to the micromechanics of granular sands is provided. Meanwhile a systematic review of micro physical descriptors is given. Next, a background of the stress force-fabric (*SFF*) relationship is presented.

A review of particle shape effect, particle crushing effect and related DEM modelling techniques for the granular sands are given. Moreover the related physical phenomenon is also presented

At the end of this chapter, the procedures of DEM is presented, followed by various boundary conditions with associated servo-controlling algorithms. In addition, the typical mechanical behavior of granular sands under these loading paths are also included.

2.2 Macromechanics background of granular sands

How to suitable describe the stress-strain behavior of granular sands is still a challenging task for both the academic researchers and practical engineers. It has been proved that the critical state soil mechanics (*CSSM*) framework proposed by Schofield and Wroth (1968) can be used to efficiently predict the granular sands behavior. Critical state in granular sands intrinsically indicates the granular packing reaches a constant stress, constant void ratio and constant volume during the external shearing.

2.2.1 Shear strength and dilatancy

The shear strength is a fundamental soil property index in practical geotechnical designs. Its

value can be determined by the Mohr-Coulomb yield criterion (1773), which can be found from any soil mechanical book (Das, 2008; Mitchell and Soga, 2005; Schofield and Worth, 1968; Wood, 1990). For cohesionless granular materials the Mohr-Coulomb yield criterion can be written as:

$$\tau = \sigma_n \tan \phi \quad (2.1)$$

where τ is the shear stress at failure, σ_n is the normal stress on the failure plane, and ϕ is the friction angle, which is generally considered as a bulk property to describe the shear strength of granular sands. A direct shear test equipment is usually adopted to measure the friction angle ϕ . Meanwhile, a typical stress-strain relationships of direct shear test rests in loose and dense sands is shown in Figure. 2.1, which can also be found from any soil mechanics text book. The loose sand possess a clear strain-hardening feature, whilst the dense sand shows a strain-softening behavior with a clear peak state. They all achieve a critical state at the large strain condition. Hence the peak friction angle ϕ_p and the critical state friction angle ϕ_{cv} are adopted to characterize the strength of sand. As an alternative laboratory device, the triaxial test is also used to determine the strength property. The friction angle can be expressed by the principal stresses for both the two tests as follow:

$$\sin \phi = \frac{\sigma_1 - \sigma_3}{\sigma_1 + \sigma_3} = \frac{q}{p}; p = (\sigma_1 + \sigma_3) / 2; q = (\sigma_1 - \sigma_3) / 2 \quad (2.2)$$

where σ_1 and σ_3 are the major and minor principle stresses, p means the effective stress, q indicates the effective deviator stress.

It is generally known that the value of peak friction angle reduces with increasing consolidated void ratio and stress level. Moreover, the triaxial test would induce a lower friction angle than the plane strain test. These early views about the peak friction angle can be seen from many soil mechanics handbook or papers (Bolton, 1986; Houlsby, 1991; Schanz and Vermeer, 1996). The critical friction angle is a unique feature at the constant volume stage (Bolton, 1986; Houlsby, 1991; Rowe, 1971; Schanz and Vermeer, 1996). Recently, many researchers continued the laboratory tests to explore the strength of granular sands by considering various more specific indexes, such as particle shape (Cho et al., 2006; Shin and

Santamarina, 2012), fabric (Been et al., 1991; Guo, 2008; Chang and Yin, 2010; Yin and Chang, 2013), particle crushing (Coop et al., 2004; Indraratna et al., 2014b), etc. Even for the unified critical state friction angle, there are still many conflicts which are mainly induced by the limited deformation capability of triaxial tests. Sadrekarimi and Olson (2011) have carried out a systematic work on triaxial tests and ring shear tests to explore the features of friction angle of sands, especially at the critical state. The tested samples were prepared by air-pulviated and moist-tamped methods. They pointed that the critical state friction angles measured in triaxial tests were independent of consolidated stresses, but related to the consolidated void ratio, which may be induced by the displacement limit of the triaxial device. For the ring shear tests, the critical friction angles are independent of the stress path, sample preparations, consolidated void ratios and consolidated pressures (over 200 kPa). Indraratna and his co-workers (2014) performed a series of triaxial tests (axial strain range 20% to 25%) on rail ballasts and showed some conflict with the studies on carbonate sands by ring shear tests (Bandini and Coop, 2011; Coop et al., 2004).

The concept of dilatancy in soil mechanics is initially described as that soil particle would lift over one another due to occurrence of sliding by Rowe (Rowe, 1962). As described by the geotechnical pioneers (Bolton, 1986; Houlsby, 1991), the understanding about the soil dilatancy mechanism can help us to know the development of stress-strain relationship due to shearing. Its magnitude can be described as the ratio of plastic volume strain rate to plastic shear strain rate. For a plane strain condition ($\varepsilon_2 = 0$), it can be represented by the ratio of plastic principle strain rates as follow (Bolton, 1986; Houlsby, 1991):

$$\sin \psi = \frac{-(\dot{\varepsilon}_1^p + \dot{\varepsilon}_3^p)}{\dot{\varepsilon}_1^p - \dot{\varepsilon}_3^p} \quad (2.3)$$

where $\dot{\varepsilon}_1$ and $\dot{\varepsilon}_3$ mean the plastic major and minor principal strain rates, and ψ is the dilation angle. Another expression (Houlsby, 1991) is used the ratio of plastic volume strain increment ($d\varepsilon_v^p$) and deviator strain increment ($d\varepsilon_q^p$) type to define the dilatancy (d), which can be expressed as:

$$d = -\frac{d\varepsilon_v^p}{d\varepsilon_q^p} \quad (2.4)$$

The essential of above two equations are the same ($\sin\psi = d$). The magnitude of dilation angle can be generally influenced by the void ratio, stress levels, particle shape effect, particle crushing, and so on. The connection between the friction angle and the dilation angle has been studied by many researchers. Among these studies, Houlsby (1991) presented an extremely clear framework for the followers to understand. The simplified saw-tooth model in Figure 2.2 is used to explain the relationship between the friction angle and dilation angle when sliding occurs. Hence, the mobilized friction angle can be rewritten as the sum of the critical state friction angle and the dilation angle as:

$$\frac{\tau}{\sigma_n} = \tan \phi = \tan(\phi_{cv} + \psi) \Rightarrow \phi = \phi_{cv} + \psi \quad (2.5)$$

where ϕ_{cv} means the critical state friction angle. This type of relationship is generally named as a flow rule (Houlsby, 1991). Two of other initially theoretical flow rules are proposed by Taylor (1948) and Rowe (1962) through respective concepts towards to a similar result. Taylor (1948) suggested to use an energy correction for calculating dilation. Its formulation can be written as:

$$\tan \phi = \tan \phi_{cv} + \tan \psi \quad (2.6)$$

This concept is also adopted by Schofield and Wroth (1968) to develop the Cam-Clay model. The other initial flow rule is proposed by Rowe (1962), who communicated with Taylor and built a new stress-dilatancy relationship. This flow rule is based on a function of the stress ratio and the strain rate ratio assuming a minimum energy ratio hypothesis. This function can be expressed as:

$$\frac{\sigma_1}{\sigma_3} = \tan^2\left(\frac{\pi}{4} + \frac{\phi_\mu}{2}\right)\left(\frac{-\dot{\varepsilon}_3}{\dot{\varepsilon}_1}\right) \quad (2.7)$$

where ϕ_μ is inter-particle friction angle. However, the dilatancy feature of a granular sand is not only affected by the stress ratio. Other indexes such as the relative density, particle shape, and crushability can also influence the rate of dilatancy. Rowe's stress-dilatancy theory (1962) is not able to evaluate the complicated mechanical responses of granular sands.

Bolton (1986) proposed an empirical flow rule by comparing the experimental data on the strength and dilatancy of 17 sands in axisymmetric or plane strain loadings with different consolidated densities and confining pressures. This empirical flow rule can be expressed as:

$$\left\{ \begin{array}{l} \phi_p - \phi_{cv} = 0.8\psi_{\max} = 5I_R; \text{ plane strain} \\ \phi_p - \phi_{cv} = 0.5\psi_{\max} = 3I_R; \text{ triaxial strain} \\ \left(\frac{-d\varepsilon_v}{d\varepsilon_1}\right)_{\max} = 0.3I_R \\ I_R = I_D(Q - \ln p) - R, I_D = \frac{e_{\max} - e}{e_{\max} - e_{\min}} \end{array} \right. \quad (2.8)$$

where ϕ_p indicates the peak friction angle, ψ_{\max} is the maximum value of dilation angle, I_R means the relative dilatancy index, I_D indicates the relative density, p is the mean effective stress [kPa], Q and R are fitting parameters which depend on the intrinsic material properties, e_{\max} and e_{\min} are the related maximum and minimum void ratio.

Houlsby (1991) compared the above four flow rules under the plane strain condition, and pointed that the differences were relatively low. Moreover, the Rowe flow rule (1962) matched well with the empirical Bolton flow rule (1986) which both fall in the middle range. However, the critical friction angle in Bolton flow rule (1986) for both plane strain and triaxial strain loadings is assumed equal, which is not according with the experimental tests. Then, Schanz and Vermeer (1996) performed extensive triaxial compression tests on Hostun sand, and extended previous plane strain flow rules to triaxial strain condition.

Some other researchers proposed indirect indexes to quantify the strength and dilatancy of granular sands. Been and Jefferies (1985) presented a state parameter $\psi = e - e_c$ to determine the dilation or compression feature of a granular sand under the same mean effective stress, which was constructed within the framework of critical state soil mechanics (Schofield and Worth, 1968). The concept of this index intuitively comes from the figure void ratio or special volume versus the logarithmic effective mean normal stress (Wroth and Bassett, 1965). Another index I_s is proposed similar as the type of relative density for describing the sand dilatancy feature during shear (Ishihara, 1993). Li and Dafalias (2000)

pointed out the drawbacks of Rowe's stress dilatancy theory and proposed a new state-dependent dilatancy for suitable predicting the granular media, where a micromechanical analysis was considered to verify the macroscopic behavior. This dilatancy function can be expressed as:

$$d = d(\eta, e, Q, C) \quad (2.9)$$

where η means the stress ratio, Q indicates internal state variables other than intrinsic material constant C and void ratio e . Afterwards, Yang and Li (2004) adopted this state-dependent dilatancy to explore the influence of density and stress level. Moreover, a linear flow rule is suggested to connect the peak friction angle and the maximum dilation angle.

Many Ph.D. dissertations have detailedly reviewed the shear strength and dilatancy for the granular sands. Here some of them are listed for easy capture of the related information, such as Sallam (2004) at the University of Florida, Li (2006) at the Hong Kong University of Science and Technology, Cox (2008) at the University of Arizona, Yang (2014) at the University of Nottingham, and so on.

2.2.2 Anisotropy

The macro mechanical behavior of a granular soil is significantly influenced by the anisotropy, which is initially distinguished into inherent anisotropy and induced anisotropy by Casagrande and Carrillo (1944). The inherent anisotropy is produced during the geologic sedimentation history in nature or sample preparation in laboratory. The latter induced anisotropy is mainly formed by external loading. Here the anisotropy study on the laboratory tests and constitutive models are briefly reviewed for introducing the fabric quantification from microscopic point of view in the followed section.

The inherent anisotropic tested sample can be prepared by pouring into tilting mold by different angles (Arthur and Menzies, 1972; Yamada and Ishihara, 1979). Many geotechnical tests, including true triaxial tests (Ochiai and Lade, 1983; Yamada and Ishihara, 1979) and hollow cylinder tests (Karstunen and Yin, 2010; Lade et al., 2008; Nakata et al., 1998;

Pradhan et al., 1979) have been performed. All these tests demonstrate that the initial anisotropy can significantly influence the granular mechanical responses, especially under small strain level.

For analyzing the induced anisotropy caused by external loading, a series of plane strain tests on dense sand have been carried out by changing the principal stress directions (Arthur et al., 1977). The results indicate that the induced anisotropy can significantly influence the stress and strain relationship. Afterwards, both monotonic (Gajo and Wood, 1999) and cyclic triaxial tests (Yamada and Ishihara, 1982) are performed to explore the pre-sheared samples. It can be found that the pre-loading history can significantly form a material anisotropy, which plays an important role in the soil behavior.

In order to reasonable predict the macro responses of granular sands, the anisotropy feature should be involved in the constitutive models. The pioneer work is proposed by Cowin (1985), who considered the fabric tensor to determine the anisotropy of the porous elastic solid. Oda and Nakayama (1989) introduced the fabric tensor to construct a continuum model for analyzing soil plasticity. Many investigators followed this framework and validated the efficiency of fabric tensors for granular materials (Azami et al., 2010; Dafalias and Manzari, 2004; Li and Dafalias, 2002; Tejchman et al., 2007; Tobita and Yanagisawa, 1992). However, the above methods usually adopted a fixed fabric tensor during the loading procedure. Recently, Li and Dafalias (2012) have presented a robust anisotropy critical state theory, where the fabric tensor can be evaluated through a proper state value.

2.3 Micromechanical description of granular sands

The macro responses of a granular sand is controlled by the development of microscopic particle interactions and surrounding voids. Using the DEM, many microscale physical properties can be captured during the resistance of external loading. It has been pointed out in the above chapter that the continuum mechanics cannot reasonably capture the mechanism of a granular media due to its discrete feature. Hence DEM can be considered as a robust tool to develop the present constitutive models, which still dominate our understanding in

geotechnical engineering. As mention by O’Sullivan (2011) in her edited book “Particulate discrete element modelling”, geomechanics should be investigated by combining the continuum and discrete consideration. Another book edited by Oda and Iwashita (1999) also gives a similar view that some continuum mechanical concepts (stress and strain) can describe a granular assembly. Therefore, in this subchapter, the average stress tensor and strain tensor are firstly presented to describe the microstructural feature through a continuum scope. Next the fabric structure are quantitatively described by the spatial distributed microscopic contact variables. Some microscopic descriptors are then defined. Afterwards, a stress-force-fabric relationship is briefly described for connecting the micro-mechanics and macro-mechanics.

2.3.1 Stress and strain tensors

The definitions of an average micro-structural stress tensor within a volume have been determined by many researchers with different mathematical considerations (Bagi, 1996; Christoffersen et al., 1981; Oda and Iwashita, 1999; Rothenburg and Bathurst, 1989). However, the essential of these formulations is the same, and can be derived into a general form. For a closed continuous domain with volume V , a distributed force $t_i(x_i)$ is loaded on its boundary S , and the body force $g_i(x)$ is acted within the domain, the equilibrium equation under a quasi-static condition is:

$$\sigma_{ij,i} - \rho g_i = 0 \quad (2.10)$$

The body force in the current study is ignored. The material boundary condition is satisfied as follow:

$$\sigma_{ij} n_j = t_i \quad (2.11)$$

where n_i represents the unit normal vector on S . Hence the statistical average stress tensor over a volume V of material can be defined as:

$$\bar{\sigma}_{ij} = \frac{1}{V} \int_V \sigma_{ij} dV \quad (2.12)$$

The stresses within each particle are assumed as the average value ($\sigma_{ij} = 0$ in the voids). Hence the above equation can be replaced by the sum of the stresses acting on all the particles ($p = \text{particle}$) within the domain.

$$\bar{\sigma}_{ij} = \frac{1}{V} \sum_{p \in V} \sigma_{ij}^p V_p \Rightarrow \bar{\sigma}_{ij} = \frac{1}{V} \sum_{p \in V} \sum_{c \in p} f_i^{pc} l_j^{pc} \quad (2.13)$$

As each contact is composed by two entities, it would be identified as two different contacts. Eq. (2.12) can be rewritten as:

$$\bar{\sigma}_{ij} = \frac{1}{V} \sum_{c \in V} f_i^c l_j^c \quad (2.14)$$

where f_i^c is the i th component of the contact force at contact c within the assembly, l_j^c is the j th component of the contact vector at contact c , V is the volume of the assembly; The illustration of these variables is described in Figure 2.3.

The microstructural expression of strain tensor for a granular media has been explored by many researchers in the past three decades (Bagi, 1996; Cambou et al., 2000; Cundall and Strack, 1979; Dedecker et al., 2000; Kruyt and Rothenburg, 1996; Kuhn, 1999; Li and Li, 2009; Liao et al., 1997; O'Sullivan et al., 2003; Satake, 2004; Thomas, 1997; Wang et al., 2007a). An early version of overview of the different microstructural strain definitions is summarized and compared by Bagi (2006). O'Sullivan (2011) then systematically discussed the calculated approaches of particulate strain. The difference of these approaches is mainly on how to efficiently capture the displacement gradients, which control the calculated strain. There are two directions for predicting a suitable displacement gradient. They are best fit approach and spatial discretization approach (also named equivalent continuum approach by Bagi (2006)). The most convenient and speedy algorithm within the best fit approaches is proposed by Cundall and Strack (1979). The related governing equations of the average of particle translation (V_i^0) and position (x_i^0) for an analyzed region are briefly shown as follow:

$$V_i^0 = \frac{\sum_{p \in N_p} V_i^p}{N_p}, \quad x_i^0 = \frac{\sum_{p \in N_p} x_i^p}{N_p} \quad (2.15)$$

where V_i^p and x_i^p are the translation velocity and centroid location for particle p , N_p is the number of particles within the analyzed domain. The measure relative velocity and position

for each particle in the calculated region to the average values are given by:

$$\tilde{V}_i^p = V_i^p - V_i^0 \quad (2.16)$$

$$\tilde{x}_i^p = x_i^p - x_i^0 \quad (2.17)$$

If the relative translation of each particle satisfies a uniform deformation rate gradient tensor α_{ij} , the relative velocity of every particle would be predicted as:

$$\tilde{V}_i^p = \alpha_{ji} \tilde{x}_j^p \quad (2.18)$$

However, in reality the above equation is usually unsatisfied. Generally, we need to seek a specific α_{ij} tensor to best fit the particle translations through a minimization principle as follow:

$$Z = \sum_{p \in N_p} (\tilde{V}_i^p - \alpha_{ji} \tilde{x}_j^p)(\tilde{V}_i^p - \alpha_{ji} \tilde{x}_j^p) \Rightarrow \min \quad (2.19)$$

where Z is the sum of the squares of difference between the actual velocity and the predicted value through the best fit method. The function Z is minimized as:

$$\frac{\partial Z}{\partial \alpha_{ij}} = 0 \quad (2.20)$$

Substituting Eq. (2.18) into Eq. (2.19) and using Eq. (2.20) to minimize, the following four equations would be obtained in 2D (3D nine equations):

$$\begin{bmatrix} \sum_{p \in N_p} \tilde{x}_1^p \tilde{x}_1^p & \sum_{p \in N_p} \tilde{x}_2^p \tilde{x}_1^p \\ \sum_{p \in N_p} \tilde{x}_1^p \tilde{x}_2^p & \sum_{p \in N_p} \tilde{x}_2^p \tilde{x}_2^p \end{bmatrix} \begin{bmatrix} \alpha_{1i} \\ \alpha_{2i} \end{bmatrix} = \begin{bmatrix} \sum_{p \in N_p} \tilde{V}_i^p \tilde{x}_1^p \\ \sum_{p \in N_p} \tilde{V}_i^p \tilde{x}_2^p \end{bmatrix} \quad (2.21)$$

where N_p is no less than 3 to guarantee the left matrix is always positive definite. All the four components can be obtained by a single LU-decomposition as well as two back substitutions for $i = 1$ or 2 (Bagi, 2006). This best-fit approach applied by Cundall and Strack (1979) is simple in calculation and valid for both 2D and 3D conditions. However, particle rotation is not accounted in the strain tensor. In addition, the shear bands or localizations cannot be easily captured for a relative large region by all the best-fit approaches (Cambou et al., 2000; Cundall and Strack, 1979; Liao et al., 1997)

Another strain calculation method is spatial discretization approach, which have been

developed by many investigators (Bagi, 1996; Dedecker et al., 2000; Kruyt and Rothenburg, 1996; Kuhn, 1999; O'Sullivan et al., 2003; Thomas, 1997; Wang et al., 2007a). These various calculated methods have their respective advantages and limitations, which are given by O'Sullivan (2011). In this dissertation, the strain calculation method proposed by Wang et al. (2007a). It can directly obtain the displacement gradient due to the movements of individual particles. Moreover, this approach does not consider the interpolation functions, which may induce erratic internal element strains (O'Sullivan et al., 2003) or overly smooth the displacement gradient (Wang et al., 2007a). The framework of this method can be seen in Figure 2.4, which includes a grid-based reference configuration and a displacement calculated algorithm. Each grid point in this method is assigned only to one particle j governed by the follow principle:

$$\frac{d_j}{r_j} \leq \frac{d_i}{r_i} \quad (i = 1, 2, \dots, N_p; i \neq j) \quad (2.22)$$

where the subscript i and j represent the particle number, r_i means the radius of particle i , d_i is the distance from the centroid of particle i to the grid point, N_p is the number of particles within the analyzed region. The grid space is applied by the Eq. (2.22) before the deformation occurs. Moreover, the spacing size in this method is suggested equivalent as the medium particle diameter (D_{50}), which has verified by Wang et al. (2007a) for capturing the shear band with an acceptable resolution. As shown in Figure 2.4, the displacement of each grid point can be calculated by the displacement and rotation of the related particle, and the calculated equation is given by:

$$\begin{aligned} u_x^g &= u_x^p + d [\cos(\theta_0 + \omega) - \cos(\theta_0)] \\ u_y^g &= u_y^p + d [\sin(\theta_0 + \omega) - \sin(\theta_0)] \end{aligned} \quad (2.23)$$

where u_x^g and u_y^g are the grid displacement components on the x and y directions, u_x^p and u_y^p are the particle displacement components along the x and y directions, d is the distance from the particle centroid to the grid point, θ_0 is the initial phase angle of the particle centroid towards to the corresponding grid point, and ω is the accumulated rotation. This strain calculated method can account for both the translations and rotations for a deformed granular assembly. Detail information about this strain calculation method can be seen in

Wang et al. (2007a).

2.3.2 Fabric structure

2.3.2.1 Void ratio

The void ratio of granular materials is an important physical characteristics associated with the relative densities, stress-strain relationship and other engineering behaviours. It can be transformed into porosity or specific volume by a fairly simple formulation. Both of these indexes can be consider to predict the density of a granular packing. O’Sullivan’s (2011) discussed that the scale effect should be carefully considered (Munjiza, 2004). Hence the statistical void region should be large enough to reduce the extra errors. Bardet and Proubet (1991) proposed a measured circle to determine the void ratio, which is illustrated in Figure 2.5. In this study, a modified version of measured circle is suggested to accurately calculate the void ratio, where the contact overlapping regions are considered. The expression is shown as follow:

$$e = \frac{A_m - \sum_{N_p} A_p + \sum_{N_c} A_c}{\sum_{N_p} A_p - \sum_{N_c} A_c} \quad (2.24)$$

where N_p is the total number of particles that lie within the global region, N_c represents the active external contacts, which include the particle-particle and particle-wall contacts, A_p is the individual particle area, A_c is the overlap area of each active contact point (which is updated in every numerical step), A_m is the area of measurement region, which can be like as a circle in Figure 2.5 or rectangular.

2.3.2.2 Coordination number

The coordination number is another index to describe the contact density at a microscopic level. It can also be used to indirectly reflect the packing relative density as well as the internal structural stability of a granular media. The initial expression of the coordination number is as follow:

$$Z = \frac{2N_c}{N_p} \quad (2.25)$$

where N_c indicates the total number of contacts, N_p is the number of particles. Each contact is shared by two particles. Thornton (2000) pointed out that many numerical simulations possessed some particles with one or no contact. These specific particles have no contribution on the stable state of stress. A modified coordination number is suggested by Thornton (2000) and used throughout this study which can be determined as:

$$Z_m = \frac{2N_c - N_1}{(N_p - N_0 - N_1)} \quad (2.26)$$

where N_0 means the number of particles with no contact, and N_1 is the number of particles with only one contact.

2.3.2.3 Contact normal orientation distribution

As shown in Figure 2.3, the contact normal can be determined as a unit vector to describe the orientations of contacts within a granular media. This spatial vectors can be statistical related to the fabric tensor, as suggested by many previous researchers (Oda and Iwashita, 1999; Satake, 1993). A fabric tensor can be generally expressed as:

$$\phi_{ij\dots l} = \frac{1}{N_c} \sum_{c \in N_c} n_i^c n_j^c \dots n_l^c \quad (2.27)$$

where n_i^k ($i = 1,2,3$) are three direction cosines of the unit vector \mathbf{n}^k with related reference axes, N_c is the total number of contacts. The general form of it is multidimensional arrays which are difficult to interpret. The most commonly used form is a simplified second-order style, which can be written as:

$$\phi_{ij} = \frac{1}{N_c} \sum_{c \in N_c} n_i^c n_j^c \quad (2.28)$$

A density function $E(n)$ can also be used to express the statistical distribution of contact normal. In the current dissertation, the second-order fabric tensor the density function is applied as:

$$E(n) = \frac{1}{2\pi} (1 + a_{ij}^c n_i n_j) \quad (2.29)$$

where a_{ij}^c indicates a second-order anisotropy tensor, which can be used to predicate the deviations from the isotropic distribution of contact unit normal vector. The integration of this

density function over the whole domain Ω is 1, as

$$\int_{\Omega} E(n)d\Omega = 1 \quad (2.30)$$

The above equation can also be rewritten as the following formulation with consideration on the inclined angle θ between the vectors.

$$\int_0^{2\pi} E(\theta)d\theta = 1 \quad (2.31)$$

For a 2D case, $E(\theta)$ should be a periodic function with the period of 2π , and expanded by a Fourier series. The second-order Fourier expression using anisotropic parameters has been presented by Rothenburg and Bathurst (1989). It can be rewritten as:

$$E(\theta) = \frac{1}{2\pi} [1 + a \cos 2(\theta - \theta_a)] \quad (2.32)$$

where a represents the anisotropy coefficients of contact normal, θ_a describes the principal direction of contact normal. Their value can be equally obtained from the fabric tensor as follow (Bathurst and Rothenburg, 1992; Dai, 2010; Guo and Zhao, 2013; Li and Yu, 2013; Seyedi Hosseininia, 2013; Wang et al., 2007b; Yin et al., 2010a; Yin et al., 2010b):

$$a = \sqrt{(a_{11}^c - a_{22}^c)^2 + (a_{12}^c + a_{21}^c)^2}; \theta_a = \frac{1}{2} \arctan\left(\frac{a_{12}^c + a_{21}^c}{a_{11}^c - a_{22}^c}\right) \quad (2.33)$$

The above components of a_{ij}^c can be determined as follow:

$$\phi_{ij} = \int_{\Omega} E(n)n_i n_j d\Omega = \frac{1}{N_c} \sum_{c \in N_c} n_i^c n_j^c \quad (2.34)$$

2.3.2.4 Contact force distribution

As described in Figure 2.3, the contact force vector (f^c) is composed of the contact normal force vector (f_n^c) and the contact tangential force vector (f_t^c). For quantitatively investigating the spatial distribution of both types of contact force vectors, two second rank tensor are applied to describe the variations of contact forces. The contact normal force vector is along the contact normal direction, and the contact tangential force vector is perpendicular to it. With the orientation of contact normal $\mathbf{n} = (\cos\theta, \sin\theta)$ and contact tangent $\mathbf{t} = (-\sin\theta, \cos\theta)$, the two tensors can be calculated by (Guo and Zhao, 2013; Li, 2006; Seyedi Hosseininia, 2013; Yang et al., 2013):

$$F_{ij}^n = \frac{2\pi}{N_c} \sum_{c \in N_c} \frac{f_n^c n_i n_j}{E(n)} \quad (2.35)$$

$$F_{ij}^t = \frac{2\pi}{N_c} \sum_{c \in N_c} \frac{f_t^c t_i^c n_j^c}{E(n)} \quad (2.36)$$

where F_{ij}^n and F_{ij}^t describe the fabric tensors of contact normal and tangential forces, N_c means the total number of contacts, f_n^c and f_t^c are the magnitude of contact normal force and contact tangential force at contact c . The angular statistical distribution of contact normal force ($\bar{f}_n(\theta)$) and contact tangential force ($\bar{f}_t(\theta)$) can also be described as second-order Fourier expressions similar as the contact normal distribution. They can be rewritten as:

$$\bar{f}_n(\theta) = \bar{f}_0 [1 + a_n \cos 2(\theta - \theta_f)] \quad (2.37)$$

$$\bar{f}_t(\theta) = -\bar{f}_0 a_t \sin 2(\theta - \theta_t) \quad (2.38)$$

where a_n and a_t are the magnitude coefficient of contact normal force and contact tangential force anisotropies, θ_f and θ_t denote the related principal directions of contact normal and tangential forces, \bar{f}_0 indicates the average contact normal force from different θ with the same weight. The magnitude of \bar{f}_0 can be determined as:

$$\bar{f}_0 = \frac{1}{2\pi} \int_0^{2\pi} \bar{f}_n(\theta) d\theta \quad (2.39)$$

The two anisotropic coefficients and related principle angles of the contact forces within a granular assemblage can be determined by the numerical discrete data through the type of the two above fabric tensors (direction-averaged), which can be equivalent as the integration of the Fourier series in the whole domain. The transforming formulations are shown as follow:

$$F_{ij}^n = \frac{1}{2\pi} \int_0^{2\pi} \bar{f}_n(\theta) n_i n_j d\theta = \frac{1}{N_c} \sum_{c \in N_c} \frac{f_n^c n_i n_j}{1 + a_{kl}^c n_k n_l} \quad (2.40)$$

$$F_{ij}^t = \frac{1}{2\pi} \int_0^{2\pi} \bar{f}_t(\theta) t_i n_j d\theta = \frac{1}{N_c} \sum_{c \in N_c} \frac{f_t^c t_i n_j}{1 + a_{kl}^c n_k n_l} \quad (2.41)$$

Substituting equation (2.37) and (2.38) into above two equation respectively, the above mentioned anisotropic parameters can be determined by:

$$a_n = \frac{\sqrt{(F_{11}^n - F_{22}^n)^2 + (F_{12}^n + F_{21}^n)^2}}{2}; \theta_f = \frac{1}{2} \arctan\left(\frac{F_{12}^n + F_{21}^n}{F_{11}^n - F_{22}^n}\right) \quad (2.42)$$

$$a_i = \frac{\sqrt{(F'_{11} - F'_{11})^2 + (F'_{12} + F'_{21})^2}}{2}; \theta_i = \frac{1}{2} \arctan\left(\frac{F'_{12} + F'_{21}}{F'_{11} - F'_{22}}\right) \quad (2.43)$$

2.3.2.5 Contact vector distribution

Similar to the discussion of contact force vectors distribution, the spatially statistical distribution of contact vectors is also investigated in this dissertation. The determination of a contact vector is a vector which connects the particle center and the contact point. Each contact vector can be decomposed to the normal and tangential components with respect to the local related coordinate system. Its magnitude is highly related to the particle shape (Li, 2006). With the same manner of contact force vectors distribution, two tensors are adopted to quantitatively characterize the contact vectors distribution within a particle assembly. They can be written as follow (Guo and Zhao, 2013; Li, 2006; Seyed Hosseinia, 2013; Yang et al., 2013):

$$V_{ij}^n = \frac{2\pi}{N_c} \sum_{c \in N_c} \frac{l_n^c n_i^c n_j^c}{E(n)} \quad (2.44)$$

$$V_{ij}^t = \frac{2\pi}{N_c} \sum_{c \in N_c} \frac{l_t^c n_i^c n_j^c}{E(n)} \quad (2.45)$$

where V_{ij}^n and V_{ij}^t describe the fabric tensor of contact normal vectors and contact tangential vectors, N_c means the total number of contacts, l_n^c and l_t^c are the lengths of contact normal vector and contact tangential vector at contact c . The angular statistical distribution of the average contact normal vector ($\bar{l}_n(\theta)$) and contact tangential vector ($\bar{l}_t(\theta)$) can also be described as second-order Fourier expressions similar as above contact forces distribution. Their expressions are shown as:

$$\bar{l}_n(\theta) = \bar{l}_0 [1 + b_n \cos 2(\theta - \theta_{bn})] \quad (2.46)$$

$$\bar{l}_t(\theta) = -\bar{l}_0 b_t \sin 2(\theta - \theta_{bt}) \quad (2.47)$$

where b_n and b_t are the magnitude coefficient of anisotropy in average contact normal and tangential vectors, θ_{bn} and θ_{bt} denote the related principal directions of average contact normal and tangential vectors, \bar{l}_0 indicates the length of average normal contact vectors from different θ with the same weight. The magnitude of \bar{l}_0 can be determined as:

$$\bar{l}_0 = \frac{1}{2\pi} \int_0^{2\pi} \bar{l}_n(\theta) d\theta \quad (2.48)$$

Similar to the contact force vectors distribution, the two tensors of contact vectors can also be equivalent to the integration of the Fourier series in the whole domain. The transforming formulations are shown as follow:

$$V_{ij}^n = \frac{1}{2\pi} \int_0^{2\pi} \bar{l}_n(\theta) n_i n_j d\theta = \frac{1}{N_c} \sum_{c \in N_c} \frac{l_n^c n_i n_j}{1 + a_{kl}^c n_k n_l} \quad (2.49)$$

$$V_{ij}^t = \frac{1}{2\pi} \int_0^{2\pi} \bar{l}_t(\theta) t_i n_j d\theta = \frac{1}{N_c} \sum_{c \in N_c} \frac{l_t^c t_i n_j}{1 + a_{kl}^c n_k n_l} \quad (2.50)$$

Substituting equation (2.46) and (2.47) into above two equation respectively, the above mentioned anisotropy parameters can be determined by:

$$b_n = \frac{\sqrt{(V_{11}^n - V_{11}^n)^2 + (V_{12}^n + V_{21}^n)^2}}{2}; \theta_{bn} = \frac{1}{2} \arctan\left(\frac{V_{12}^n + V_{21}^n}{V_{11}^n - V_{22}^n}\right) \quad (2.51)$$

$$b_t = \frac{\sqrt{(V_{11}^t - V_{11}^t)^2 + (V_{12}^t + V_{21}^t)^2}}{2}; \theta_{bt} = \frac{1}{2} \arctan\left(\frac{V_{12}^t + V_{21}^t}{V_{11}^t - V_{22}^t}\right) \quad (2.52)$$

2.3.3 Stress-force-fabric relationship

Rothenburg and his co-workers (Rothenburg and Bathurst, 1989; Rothenburg and Bathurst, 1992; Rothenburg and Selvadurai, 1981) proposed a connection bridge between the components of the stress tensor for a granular assembly of particles and the statistics distribution of contact normal, contact forces and contact vectors in micro-scale, where the granular system is under the static equilibrium condition. This connection is named as stress-force-fabric (*SFF*) relationship. Many numerical tests have been carried out to verify the accuracy of the measured stress ratio of a loaded granular media and the predicted stress ratio using *SFF* (Li, 2006; Mirghasemi et al., 1997, 2002; Rothenburg and Bathurst, 1989; Rothenburg and Bathurst, 1992; Rothenburg and Selvadurai, 1981; Seyed Hosseinia, 2012, 2013; Yang et al., 2013). In this review chapter, the detail derivation of *SFF* will be explored for easy understanding. Firstly, the micro-structural definition of stress tensor in equation (2.14) would be reconsidered. Its expression is replaced by the statistics of the microscopic average quantities. The stress tensor can be rewritten as:

$$\sigma_{ij} = \frac{N_c}{V} \int_0^{2\pi} \bar{f}_i(\theta) \bar{l}_j(\theta) E(\theta) d\theta \quad (2.53)$$

where $E(\theta)$ is the normalized contact orientation distribution with orientation θ , $\bar{f}_i(\theta)$ and $\bar{l}_j(\theta)$ are the average force and average length of contact vectors acting associated with the same contact normal. The orientation of contact normal can also be defined as $\mathbf{n} = (\cos\theta, \sin\theta)$ and $\mathbf{t} = (-\sin\theta, \cos\theta)$. Due to the symmetric feature of disk and sphere ($\bar{l}_j(\theta) = \bar{l}_0 n_j$), the value of \bar{l}_0 is nearly the mean of the particle radius. However, for irregular particles $\bar{l}_j(\theta)$ is not equivalent to $\bar{l}_0 \sin\theta$. The magnitude of contact vectors is highly dependent on the particle shape. Meanwhile, the average contact force and average contact vector on each contact can also be decomposed into a normal and a tangential component (Seyedi Hosseininia, 2013).

$$\begin{cases} \bar{f}_i(\theta) = \bar{f}_n(\theta) n_i + \bar{f}_t(\theta) t_i \\ \bar{l}_i(\theta) = \bar{l}_n(\theta) n_i + \bar{l}_t(\theta) t_i \end{cases} \quad (2.54)$$

Substituting equation (2.54) into equation (2.53) and rewritten as:

$$\sigma_{ij} = \frac{N_c}{V} \int_0^{2\pi} \bar{f}_i(\theta) \bar{l}_j(\theta) E(\theta) d\theta = \frac{N_c}{V} \int_0^{2\pi} (\bar{f}_n(\theta) n_i + \bar{f}_t(\theta) t_i) (\bar{l}_n(\theta) n_j + \bar{l}_t(\theta) t_j) E(\theta) d\theta \quad (2.55)$$

Substituting the second-order Fourier series of contact forces, contact vectors and contact normal into above formulation, the stress components can be obtained as follow:

$$\begin{aligned} \sigma_{11} = & \frac{N_c \bar{f}_0 \bar{l}_0}{2V} \left\{ 1 + \frac{1}{2} [a \cos(2\theta_a) + a_n \cos(2\theta_f) + a_t \cos(2\theta_t) + b_n \cos(2\theta_{bn}) + b_t \cos(2\theta_{bt})] \right. \\ & + \frac{1}{2} [a \cdot a_n \cos 2(\theta_a - \theta_f) + a \cdot b_n \cos 2(\theta_a - \theta_{bn}) + a_n \cdot b_n \cos 2(\theta_f - \theta_{bn}) + a_t \cdot b_t \cos 2(\theta_t - \theta_{bt})] \\ & + \frac{1}{8} a \cdot a_n \cdot b_n [\cos 2(\theta_a + \theta_f - \theta_{bn}) + \cos 2(\theta_a - \theta_f + \theta_{bn}) + \cos 2(\theta_a - \theta_f - \theta_{bn})] \\ & + \frac{1}{8} a \cdot a_n \cdot b_t [\cos 2(\theta_a - \theta_f - \theta_{bt}) + \cos 2(\theta_a - \theta_f + \theta_{bt}) - \cos 2(\theta_a + \theta_f - \theta_{bt})] \\ & + \frac{1}{8} a \cdot a_t \cdot b_n [\cos 2(\theta_a - \theta_t - \theta_{bn}) + \cos 2(\theta_a + \theta_t - \theta_{bn}) - \cos 2(\theta_a - \theta_t + \theta_{bn})] \\ & \left. + \frac{1}{8} a \cdot a_t \cdot b_t [\cos 2(\theta_a - \theta_t - \theta_{bt}) - \cos 2(\theta_a + \theta_t - \theta_{bt}) - \cos 2(\theta_a - \theta_t + \theta_{bt})] \right\} \end{aligned} \quad (2.56a)$$

$$\begin{aligned}
\sigma_{22} = \frac{N_c \bar{f}_0 \bar{l}_0}{2V} & \left\{ 1 - \frac{1}{2} [a \cos(2\theta_a) + a_n \cos(2\theta_f) + a_t \cos(2\theta_t) + b_n \cos(2\theta_{bn}) + b_t \cos(2\theta_{bt})] \right. \\
& + \frac{1}{2} [a \cdot a_n \cos 2(\theta_a - \theta_f) + a \cdot b_n \cos 2(\theta_a - \theta_{bn}) + a_n \cdot b_n \cos 2(\theta_f - \theta_{bn}) + a_t \cdot b_t \cos 2(\theta_t - \theta_{bt})] \\
& - \frac{1}{8} a \cdot a_n \cdot b_n [\cos 2(\theta_a + \theta_f - \theta_{bn}) + \cos 2(\theta_a - \theta_f + \theta_{bn}) + \cos 2(\theta_a - \theta_f - \theta_{bn})] \\
& - \frac{1}{8} a \cdot a_n \cdot b_t [\cos 2(\theta_a - \theta_f - \theta_{bt}) + \cos 2(\theta_a - \theta_f + \theta_{bt}) - \cos 2(\theta_a + \theta_f - \theta_{bt})] \\
& - \frac{1}{8} a \cdot a_t \cdot b_n [\cos 2(\theta_a - \theta_t - \theta_{bn}) + \cos 2(\theta_a + \theta_t - \theta_{bn}) - \cos 2(\theta_a - \theta_t + \theta_{bn})] \\
& \left. - \frac{1}{8} a \cdot a_t \cdot b_t [\cos 2(\theta_a - \theta_t - \theta_{bt}) - \cos 2(\theta_a + \theta_t - \theta_{bt}) - \cos 2(\theta_a - \theta_t + \theta_{bt})] \right\}
\end{aligned} \tag{2.56b}$$

$$\begin{aligned}
\sigma_{12} = \sigma_{21} = \frac{N_c \bar{f}_0 \bar{l}_0}{2V} & \left\{ \frac{1}{2} [a \sin(2\theta_a) + a_n \sin(2\theta_f) + a_t \sin(2\theta_t) + b_n \sin(2\theta_{bn}) + b_t \sin(2\theta_{bt})] \right. \\
& + \frac{1}{2} [a \cdot a_t \sin 2(\theta_a - \theta_t) - a \cdot b_t \sin 2(\theta_a - \theta_{bt}) - a_n \cdot b_t \sin 2(\theta_f - \theta_{bt}) - a_t \cdot b_n \sin 2(\theta_t - \theta_{bn})] \\
& + \frac{1}{8} a \cdot a_n \cdot b_n [\sin 2(\theta_a + \theta_f - \theta_{bn}) + \sin 2(\theta_a - \theta_f + \theta_{bn}) - \sin 2(\theta_a - \theta_f - \theta_{bn})] \\
& + \frac{1}{8} a \cdot a_n \cdot b_t [\sin 2(\theta_a - \theta_f + \theta_{bt}) - \sin 2(\theta_a + \theta_f - \theta_{bt}) - \sin 2(\theta_a - \theta_f - \theta_{bt})] \\
& + \frac{1}{8} a \cdot a_t \cdot b_n [\sin 2(\theta_a + \theta_t - \theta_{bn}) - \sin 2(\theta_a - \theta_t + \theta_{bn}) - \sin 2(\theta_a - \theta_t - \theta_{bn})] \\
& \left. - \frac{1}{8} a \cdot a_t \cdot b_t [\sin 2(\theta_a + \theta_t - \theta_{bt}) + \sin 2(\theta_a - \theta_t + \theta_{bt}) + \sin 2(\theta_a - \theta_t - \theta_{bt})] \right\}
\end{aligned} \tag{2.56c}$$

Since all the anisotropy coefficients are smaller than 1, the polynomials equal or beyond three orders can be neglected. The above equations can be simplified as the followed equations:

$$\begin{aligned}
\sigma_{11} = \frac{N_c \bar{f}_0 \bar{l}_0}{2V} & \left\{ 1 + \frac{1}{2} [a \cos(2\theta_a) + a_n \cos(2\theta_f) + a_t \cos(2\theta_t) + b_n \cos(2\theta_{bn}) + b_t \cos(2\theta_{bt})] \right. \\
& \left. + \frac{1}{2} [a \cdot a_n \cos 2(\theta_a - \theta_f) + a \cdot b_n \cos 2(\theta_a - \theta_{bn}) + a_n \cdot b_n \cos 2(\theta_f - \theta_{bn}) + a_t \cdot b_t \cos 2(\theta_t - \theta_{bt})] \right\}
\end{aligned} \tag{2.57a}$$

$$\begin{aligned}
\sigma_{22} = \frac{N_c \bar{f}_0 \bar{l}_0}{2V} & \left\{ 1 - \frac{1}{2} [a \cos(2\theta_a) + a_n \cos(2\theta_f) + a_t \cos(2\theta_t) + b_n \cos(2\theta_{bn}) + b_t \cos(2\theta_{bt})] \right. \\
& \left. + \frac{1}{2} [a \cdot a_n \cos 2(\theta_a - \theta_f) + a \cdot b_n \cos 2(\theta_a - \theta_{bn}) + a_n \cdot b_n \cos 2(\theta_f - \theta_{bn}) + a_t \cdot b_t \cos 2(\theta_t - \theta_{bt})] \right\}
\end{aligned} \tag{2.57b}$$

$$\sigma_{12} = \sigma_{21} = \frac{N_c \bar{f}_0 \bar{l}_0}{2V} \left\{ \frac{1}{2} [a \sin(2\theta_a) + a_n \sin(2\theta_f) + a_t \sin(2\theta_t) + b_n \sin(2\theta_{bn}) + b_t \sin(2\theta_{bt})] \right. \\ \left. + \frac{1}{2} [a \cdot a_t \sin 2(\theta_a - \theta_t) - a \cdot b_t \sin 2(\theta_a - \theta_{bt}) - a_n \cdot b_t \sin 2(\theta_f - \theta_{bt}) - a_t \cdot b_n \sin 2(\theta_t - \theta_{bn})] \right\} \quad (2.57c)$$

The invariants of the average stress tensor are as:

$$\left\{ \begin{array}{l} \sigma_n = \frac{\sigma_{11} + \sigma_{22}}{2} \\ \tau_f = \sqrt{\left(\frac{\sigma_{11} - \sigma_{22}}{2}\right)^2 + \sigma_{12}^2} \end{array} \right. \quad (2.58)$$

Similar to equation (2.57), eliminating the third and higher orders, the general form of the two invariants ratio can be simplified as:

$$\frac{\tau_f}{\sigma_n} = \frac{\sqrt{a^2 + a_n^2 + a_t^2 + b_n^2 + b_t^2 + 2a \cdot a_n \cos 2(\theta_a - \theta_f) + 2a \cdot a_t \cos 2(\theta_a - \theta_t) + 2a \cdot b_n \cos 2(\theta_a - \theta_{bn}) + 2a \cdot b_t \cos 2(\theta_a - \theta_{bt}) + 2a_n \cdot b_n \cos 2(\theta_f - \theta_{bn}) + 2a_n \cdot b_t \cos 2(\theta_f - \theta_{bt}) + 2a_t \cdot b_n \cos 2(\theta_t - \theta_{bn}) + 2a_t \cdot b_t \cos 2(\theta_t - \theta_{bt}) + 2a_n \cdot a_t \cos 2(\theta_f - \theta_t) + 2b_n \cdot b_t \cos 2(\theta_{bn} - \theta_{bt})}}{2 + a \cdot a_n \cos 2(\theta_a - \theta_f) + a \cdot b_n \cos 2(\theta_a - \theta_{bn}) + a_n \cdot b_n \cos 2(\theta_f - \theta_{bn}) + a_t \cdot b_t \cos 2(\theta_t - \theta_{bt})} \quad (2.59)$$

Since the magnitudes of average contact normal and tangential vectors anisotropy are very small, especially for disk or sphere particles, the above equation can be reduced as:

$$\frac{\tau_f}{\sigma_n} = \frac{\sqrt{a^2 + a_n^2 + a_t^2 + 2a \cdot a_n \cos 2(\theta_a - \theta_f) + 2a \cdot a_t \cos 2(\theta_a - \theta_t) + 2a_n \cdot a_t \cos 2(\theta_f - \theta_t)}}{2 + a \cdot a_n \cos 2(\theta_a - \theta_f)} \quad (2.60)$$

With the assumption of coincident $\theta_a = \theta_f = \theta_t$, equation (2.59) can be further decomposed as:

$$\frac{\tau_f}{\sigma_n} = \frac{\sqrt{a^2 + a_n^2 + a_t^2 + 2a \cdot a_n + 2a \cdot a_t + 2a_n \cdot a_t}}{2 + a \cdot a_n} = \frac{a + a_n + a_t}{2 + a \cdot a_n} \quad (2.61)$$

2.4 Particle shape effect of granular sands

2.4.1 Macro and micro responses

Particle shape plays an important role in both the macro and micro scales behavior of a

granular assembly. From a macro perspective, many researchers have found that the strength properties of granular materials are highly related to the particle shape. This point has been verified from experimental tests to numerical simulations (Abedi and Mirghasemi, 2011; Azéma and Radjaï, 2010; Cho et al., 2006; Rothenburg and Bathurst, 1992; Shin and Santamarina, 2012; Wei and Yang, 2014). Moreover, granular packing density can be influenced by particle shapes. Abbireddy and Clayton (2010) performed a series numerical tests to explore the relationships of initial void ratios and particle shape, which can influence the maximum and minimum void ratios of a granular packing. They also proposed an effective method to produce suitable loose and dense samples for DEM simulations. Other investigations have also been carried out to explore the relationship between particle shape and packing density (Biarez and Hicher, 1994; Abbireddy and Clayton, 2010; Azéma and Radjaï, 2010; Cho et al., 2006; Jia and Williams, 2001; Salot et al., 2009). Furthermore, both the static and dynamic liquefaction can be influenced by the particle shape (Kuhn et al., 2014; Vaid and Chern, 1985; Wei and Yang, 2014; Yang and Wei, 2012). Wei and Yang (2014) carried out extensive laboratory triaxial tests on several types of sand-fines mixtures to explore the role of grain shape in static liquefaction, where the fines of rounded shape can increase the potential of liquefaction compared with the angular shape. From a micro perspective, particle shape can influence the contact force distribution (Azéma and Radjaï, 2012; Azéma et al., 2007; Yang and Cheng, 2015). Meanwhile, the global average value and the probability density distribution of the friction mobilization can also be influenced by particle shape effect (Azéma and Radjaï, 2012). In addition, the statistics of micro anisotropic coefficient are highly depend on the particle shape (Antony and Kuhn, 2004; Azéma and Radjaï, 2010, 2012; Pena et al., 2007).

2.4.2 Particle shape descriptor

Many previous studies have been carried out to quantify the shape characteristics of granular sands. However, a general description index of the particle shape remains unavailable. In this subchapter, the existing particle shape descriptors will be briefly reviewed. Generally, the particle shape is 3D in nature. However, 3D measurements need a sophisticated devices, which is highly dependent on the minimum particle size and the orthogonally placing manner.

Even for the present computer image processing techniques, a general characterization of 3D particle shape remains extremely complex. Hence more particle shape descriptors are constructed by 2D, which is always a form of a projection or a sectional image (Blott and Pye, 2008; Pourghahramani and Forssberg, 2005; Sallam, 2004). Since this dissertation is centered on 2D numerical tests, only 2D shape descriptors are introduced. Many particle shape indexes have been proposed with respective scope in the past century. The most widely used shape formulation is the 2D form of Wadell's roundness (1932). Other commonly used particle shape descriptors in geotechnical discipline are Aspect ratio and Circularity, which are simplified for describing 2D particle shape. Two of previous review papers (Blott and Pye, 2008; Pourghahramani and Forssberg, 2005) have systematically discussed and compared the previous particle shape descriptors. Meanwhile, Cox (2008) also summarized the history of grain shape characterization approaches in his thesis report. In this dissertation, the author mainly refers to the recent popular categories of particle shape indexes especially in geotechnical discipline. Cho et al. (2006) presented a systematic work on the particle shape effect of natural and crushed sand, where the three important shape indexes sphericity, roundness and roughness are adopted to quantify the properties of density, stiffness and strength. These three shape indexes based on independent scales are developed by previous researchers (Barrett, 1980; Krumbein and Sloss, 1951; Powers, 1953; Wadell, 1932). Mitchell and Soga (2005) also presented a similar methodology to describe the particle shape by three sub-quantities at different scales. These specific shape descriptors presented by the above mentioned researchers are illustrated in Figure 2.6. Other advanced techniques for qualitatively accounting for the particle shape include Fourier mathematical approach (Bowman et al., 2001; Ehrlich and Weinberg, 1970) and Fractal analysis method (Kennedy and Lin, 1992; Orford and Whalley, 1983; Vallejo, 1995). The expression of Fourier series in (R, θ) is followed as (Bowman et al., 2001):

$$R(\theta) = R_0 + \sum_{n=1}^N A_n \cos(n\theta) + \sum_{n=1}^N B_n \sin(n\theta) \quad (2.62)$$

where $R(\theta)$ is the radius at angle θ , N is the total number of harmonics, n is the harmonic number. The other three coefficients can be determined by:

$$\left\{ \begin{array}{l} R_0 = \frac{1}{2\pi} \int_0^{2\pi} R(\theta) d\theta \\ A_n = \frac{1}{\pi} \int_0^{2\pi} R(\theta) \cos(n\theta) d\theta \\ B_n = \frac{1}{\pi} \int_0^{2\pi} R(\theta) \sin(n\theta) d\theta \end{array} \right. \quad (2.63)$$

The Fourier descriptors can be expressed as:

$$D_n = \frac{\sqrt{A_n^2 + B_n^2}}{R_0} \quad (2.64)$$

The Fourier method with a clear mathematical framework can be considered to exactly quantify the particle shape effect. However, more than 5 Fourier descriptors are related to the particle shape (Mollon and Zhao, 2012). This extremely complicated situation may be not suitable for practical geotechnical studies. Detailed information about these Fourier descriptors are given in Figure 2.7. In addition, the natural sand cannot be strictly described by a unique and precise fractal dimension. Sukumaran and Ashmawy (2001) proposed a discretizing 2D projection of a particle and analyzing the projected outline with an external circle. This particle shape descriptor requires only two parameters.

2.4.3 Particle shape modelling

Generally, particle shape can influence the overall mechanical responses of granular materials. Hence the modelling methodologies of particle shape effect is an important research issue for the granular system. The traditional modelling is to adopt circle or sphere to simulate individual particle. However, this regular modelling may bring in excessive rotation, which would induce a lower shear resistance (Bardet and Proubet, 1992). Extensive modelling approaches emerge to consider particle shape effect. These methods can be mainly divided into two groups (1) rolling resistance model; (2) irregular geometry. The rolling resistance model is an indirect method which adds an artificial rotation torque at the contact points for traditional circles or spheres. It is initially presented by Iwashita and Oda (1998, 2000). Afterwards, many different rolling resistance models are constructed by versatile consumptions (Ai et al., 2011; Belheine et al., 2009; Jiang et al., 2005; Mohamed and Gutierrez, 2010; Tordesillas and Walsh, 2002; Wensrich and Katterfeld, 2012; Zhao and Guo,

2014). The other approach is to directly generate particles using irregular geometries through many different ways, e.g., ellipse or ellipsoids (Ng, 1994, 2004; Rothenburg and Bathurst, 1992), polygons (Azéma et al., 2007; Estrada et al., 2011; Mirghasemi et al., 1997; Seyedi Hosseininia, 2012), and combining clusters/clumps (Abedi and Mirghasemi, 2011; Ferrellec and McDowell, 2010; Jensen et al., 1999; Lu and McDowell, 2007; Yang and Dai, 2010; Yang et al., 2012, 2013; Zhou et al., 2013). Recently, Mollon and Zhao (2012, 2013, 2014) undertook a systematic work to generate much more complicated and accurate particles for discrete modelling from 2D to 3D analysis.

2.5 Crushable granular materials

2.5.1 One dimensional compression

The mechanical and deformable features of a granular assembly under one dimensional compression are very important for many problems in geotechnical engineering. One dimensional compression usually relate the void ratio (e) and vertical effective stress (σ_v), which are generally plotted as semi-logarithm in Figure 2.8. The governing principle can be expressed as follow:

$$\begin{cases} e = e_0 - \lambda \ln \sigma_v, & \text{Loading} \\ e = e_k - \kappa \ln \sigma_v, & \text{Unloading} \end{cases} \quad (2.65)$$

where λ is the gradient of loading compression line, κ indicates the gradient of unloading straight line. e_0 and e_k mean the void ratio at 1 kPa. Moreover, a typical compression curve of crushable granular materials undergoes an extremely high axial pressure (800 MPa) is given in Figure. 2.8 from Yamamuro and his co-workers (1996). The studies on one dimensional compression behavior of a granular medial can be generally divided into experimental and numerical directions.

Initially, the experimental tests are briefly reviewed. It is generally known that particle crushing effect can be ignored under low confining pressure. Hagerty et al. (1993) carried out a series of one dimensional compression test with consideration on particle crushing under

extremely high pressure (689 MPa). They also reviewed previous one dimensional compression tests of sands, and pointed that the confined compression procedure can be categorized into three stages from a large stress range. Their experimental results shown that particle crushing greatly increased with particle angularity and median particle size. Meanwhile, the initial crushing stress is related to the relative density. Yamamuro et al. (1996) designed a new one dimensional compression apparatus for applying extremely high pressure (up to 800 MPa). They found that the effects of initial void ratio could be ignored at high pressures, where the plots of e versus logarithm of σ_v were merged into a single curve. Nakata et al. (2001a) carried out a large number of one dimensional compression tests on silica sands, and found that the yielding characteristics is related to the particle size distribution. They also explored the developments of the gradient coefficients of loading compression lines. Moreover, the effects of initial void ratio and particle size distribution during the whole crushable confined compression behavior were investigated. In addition, this paper significantly influenced the followed researchers on the topic of crushability of granular materials. The important conclusions of this experimental study is shown in Figure. 2.9, where the points P in the compressional curve are distinct yield points. The physical feature of these yield points is conventionally used to distinguish the elastic and plastic deformation regions. For a crushable particular system, the stress at yield point is commonly related to the initiation of marked particle crushing (Coop and Lee, 1993; Nakata et al., 2001a; Yamamuro et al., 1996). Afterwards, Nakata et al. (2001b) found that the magnitude of yield stress can be influenced by the particle size, single particle crushing strength, and initial void ratio. Moreover, the non-uniform distribution of inter-particle stresses was considered to introduce a ratio of single particle strengths to the mean value of the characteristic tensile stress. Mcdowell and Humphreys (2002) reexamined the yielding feature of brittle granular material subjected to one dimensional compression. They found that the measured yield stress is proportional to the Weibull (1951) 37% particle tensile strength of the constituent particles. Meanwhile, more than 30 particles for each material were diametrically compressed to explore the Weibull statistical pattern of tensile strengths. Graham et al. (2004) carried out many groups of one dimensional compression tests for densely crushable sand with the

emphasis on the temperate effects (up to 100° C). Experimental results shown that the temperature effect could be ignored. Uygur and Doven (2006) carried out monotonic and cyclic oedometer tests on sand at elevated stress levels. These tests showed a linear relationship between compressibility index and relative density. In addition, repetitive loading cycles increased the probability of particle crushing, which may induce a higher compressibility and volume strain. More than 100 sands have been carried out to clarify the role of particle rearrangement and particle damage on primary and secondary compression by Mesri and Vardhanabhuti (2009), where the yield stress and lateral pressure coefficient are also discussed. Altuhafi and Coop (2010) carried out series of compression tests of sand for identifying the evaluation of particle characteristics. Although the tensile strength of a single particle is the main factor to control the crushing behavior, the initial void ratio and particle size distribution can still highly influence the probability of particle breakage. For a well graded samples, it is difficult to emerge a unique normal compression line, where particle breakages are not significant. The experimental results also imply the concept of critical grading of a granular material, where the feature of particle size distribution is a stable and fractal. Cil and Alshibli (2014) performed a series of one dimensional compression tests with an emphasis on the specimen aspect ratio. An advance synchrotron microtomography technique is applied to evaluate the particle fracture and deformation behavior.

The alternative numerical approaches have been considered by many researchers for studying the mechanism of crushable granular material within the confined system during the past 20 years. McDowell et al. (1996) developed a conceptual isosceles right angled triangles to explore the microscopic origins of the crushable granular materials, where a statistical method was introduced to evaluate the probability of breakage for each particle. The governing formulation is coupled by the applied stress, particle size and coordination number. Afterwards, McDowell and Bolton (1998) carried out series of numerical single particle fracture tests to verify the Weibull statistical pattern of tensile strengths of grains of various mineralogy and size. They found that the yield stress was related to the average grain tensile strength. Particle fractures would induce a self-similar geometry configuration. In addition,

the comminution limit of particle size would influence the magnitude of void ratio of a granular assemblage. Cheng et al. (2003) performed a systematic numerical simulation to quantitatively compare with the experimental tests data of the silica sand. The numerical tools could support to provide value insights for exploring the micromechanical origins of soil plasticity. Lobo-Guerrero et al. (2006) visualized the procedure of individual particle crushing in one dimensional compression. Ben-Nun and Einav (2010a) compressed the crushable granular assemblies into an ultimate fractal topology with a specific fractal dimension. They found that the ultimate packing was insensitive with the initial void ratio and particle size distribution. Meanwhile, the fractal dimension is irrespective with the failure criteria of each particle within a granular assembly. And then, Ben-Nun et al. (2010b) revealed a novel attractor in the spatial distribution of contact forces within a granular materials during confined comminution. In addition, they proposed a log-normal distribution to describe the contact force distribution at the ultimate state. Walker et al. (2011) investigated the process of confined comminution by the methodology of complex networks. They pointed that an ultimate contact network possessed a scale-free degree distribution as well as a small world properties. McDowell and Bono (2013) studied particle crushing and the developed procedure of fractal grain size distributions. The yield stress is dependent on the average particle octahedral shear strength. Minh and Cheng (2013) carried out series of numerical one dimensional compression tests for exploring the effects of particle size distribution. However, particle crushing effect is ignored within these numerical tests. They then explored the force transmission by bimodal particle size distribution under one dimensional compression (Minh et al., 2014). The maximum packing efficiency in their studies is the mixture of 30% smaller silt sands. Recently, Yang and Cheng (2015) investigate the contact forces and coordination number distribution of a crushable granular assemblage during one dimensional compression. A simple method is developed to reveal the fractal distribution of contact forces in comminuted granular materials.

2.5.2 Particle crushing modelling

The numerical modellings of a crushable grain have been constructed by many previous investigators through various algorithms, which include Finite element method (FEM),

Material point method (MPM), Discrete element method (DEM) and others. As the numerical research tool in this dissertation is DEM, other numerical approaches for crushing modelling are only briefly reviewed.

Tang (1997) proposed a modified FEM approach (RFPA^{2D}) to simulate the progressive rock failure. The heterogeneity of rock parameters, elastic modulus reduction and even rate of failed elements are considered in this method. Tang et al. (2001) verified the RFPA^{2D} by simulating the Brazilian tests with a disk shape. Meanwhile, the effects of particle shape were considered. Liu et al. (2005) applied this code to explore the internal grain breakage of a confined packing. Although these investigations have captured reasonable numerical results, the essential of this continuum approach is based on the assumed constitutive model, which is not suitable for investigating the granular media, especially for consideration on particle crushing. Sulsky and Schreyer (2004) employed the numerical MPM to study the spall failure in brittle materials. Meanwhile, they developed an initial criterion to install a discrete constitutive equation model for simulating material failure. Li et al. (2011) proposed a new statistical failure criterion in MPM to investigate the impact failure of brittle particles.

Particle crushing modellings in the DEM are mainly divided into two alternative algorithms: replacing the breaking particles with new smaller fragments or using a bonded agglomerate. McDowell and Harireche (2002) applied the bonded agglomerates to explore particle breakage behavior during the normal compression. The Weibull distribution of each bond in an agglomerate was proposed to capture a qualitative normal compression lines compared with the experimental tests, but the particle number in their study is very limited. Jensen et al. (2001) adopted the clusters to explore the particle damage on interface behavior. Cheng et al. (2003) used the bonded agglomerates to perform a systematic study of crushable soil on various loading paths. They also showed many micro insights to interpret the macroscopic responses. Moreno et al. (2003) employed the bonded agglomerates to explore the oblique impact damage process. Lim and McDowell (2005) carried out single particle crushing tests by using bonded agglomerates. Numerical Oedometer tests on these bonded aggregates of a crushable ballast particles were performed to compare with the laboratory tests. Bolton et al.

(2008) used the bonded agglomerate to study the fundamental features of crushable granular soils through normal compression and triaxial shear tests. Wang and Yan (2011) applied the bonded agglomerates to investigate the role of particle crushability during plane shear tests. Cil and Alshibli (2014) used the bonded agglomerates to explore the confined compression test. Although the bonded agglomerates have been verified through many previous studies, at present, a general modelling framework of an agglomerate is still not available. There still exist many uncertain problems such as the number of sub-particles as well as the particle size distribution within an individual agglomerate. Moreover, the magnitude of bonding strength is set with certain artificial value. Another major particle crushing modelling in DEM is performed through replacing breaking particles with smaller new fragments. Tsoungui et al. (1999) proposed a new failure criterion on an individual grain based on the related surrounding contact forces. The failure particle in their study was replaced by twelve fragments of four different volume as shown in Figure 2.10 (a), where the mass conservation is not suitable. Lobo-Guerrero and his co-workers (2005; 2006) presented a particle breakage criterion to visualize the granular crushing under shear or compress load. This criterion is governed by a threshold of tensile strength, which is dependent on the coordination number, particle size and maximum contact force. In addition, mass conservation is not complied as shown in Figure 2.10 (b). Ben-Nun and Einav (2010a) proposed a physical mass conservation law as illustrated in Figure 2.10 (c) for exploring the feature of self-organization of crushable granular during confined comminution. Meanwhile, they found that the ultimate fractal dimension was insensitive with initial void ration and particle size distribution. Afterwards, Ben-Nun et al. (2010b) applied their particle failure modelling framework to study the force attractor in the confined comminution system of a crushable granular assembly. They published their findings on Physical Review Letter, which is an extremely significant original publisher. McDowell and Bono (2013) proposed an octahedral shear stress controlled failure criterion of an individual particle. Meanwhile, the replaced 3D algorithm is similar as the 2D approach of Ben-Nun and Einav (2010). Yang and Cheng (2015) used the tensile strength failure criterion for an individual particle to systematically study the one dimensional compression of a granular assemblage. They proposed a simple statistical model to reveal the fractal distribution of contact forces in comminuted granular materials.

2.6 Discrete element method (DEM)

2.6.1 Brief description of DEM

A granular material is basically composed of series of contact particles and surrounded voids. This discrete nature cannot be well described by the continuum theory. When external load applies onto the granular assembly, particles would transfer force via the inter-particle contacts to resist external stresses. Moreover, the interacted contacts and the corresponding voids would be simultaneously emerge or vanish. This special microscopic structure feature crucially determine the macroscopic mechanical responses. Hence, the main challenge for the granular material is to suitably capture the evaluation of microscopic contact information. For this purpose, the numerical discrete/distinct element method (DEM) (Cundall and Strack, 1979) is proposed as a robust research tool which can effectively capture the mechanical behavior of granular materials, with an emphasis on particle-scale kinematics and forces.

As is mentioned above, DEM is initially developed by Cundall (1971) for investigating the motion and deformation of rock as a block system. Another pioneer contribution within the block system is proposed by Shi (1992), who used an implicit formulation to describe the interaction between the individual blocks. This approach is named as discontinuous deformation analysis (DDA). The above two block DEMs are quite different theoretically, the former one is a force method with an explicit computing scheme, while the later one is a displacement method with an implicit computing scheme. However, a rock mass and a granular media have a different element scale. DDA is more suitable for blocky medium where the number of variables are not major, but will be extremely time consuming for granular medium. Since the focus of this dissertation is to study the mechanical behavior of granular materials, only the early original contributions of block DEM (Cundall, 1971; Shi, 1992) are reviewed in this chapter. The purpose is for introducing the particulate DEM for granular materials in the geotechnical discipline. Cundall and Strack (1979) firstly extended the block DEM to investigate the granular materials at a particle scale. Particles in this particulate DEM are assumed to rigid with soft contacts, where a moderate overlap is permitted between two entities (ball and ball or ball and wall) during each numerical cycle.

The active overlap is controlled by a force-displacement law to calculate the contact forces. In addition, this controlling algorithm is different from the other particulate DEM such as contact dynamics method (Jean, 1999) and the implicit computing code (Salami and Banks, 1996). Henceforth, the DEM in this dissertation only represents the particulate scale for the granular materials.

Based on the particulate DEM framework, the initial computer code BALL (Cundall and Strack, 1978) is constructed for studying the two dimensional (2D) granular material with ideal circle shape. Afterwards, an extension three dimensional (3D) version TRUBAL (Strack and Cundall, 1984) is available. These two codes are the fundamental platform for other DEM codes developments at the initial stage, including DISC (Bathurst and Rothenburg, 1992), ELLIPSE2 (2D) (Ng, 1994), ELLIPSE3 (3D) (Lin and Ng, 1995), POLY (Mirghasemi et al., 1997). These numerical codes can be considered various shapes of particle, from regular circle/sphere to irregular polygon/polyhedral. Jing and Stephansson (2007) have reviewed the development of DEM codes from 1980s to 1990s. Nowadays, the most widely computing DEM codes in geotechnical discipline are PFC^{2D} and PFC^{3D} (particle flow code in two dimension/three dimension) (Itasca, 2000). In this dissertation, the PFC^{2D} is mainly adopted for the numerical investigations. In addition, some open source codes are also proposed and developed very fast, e.g., YADE (Kozicki and Donzé, 2008), LAMMPS (Plimpton et al., 2007), OVAL (Kuhn, 2006). O'Sullivan (2011) has also summarized the recent DEM codes. A comprehensive information about the DEM codes can be seen on the internet Wikipedia.

Cundall (2001) presented a perspective of DEM in geomechanics and demonstrated the advantages of DEM modelling over classical constitutive modelling. While flow rules, plastic potential functions, dilation angles, hardening rules and other constitutive relations and parameters, which are practically arbitrary and curve-fitting oriented procedures, are used in classical formulation of soil models. The DEM has the advantage of reproducing these behaviors using only the basic parameters of the particle and the particle state. In addition, two important review papers (O'Sullivan, 2011; Zhu et al., 2008) have summarized the application of DEM for investigating granular assemblies.

2.6.2 Governing principles

The main DEM code in this dissertation is PFC^{2D} , which is developed by Itasca Consulting Group. This program adopts an explicit finite time integration using the acceleration of the individual balls/particles through Newton's second law. The contact forces and relative displacement are determined by a force-displacement law and updated at every numerical cycle, using vanishing and emerging contacts. The calculation cycle in DEM then involves repeatedly applying the law of motion to each particle, a force-displacement law to each contact, and a constant updating of wall positions (Itasca, 2005). The illustration of the calculation cycle is shown in Figure. 2.11.

The force displacement law relates the relative displacement between two entities at a contact to the contact force generating on them. All the contacts arise from contact occurring at a single point, which includes two contact types. For contacts between balls, the normal vector is directed along the line between two ball centers. For ball-wall contact, the normal vector is directed along the line defining the shortest distance between the ball center and the wall. As shown in Figure 2.12, a typical contact force f^c can be divided into a normal and shear component with respect to the contact plane.

$$f^c = f_n^c + f_s^c \quad (2.66)$$

where f_n^c is the normal contact force, f_s^c is the shear contact force. These two force components can be calculated by the force-displacement law in Figure 2.13. Hence, the normal contact force can be determined as follow:

$$f_n^c = K_n U_n \quad (2.67)$$

$$\Delta f_s^c = K_s U_s, \quad f_s^c + \Delta f_s^c \leq \mu f_n^c \quad (2.68)$$

where Δf_s^c is the shear contact force increment, K_n is the normal stiffness, K_s is the tangential stiffness, U_n is the relative normal displacement, U_s is the incremental tangential displacement, and μ is the friction coefficient to limit the shear contact force. There are two principle contact stiffness models in PFC^{2D} for studying the granular materials. One is the linear contact stiffness model, which can be assumed by the two contacting entities at in

series:

$$K^n = \frac{K_a^n K_b^n}{K_a^n + K_b^n} \quad (2.69)$$

$$K^s = \frac{K_a^s K_b^s}{K_a^s + K_b^s} \quad (2.70)$$

The subscripts a and b denote the two balls in contact. In addition, the other one is simplified Hertz-Mindlin model, which defined by the shear modulus G and Poisson's ratio ν of the two contacting balls with radii R_a and R_b . Moreover the stiffness value is influenced by the depth of overlap U_n . The contact and tangential stiffness can be determined as follows:

$$K^n = \left(\frac{2\langle G \rangle \sqrt{2\tilde{R}}}{3(1-\langle \nu \rangle)} \right) \sqrt{U_n} \quad (2.71)$$

$$K^s = \left(\frac{2(\langle G \rangle)^2 3(1-\langle \nu \rangle) \tilde{R}^{1/3}}{2-\langle \nu \rangle} \right) |f_n^c|^{1/3} \quad (2.72)$$

The multipliers in the above equations are a function of the geometric and material properties of the two entities in contact. For the ball-ball contact, the multipliers depend on the followers:

$$\tilde{R} = 2 \frac{R_a R_b}{R_a + R_b}, \quad \langle G \rangle = \frac{1}{2}(G_a + G_b), \quad \langle \nu \rangle = \frac{1}{2}(\nu_a + \nu_b) \quad (2.73)$$

For the ball-wall contact, the multipliers can be determined:

$$\tilde{R} = R_{ball}, \quad \langle G \rangle = G_{ball}, \quad \langle \nu \rangle = \nu_{ball} \quad (2.74)$$

The selection of contact stiffness model also requires careful consideration. Firstly, the simplified Hertz-Mindlin model can be directly derived from particle material properties. For the collision and small strain problems, the difference between the linear contact model and non-linear Hertz-Mindlin model is obvious (Kumar et al., 2014; O'Sullivan, 2011). However, the numerical specimens in this study are all in the process of quasi-static behavior, where the small-strain response is also ignored in this study. In addition, previous investigation (Mirghasemi et al., 1997) has pointed that choosing a suitable magnitude of the linear contact stiffness will show a similar macroscopic behavior as that for Hertz-Mindlin, especially under the large strain response. Moreover, recently many researchers still adopt linear contact

models to represent the mechanical responses of granular assemblages (Abedi and Mirghasemi, 2011; Jensen et al., 1999; Jiang et al., 2009; Kumar et al., 2014; Seyedi Hosseininia, 2012, 2013). Furthermore, the computation efficiency of Hertz-Mindlin is extremely lower than the linear contact model, therefore, the author adopt the linear stiffness contact model in this dissertation for simplicity.

The law of motion for single particle is determined by the resultant force and moment upon it. The translation motion is induced by the result force. Meanwhile, the rotation motion is determined by the resultant moment. Some physical symbols for the particle are defined: position x_i , velocity \dot{x}_i , acceleration \ddot{x}_i , its angular velocity ω , and angular acceleration $\dot{\omega}_i$. The determined equations of the translational and rotational motion can be written as follows:

$$\sum_{c=1}^N f_n^c + mg = m\ddot{x} \quad (2.75)$$

$$M = I\dot{\omega} \quad (2.76)$$

where m is the total mass of the particle, g is the body force acceleration, M is the result moment, I is the inertial moment of the particle.

The above two equations are integrated using a centered finite difference algorithm, including a time step Δt . The translation and angular velocities can be computed at the mid-intervals of $t \mp n\Delta t/2$, while other quantities x, \ddot{x} , and $\dot{\omega}$ can be determined by the primary intervals of $t \mp n\Delta t$. The integration of both translation and angular velocities at time $(t + \Delta t/2)$ can be computed as:

$$\dot{x}^{(t+\Delta t/2)} = \dot{x}^{(t-\Delta t/2)} + \left(\frac{\sum_{c=1}^N f_n^c}{m} + g \right) \Delta t \quad (2.77)$$

$$\dot{\omega}^{(t+\Delta t/2)} = \dot{\omega}^{(t-\Delta t/2)} + \left(\frac{M}{I} \right) \Delta t \quad (2.78)$$

The solutions of motion in the above equations are integrated through a centered finite-difference scheme. A critical time step is applied to stable the computed procedure, which is dependent on the minimum eigen-period of the total system. A simplified procedure is considered to estimate the critical timestep at the beginning of each cycle. The following

equations can be used to determine the value of the above critical timestep in PFC^{2D} :

$$t_{crit} = \begin{cases} \sqrt{m / k^{tran}}, & \text{translation motion} \\ \sqrt{I / k^{rot}}, & \text{rotational motion} \end{cases} \quad (2.79)$$

where k^{tran} is the translation stiffness and k^{rot} is the rotational stiffness for each particle.

The final critical timestep using for computation is set as a fraction of the minimum value of all estimated timestep in Eq. (2.77) for a granular media. It is well known that only sliding mechanism may not be efficient to control the granular assemblages within a quasi-static system, therefore, damping is artificially introduced to avoid the non-physical vibrations that develop at the contacts. Two most common damping models are the mass damping and local non-viscous damping. Cundall (1987) pointed out some limitations of the mass damping and suggests to use the local non-viscous damping to simulate the quasi-static response of a granular media, where only acceleration motion is damped. In addition, the non-dimensional damping constant is also frequency independent. Detailed discussion on the damping model has been investigated by O'Sullivan (2011). In this thesis, the governing equations of the local non-viscous damping are presented as follows:

$$F_{(i)} + F_{(i)}^d = M_{(i)} A_{(i)}; \quad i = 1...3 \quad (2.80)$$

$$M_{(i)} A_{(i)} = \begin{cases} m\ddot{x}_i, & \text{for } i = 1...2; \\ I\dot{\omega}, & \text{for } i = 3 \end{cases} \quad (2.81)$$

where $F_{(i)}$ are the generalized forces including the portion from the gravity force, $M_{(i)}$ and $A_{(i)}$ are the mass and acceleration components. $F_{(i)}^d$ indicates the damping force, which can be determined as follow:

$$F_{(i)}^d = -\zeta |F_i| \text{sign}(v_i), \quad i = 1...3 \quad (2.82)$$

extended the generalized velocity,

$$v_{(i)} = \begin{cases} \dot{x}_{(i)}, & \text{for } i = 1...2; \\ \omega, & \text{for } i = 3 \end{cases} \quad (2.83)$$

where ζ is the damping constant to control the input damping force.

2.6.3 DEM boundary conditions and load paths

Similar to the finite element method (FEM), boundary conditions and associated servo algorithms within DEM are very important for the numerical modelling. In this subsection, the boundaries types, controlling conditions, and traditional geotechnical laboratory loading servo-control algorithms are briefly presented.

2.6.3.1 Boundary types

In DEM, there are mainly three types of boundaries which include the rigid wall, membrane, and periodic boundary. The illustrations of the three boundaries can be seen in Figure 2.14.

Rigid wall is the most commonly used boundary type to mimic the interactions between particles and machine components. The boundary inertia effect can be ignored for this type wall. Moreover, the interacted force between particle and wall cannot influence the motion of the rigid wall. Furthermore, contacts between wall and wall aren't be considered. In addition, particles contacted with the wall may move outside the boundary, when the wall stiffness is very low or the timestep is not suitable (O'Sullivan, 2011). Users need to write a servo-control algorithm to move the wall to achieve a required stress, volume or stiffness state. The interaction surfaces of a rigid wall can be simulates as planar or curved. Many previous investigations have adopted this boundary to perform the element tests or practical problems. For example, many researchers have used the rigid wall to reproduce the traditional geotechnical laboratory tests, which contain the biaxial shear, one dimensional compression, and triaxial tests (Calvetti, 2008; Cheng et al., 2003; Cheung and O'Sullivan, 2008; Gong et al., 2011; Guo and Zhao, 2013; Li and Li, 2009; Minh and Cheng, 2013; Yang and Dai, 2010). Other researchers also have considered the rigid wall as connected pieces to mimic the practical studies, such as hopper (Cheng et al., 2010; Cheng et al., 2009; Langston et al., 1996), pile penetration (Jiang et al., 2006; Lobo-Guerrero and Vallejo, 2005; Zhang et al., 2012), flume test (Banton et al., 2009; Valentino et al., 2008), and rough interface (Wang and Jiang, 2011) etc.

A stress controlled flexible membrane is an alternative boundary, which are mainly produced by two approaches. The first approach is linked string small balls to generate the rubber

membrane (Bardet and Proubet, 1991; Iwashita and Oda, 1998; Wang and Leung, 2008). A slight dispute is how to suitably determine the moving laws of four fictitious balls at the intersections of loaded rigid wall and confined flexible membrane. Moreover, the reasonable value of property parameters of membrane particles is still questionable. The secondary approach is directly applied the force on the outermost particles (Cheung and O'Sullivan, 2008; O'Sullivan, 2011), which are updated for each numerical cycle. This method cannot efficiently obtain the area/volume changing. In addition, the applied force is direct towards the center but not on the particle surface. Hence the above two approaches have respective advantages and limitations. Meanwhile, it should be noted here that the flexible boundary is more efficient to simulate the nature strain localization than the rigid boundary. However, this boundary type cannot be used to simulate “undrained” tests.

Another commonly used boundary within DEM is a periodic boundary, which is treated as infinitely repeating the identical representative subdomain to generate a granular assemblage. The macro mechanical behavior can be represented by the responses of repeated identical representative volume element (RVE) (O'Sullivan, 2011). The strain-controlled or stress-controlled test can also be controlled by a servo-system analogous to the rigid and membrane boundary. Some researchers have considered this boundary to perform the DEM simulations (Cundall, 1989; Thornton, 2000; Thornton and Antony, 2000). However, some limitations still exist. Using this boundary type, the idealized stress homogeneous is significantly different from the nature sands. Moreover, strain localization cannot be easily developed under the periodic boundary.

The above three boundaries have respective advantages and limitations. Reader needs to know the differences between these boundary types. In this dissertation, the rigid wall is adopted throughout the numerical simulations for the requirement of continuity and simplicity.

2.6.3.2 Controlling boundaries

The rigid walls in this study can be servo-controlled by two approaches, which include strain

controlled and stress controlled. Figure 2.15 shows a brief description of the specimen boundary. The strain controlled approach is similar as the displacement condition in FEM. It would be achieved through a prescribed velocity algorithm. Moreover, the boundary velocity should keep at a low level to eliminate the inertial effect, which would influence the granular system to achieve a quasi-static condition. The strain in this dissertation is the engineering strain which can be calculated by the displacements of boundary on the x and y directions.

$$\varepsilon_x = \frac{L_x - L_{x0}}{L_{x0}}; \varepsilon_y = \frac{L_y - L_{y0}}{L_{y0}} \quad (2.84)$$

where L_x and L_y are the current sample lengths, L_{x0} and L_{y0} are the reference sample lengths.

Force cannot be directly applied on the rigid wall. Hence, in DEM the interaction forces between particles and boundary would be generated by the applied velocity, which is also the reason for the relative displacement and overlap between two entities. The stresses (σ_{xx} and σ_{yy}) on the boundary can be computed by the total contact force on the boundary and the related contact area as follow:

$$\sigma_{xx} = \frac{\sum f(x)}{2L_y T}, \quad \sigma_{yy} = \frac{\sum f(y)}{2L_x T} \quad (2.85)$$

where $f(x)$ and $f(y)$ are the interaction forces between particles and walls along the x and y directions, T is the thickness of the disk shape particle. In this study, the particle thickness is set as a unit length. Since the rigid wall cannot directly applied force, the stress-controlled boundary is constructed by a numerical algorithm, which alters the wall velocity and monitors the interacted stress at each numerical step. The differences between the monitoring stress and the target stress should satisfied a restricted condition, then go to the next loading procedure. The following principles of this servo-controlled boundary is shown below. Here the target stress normal to the x and y direction is selected as an example as follow:

$$\dot{u}_i^{(w)} = G_i^{meas} (\sigma_i^{meas} - \sigma_i^{req}) = G_i \Delta \sigma_i \quad (i = x, y) \quad (2.86)$$

$$\left| \Delta \sigma_i / \sigma_i^{req} \right| \leq tolerance \quad (i = x, y) \quad (2.87)$$

where $G_i = \frac{\gamma A_i}{k_{ni}^{(w)} N_{ci} \Delta t}$ ($i = x, y$), A_i is the wall area, N_{ci} is the number of contacts on the wall, Δt is the time increment, γ is a relaxation factor $\in (0,1)$, and tolerance is an artificial convergence value. The relaxation factor and convergence are taken as 0.5 and 0.005, respectively, which are typical values that have been used in previous studies.

2.6.3.3 Implementation of different loading conditions

In this subsection, the DEM implemented procedures of the mimicked traditional geotechnical laboratory tests are briefly reviewed. These laboratory tests using different devices are mainly included oedometer test, direct shear test, triaxial test, etc. They can be used to get the strength and deformation properties of granular sands, even for the non-coaxial phenomenon (simply shear or hollow cylinder test). However, for the demand of computing efficiency, all the numerical studies are performed on 2D. Moreover, the research focused on the oedometer and triaxial tests, which are simplified as one dimensional confined normal compression and two dimensional biaxial shear. Each numerical test can be generally divided into three steps: initial sample preparation, isotropic consolidation, and loading. The initial sample can be generated by three approaches, which are expansion, compression and deposition. Since the inherent anisotropy is ignored in this dissertation, the widely used expansion method is adopted for numerical studies in this thesis.

Isotropic consolidation step is achieved by a stress-controlled algorithm of boundary walls. The governing principles of this stage can be seen from Eq. (2.83) to Eq. (2.85). In addition, the detailed numerical framework of isotropic consolidation that is proposed and adopted in current study is presented in Figure 2.16 and Figure 2.17. The main servo-controlled patterns are similar to those of Li (2006) and Dai (2010). A stress condition of 5 kPa is used to compress the sample under a temporary numerical liquefaction condition.

Biaxial shear tests can be classified into two kinds: drained and “undrained” conditions. As shown in Figure 2.15, wall 1 and 3 are chosen as the loading platens, and the other two walls are recognized as the confining boundaries. For the biaxial drained test, the loading platens are served by strain-controlled, which is set as a constant strain rate of 5% per minute (Jiang

et al., 2013; Zhang et al., 2013), which can efficiently control the granular assemblage remains in the quasi-static condition. Moreover, the confining walls are controlled by a stress manner boundary through Eq. (2.85) and Eq. (2.86). For the biaxial “undrained” test, it is essentially a constant volume test. Hence the velocity of confining boundary would justify each step to make the sample constant area. The velocity algorithm for the confined boundary is as follow:

$$L_x L_y = (L_x - 2\dot{u}_c \Delta t)(L_y - 2\dot{u}_l \Delta t) \Rightarrow \dot{u}_c = -\dot{u}_l L_x / (L_y - 2\dot{u}_l \Delta t) \quad (2.88)$$

where \dot{u}_c is the velocity of two confined walls, \dot{u}_l is the velocity of the two loading platens. The one dimensional compression test is usually used to evaluate the volume change feature of a granular assemblage. After the sample is consolidated to the target stress level, one pair of two opposite boundaries are selected as the loading platens, which are controlled by a constant strain rate. Meanwhile the other two walls are fixed.

Figures

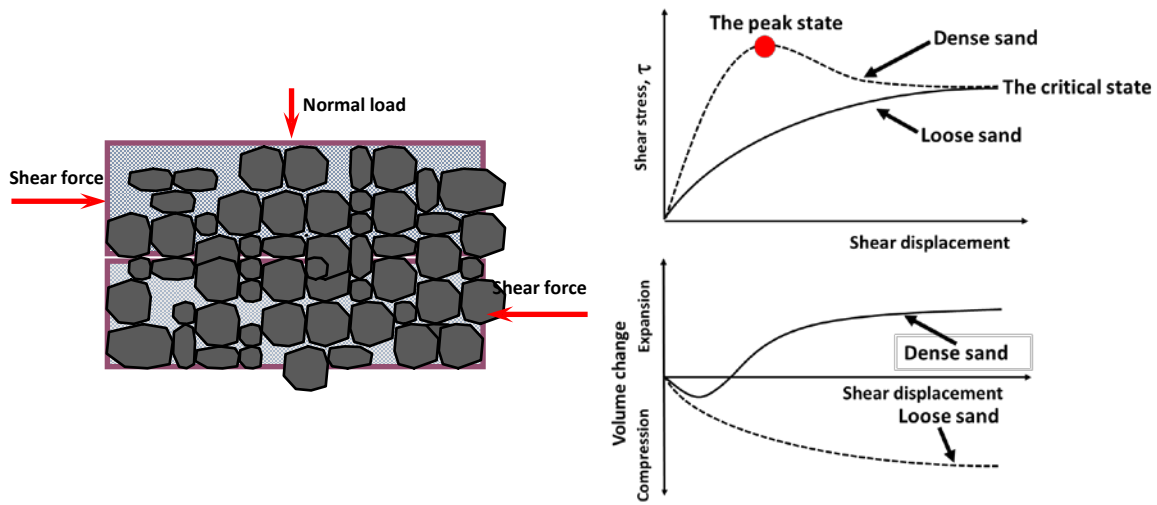


Figure 2.1: Illustration of direct shear test on dense and loose sands.

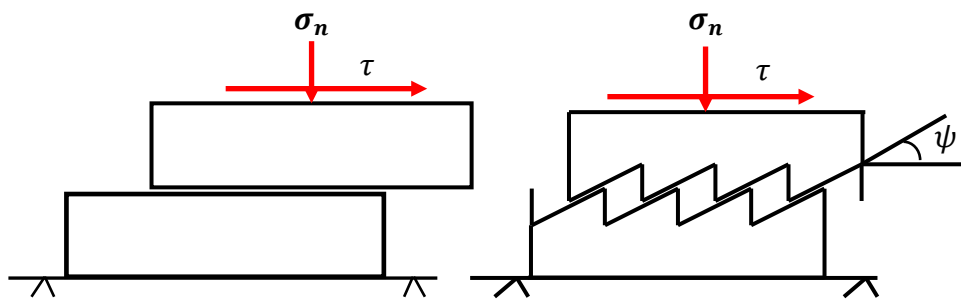


Figure 2.2: Schematic of saw-tooth model for dilatancy from Houlsby (1991).

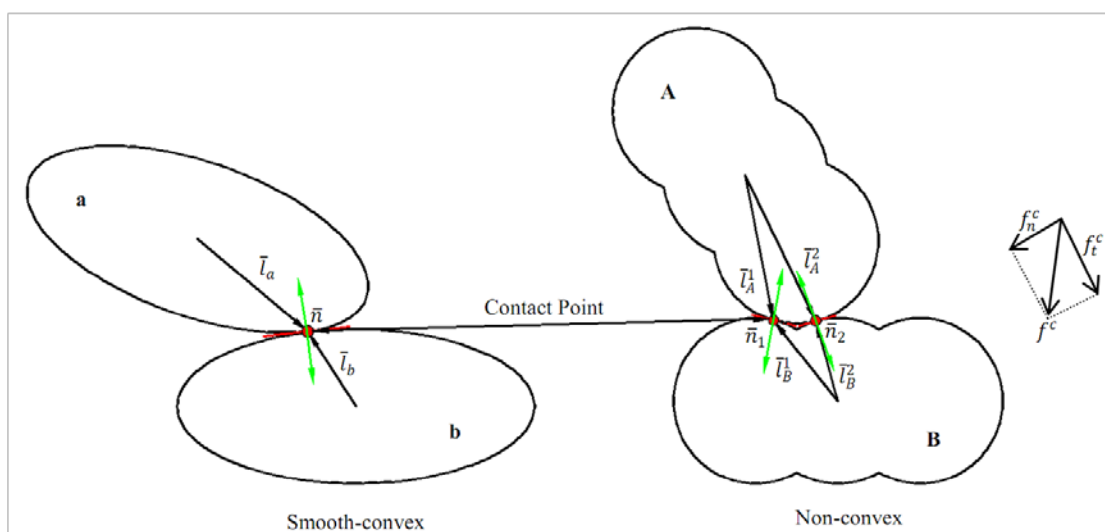


Figure 2.3: Illustration of the associated contacts, contact normal (\mathbf{n}), contact force vector (\mathbf{f}), and contact vector (\mathbf{l}).

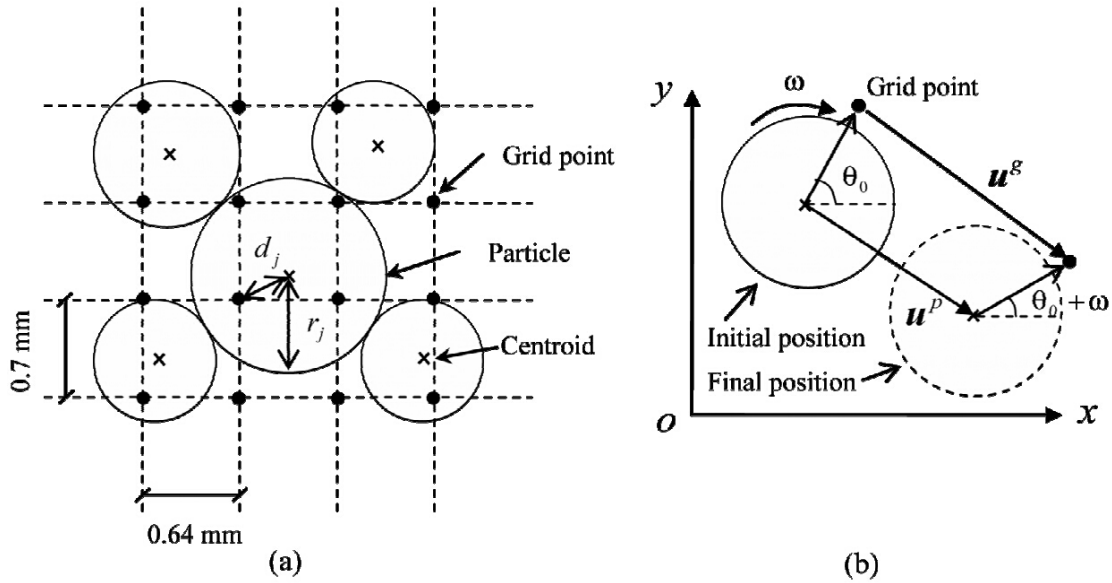


Figure 2.4: Illustration of the strain calculation method from Wang et al. (2007a).

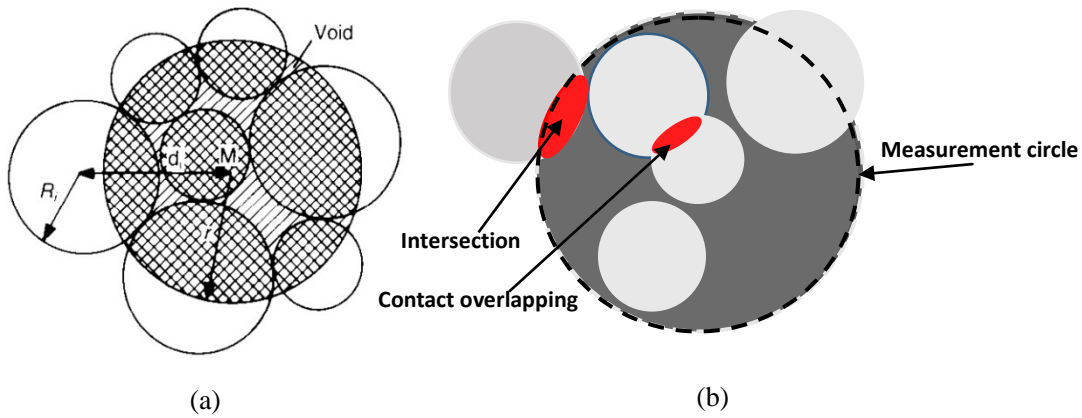


Figure 2.5: Schematic of measurement circle (a) from Bardet and Proubet (1991); (b) current calculated version.

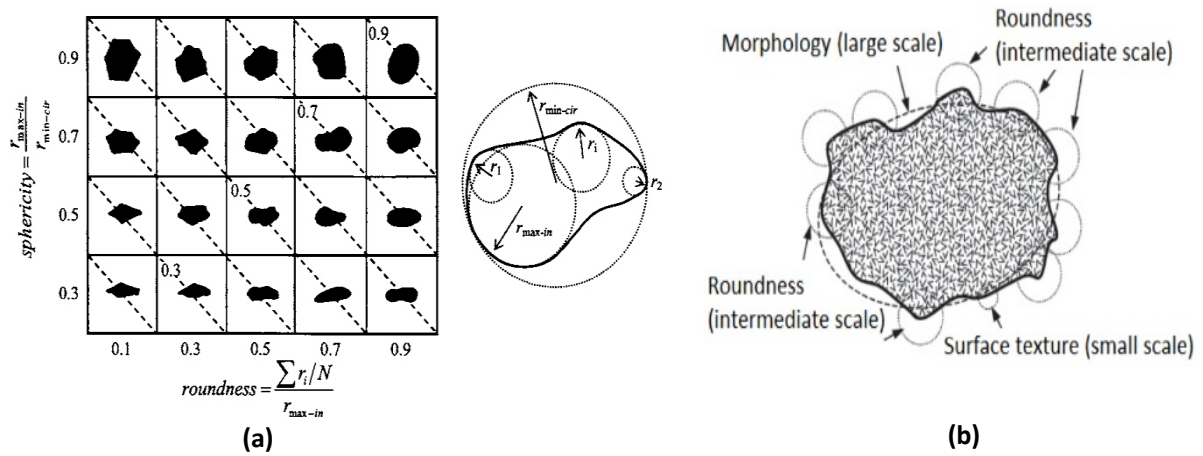


Figure 2.6: Illustrated of particle shape determination: (a) from Cho et al. (2006); (b) from Mitchell and Soga (2005).

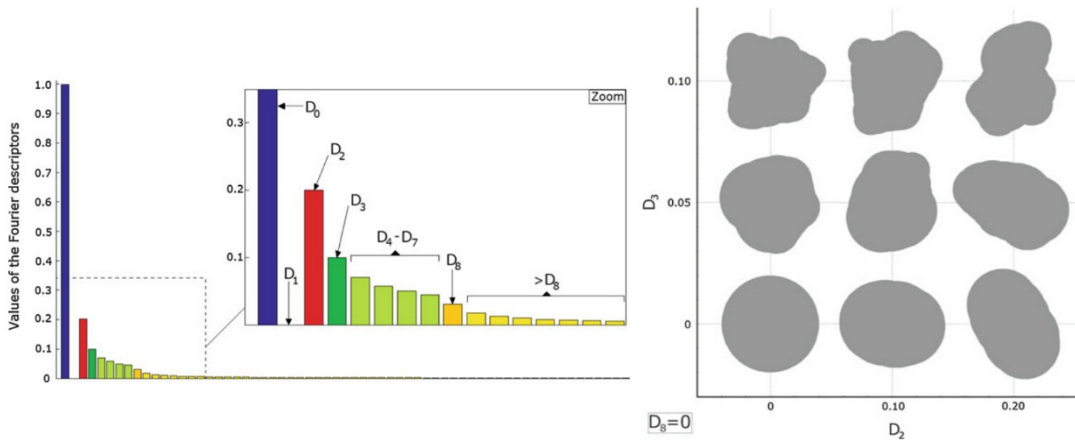


Figure 2.7: Illustrated of Fourier descriptors from Mollon and Zhao (2012).

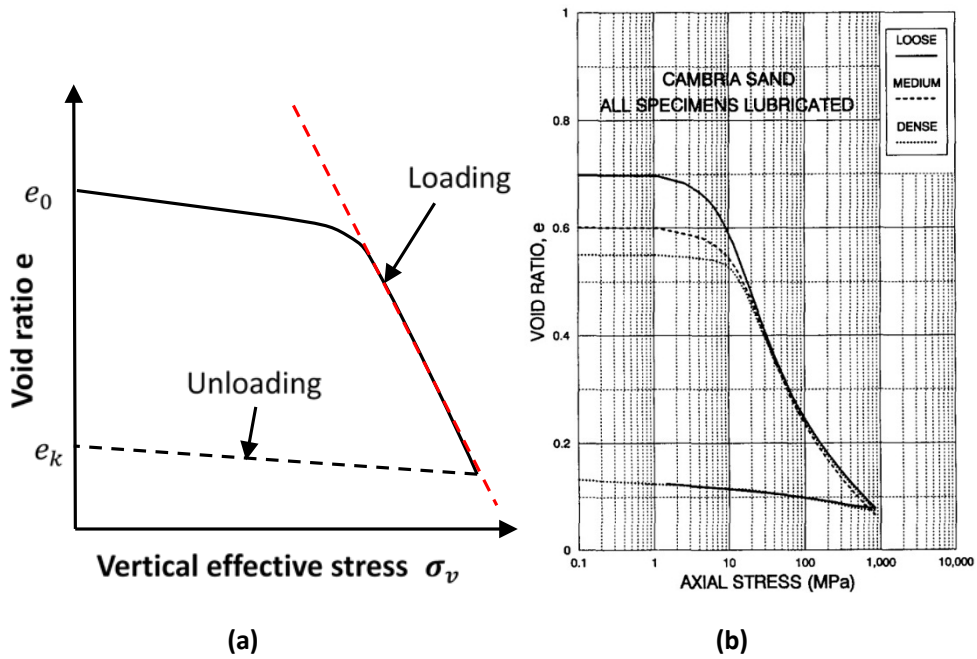


Figure 2.8: Schematic illustration of one dimensional compression behavior of sands: (a) idealized illustration; (b) experimental data from Yamamuro et al. (1996).

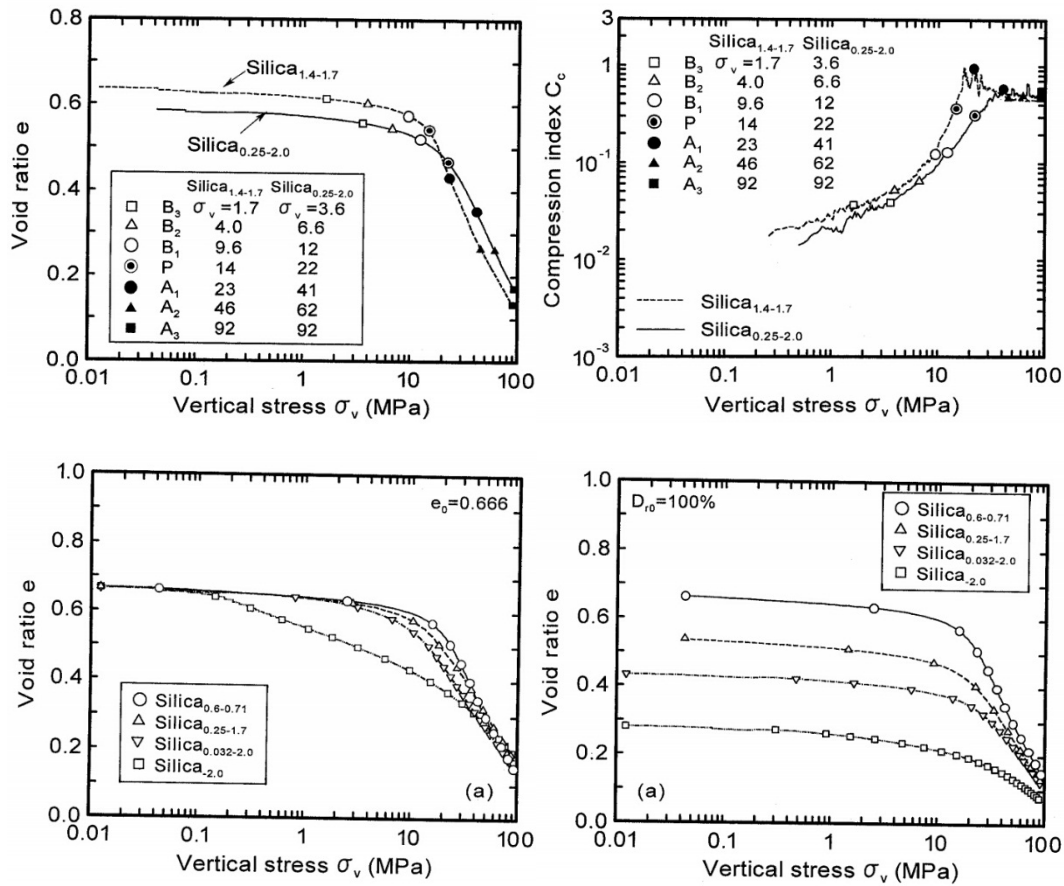
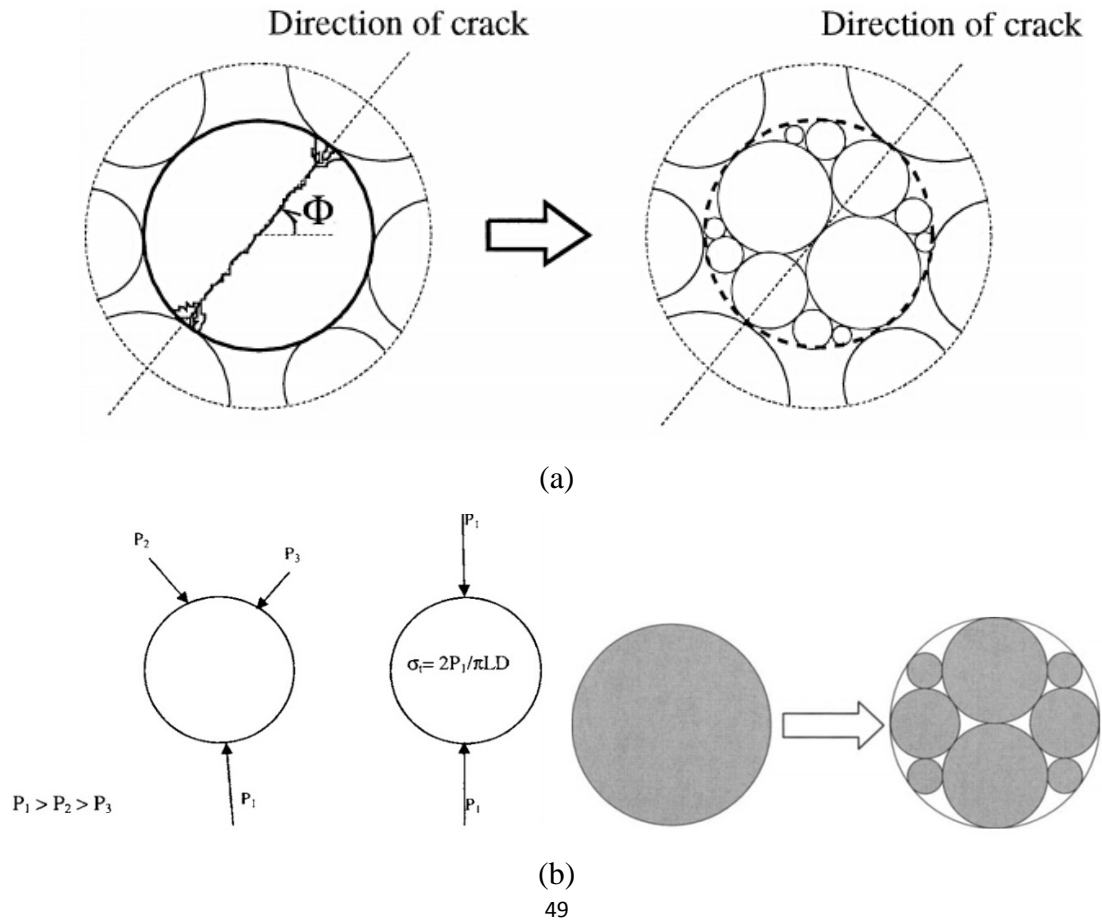


Figure 2.9: Experimental data of one dimensional compression from Nakata (2001a).



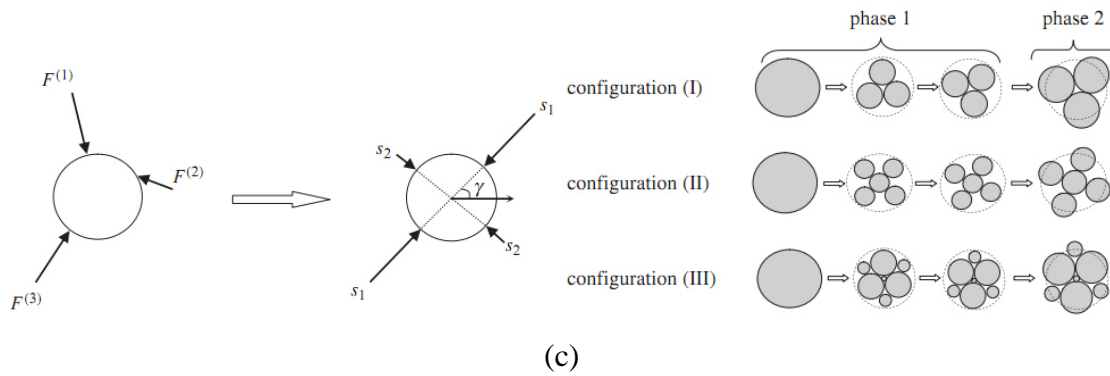


Figure 2.10: Schematics of failure criterion of a broken particle and the related post-crushing replacing manners: (a) from Tsoungui et al. (1999); (b) from Lobo-Guerreo and his co-workers (2005, 2006); from Ben-Nun and Einav (2010).

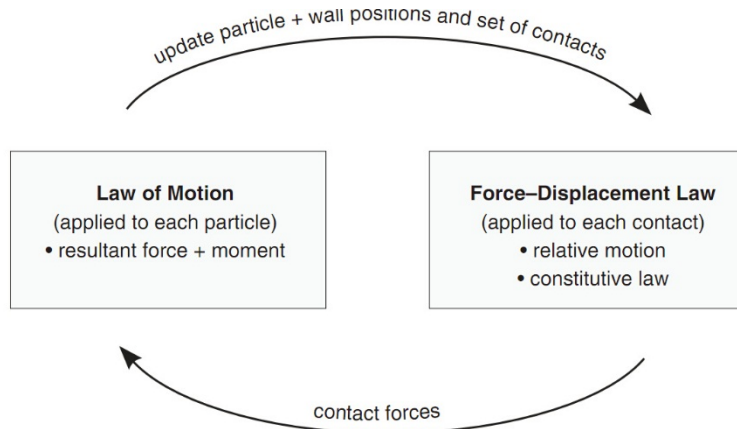


Figure 2.11: Illustration of calculation cycle in PFC^{2D} (Itasca, 2005).

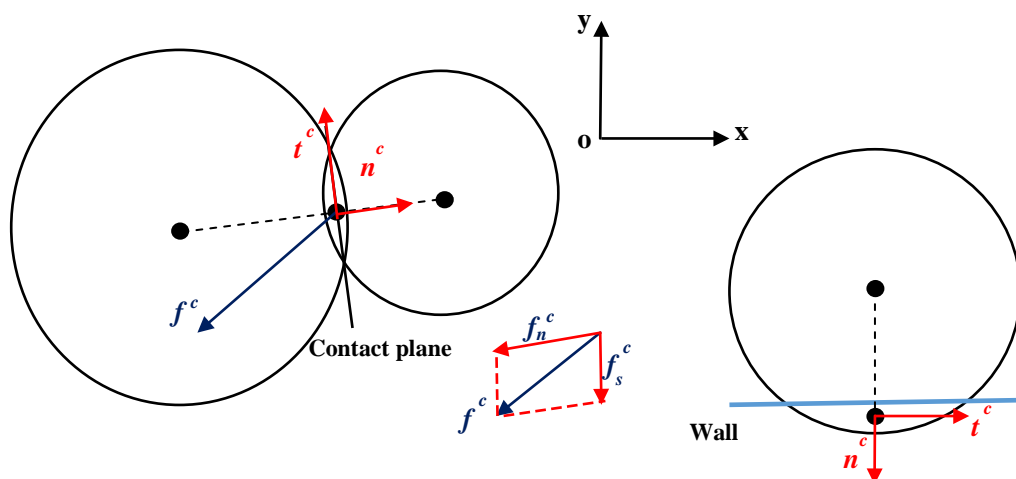


Figure 2.12: Diagram of contact c between two entities.

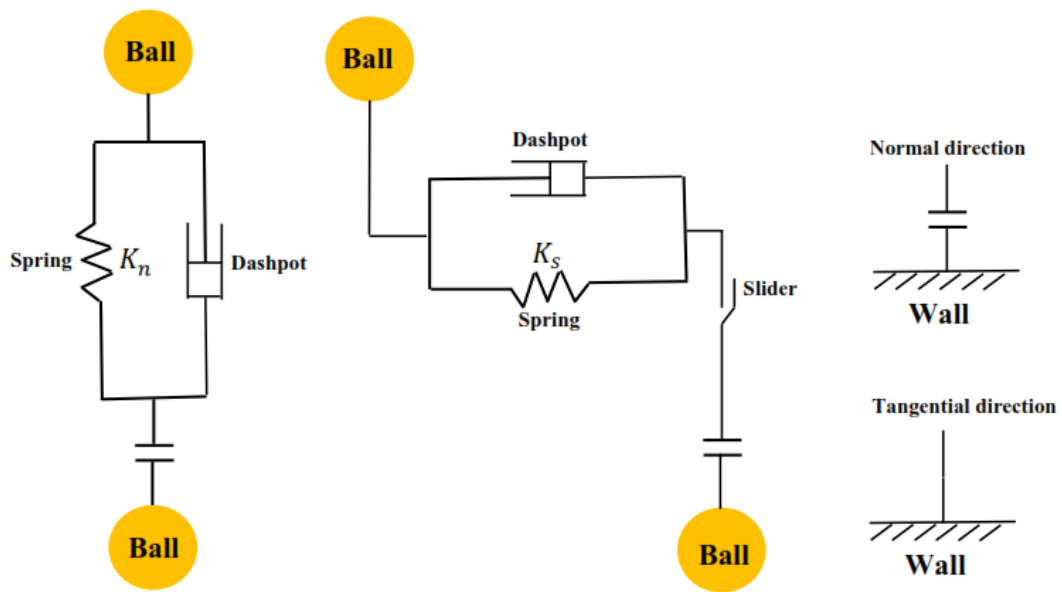
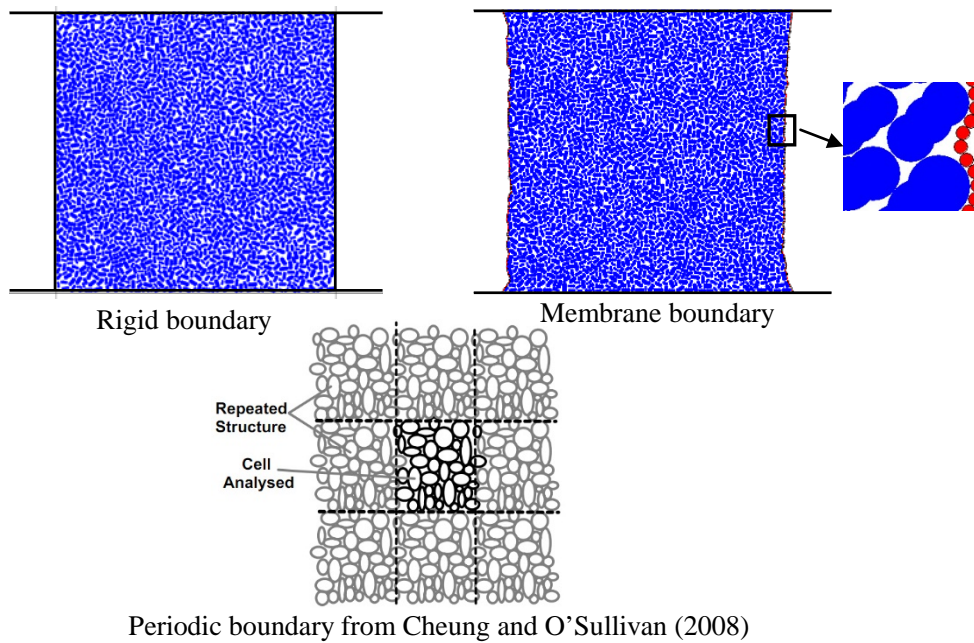


Figure 2.13: Illustration of the contact law for both ball-to-ball and ball-to-wall contacts.



Periodic boundary from Cheung and O'Sullivan (2008)

Figure 2.14: Schematic of the three boundary types within the DEM program.

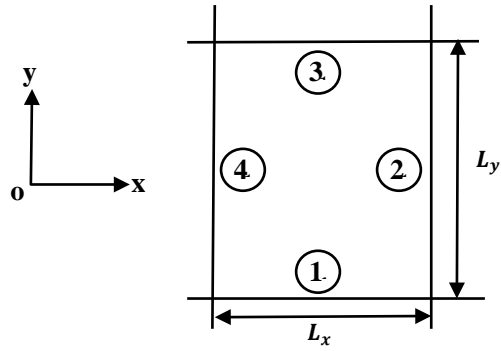


Figure 2.15: A schematic of specimen boundary.

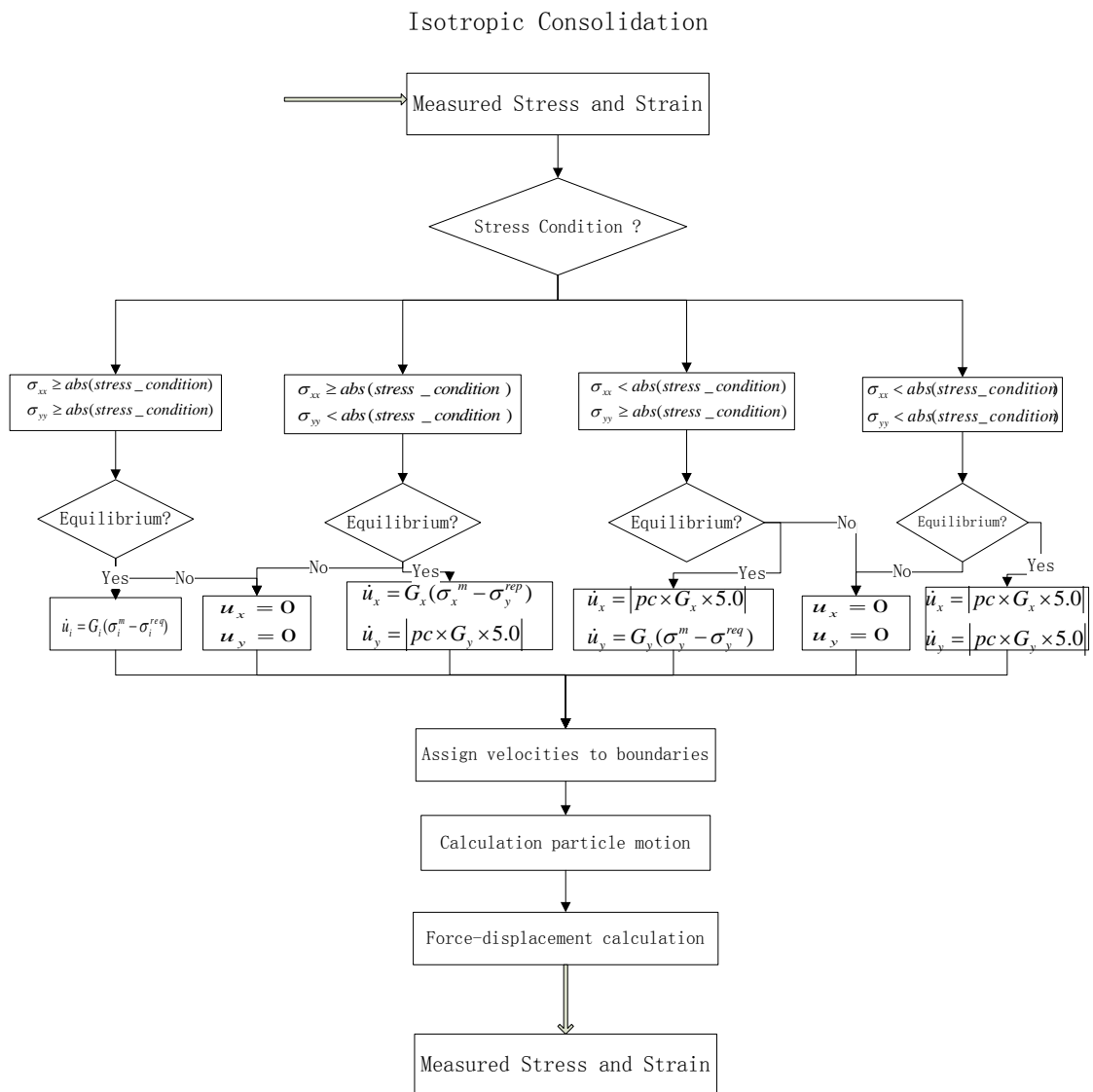


Figure 2.16: The detailed procedure for isotropic consolidation.

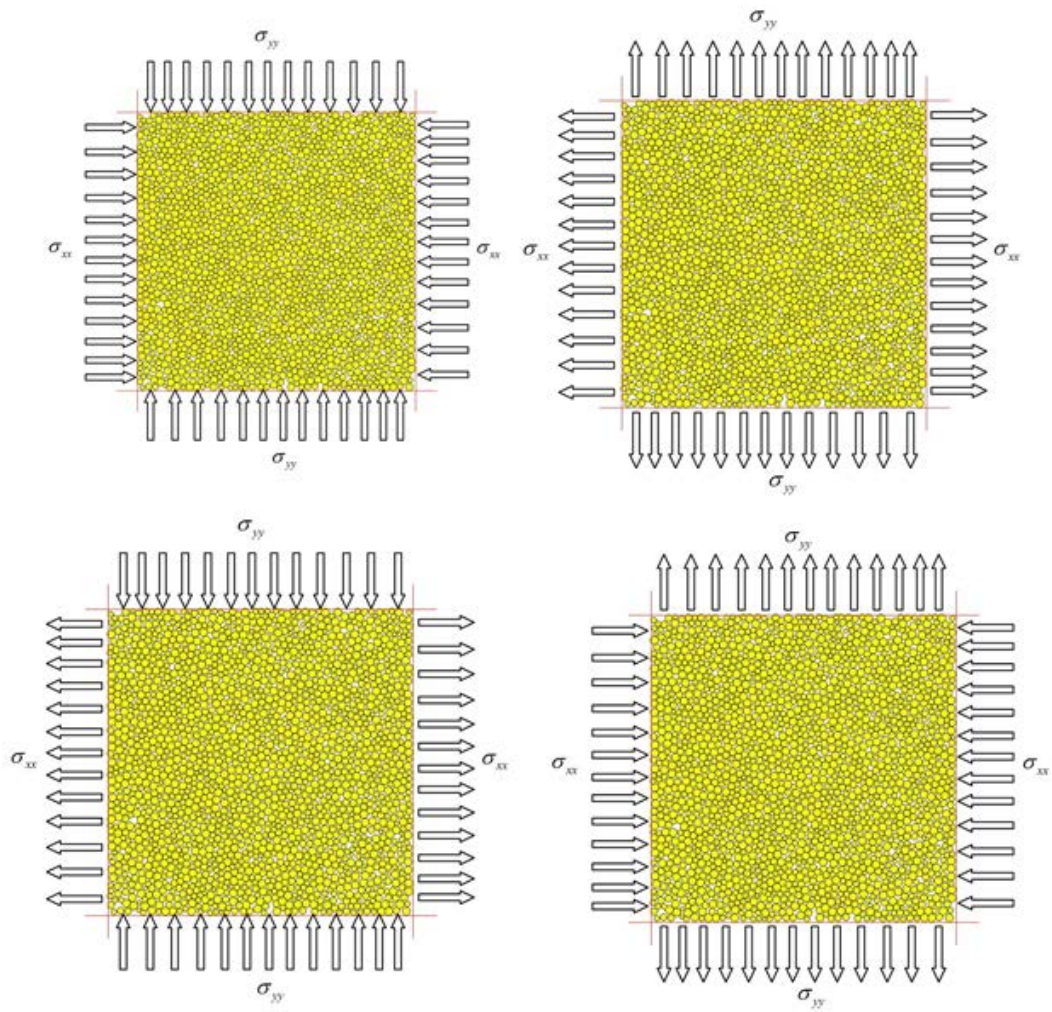


Figure 2.17: Schematic illustration of isotropic consolidation.

CHAPTER 3

Analysis of non-convex grains from micro to macro scales

3.1 Introduction

Particle shape can directly influence the structural features of granular assemblies, which ultimately control the mechanical properties of the granular material. Generally speaking, the peak friction angle and the peak dilation angle of circular disks (2D) or spheres (3D) are significantly lower than those of natural sand, which has an irregular particle shape. Many previous studies have aimed to determine the shape effect of granular materials. Two main approaches exist for investigating the shape effect. The first approach is to establish the rolling resistance model, which has been discussed in the section 2.4. However, the real rotation mechanism (instead of an artificial mechanism) is constrained by the particle's geometry, which may induce an asymmetric stress tensor for an individual particle. The second approach generates an appropriate model of the grain shape, in which the modelling geometry of the irregular particles can be divided into two main groups by contact: (1) a smooth-convex shape and (2) a non-convex shape. Smooth-convex particles can be generated using arbitrary functions or superquadric formulations based on previous work. The simplest smooth-convex shape is an ellipse. An ellipse shape has been used in many studies (Ng, 1994; Rothenburg and Bathurst, 1992). The non-convex particles can be formed by polygonal (Mirghasemi et al., 1997, 2002; Seyedi Hosseininia, 2012, 2013) or by combining clusters (Abedi and Mirghasemi, 2011; Jensen et al., 1999; Jensen et al., 2001; Lu and McDowell, 2007) . Some advanced engineering techniques (Digital, SEM, and X-ray) and robust algorithms have also been applied to establish realistic microscale particle geometry for the three-dimensional (3D) condition (Alonso-Marroquín and Wang, 2009; Ferrellec and McDowell, 2010; Fu et al., 2012; Fu et al., 2006; Liu et al., 2013; Wang et al., 2007; Williams et al., 2014). There is no doubt that real physical grains are 3D in geometry; however, more artificial assumptions are required in the realistic geometry algorithms. Moreover, 3D simulations require significantly higher-performance devices, or even parallel analysis.

Although, the direct comparison between 2D and 3D simulations are unavailable. The findings from the 2D simulations can also give an implication to the 3D simulations, which will be carried out in the future 3D study. Many previous studies have demonstrated that a 2D discrete element model can adequately capture various complex mechanical features of granular materials (Abedi and Mirghasemi, 2011; Jiang et al., 2014a; Jiang et al., 2014b; Jiang et al., 2006; Luding, 2005; Ng, 1994; Rothenburg and Bathurst, 1989; Rothenburg and Bathurst, 1992; Seyed Hosseinia, 2012, 2013; Wang et al., 2007b; Wang et al., 2007a). Moreover, the visual deformation patterns and force chains are easily captured by 2D analysis; therefore, this study uses 2D numerical simulations, which are sufficient for the fundamental study of the physical and mechanical properties of the granular assemblages. The author here choose to combine clusters to generate non-convex particles for the shape effect analysis, which can lead to a better understanding of the problem.

Although non-convex particles are well recognised in the real granular world, they are still not fully understood either on a laboratory experimental scale or through simulated numerical methods, particularly for quantitative analysis. A quantitative analysis study is thus important to understand the more detailed behaviour of granular materials. Many different quantitative shape descriptors have been proposed for this purpose in previous studies, which can be seen in Section 2.4. However, there are very few comparisons of mechanical properties performed on these common particle shape definitions, particularly for non-convex shapes. In the present study, eight different particle shapes are evaluated using four quantitative shape descriptors to address this insufficiency. This methodology provides an additional approach for a suitable and adequate shape index. Next, quantitative relationships between particle shape and strength indexes are investigated. In addition, the patterns of strain localization for different shapes are captured. The relationships between particle shape and microscale fabric parameters are also evaluated at the peak state (peak stress ratio $(\frac{\tau_f}{\sigma_n})_{\max}$) and critical state (stress ratio $\frac{\tau_f}{\sigma_n} = \text{constant}$). Moreover, the accuracy of stress-force-fabric (SFF) (Christoffersen et al., 1981; Guo and Zhao, 2013; Li and Yu, 2013; Rothenburg and Bathurst, 1989; Seyed Hosseinia, 2013) is investigated, with special consideration of the accuracy of

average contact normal forces and the distribution of contact vectors. In this thesis, an evaluation of particle interlocking effects from peak state to critical state is also presented to address the particle shape effect using a probabilistic approach (Zhou et al., 2013). The distributions of force chains for different shapes are also compared quantitatively by the shape descriptor. The inter-particle force network is a striking feature that determines the mechanical properties of granular mass (Radjai et al., 1996; Sun et al., 2010). It can be used to describe the strength variation at critical state in a microscale model. Additionally, the author finds that the relationship between the strong force network and the confining pressures can explain the decrease in the strength indexes with the increased confining intensities.

This chapter presents a comprehensive analysis of particle shape effects using the discrete element method (DEM), which captures the micro mechanical behaviour of the granular assembly. The followed section of this chapter will describe the definitions for the particle shape indexes, which are analysed and compared in a later section. Meanwhile, the DEM modelling details are also briefly introduced in this section. Next, the numerical findings and discussion are presented.

3.2 Investigation scheme

3.2.1 The compared particle shape descriptors

Using the DEM method, rigid particles with soft contacts can be used to reflect the contact geometry and evaluate the fundamental features of a cohesionless material. Seven non-convex particles are employed in the present DEM analysis, where each irregular particle is expanded using a standard element to prevent incorrect moments of inertia. Hence, the combined clump density is modified and reassigned ($\rho_{\text{clump}} = \frac{V_{\text{clump}}\rho_{\text{disk}}}{(V_{\text{overlap}}+V_{\text{clump}})}$). Next, the numerical results are compared. The particle shape categories are shown in Figure 3.1(a) and Table 3.1. Four simple quantitative shape indexes (Figure. 1(b)) are considered: elongation (AR), circularity, shape parameters SF and AF. The definitions of these indexes are presented by several investigators (Cho et al., 2006; Sukumaran and Ashmawy, 2001) as follows:

$$AR = \frac{EL_{\min}}{EL_{\max}}, \quad (3.1a)$$

$$Circularity = \frac{D_{\max-in}}{D_{\min-out}}, \quad (3.1b)$$

$$SF = \frac{\sum_{i \in N} |\alpha_{i_grain}|}{N \cdot 45^\circ} 100\%, \quad (3.1c)$$

$$AF = \frac{\sum_{i \in N} (\beta_{i_grain} - 180^\circ)^2 - [(360^\circ)^2 / N]}{3(180^\circ)^2 - [(360^\circ)^2 / N]}, \quad (3.1d)$$

where EL_{\min} and EL_{\max} are the smallest axis and largest axis, $D_{\max-in}$ and $D_{\min-out}$ are diameters of the largest inscribed circle and smallest circumscribed circle, respectively, α_{i_grain} is the difference in orientation between the particle chord vector and the related circle, β_{i_grain} is the difference between 180° and the internal angle of the particle, and N is the number of interval points.

The detailed values for the above shapes are shown in Table 3.1, and the sampling interval is set at 9° ($N=40$) to represent the degree of angularity and the surface roughness for each shape. A small interval (4.5°) is also chosen to capture the quantities of the rhombus, where the difference between 4.5° and 9° is very small. Hence, the interval number ($N=40$) is adequate for the quantitative analysis of the particle shape, as was suggested by the initial supporters of this idea (Sukumaran and Ashmawy, 2001). In this thesis, different definitions for the particle shape are compared to obtain an improved curve-fitting analysis and understanding.

3.2.2 DEM simulation details

In the present biaxial numerical simulation, the numerical sample initially contains 9,506 circular particles with dimensions of 100 mm (W) \times 200 mm (H). The numerical specimen illustration (Figure. 3.2), which can easily be used to capture the internal deformation of a granular sample, was first proposed by Jiang et al. (2006) for effectively evaluating the deep penetration mechanisms in granular materials. The particle size distribution (PSD) is also

shown in Figure 3.2. The mean particle diameter (d_{50}) is 1.62 mm with a uniformity coefficient of $C_u = 1.47$. After an initial porosity (0.16) is obtained, seven irregular particles will replace the initial disk with an equivalent area and the same center location. The orientation of the irregular particles is arbitrarily distributed in the range of 0° to 360° . A comparison of the mechanical properties is performed, using a biaxial loading test on single shapes. During the servo-control mechanism, the sample is subjected to a target consolidated pressure (100, 300, and 500 kPa). In this study, the loading rate is a constant strain rate of 5% per minute, and the confining stress on the lateral walls is constant. All simulations in this thesis are maintained in a plane strain condition. The contact model selection also requires careful consideration. For the collision and small-strain problems, the difference between the linear contact and non-linear contact model is obvious (Kumar et al., 2014; O'Sullivan, 2011). However, the numerical specimens in this study are all within the process of quasi-static shearing, where the small-strain response is ignored in the element tests. Additionally, previous study (Mirghasemi et al., 1997) has found that choosing a suitable magnitude for the linear contact stiffness will produce macroscopic behaviour similar to Hertzian behaviour, especially for the large-strain response. Moreover, many researchers adopted linear contact models and were able to adequately represent the mechanical responses of granular media (Abedi and Mirghasemi, 2011; Jensen et al., 1999; Jiang et al., 2009; Kumar et al., 2014; Seyedi Hosseininia, 2012, 2013). Therefore, for simplicity, the author used the linear contact model in the numerical simulations. It is well known that using only a sliding mechanism may not be efficient to control the granular packing within a quasi-static system. Therefore, local non-viscous damping is artificially introduced in this study, to avoid the non-physical vibrations that develop at the contacts. This damping model only damps the acceleration motion. The non-dimensional damping constant is also frequency-independent. The damping model has been discussed in detail by O'Sullivan (2011). The values of the numerical parameters are provided in Table 3.2. The internal-particle friction coefficient follows previous studies of the author and other researchers (Abedi and Mirghasemi, 2011; Jiang et al., 2011; Seyedi Hosseininia, 2012, 2013; Wang et al., 2007b; Wang et al., 2007a). Additionally, the particle density, damping coefficient and contact stiffness used for the present study are very close to those in the above studies. For a better comparison of particle shape effects,

equal input parameters are used for the mimic samples.

3.3 Numerical findings and discussions

3.3.1 Strength and deformation for the prior shape descriptor

The particle shape can directly influence granular stress-strain behaviour, especially for the critical state, as shown in Figure 3.3(c). The quantitative analysis for the particle shape effect is shown, with the strength and dilation characteristics (Figure 3.3 and 3.4). The different particle shape descriptors (Eq. 3.1) are considered to evaluate the trend of the peak friction angle $(\sin(\phi_{\text{mobilized}})_{\text{max}} = (\frac{\tau_f}{\sigma_n})_{\text{max}})$ (Figure 3.4(a)), critical friction angle $(\sin\phi_{\text{mobilized}} = \frac{\tau_f}{\sigma_n} = \text{constant})$ (Figure 3.4(b)), and peak dilation angle $(\sin\psi_{\text{max}} = (-\frac{d\varepsilon_1+d\varepsilon_2}{d\varepsilon_1-d\varepsilon_2})_{\text{max}})$ (Figure 3.4(c)) through the fitting comparisons of the exponential function. The comparative results show that the SF index provides the best fit, where the associated adjusted residual square is approximately 1.0. The aspect ratio and AR indexes produce poor results in the discrete regression analysis. Hence, the SF index is suggested to evaluate the granular mechanical behaviour from the micro-to-macro scale in the following sections. The peak friction in these granular assemblies is dramatically increased for a low SF value, and slightly decreased for a large SF coefficient. The shape of the particle, particularly for a higher SF value, will play an important role in the global mechanical behaviour. The critical friction angle (mean value in the critical state) is directly increased by the SF coefficients. Particles with higher SF values are more difficult to realign at the large deformation state, which may directly increase the critical friction angle. The peak dilation angle then decreases faster than the peak friction angle associated with a larger SF value. Unless otherwise specified, the following section is studied under 100 kPa.

Previous studies have proved that shear can induce strain localisation within granular material under rigid or flexible boundaries (Desrues and Viggiani, 2004; Gao and Zhao, 2013; Jiang et al., 2014a; Jiang et al., 2011). It is clear in Figure 3.5 that the ultimate shear bands (i.e., 15% strain) for the irregular particles are much more obvious than those for the disk sample. Accumulated shear strain in Figure 3.5(b) was calculated using the mesh-free strain approach

proposed by Wang et al. (2007a). Nevertheless, the localisation patterns exhibit disparities for different samples. Particle shape can directly influence the evaluation of strain localisation in the granular media. Additionally, the rose distributions of the contact normal force magnitudes and associated numbers are investigated at the critical state (15% strain) for typical shapes (Figure 3.5(c)) to evaluate the progressive behaviour of the granular media using advanced visualization techniques to display two micro-anisotropy parameters in the same figure. Figure 3.5(c) can also be used to explain the differences between the macro-mobilised strength and shear bands for these shapes. It can be found in the below figure that the variation of the measured shear bands are only sensitive between the circle and irregular shapes. For different irregular assemblages, the orientation angles are close to each other. This result is matched with previous studies (Mohamed and Gutierrez, 2010) of the biaxial shearing of rolling resistance samples, where the orientations of shear bands are only sensitive with smaller rolling resistance coefficients (<0.1). A more intense degree for the contact normal force can induce a higher critical strength. Additionally, the low anisotropic distribution of the contact number for circular particles cannot easily generate an obvious strain concentration. The development of these micro-statistical variables can help explain the anisotropy development in later parts of the study.

3.3.2 Micro anisotropic parameters and SFF

To quantify the arrangement of contacts, the second-order Fourier series represent the shape of the contact orientation distribution, the mean contact force distribution, and the mean contact vector distribution. The determination of these physical indexes have been discussed in details in the above literature review chapter. In this chapter, the way to choose the average normal contact vector (\bar{l}_0) and the average normal force (\bar{f}_0) over all contacts are firstly discussed. These two indexes can be determined as follow:

$$\bar{f}_0 = F_{ii}^n = \frac{1}{2\pi} \int_0^{2\pi} \bar{f}_n(\theta) d\theta = \frac{1}{N_c} \sum_{c \in N_c} \frac{f_n^c n_i n_i}{1 + a_{kl}^c n_k n_l} \neq \frac{1}{N_c} \sum_{c \in N_c} f_n^c, \quad (3.2a)$$

$$\bar{l}_0 = V_{ii}^n = \frac{1}{2\pi} \int_0^{2\pi} \bar{l}_n(\theta) d\theta = \frac{1}{N_c} \sum_{c \in N_c} \frac{l_n^c n_i n_i}{1 + a_{kl}^c n_k n_l} \neq \frac{1}{N_c} \sum_{c \in N_c} l_n^c. \quad (3.2b)$$

Figure 3.6 (a) shows the accuracy of the SFF relationship for different average contact normal

forces versus the axial strain for two cases. $\bar{f}_0 = \frac{1}{N_c} \sum f_n^c$ will induce a significantly higher stress ratio than the average anisotropic determination in Eq. 3.2(a), which is nearly the same as the monitored data. Hence, the average normal force that is selected is very important. The figure is useful for determining the effect of the induced anisotropies in Figure 3.6(b), (c), and (d), where the critical state parameters are the mean values within the critical regimes. The particle SF coefficients can directly influence fabric development in the granular assembly at the peak/critical state. With the exception of the contact normal anisotropy coefficient, the magnitudes of these fabric parameters are larger at the peak state. These figures show that the anisotropy coefficients at the critical state are increasing nearly linear with the associated particle SF coefficient. Additionally, the contact normal, which can describe the geometry contact, shows the highest increasing gradient. However, particle shape displays a threshold effect for these fabric parameters, except for the contact tangential anisotropic coefficient, which has only a minor contribution to the friction and dilation angle at the peak state. This microscale statistical information can also be used to explain the variation of macroscale strength indexes in Figure 3.4.

The evolution of the mean contact normal vector anisotropy (parameter b_n) and the contact tangential vector anisotropy (parameter b_t) is presented in Figures. 3.7(a) and (b) and is determined using the discrete data. The selected rose distributions of the contact vectors at the critical state are also shown for the Elongated5 category, where the Fourier series fit with the collected data from the numerical results. These results are interesting and useful, but are seldom considered in studies. The magnitudes of b_n and b_t depend on the contact normal distribution along the vertical and horizontal directions through the whole deviatoric loading. Their related values have a smaller magnitude than the minimum values of the other anisotropy coefficients, except for Elongated5 (Figures. 3.7(a) and (b)) where the values of b_n and b_t for Elongated5 at the critical state are close to the minimum value of a_t in Figure 3.6 (d). Hence the anisotropic coefficients of the contact vectors and the related principal angles can also be influenced by the particle's shape, especially for a high SF value.

The general SFF formulation (Eq. (2.59)) may be more accurate than the simplified expression (Eqs. (2.60) & (2.61)) in Figure 3.8. Hence, the general SFF relationship is suggested as a means of verifying the monitored data in the granular assemblages and the microscale fabrics evaluation. The magnitude of the contact vector cannot be ignored for the high SF grains.

3.3.3 Friction mobilization and force chain distribution

The probability distribution of the sliding friction mobilisation index I_m can determine the shape effect (Zhou et al., 2013). The definition of I_m is:

$$I_m = \frac{|f_t^c|}{\mu f_n^c} \quad (3.3)$$

The probability value of I_m at the plastic portion ($I_m=1.0$) in the peak state is significantly higher than that in the critical state, which is always associated with a larger particle interlocking effect, and can explain the strength variation between the peak and critical states. The particle shape may have a threshold effect, based on the uniform gradient of the sliding friction from the centre of the shear band (Figure 3.9(a)). Figure 3.10(b) shows that the average I_m increases linearly with SF, and the incremental gradient and magnitude are significantly lower at the critical state than at the peak state.

The semilogarithmic plot of the probability distribution of the contact normal force normalised by the mean contact force $\langle f_n^c \rangle$ is given in Figure 3.10 at the critical state. For all of the shapes in this thesis, the probability density of the normalised contact normal force essentially follows a power-law decay:

$$P(f_n^c) \propto \begin{cases} (f_n^c / \langle f_n^c \rangle)^\alpha & f_n^c < \langle f_n^c \rangle \\ e^{\beta(1-f_n^c/\langle f_n^c \rangle)} & f_n^c > \langle f_n^c \rangle \end{cases}, \quad (3.4)$$

where α and β represent the variation indexes. Here we only focus on the distribution of the strong force, which resists the major external load transfer. β decreases with increasing SF, which shows the intensity of inhomogenous contact normal force shift. This microscale force chain information can also be used to explain the variation in a_n in Figure 3.6(c). Additionally, the higher strong force percentage can increase the strength indexes.

3.3.4 Confining pressure effect

Figure 3.11 shows the strength indexes of biaxial compression tests under different confining pressures. The peak friction angle and critical state friction angle are slightly decreased with the increased confining pressures. Whereas, the peak dilation angle is highly decreased. Particle shape still plays an important role in the friction angles, even under higher confining pressures, and especially for the critical state. Additionally, the strain value at peak friction angle and peak dilation angle is enlarged by the increased confining stress in Figure 3.11(d). There is also a small saturation SF value for the peak dilation angle under the higher confining stress level. The variation in these strength indexes can also be explained by the strong force distribution in Figure 3.11(e). The green arrow indicates that the coefficient of β decreases with increasing confining pressure.

3.4 Conclusions

This chapter quantitatively analyses the particle shape factor through a series of numerical studies of non-convex irregular particles, using a significant amount of computer analysis. SF provides a better evaluation of the granular mechanical behaviour than do other particle shape indexes. The critical state friction angle increases linearly with the SF value. The strong force chain in the higher SF granular assemblies will occupy a larger portion of the assemblage contacts, which will increase the packing resistance. Additionally, the peak friction/dilation angle shows a nonlinear correlation with SF where there exists a threshold value. Furthermore, all of the strength indexes decrease with increasing confining pressure, especially for the dilation angle. It is remarkable that the coefficient of β for the contact force decreases with increasing confining pressure. This study also found that shear localisation patterns are sensitive to the particle shape. It is difficult to generate a shear band for circular particles with a low anisotropic level of the contact normal.

The average contact normal force is also found to influence the accuracy of the SFF formulation. The magnitudes of fabric parameters are higher at the peak state, except for the contact normal anisotropic coefficient with a larger SF. The contact tangential force anisotropic coefficient shows a linear, increasing relationship with SF at both the peak and

steady states, but its contribution to the macroscale strength is smaller than that of the other fabric parameters. The anisotropic coefficients of the contact vectors and the related preferred angles can also influence the SFF relationship. Hence, the general formulation of the SFF relationship is suggested for representing the mechanical behaviour of irregular granular media.

The probability distributions of friction mobilisation and contact force display an inhomogeneous distribution within the granular packing. The microscale average I_m increases with SF magnitude, especially at the peak state. The higher strong force percentage also increases with SF. The end of contact force distribution is used to explain how macroscale strength varies with the particle shape index and confining pressure level.

Tables

Table 3.1: Quantitative value of the shape indexes.

Category	Aspect ratio	Circularity	SF (%)	AF (%)
Circular	1.0	1.0	0	0
Elongated1	0.952	0.952	4	0.1
Elongated2	0.909	0.909	8	0.4
Elongated3	0.80	0.80	19.8	1.9
Elongated4	0.667	0.667	33.3	3.88
Elongated5	0.50	0.5	45.8	13.2
Triangular	0.957	0.722	34.5	10.4
Rhombus	0.804	0.710	35.1 ($N=40$)	12.9
			33.6 ($N=80$)	12.96

Table 3.2: Input microscale parameters in DEM simulations.

Sand particles	Density (kg/m^3)	2600
	Normal/shear contact stiffness (N/m)	1×10^8
	Inter-particle frictional coefficient	0.5
	Local non-viscous damping	0.45
Confining boundaries	Normal contact stiffness (N/m)	1×10^7
	Frictional coefficient	0.0

Figures

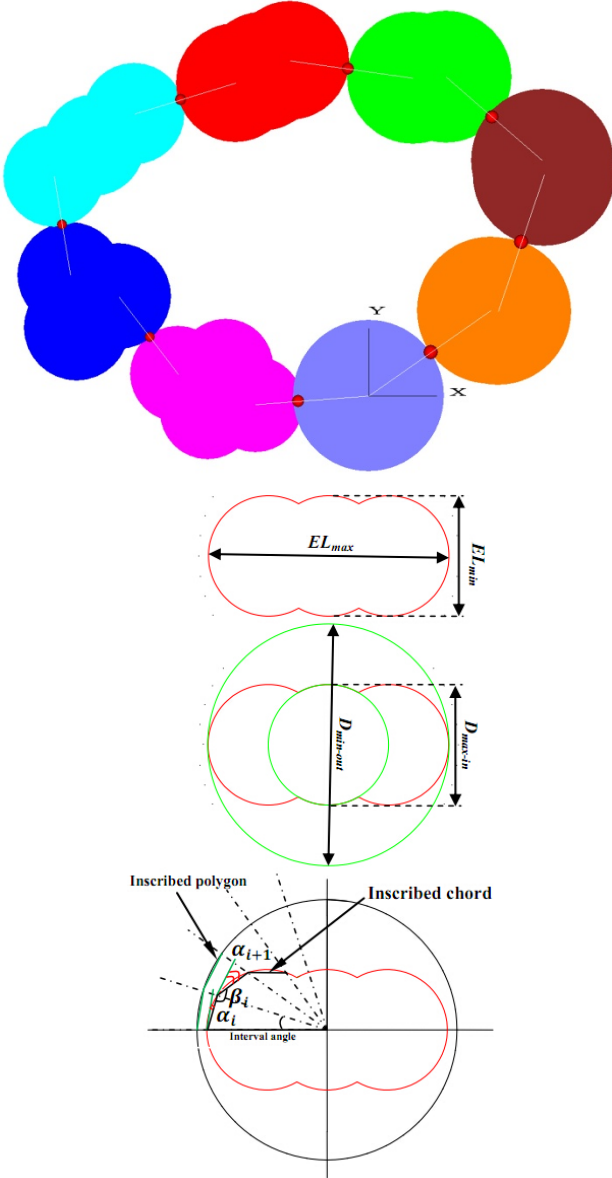


Figure 3.1: (a) Schematic of the particle shapes; (b) illustration of different particle shape indexes.

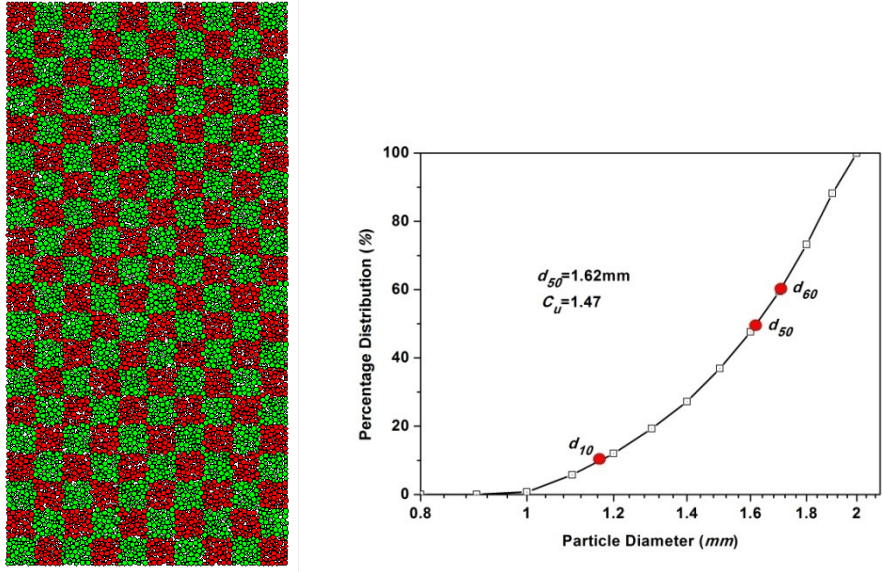
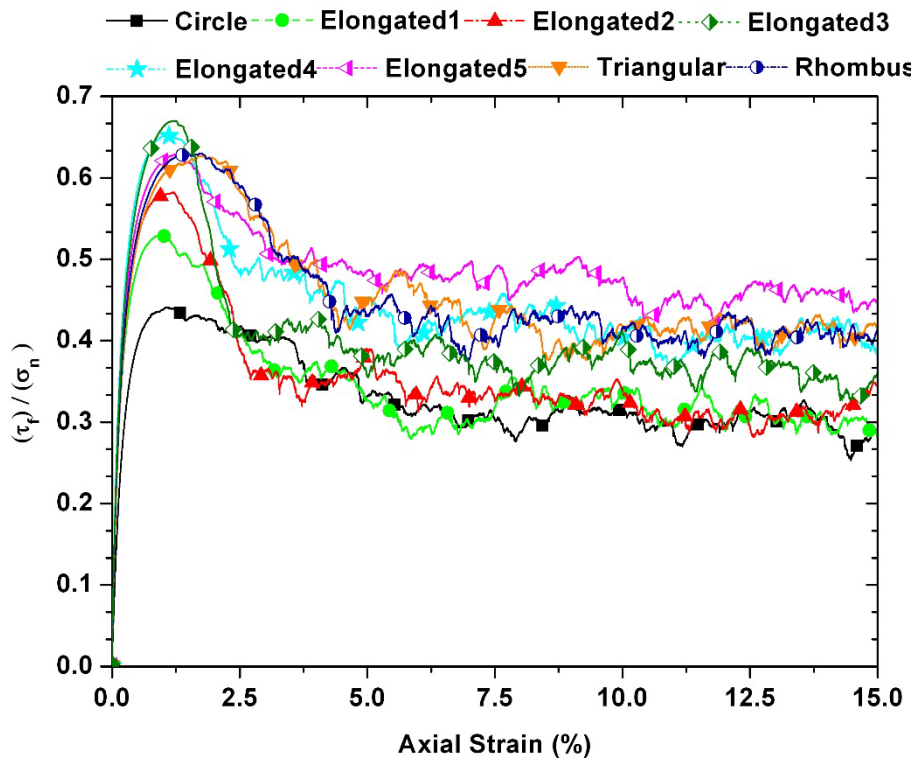


Figure 3.2: Schematic of the numerical specimen and particle size distribution.



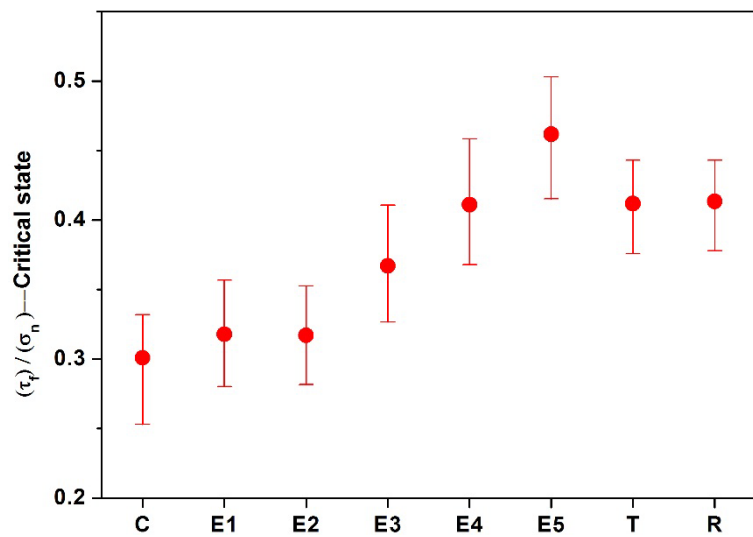
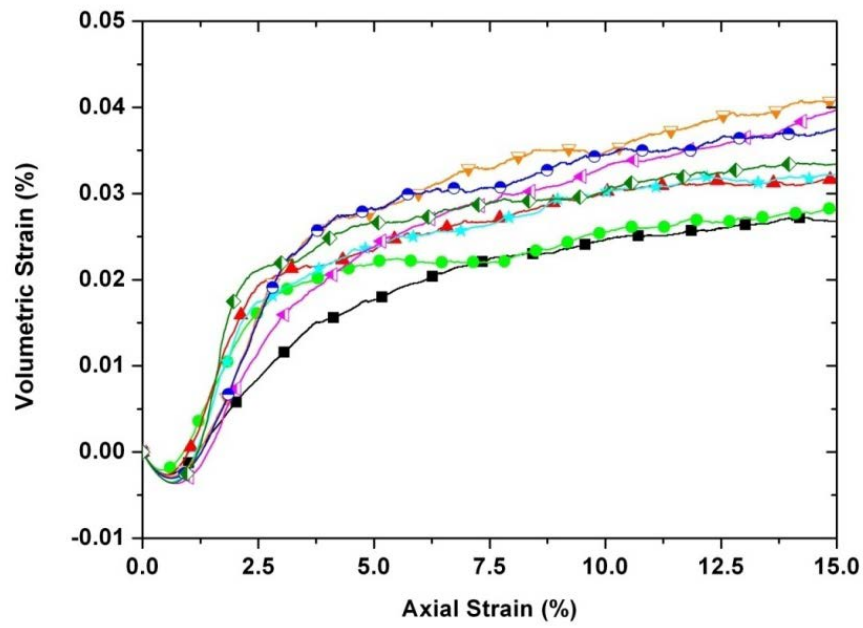
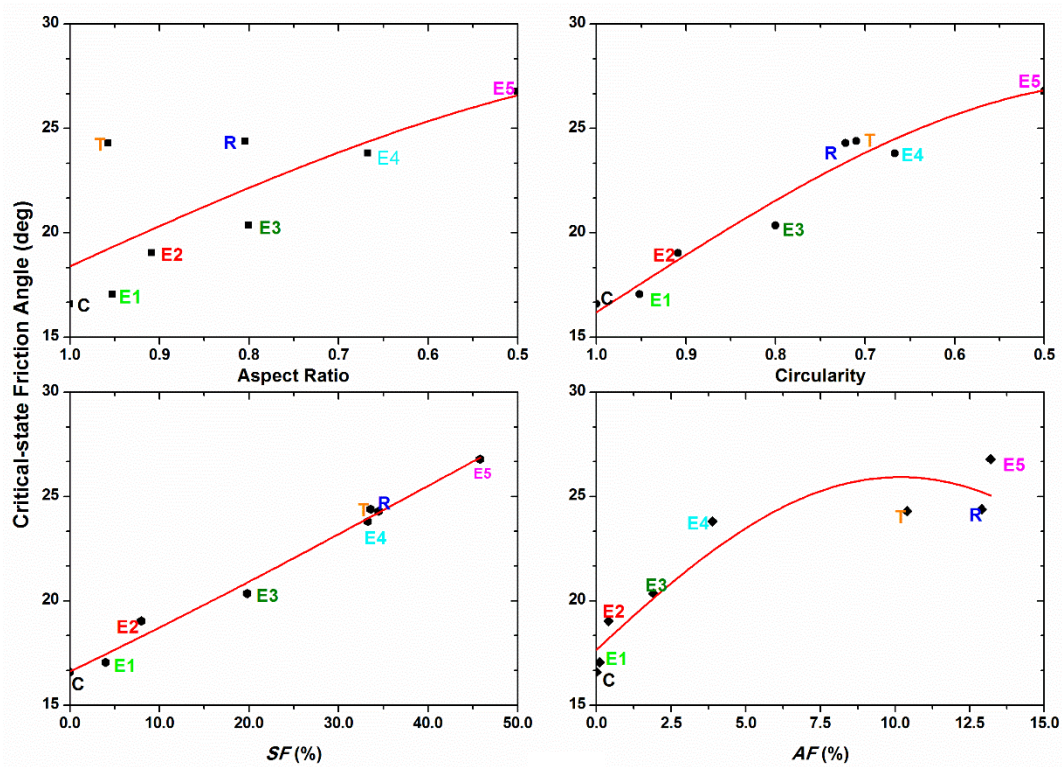
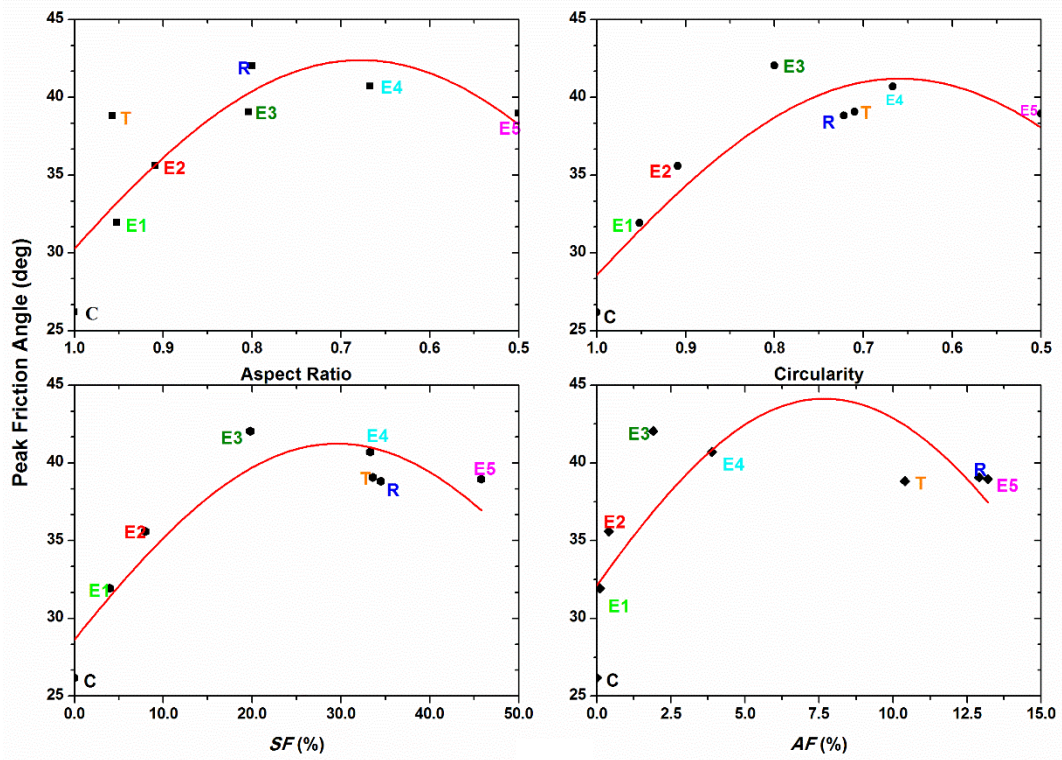


Figure 3.3: Macroscopic behaviour of the numerical results (a) relationship between the principal stress ratio and the axial strain; (b) relationship between the volumetric strain and the axial strain; (c) error bars of the stress ratio in the critical state.



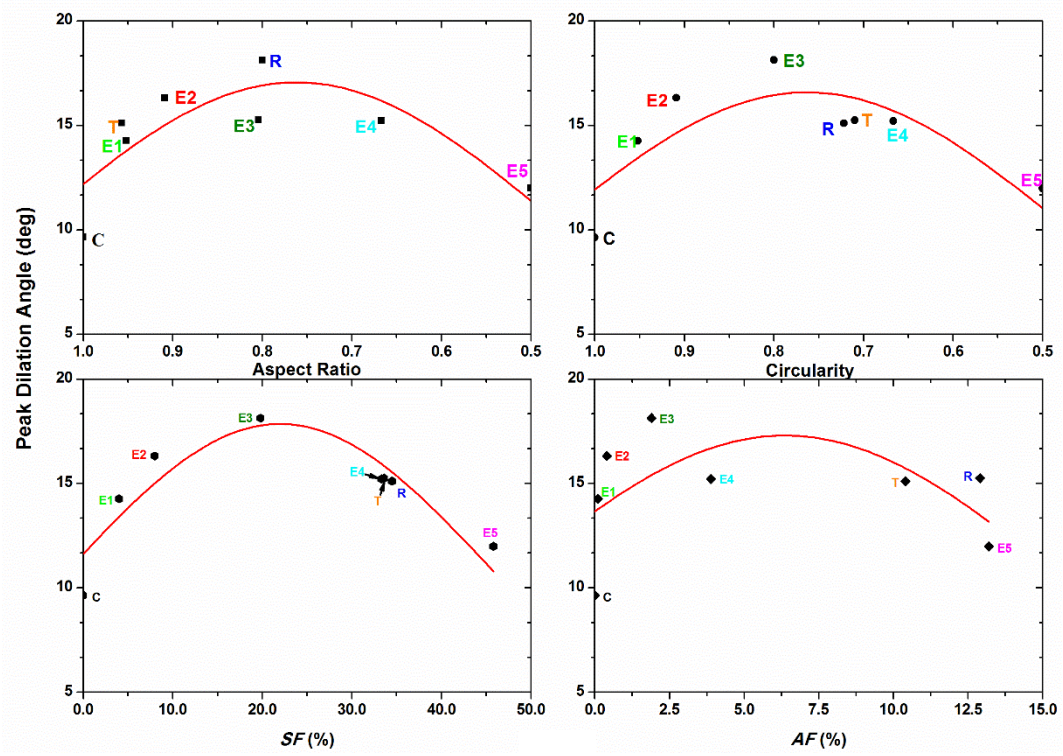
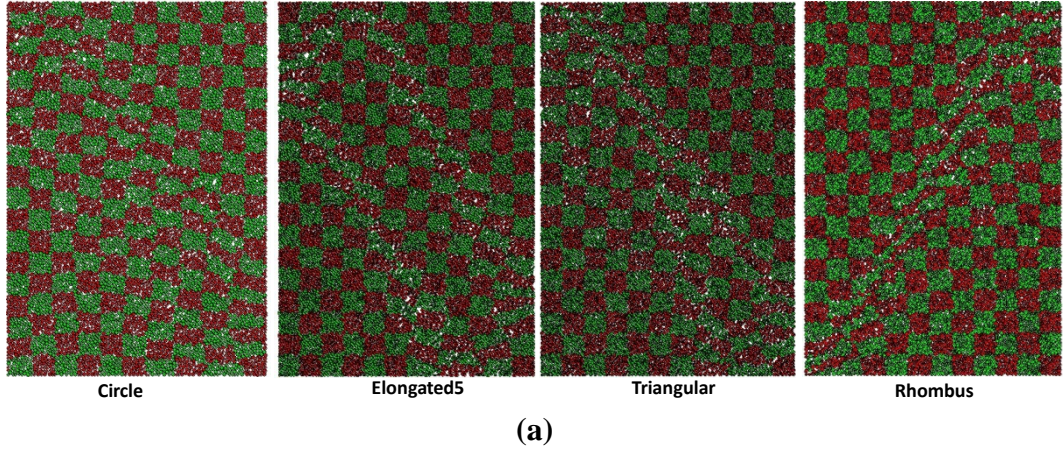
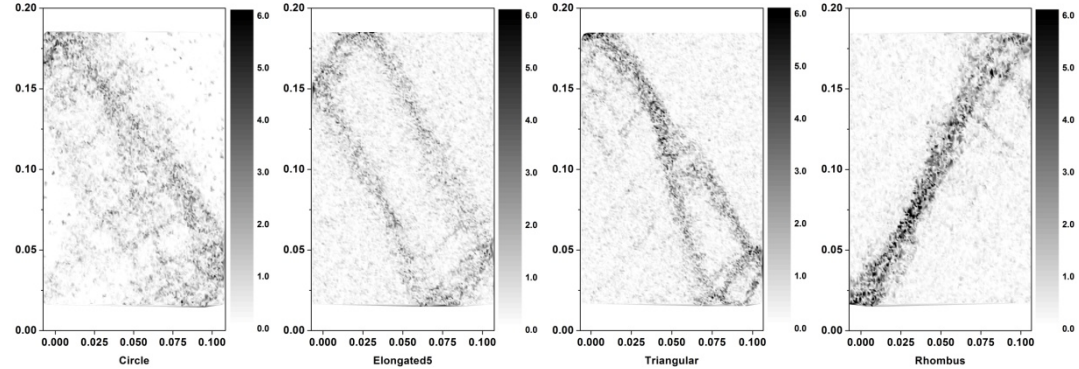


Figure 3.4: Peak friction angle (a), critical friction angle (b), and peak dilation angle (c) versus different shape quantitative indexes.



(a)



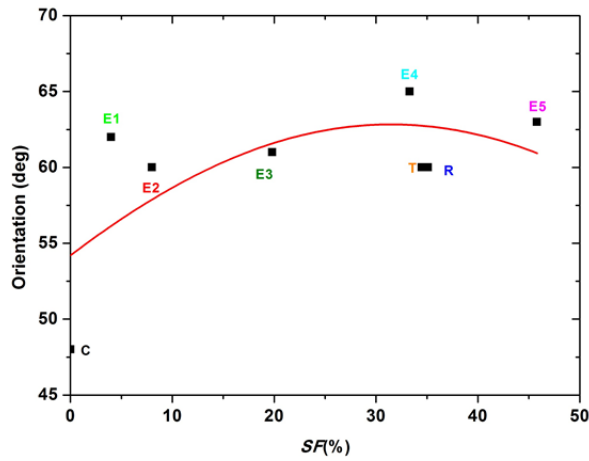
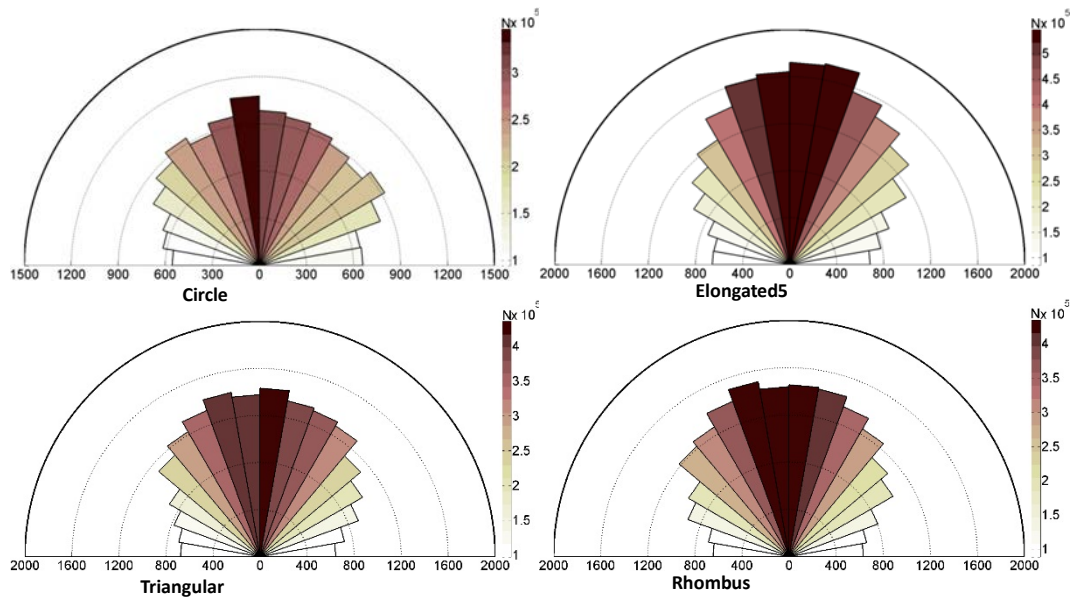
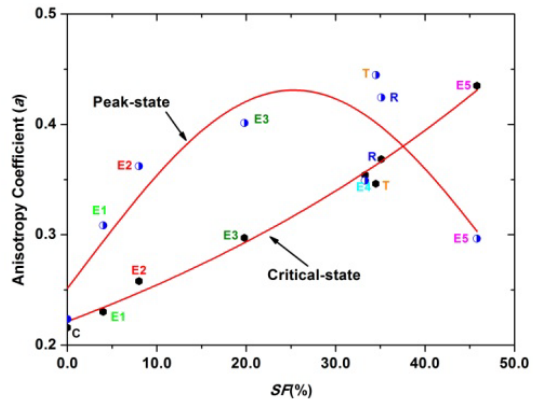
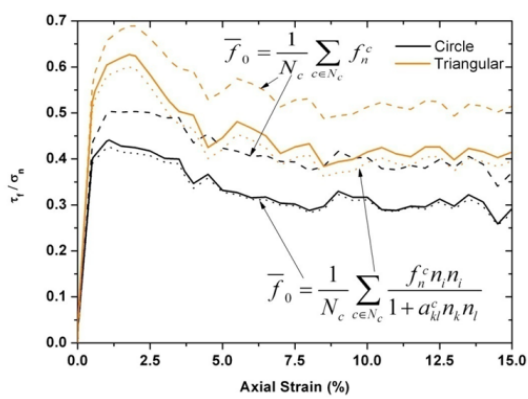


Figure 3.5: Macroscale granular deformation observations and microscale rose diagrams at the critical state (15% axial strain) (a) painted grid distribution, (b) accumulated shear strain distribution, (c) statistical particle contact orientation and the related contact normal force, (d) effect of the SF value on the orientation of shear band.



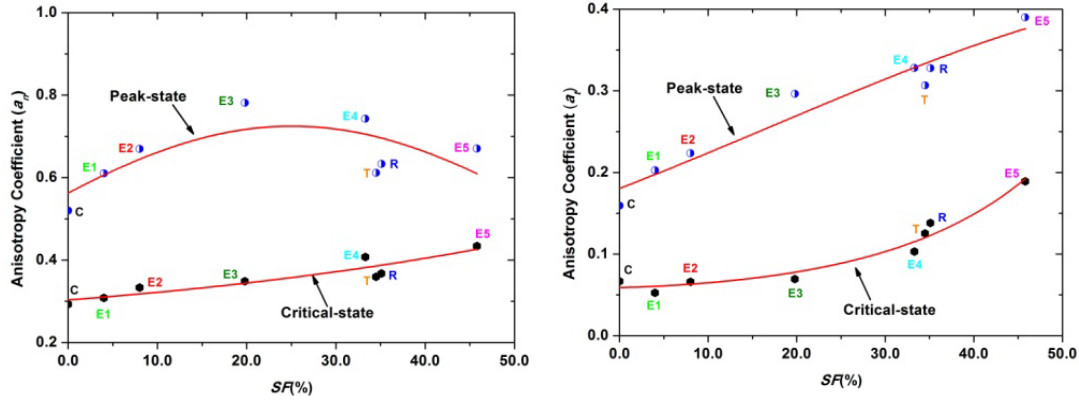


Figure 3.6: Illustration of the accuracy of the SFF relationship with collected data for different average contact normal forces (Eq. 3.2(a)) (a), relationship between respective anisotropic coefficients of contact normal (b), contact normal force (c), contact tangential force (d) and SF.

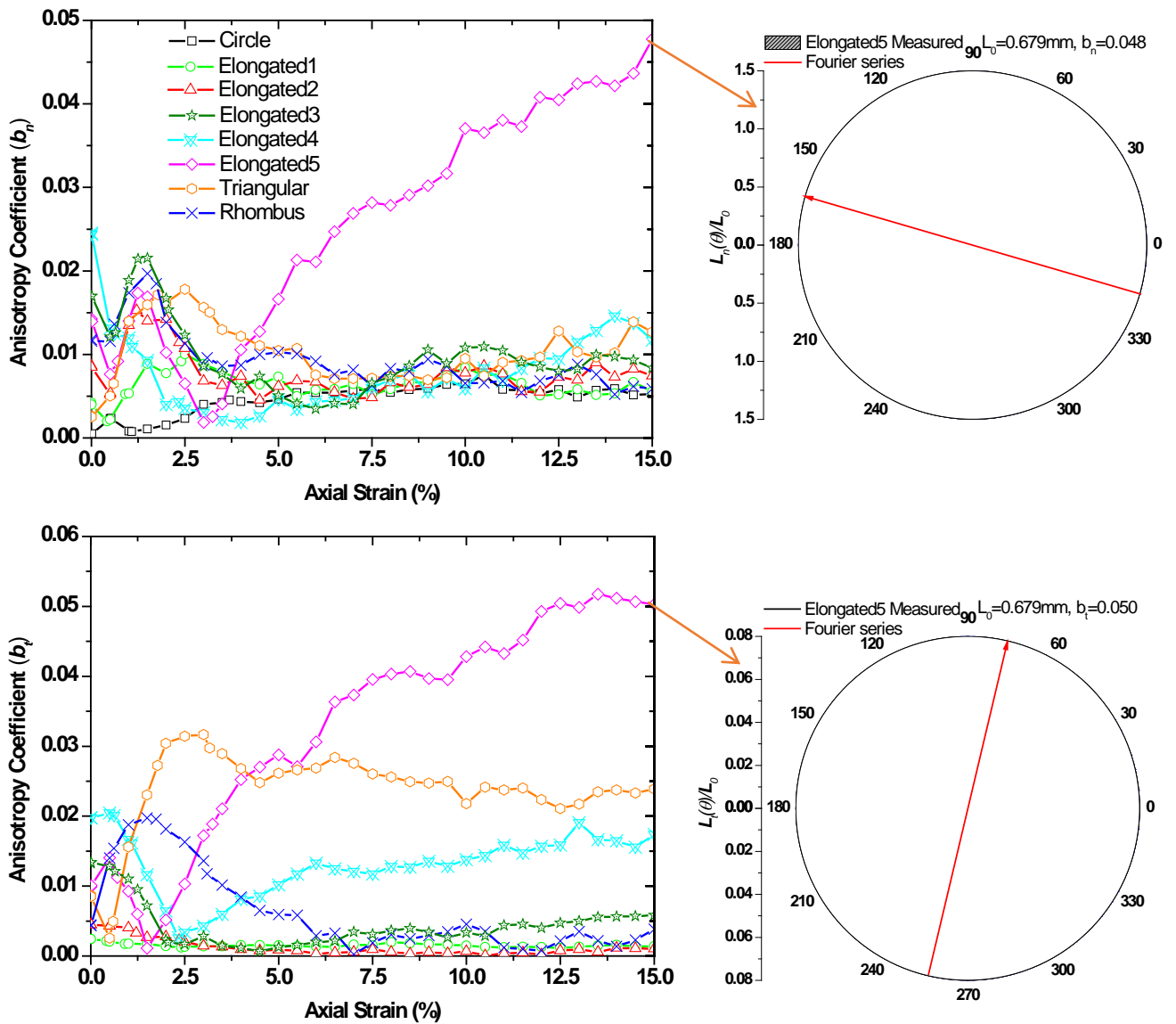


Figure 3.7: Contact normal vector anisotropy coefficient (a) and contact tangential vector anisotropy coefficient (b) versus axial strain (polar distribution of Elongated5 at critical state).

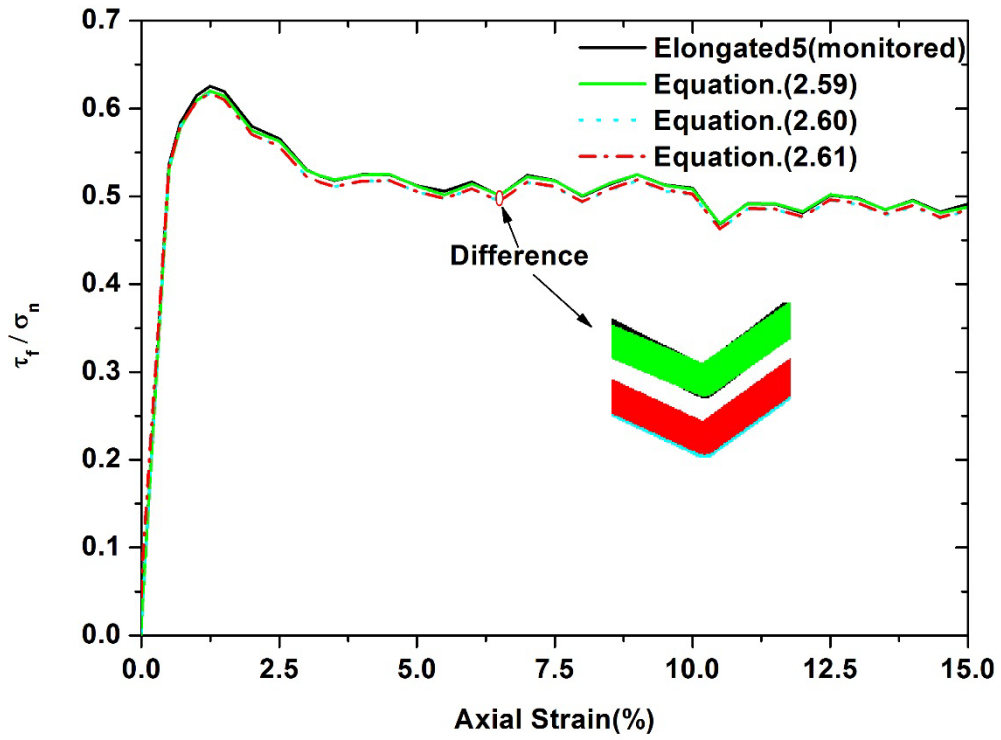
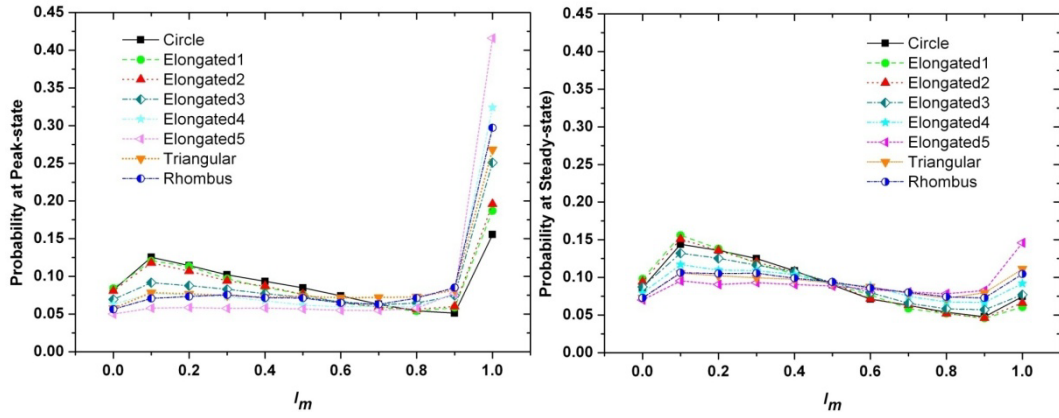
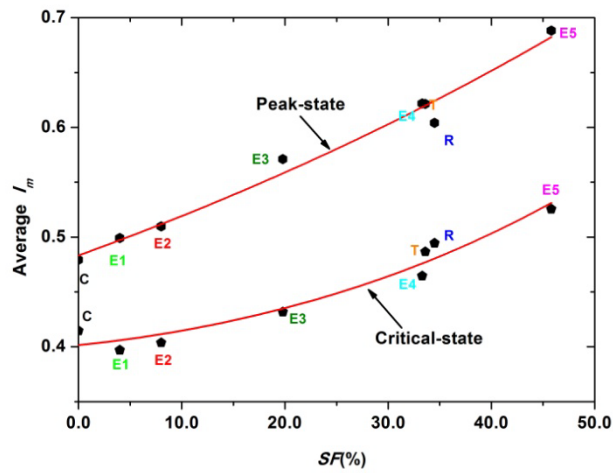


Figure 3.8: Comparison of the relationship between the stress force and the fabric evaluation from the general SFF relationship with the simplified forms.

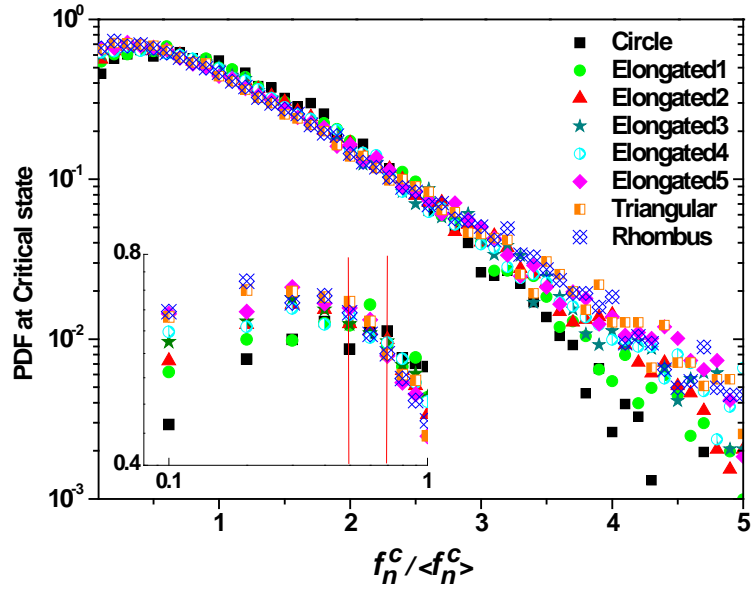


(a)

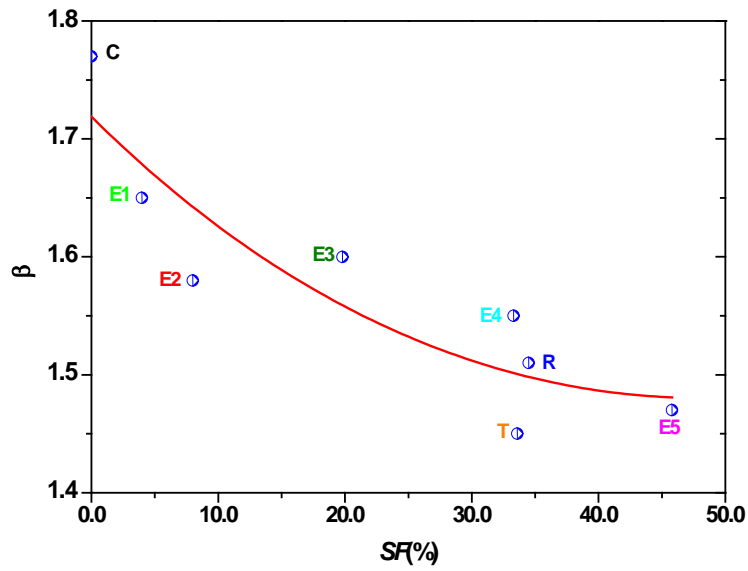


(b)

Figure 3.9: The probabilistic distribution of the friction mobilisation: (a) the mobilisation index I_m at the peak state and critical state and (b) the average value of I_m correlated with SF at the peak state and critical state.



(a)



(b)

Figure 3.10: (a) Probability distribution function of normalised normal force at the critical state (15% axial strain); (b) relationship between the strong force exponent and SF.

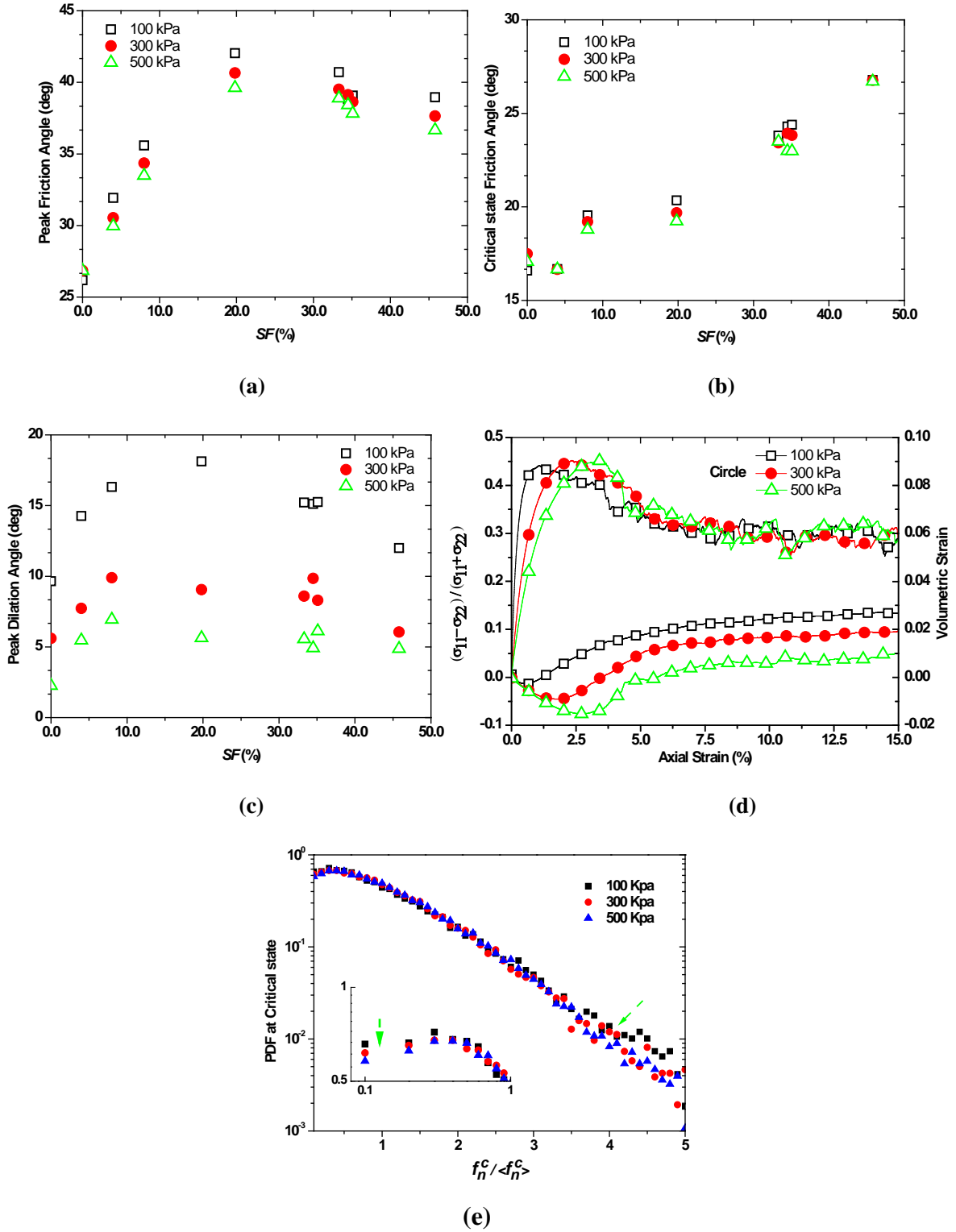


Figure 3.11: Strength indexes and PDF of normalised normal force under different confining pressures: (a) peak friction angle, (b) critical state friction angle, (c) peak dilation angle, (d) macro-responses of Circle, and (e) Elongated5 at the critical state (15 % axial strain).

CHAPTER 4

The development of contact types within different mixtures of shapes

4.1 Introduction

Particle shape can directly influence the microstructure features of granular assemblies, which play an important role in controlling the macro mechanical responses. Previous researchers have made a great effort to explore the effect of particle shape through a theoretical way in two major directions: the physical consideration (rolling resistance models) or the geometry consideration (simple irregular particle shapes), which have systematically discussed in Section 2.4. Mollon and Zhao (2012, 2013, 2014) recently undertook a systematic work to generate the accurate realistic particles for discrete modelling from 2D to 3D analysis. The procedure of their framework stems initially from the Fourier-Voronoi approach to generate complex particle shapes with their orientation under arbitrary boundary conditions in 2D. They directly extended this method to 3D by choosing arbitrary 2D contours. However, this approach will incur uncertainty effects. To overcome the drawbacks, they applied the random field theory to develop the 3D algorithm. Although these methods for generating the realistic particle shapes are meaningful, extremely complicated geometry will result in excessive contact points during the collision between two particles. Additionally, for the granular assemblages under this contact detecting algorithm, the computation speed will be too low. Moreover, the error for determining the overlapping zone will increase with the use of complicated geometries; this is a natural but unavoidable consequence. Researchers must therefore choose between the computation speed and the complexity of the analysis. If the study aims to determine the constant correlation from the contact information, simple shapes should be used, which are sufficient to obtain a fast calculation time. However, at present, the traditional micro statistical information (Rothenburg and Bathurst, 1989) for the whole domain cannot explain the sudden, unpredictable macro response. To achieve better modelling of the macro behaviour, some descriptors in the deeper micro scales are presented. There are two major ways to approach this: using the contact cycles (loop) (Tordesillas et al., 2011;

Walker and Tordesillas, 2010) or contact types (Azéma and Radjaï, 2010, 2012; Minh and Cheng, 2013; Minh et al., 2014; Szarf et al., 2011). These approaches are all crucial mesoscopic structures and can be considered to explore the mechanism of load resistance and self-organisation within the granular systems. Additionally, compared with the contact loops, the contact types are easier to determine. Therefore, the author here employ the different contact types to explore the micro statistical information.

Many traditional experiments are still performed to capture the macro responses of the particle shape effect (Härtl and Ooi, 2011; Shin and Santamarina, 2012; Yang and Wei, 2012) . With an emphasis on inter-particle contact information, some advanced and expensive imaged devices such as X-ray CT are also applied to describe the granular assemblages quantitatively (Andò et al., 2012; Hall et al., 2010) to evaluate the particle interaction behaviour, which can be useful in developing a theory of contact mechanics. However, these devices cannot provide information about a particle's contact with its neighbouring particles. The discrete element method proposed by Cundall and Strack (1979), which is adopted in this thesis, is an alternative and economic approach to investigate the micro and macro mechanical behaviour of granular materials.

The aim of this study is to address the variation of the four contact types under the biaxial loading procedure within the particle shape mixtures from $\eta_m = 0.0$ to 1.0. The mixture of shapes implemented in this work is the same as the binary mixture of particles used to investigate the effects of PSD (Miao and Airey, 2013; Minh and Cheng, 2013; Voivret et al., 2009). This is an effective way to quantify the parameters. Recently, Shin and Santamarina (2012) performed useful laboratory tests to study the mechanical response of sand mixtures made of round and irregular grains under lower confining stress, where the crushing effect can be ignored. This paper also intends to attract other researchers to discuss the crushing effect with the particle shape developed by Xiao and Liao (2014). In addition, we can observe many quantitative shape descriptors in the previous literatures (Azéma and Radjaï, 2010; Cho et al., 2006; Matsushima and Chang, 2011; Sukumaran and Ashmawy, 2001; Szarf et al., 2011) , and there is no index that can handle all of the complicated granular behaviour. Moreover, there

are seldom absolute findings or linear relationships after using those shape indexes. In the work by Azéma and Radjaï (2010), on the stress-strain relation of elongated particles, the shape index shows a nonlinear variation for the solid fraction in the whole domain (0.0, 1.0), with a saturation near $\eta = 0.4$. Accordingly, Shin and Santamarina (2012) found that the correlation of void ratio increases with the increased angular mass portions, where the angular particle may possess certain degree of roughness rather than the sphericity index of 0.55. Fortunately, the practical engineering index, the friction angle, shows a nearly linear curve in the whole domain (Azéma and Radjaï, 2010, 2012; Shin and Santamarina, 2012). As mentioned above, the granular media exhibits many questionable and uncertain behaviours, particularly under complicated external conditions. To reduce the major nonlinear factors, the authors of this work chose to mix a medium of irregular non-convex particles (Elongate) with circular disks. Moreover, the crushing effect is ignored throughout the loading procedure. The detailed contact information during the whole loading procedure is divided into four respective contact types: circle-circle contacts (CC), circle-elongate contacts (CE), simple elongate-elongate contacts (EE1) and multiple elongate-elongate contacts (EE_m). Hence, in a mixture of packed shapes, the development of these various contact types with the associated force chains, mobility and fabrics, is interesting and can enhance our understanding of the granular media in a deeper scale.

In the following sections, we first give a brief introduction to the basic information about the samples and contact types. Then, some macro simulation results are presented. The detailed force chains distributions, friction mobilisations and fabrics are explored using the four respective contact types within the varied shape mixtures (η_m). Finally, the main conclusions of this chapter are presented.

4.2 Investigation scheme

4.2.1 Particle shape mixtures and contact types

The numerical samples in this study contain the same number (9506) and PSD as those by Azéma and Radjaï (2010), where two shapes are used for the descriptor η_m (ranging from 0.0 to 1.0) to express the mass portion of the elongate particles. The schematic shapes of the two

samples are shown in Figure 4.1. Additionally, a list of the shape mixture samples with their respective mass contents is given in Table 4.1. The shape index of the elongate particle (non-convex) used in this study is 0.5, as calculated by Azéma and Radjaï (2010). PSD and the four contact types are shown in Figure 4.2. The mean particle diameter (d_{50}) is 1.5 mm with a uniformity coefficient $C_u = 1.47$. In this study, the aim is to investigate the correlations of micro contact information of shape mixtures using the four assumed contact types. Each contact type can be identified during each collision. Illustrations of the contact types in two shape mixtures at the initial isotropic state can be observed in Figure 4.3. It can be observed that the contact types can control the structure feature of the normal force chains.

4.2.2 DEM simulation details

A dense packing for the circles sample ($\eta_m = 0.0$) was first randomly distributed by the PSD inside a rectangular region with dimensions of 100 mm(W) \times 200 mm (H). Subsequently, the whole packing expands to the target initial porosity (0.16) through the iterative servo controls. In addition, the circle assemblage plays the mother role, where other η_m mixtures replace the mother particle with the elongate one using an equivalent area and the same centre location. Each replacement also iterates to the balance state in the analysis. All of the mixture samples are prepared using the same procedure. To ensure the generation of homogenous dense assemblages, gravity is ignored to avoid force gradients, where the isotropic stress is gradually increased to the target confining pressure (100kPa). The isotropic samples of shape mixtures are then subjected to vertical compression by a constant strain rate of 5% per minute while the confining stress on the lateral walls is constant. All of the simulations in this study are maintained in a plane-strain condition. Moreover, the linear contact model and the non-viscous damping model are considered throughout this study. The values of the numerical parameters are provided in Table 4.2.

4.3 Numerical findings and discussions

4.3.1 Macroscopic results for the contact types

In this section, we first consider the stress-strain response and the solid fraction variation throughout the loading procedure. The average stress tensor in the granular media can be

calculated using the micro quantities of the contact forces and contact vectors. Detail information about the stress tensors can be seen in Chapter 2.

Figure 4.4 shows the variation of the mobilised internal friction angle ($\sin\phi_{\text{mobilized}} = \frac{\sigma_1 - \sigma_3}{\sigma_1 + \sigma_3}$) against the axial strain for different values of η_m . For the initial dense isotropic packing, all of the samples show a peak-residual curve with small fluctuations at the residual state. Additionally, the peak friction angle shows a linear increasing relation with the increasing η_m . However, the peak dilation angle gives a different relation for the granular behaviour; for instance, the packing can be easily compressed at $\eta_m = 0.1$. A subtle increasing trend can be found between 0.1 and 0.3. The further increase of elongate particles has no noticeable influence on the peak dilation angle. The error bars in Figure 4.4 (c) shows the fluctuations at the steady state (critical/residual state) in Figure 4.4(a). It can be observed that the steady friction angle shows a linear increasing relation, except for the ranges of (0.2, 0.3) and (0.6, 0.7). Although the relation is somewhat nonlinear in some ranges, the overall relation can be considered as an approximate linear correlation. The nonlinear relation may be induced by the elongate particle with the non-convex feature, which shows a different behaviour from the convex particle. These macro behaviours are explored at the deeper micro scales in the following sections.

In Figure 4.5, the evolution of the void ratio with different η_m values is given at different axial strain levels. All of the packing cases show a significant dilation behaviour that is caused by the initial dense packing. Moreover, the global behaviour of the void ratio is a linear decrease with increasing η_m , except for some isolated points that are marked in the figure with a red circle. This phenomenon is consistent with previous investigations (Azéma and Radjaï, 2010, 2012; Saint-Cyr et al., 2011) in low η values. In contrast with the numerical simulations with non-convex object (Saint-Cyr et al., 2011) or some uncertain experimental tests (Shin and Santamarina, 2012), an opposite trend is obtained. As noted above, this study focuses on the linear relation, which is interesting and easily controlled. Furthermore, the two subtle points also provide a clue to determine the effect of a low mass percent of round or

irregular particles, which can significantly influence the geometrical topology of the granular media. This macro response may inspire us to reconsider the material theory.

4.3.2 Microscopic results for the contact types

In this section, we analyse the four contact types, shown in Figure 4.6(a), for different η_m values at steady state. In addition, the information associated with the normalised contact normal forces is shown in Figure 4.6(b), where the ratio (K) is determined between the average contact normal force of four respective contact types ($\langle f_{nt}^c \rangle$) and the global average contact normal force ($\langle f_n^c \rangle$) using the following equation:

$$K = \frac{\langle f_{nt}^c \rangle}{\langle f_n^c \rangle} \quad (4.1)$$

It can be observed from Figure 4.6(a) that the contact types have a linear relationship with η_m , except for the CE contact. These variations are reasonable and easy to understand. The interesting finding is that the K value of the contact type EE1 is always greater than that of EEm contacts. The CC contacts are nearly equal to the CE contacts at $\eta_m = 0.3$. A similar situation is evident between the CE and EE1 contacts at $\eta_m = 0.7$. For the normalised contact normal force in Figure 4.6(b), the ratios of the four contacts increase linearly with increasing η_m . To interpret the contact force between the overlapping particles, the ratio K must be multiplied by the contact points. Hence, the EE1 contacts are the lowest between the individual particles at the critical state. We can easily find that only the ratios of EE1 at the interval (0.2, 0.3) and of CC at the interval (0.6, 0.7) are decreased, which may be the reason for the variation of the steady friction angle at the residual state in the two ranges.

The properties of friction mobilisation can also be considered as a basic index to describe the microscopic interlocking effect, which would induce the variation of the shear strength for different values of η_m . This descriptor I_m can be defined by Eq. (3.3). In the current chapter, I_{gm} describes the global average mobility; I_{cm} expresses the mean value of the mobilisation index for the associated contact type. Further, the I_{gm} in Figure 4.7(a) increases slightly with the increased η_m , except for the ranges noted above when discussing Figure 4.4(c). Moreover, the statistical micro mobility can be used to explain the variation of the macro shear strength.

However, the global statistical information is extremely ambiguous and lacks a clear direction. The index of I_{cm} can provide some guiding information in Figure 4.7(b), where the capability of the mobility for all four contacts declines in the two intervals $\eta_m=(0.2, 0.3)$ and $\eta_m=(0.6, 0.7)$. For the two subtle points in Figure 4.5, we can also find that the values of I_{cm} for CC at $\eta_m = 0.1$ and EEm at $\eta_m = 0.8$ are lower than those of their neighbouring domains. Hence, a very little percentage of round or irregular particles can significantly influence the mobility property of the main granular mass.

Figure 4.8 shows the probability of I_m for values of η_m at the steady state. The weakly mobilised contacts decrease with an increasing η_m . These weakened mobility contacts can be replaced by the strongly, nearly sliding contacts, which are composed of the weak force zone (network). Additionally, the probability density function (pdf) for all of the contact types for I_m in Fig. 8 has the same trend as that of the contact portions in Figure 4.6 (a). Another interesting finding is that the pdf of I_m for the CE contact almost overlaps between the regions where η_m ranges from 0.3 to 0.6, where the frictional angle is strongly increased (Figure 4.4(c)). The CC contacts in all groups show a decreasing trend, except for the slide point ($I_m = 1.0$), suggesting that the shape mixtures cannot significantly influence the CC contacts. A similar situation is also observed for the EE1 and EEm contacts.

The semilogarithmic plot of the probability distribution of the contact normal force, normalised by the mean contact force $\langle f_n^c \rangle$ at the steady state, is shown in Figure 4.9. For all of the shape mixtures described in this study, the probability density of the normalised contact normal force essentially follows a decay power law determined in Eq. 3.4. For the global contact normal force in Figure 4.9(a), α increases with increasing η_m , and β increases with increasing η_m . These findings are reasonable and easy to understand. Our focus is on the pdf of the contact normal force for the four contact types in the other four figures. In this chapter, the contact force is statistically cumulated by the individual contact because the same contact type between two overlapped particles may include more than one contact points. It can be found from Figure 4.9(b) that the decreased CC contact probability in Figure 4.8(b) is just a decrease at the weak force chain. The strong force chains are stable, except when $\eta_m > 0.9$.

In addition, the pdf of the contact normal forces in CE contacts is nearly stable in the range from $\eta_m = 0.3$ to 0.7. Furthermore, the pdf of the EE1 and EEm contacts increases linearly with increasing η_m for both the weak and strong forces (Figure 4.9(d)). These findings give us another indication that the micro contact forces also show the same behaviour as the contact numbers portion in Figure 4.6(a).

Figure 4.10 shows the average friction mobilisation with the associated normalised contact force at the critical state. In Figure 4.10(a), it can be observed that the value of I_{fm} decreases with the increasing normalised contact normal forces. In this figure, I_{fm} decreases with the normalised contact forces. Hence, the high mobilised particles always remain at the weak force chains. Additionally, I_{fm} increases with increasing η_m . The main trend of I_{fm} for the four contacts in Figure 4.10 is as low shift that becomes parallel to the horizontal direction. These variations coupled with the contact percent in Figure 4.6(a) can explain the separated I_{fm} in Fig. 10(a). The contact information for the respective contacts can control the global statistical trend, which can give the macro responses a much more reasonable direction. These correlations are only suitable for a medium-level normalised contact normal force, where the data at the end are discrete at a large normalised contact normal force.

Using the second-order Fourier series expressions, the micro contact information in the polar domain can be calculated to describe the development of fabric in the granular systems. Previous researchers have constructed a bridge between the micro fabric parameters and macro stress responses, referred to as the stress-force-fabric relationship. Detailed discussion on the SFF and related anisotropic parameters can be seen in Chapter 2. In biaxial shearing, the principal angles are nearly along the loading direction, and the difference can be ignored. Hence, we can focus on the magnitude of these anisotropic parameters for the respective contact types at the critical state. It can be observed from Figure 4.11 that the three global anisotropic parameters show a linearly increasing trend with increasing η_m , except for some intervals such as a_c in (0.6, 0.7) and a_{ft} in (0.2, 0.3), where the relations are decreasing. The SFF relationship is constructed to connect the micro anisotropic parameters and macro strength indexes because the two anisotropic coefficients can be used to explain the variation

of frictional angle, as shown in Figure 4.4(c) and given by Eq. 2.60. The anisotropic coefficients for the four contact types can explain the two regions above. A decreasing a_c is induced by the extremely decreased contact normal coefficient for CE, which is larger than the increasing gradient of EE1 and EEm. Another interesting finding is that the larger portion of EE1 contacts at high η_m values cannot effectively increase its related a_c compared with EEm contacts. However, the a_{fn} and a_{ft} coefficients for the above two contact types match well the trend in Figure 4.6(a). The CE contacts also play a key role in the three anisotropic parameters when η_m is lower than 0.7.

4.4 Conclusions

Deeper investigations into the micro scales, the development of the four contact types and the associated contact information within the shape mixtures η_m are used to explore the macro mechanical response using the discrete element method. To avoid excessive parameters in the study, some major linear regions are chosen. We explain the subtle points in the variation of the void ratio for the small, round or irregular particles through the information from the different contact types, where I_{cm} for CC at $\eta_m = 0.1$ and EEm at $\eta_m = 0.8$ are lower than their neighbouring domains. The ratio K of the four contacts can also be considered to explain the variation of the steady friction angle, particularly at the decreasing ranges of (0.2, 0.3) and (0.6, 0.7). Additionally, the index I_{cm} for the four contacts decreases in the two intervals, providing another direction to explain the macro strength. Another interesting finding is that the pdf of I_m for the CE contact nearly overlaps at η_m values from 0.3 to 0.6. For the end of the strong force chains, the probability of the CC contact is approximately the same. However, the pdf curves of the normalised contact forces of EE1 and EEm show a nearly linear increasing relationship with an increasing η_m . The main trend of I_{fm} for the four contacts can explain the separated global I_{fm} with increasing η_m . It is also notable that the anisotropic coefficient of a_c is not sensitive to the contact portions of EE1 and EEm. For the regime of $\eta_m < 0.7$, the CE contacts play an important part in the three fabric parameters. Future work will consider different contact types in the anisotropic shearing. The methodology proposed in this study, through the scope of the development of contact types, will help us to construct a bridge between the inherent heterogeneous samples and the final states.

Tables

Table 4.1: Sample shape mixtures for DEM simulations.

Category	Circle mass content (%)	Elongate mass content (%)	η_m
1	100	0	0.0
2	90	10	0.1
3	80	20	0.2
4	70	30	0.3
5	60	40	0.4
6	50	50	0.5
7	40	60	0.6
8	30	70	0.7
9	20	80	0.8
10	10	90	0.9
11	0	100	1.0

Table 4.2: Input micro parameters in DEM simulations.

	Density (kg/m^3)	2600
Sand particles	Normal/Shear contact stiffness (N/m)	1×10^8
	Inter-particle frictional coefficient	0.5
	Local non-viscous damping	0.45
Confining boundaries	Normal contact stiffness(N/m)	1×10^7
	Frictional coefficient	0.0

Figures

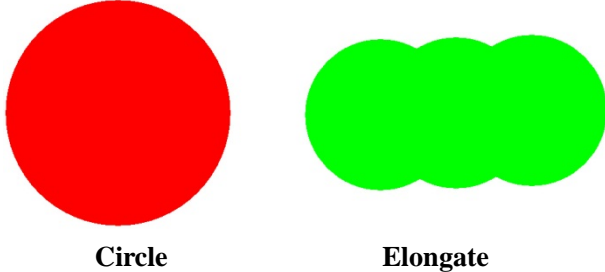


Figure 4.1: The two shapes used for the mixture analysis.

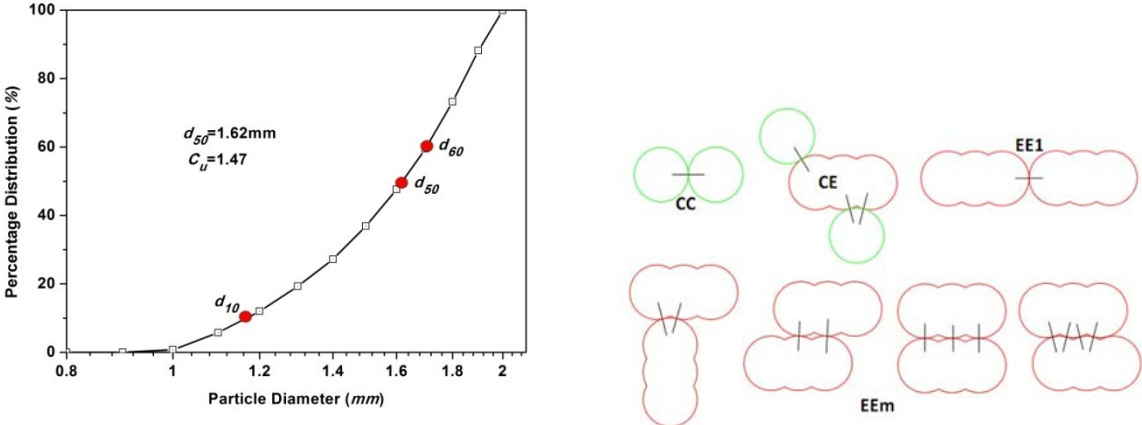
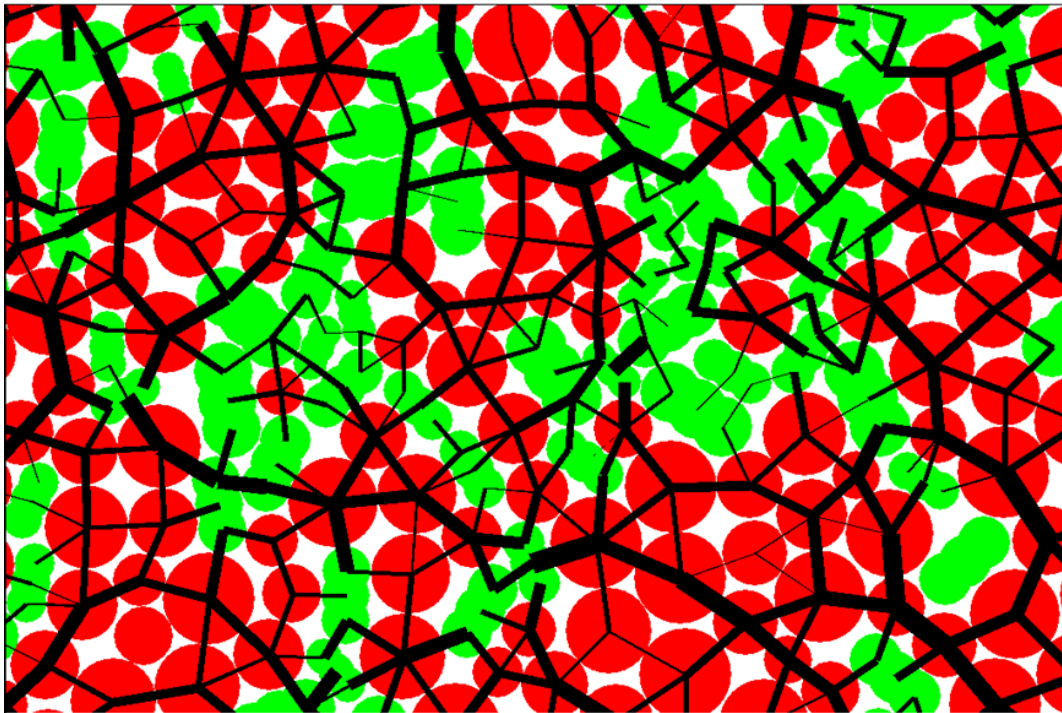
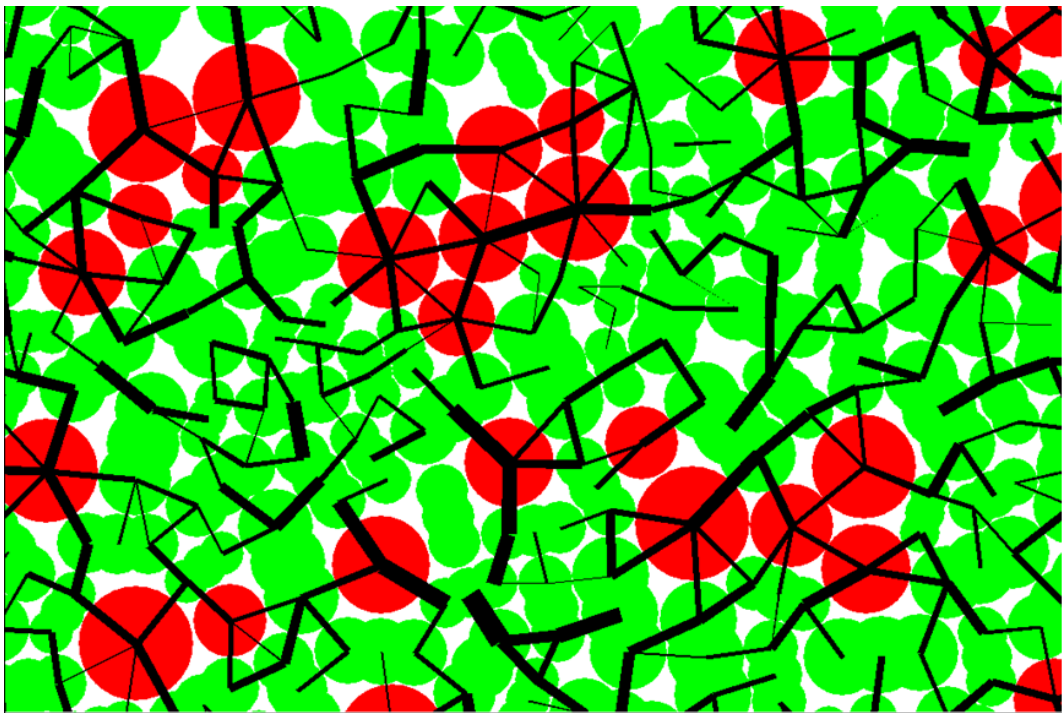


Figure 4.2: Schematic of the PSD and the four contact types within the shape mixtures.

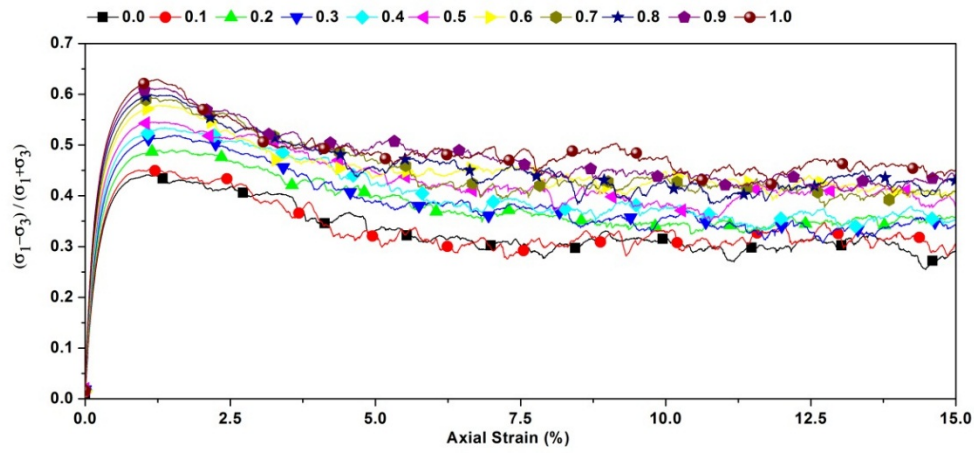


(a) $\eta_m = 0.3$

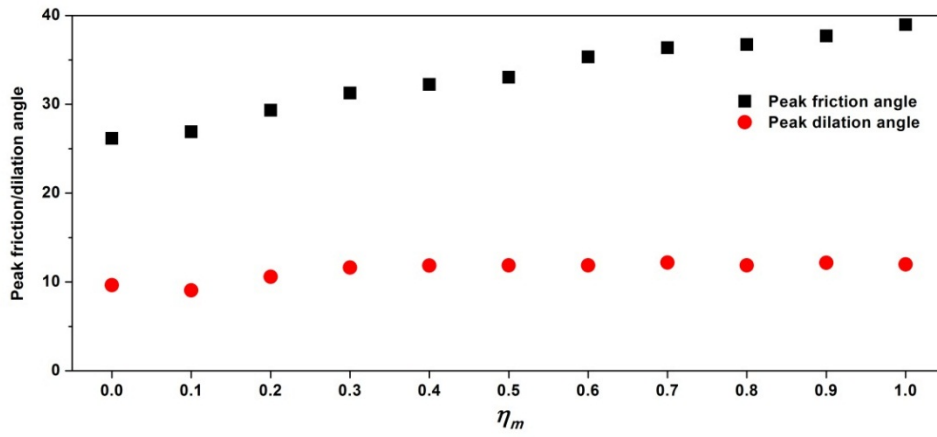


(b) $\eta_m = 0.7$

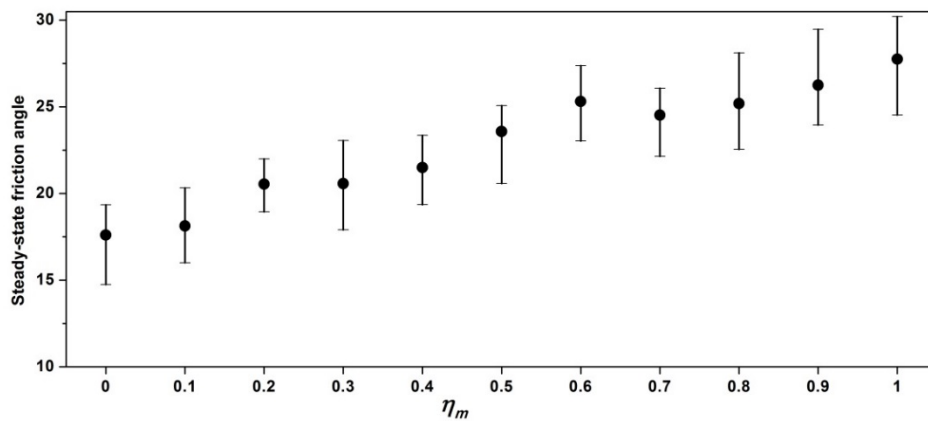
Figure 4.3: Snapshots of normal force chains for the two shape mixtures: (a) $\eta_m = 0.3$; (b) $\eta_m = 0.7$.



(a)



(b)



(c)

Figure 4.4: Macro strength curves for different shape mixtures (a) the variation of sine value of internal friction angle along the axial strain, (b) peak friction/dilation angle, (c) error bars of friction angle at the steady state.

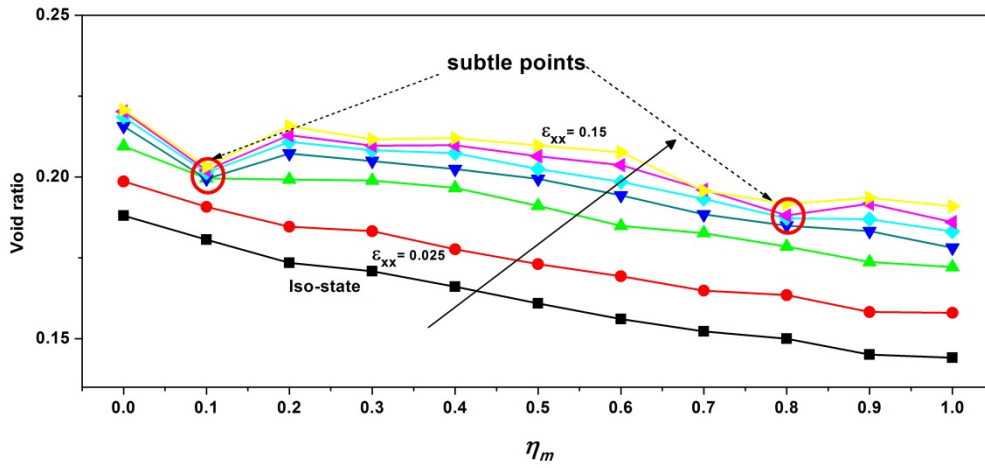
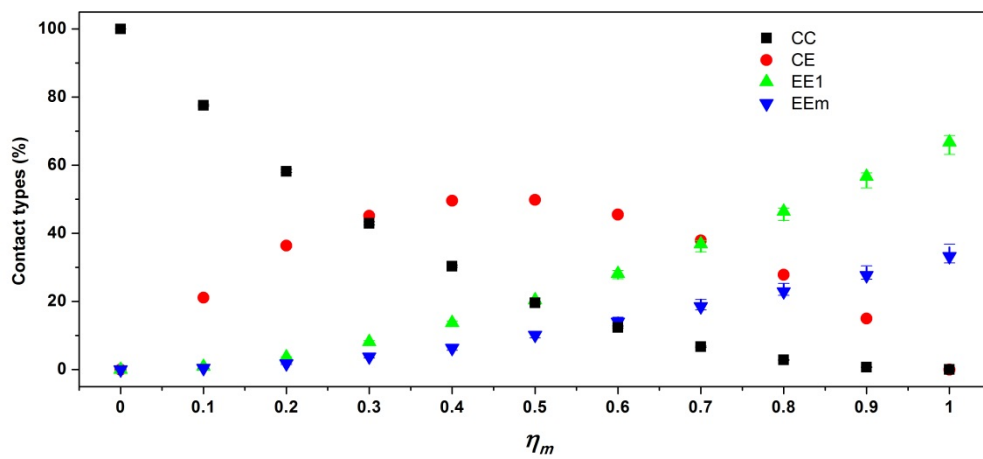
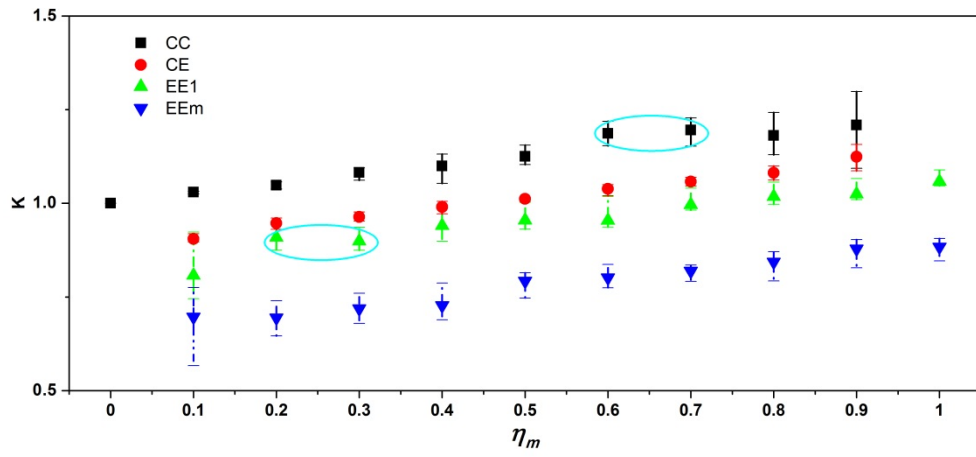


Figure 4.5: Void ratio as a function of the various shape mixtures at different axial strain level from isotropic state to critical state.

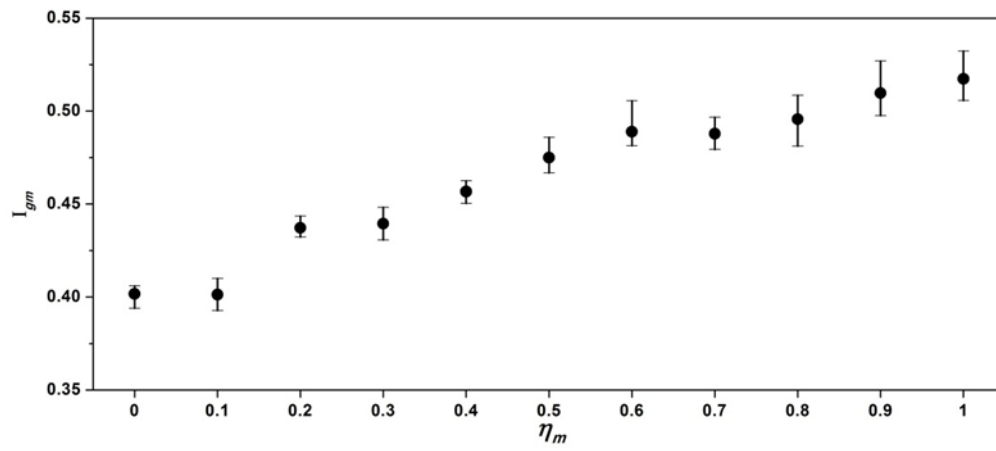


(a)

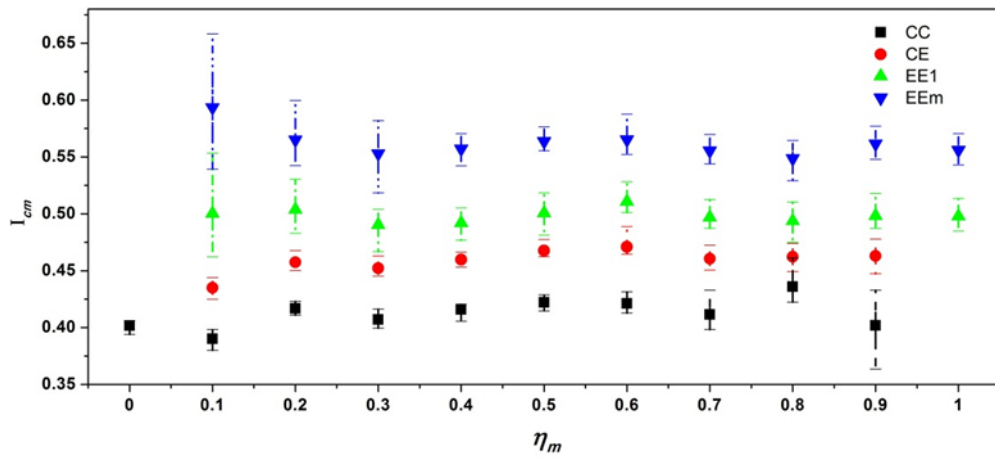


(b)

Figure 4.6: (a) error bars of the four contact types propagate at the critical state; (b) error bars of the normalised contact forces at the critical state.

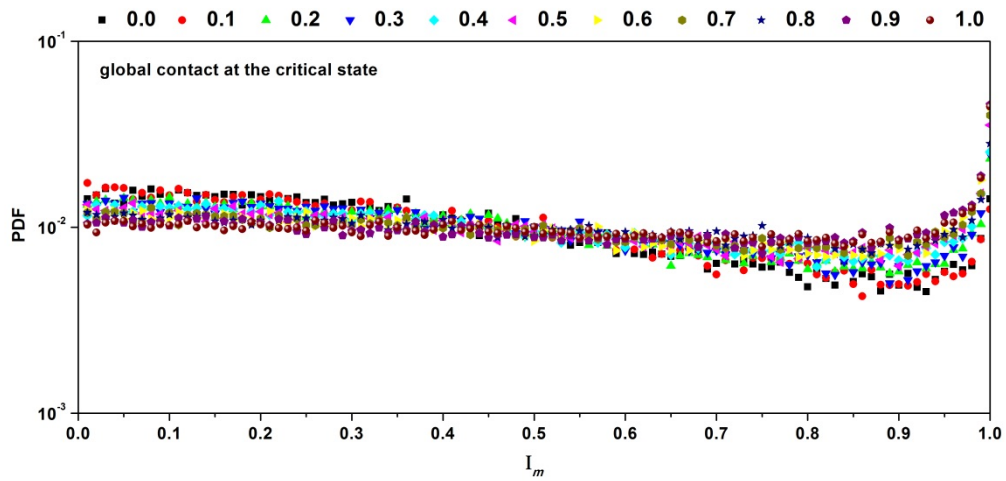


(a)

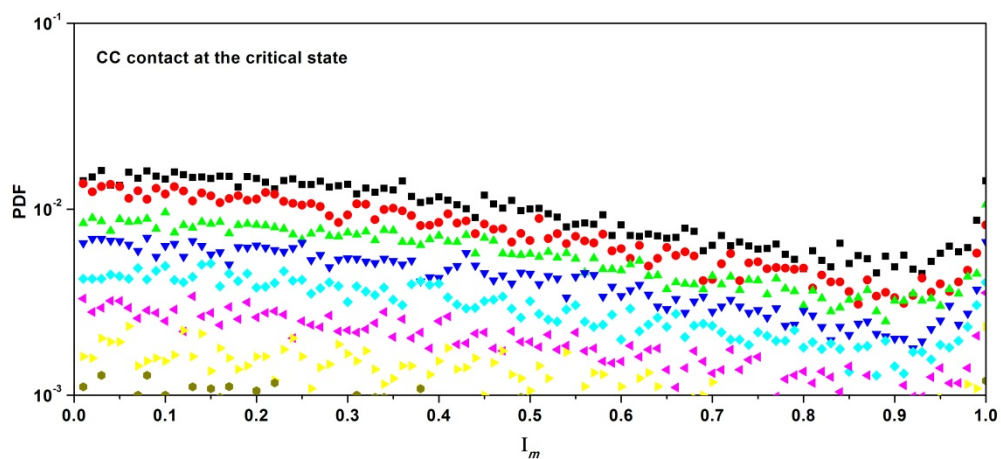


(b)

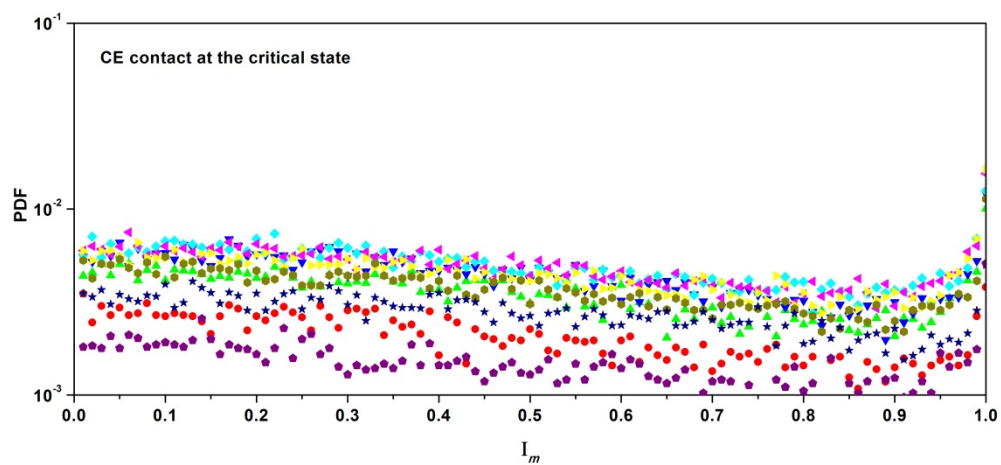
Figure 4.7: Friction mobilisation for different η_m at the critical state (a) the variation of I_{gm} ; (b) the variation of I_{cm} .



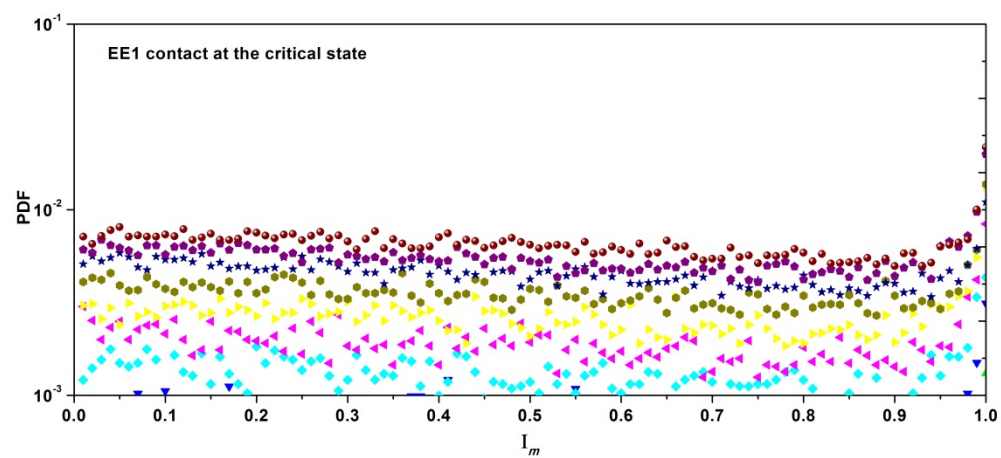
(a)



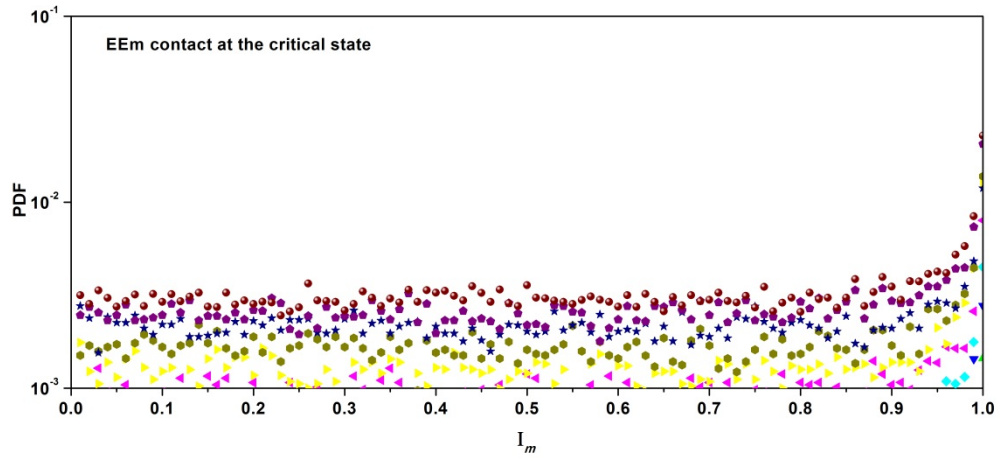
(b)



(c)

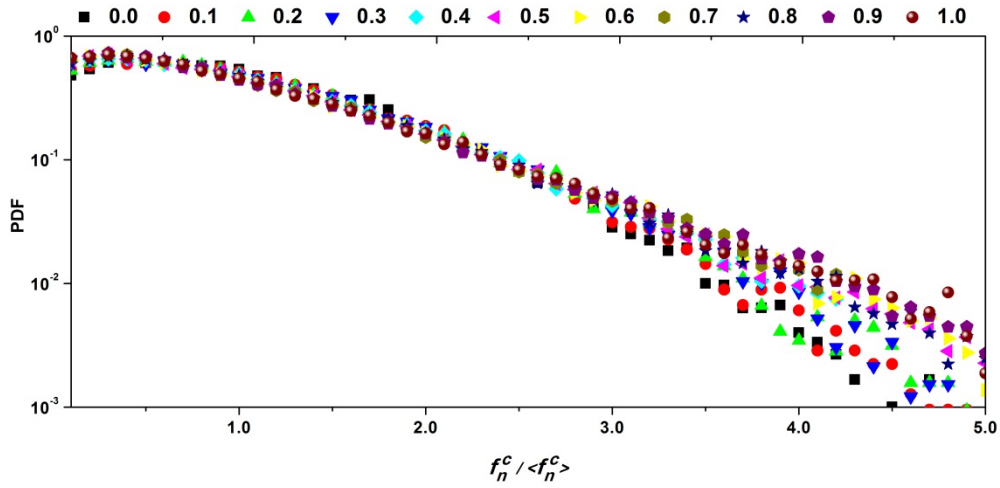


(d)

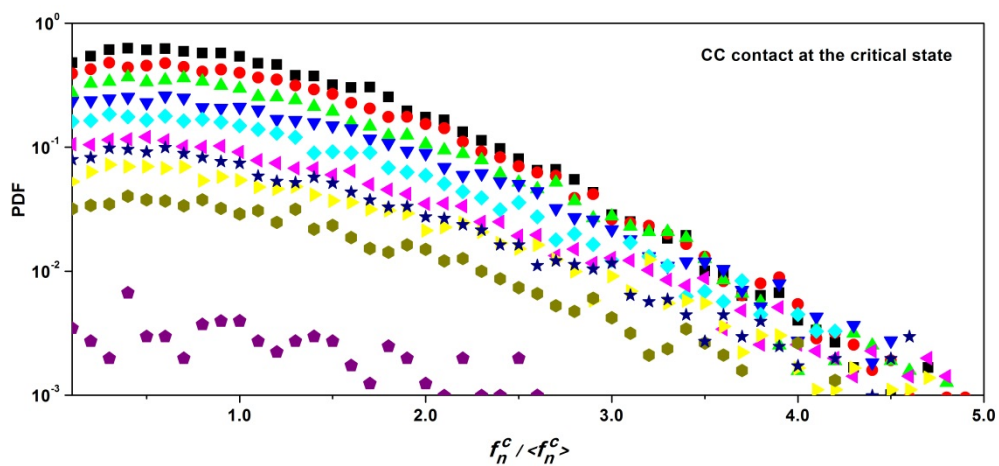


(e)

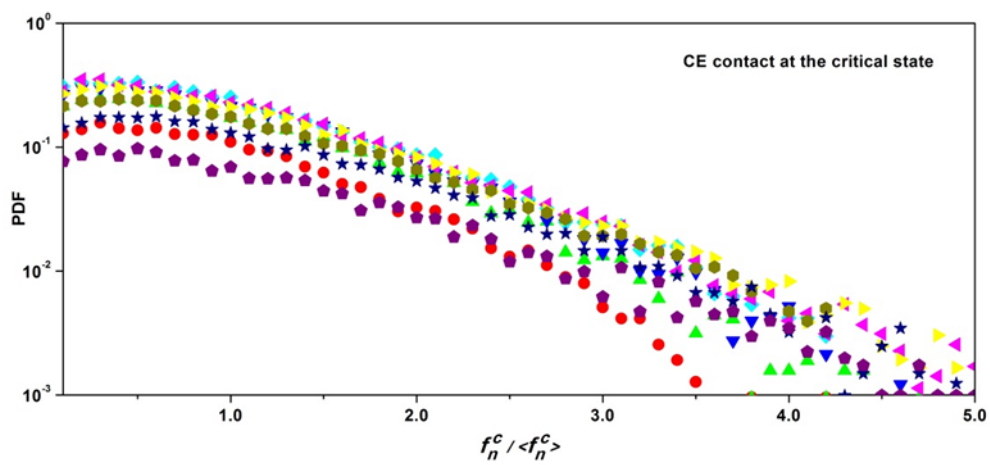
Figure 4.8: Probability distribution of the mobilisation I_m for different η_m at the critical state (a) global mobility distribution; (b) CC contact distribution; (c) CE contact distribution; (d) EE1 contact distribution; (e) EEm contact distribution.



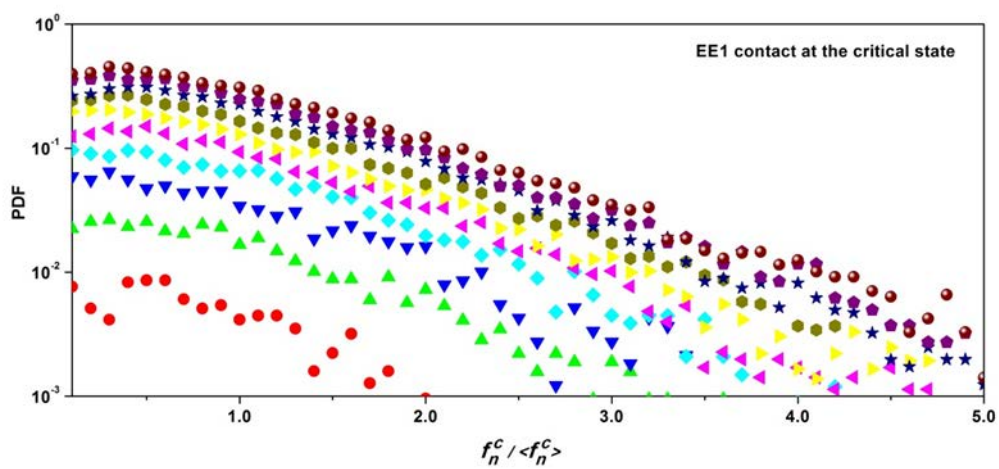
(a)



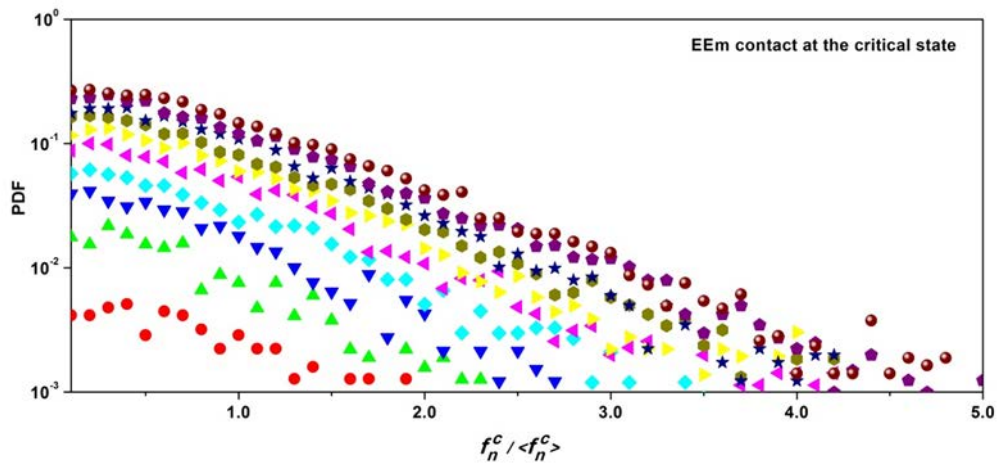
(b)



(c)

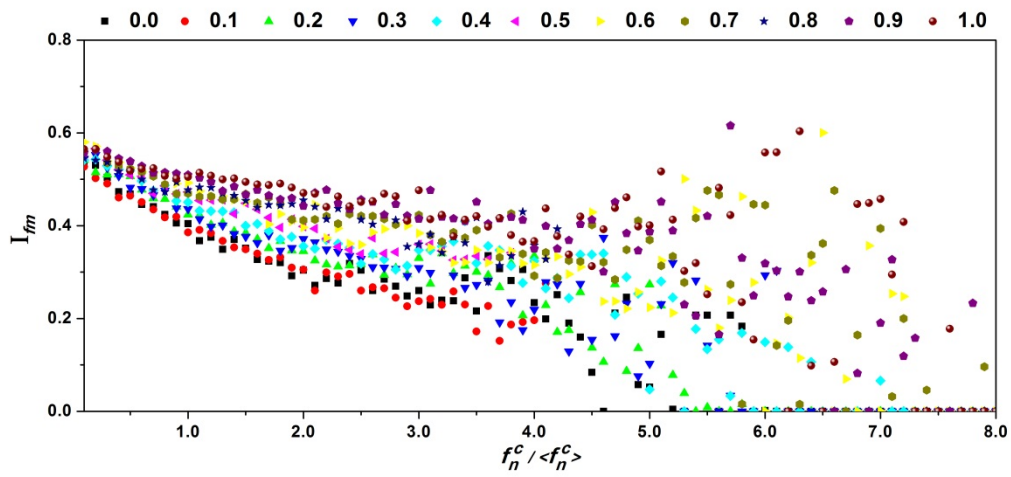


(d)

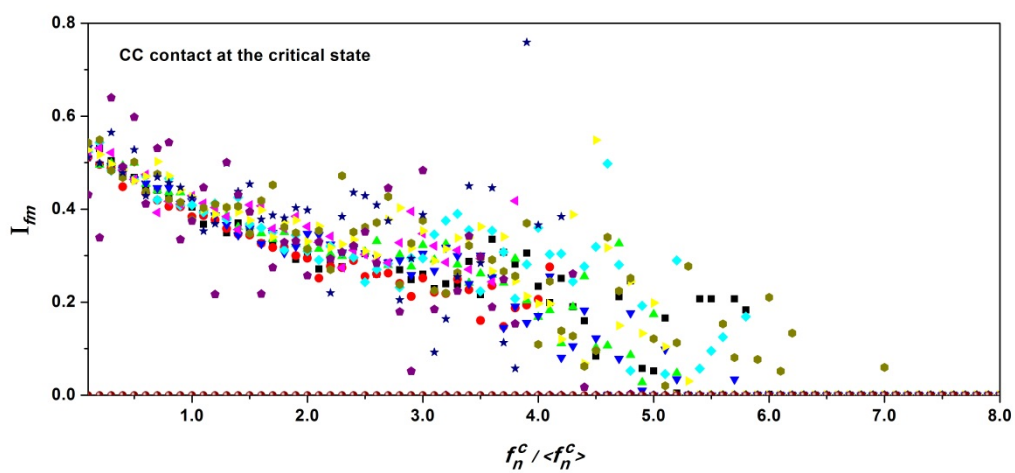


(e)

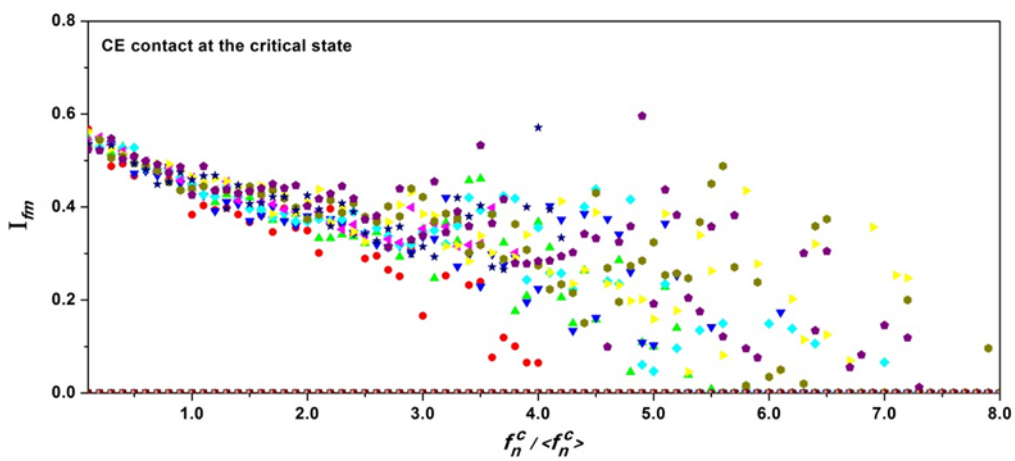
Figure 4.9: Probability distribution of normalised contact normal force at the steady state for different η_m (a) all contact types distribution; (b) CC contacts distribution; (c) CE contacts distribution; (d) EE1 contacts distribution; (e) EEm contacts distribution.



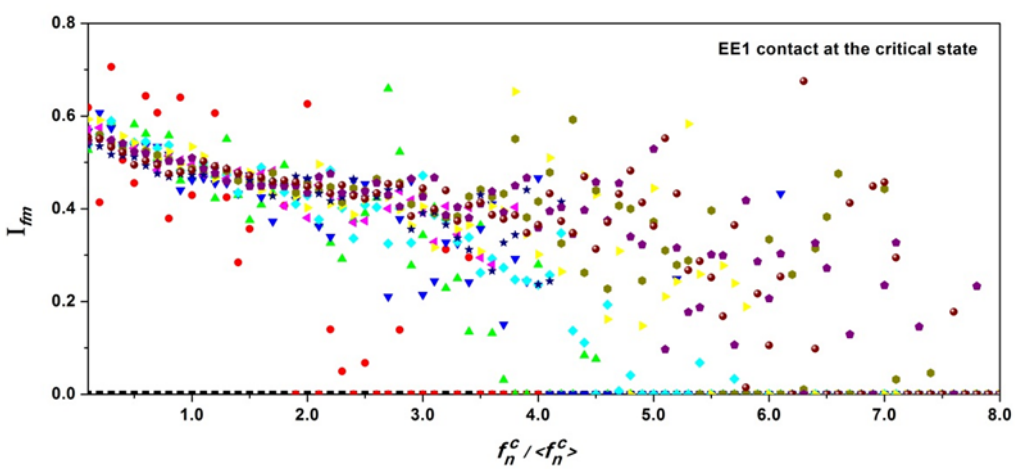
(a)



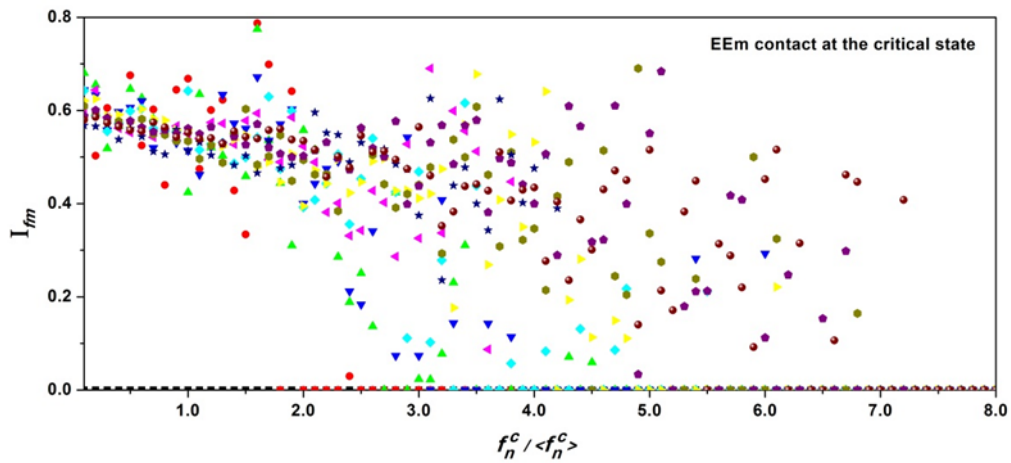
(b)



(c)

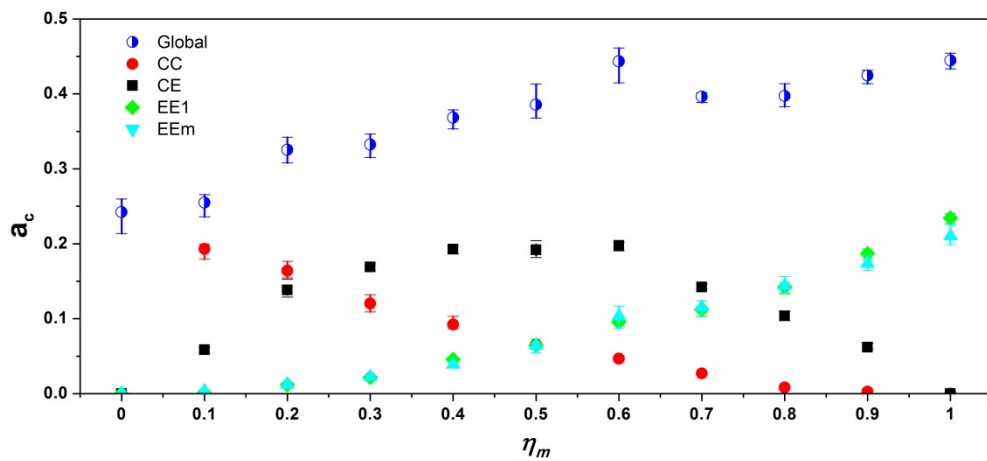


(d)

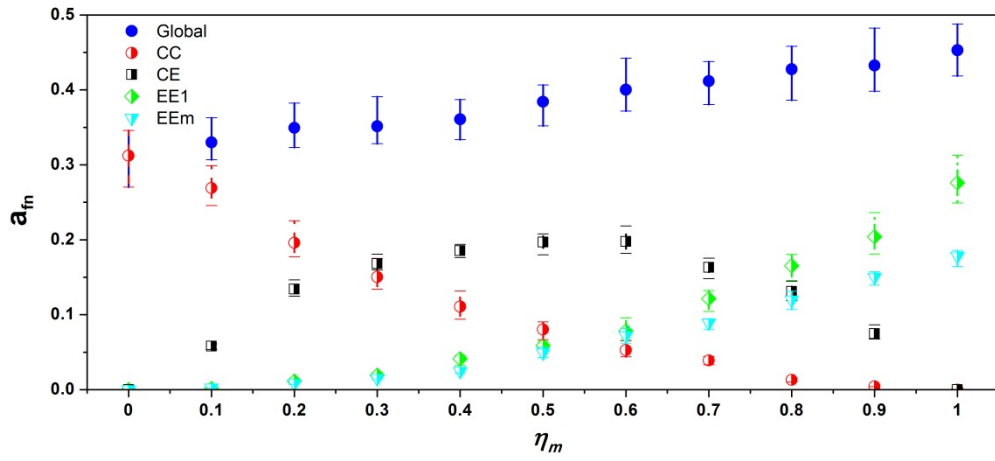


(e)

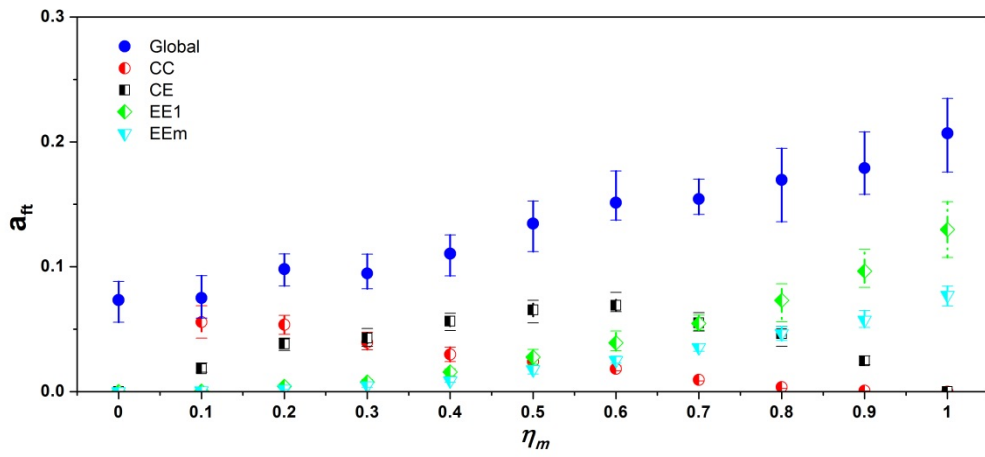
Figure 4.10: Average friction mobilisation I_{fm} with the associated normalised contact normal force at the steady state for the η_m (a) all contact types distribution; (b) CC contacts distribution; (c) CE contacts distribution; (d) EE1 contacts distribution; (e) EEm contacts distribution.



(a)



(b)



(c)

Figure 4.11: Error bars of anisotropic coefficients at the critical state: (a) coefficients of contact normal for the four contact types; (b) coefficients of contact normal force for the four contact types; (c) coefficients of contact tangential force for the four contact types.

CHAPTER 5

Study of rolling resistance model and irregular particle shape during the “undrained” tests

5.1 Introduction

Particle shape can directly influence the structural features of granular assemblies, which ultimately control the mechanical properties of granular material. Generally speaking, the strengths obtained by the discrete element method (DEM) using disk or spherical particles are much lower than those of natural sand, which has an obviously interlocking effect induced by the irregular particle shape. Previous researchers have made great efforts to explore the effect of particle shape through a theoretical way in two major directions: physical consideration (rolling resistance models) or geometry consideration (irregular particle shapes). These two modelling methodologies have been briefly discussed in Chapter 2.

The first approach is to add an artificial rotation torque at the contact points for disks or spheres, and generally named as “rolling resistance model”. This model is distinctly different from the original standard DEM, where particle rotation can only be generated by the frictional force through the conservation of angular momentum at the contact points. The rolling resistance model is firstly incorporated in DEM for simulating the shear band development by Iwashita and Oda (Iwashita and Oda, 1998, 2000). After then, many different rolling resistance models have been constructed at the contact regions (Bardet and Huang, 1993; Belheine et al., 2009; Estrada et al., 2008; Jiang et al., 2005; Mohamed and Gutierrez, 2010; Zhao and Guo, 2014; Zhou et al., 2013; Zhou et al., 1999). A detailed review work about the rolling resistance models in discrete element simulations has been summarized by Ai et al. (2011), where the rolling resistance models are classified into four directions: (1) directional constant torque models (Zhou et al., 1999); (2) viscous model (Kondic, 1999); (3) elastic-plastic spring dashpot model (Belheine et al., 2009; Estrada et al., 2008; Iwashita and Oda, 1998, 2000; Mohamed and Gutierrez, 2010; Zhao and Guo, 2014); (4) contact

independent models (Sakaguchi et al., 1993). The direction constant model may face mathematical discontinuity when the relative angular velocity is zero. In addition, the contact independent models are lack of realistic physical meaning, which have been reported by Ai et al. (2011). The most commonly used rolling resistance model in their review paper is the elastic-plastic spring dashpot model. Recently Huang (2014) presents an efficient way for dividing the rolling resistances models only by the related magnitude of the normal contact force and the evaluation of the relative angular motion. Likewise, for the elastic-plastic rolling resistance models, the difference is determined by the definitions of rolling stiffness (Ai et al., 2011; Belheine et al., 2009; Iwashita and Oda, 1998, 2000; Jiang et al., 2005; Mohamed and Gutierrez, 2010; Tordesillas and Walsh, 2002; Wensrich and Katterfeld, 2012; Zhao and Guo, 2014). The other approach is to directly generate particles using irregular geometries through many different ways, e.g., ellipse or ellipsoids, polygons, and combining clusters/clumps. These particle generation methodologies have been discussed in Chapter 2.

Many previous studies have shown that rolling resistance models can nearly capture the stress-strain and strain localization responses of irregular granular materials. However, the link between the rolling resistance model and the mechanism of realistic particle shape is still a major challenging issue. Zhou et al. (2013) carried out a systematic DEM biaxial tests to compare the rolling resistance model and simplified clump particles. They concluded that the rolling resistance model cannot replace the irregular particle to produce analogous strain localization and energy dissipation behaviors for the granular materials. Additionally, the selection of a rolling resistance coefficient represents an artificial trial without a clear physical reasoning. Recently, some researchers attempt to construct a bridge to connect the rolling resistance model and irregular particle shape through a reasonable physical formulation. Estrada et al. (2011) found a simple equation to identify the effect of rolling resistance for the disk by a regular polygonal grain with variable number of sides. However, the compared range of rolling resistance coefficients is very small from 0.0 to 0.15. In addition, the boundary condition for these numerical tests is monotonous under simple shear. Wensrich and Katterfeld (2012) proposed a simple geometric argument to estimate the rolling resistance coefficient from the ratio of the average eccentricity to the effective rolling radius. Meanwhile,

they pointed out that the proposed method can partially predict the irregular clumped particles. Since the rolling resistance can only artificially resist rolling motion, while the realistic shape can both induce and resist particle rotation. The quantitative relationship between rolling resistance coefficient and irregular shape still remains poorly known. In addition, to describe quantitatively the rolling resistance coefficient, the validity of the rolling resistance model is much more important. Likewise, it is still questionable whether the rolling resistance model can fully replace the irregular particle to produce similar patterns of shear localization, mesoscopic structure, fabrics and probability distribution of contact information. Moreover, most references are related to biaxial or simple shear tests, and the “undrained” mechanical response is seldom considered. In particular, the macro and micro responses at some characteristic states such as liquefaction, quasi-steady, phase transformation, and critical state are seldom studied. In the current chapter, for clarifying the difference between the disk particles with the rolling resistance model and the irregular shape grains, the original Iwashita and Oda (1998, 2000) rolling resistance model is considered due to its efficiency and simplicity. Moreover, the effects of surface roughness and bonding are ignored in this rolling resistance model. Meanwhile, the irregular shape is generated by using the clusters/clumps technique. Two simple clumps (Elongate and Triangular) are employed in the current study for comparing with the rolling resistance model.

This chapter is organized as follow: the methodology of rolling resistance model is firstly introduced. Then, the DEM sample preparation and “undrained” tests are described. Additionally, both the macroscopic and microscopic mechanical responses for the rolling resistance model and clumps are compared and discussed in Section 5.3. Finally, a conclusion about the main findings from this study will be given.

5.2 Investigation scheme

5.2.1 Rolling resistance model

The simulations are carried out using the DEM, which adopts an explicit computation scheme and assumes the rigid particles with soft contacts. The mechanical interactions for the contact entities between ball-ball and ball-wall are determined by the contact laws. Figure. 5.1 (a)

shows the illustration of the rolling resistance model. The contact force can be determined from Eq. (2.66) to Eq. (2.68) as shown in Figure 5.1 (b). In traditional DEM, particle can freely rotate with no restriction. The angular momentum for individual particle is only determined by the torque resulting from the shear contact force as follow:

$$I \frac{\partial w}{\partial t} = \sum_{c=1}^n f_s^c r \quad (5.1)$$

where I is the polar moment of inertial of a disk particle, w is the polar angular velocity, r is the particle radius, and n is the number of contacts surrounded a disk. The rolling resistance torque at the contact points is added into the angular momentum equation for each particle, and the above Eq. (5.1) can be rewritten as:

$$I \frac{\partial w}{\partial t} = \sum_{c=1}^n (f_s^c r + M_i) \quad (5.2)$$

where M_i is the rolling resistance at the c^{th} contact. The rolling resistance simulates the restriction on a particle rolls over another, at which the contact normal force will induce an interlocking effect between the effective touching area. The rolling resistance model in Figure 5.1 (a) contains an elastic spring, a dashpot, a slider and a no-tension joint, which can be considered as an elastic-plastic model. The elastic part of the rolling resistance torque can be written as:

$$M_i = -K_r \theta_r - C_r \frac{\partial \theta_r}{\partial t} \quad (5.3)$$

where K_r is the rolling stiffness, θ_r is the relative rotation between two particles, C_r is the viscosity coefficient. In the current study, all the numerical samples are under quasi-static condition, hence the viscosity coefficient can be set as zero (Zhou et al., 2013). The value of K_r can be determined by previous study on cylinders (Bardet and Huang, 1993):

$$K_r = 2rf_n^c J_n \quad (5.4)$$

where J_n is a dimensionless parameter, and its value varies from 0.25 to 0.5 depending on the particle roundness. Since perfectly rigid discs are considered in this study, J_n is fixed as 0.5 for all the simulations (Ai et al., 2011; Mohamed and Gutierrez, 2010; Zhou et al., 2013). The rotation slider is analogous to a shear slider, hence a threshold moment is considered as a perfect plastic behavior (Figure 5.1(b)).

$$M_i \leq \eta f_n^c \quad (5.5)$$

where η is the coefficient of rolling resistance with a dimension of length. Once the resistance exceeds the threshold moment, particle will roll without restriction with any further rotation resistance. Iwashita and Oda (2000) decomposed this coefficient into two parts (1) a typical length B , which is equal to half of the contact width between two contacting particles; (2) a dimensionless parameter β . Moreover, the typical length B is dependent on the average radius $\langle R \rangle$ and shape parameter δ (Jiang et al., 2005; Mohamed and Gutierrez, 2010). Therefore the rolling resistance coefficient η can be rewritten as:

$$\eta = B\beta = \langle R \rangle \delta \beta = \langle R \rangle \alpha \quad (5.6)$$

where $\langle R \rangle$ denotes the average radius of two contacting particles with radius r_1 and r_2 as $\langle R \rangle = (2r_1r_2)/(r_1 + r_2)$, α is a combined coefficient of two dimensionless parameter δ and β . The parameter α is the final form of rolling resistance coefficient. Additionally, the physical meaning of α is similar to the internal friction coefficient, and its range is from 0.0 to 1.0. Substituting Eq. (5.6) into Eq. (5.5), the moment threshold can be rewritten as:

$$M_i \leq f_n^c \langle R \rangle \alpha \quad (5.7)$$

The rolling resistance model described above was implemented in the framework of DEM. This secondary developed model would be adopted to carry out the numerical undrained tests and compare with the irregular clump particles. For verifying the developed rolling resistance model, a pure rolling and a pure shearing element tests are carried out and compared with the thresholds of moment torque and contact shear force. Detailed information about the element tests are shown in Figure 5.2. It can be found that the present rolling resistance model is effective to obtain the assumed mechanical behavior (Figure 5.1(b)) between the particles' contacts.

5.2.2 DEM simulation details

In the present numerical “undrained” test, all the samples are composed of 9127 disk grains or irregular clumps. The particle size distribution (PSD) and particle morphology are shown in Figure 5.3. The mean particle diameter (d_{50}) is 1.62mm with a uniformity coefficient of $C_u=1.47$. Particles are randomly distributed in a rectangular box with dimensions of 100

mm (W) \times 200 mm (H). The intention of this chapter is to compare the disks installed rolling resistance model and the irregular clumps at some characteristic states in Figure 5.3. Initially, the target is to make a suitable isotropic sample, which can produce the liquefaction, quasi-steady or dilate features during the monotonic “undrained” shearing. In addition, for the consolidated samples of disks and irregular clumps, the void ratios are different. Moreover, the common technique for generating different densities consolidated samples is to change the internal friction coefficient during the isotropic consolidated procedure. Upon fulfilling the consolidated state ($p_c=100$ kPa), the internal friction coefficient μ is fixed as 0.5. In addition, the rolling resistance coefficient is switch off until the undrained shearing stage. After series of trial and back tests, loose packing disk particles are obtained with a void ratio nearly 0.24. Different rolling resistance coefficients are then implemented to examine the effect of the rolling resistance. Detailed information can be seen in Table 5.1. Additionally, the irregular clump samples are generated by replacing the initial disk particles with an equivalent area and the same center location before the isotropic consolidated stage. The orientation of the irregular grains is arbitrarily distributed in the range of 0 to 360 degrees. Next, the irregular assemblages are isotropically consolidated to achieve the target confining pressure. In addition, the relative density is still controlled by the internal friction coefficient. After the isotropic consolidated procedure, the granular packings obtain different void ratio from loose to dense (Table 5.2). During the subsequent “undraind” shearing, μ is fixed at 0.5. Using an undrained shearing test on each specimen, a comparison of the mechanical properties would be performed in the later section. Since water is not considered, the undrained condition can be equivalent to a constant area test, which is controlled by a servo system between the loading plate and the confining plate. The values of the numerical parameters are provided in Table 5.3. Note that four boundary walls are assumed with no friction to eliminate the boundary arch effects.

For easily understanding the mechanical responses of sand under monotonic “undrained” shear behavior, a typical illustration for different initial densities is shown in Figure 5.4, where q represents the deviator stress, p indicates the effective mean stress, u denotes the excess pore water pressure and ε_a is the axial strain. The phase transformation in Figure 5.4,

which corresponds well with the state of minimum effective mean stress, indicates the deformation response of granular soil changing from contractive to dilative (Vaid et al., 1990; Yang and Dai, 2010; Yoshimine et al., 1998). When the sand is loose, a static liquefaction will emerge due to the fast generated excessive pore water pressure, which will replace the stress components (q and p) to sustain the load transferring during the continuous deformation. Moreover, some catastrophic disasters (e.g. debris flow and landslides) are induced by the liquefaction, where the soil completely lost the shear strength. For a medium sample in Figure 5.3, there exists a special phase transformation state named quasi-steady state (Alarcon-Guzman et al., 1988; Ishihara et al., 1975), which represents a temporary liquefaction and then regains certain strength to achieve an even higher peak strength with further strain. However, there still exists a conflict about the reality of the quasi-steady state (Been et al., 1991; Zhang and Garga, 1997), whether it is an intrinsic property or a test-induced behavior for the granular materials. Many investigations including the experimental and numerical studies (Gong et al., 2011; Guo and Zhao, 2013; Vaid et al., 1999; Yang and Dai, 2010; Yoshimine et al., 1998) have proved that the quasi-steady state is a real material behavior of granular materials. DEM is a robust tool to eliminate the restrictions from the traditional laboratory devices (e.g. end restraint or friction). For a dense sample in Figure 5.4, there is a phase transformation emerge at a very small strain, and the pore water pressure will then turn from positive to negative. Additionally, a critical state with constant deviatoric stress and a unified critical state line in Figure 5.4 can be found at large strain level. The slope value of the critical state line is $M = q/p$, which can also be expressed by the ratio of critical macro friction angle (φ_{uc}) at the critical state $M = 6 \sin \varphi_{uc} / (3 - \sin \varphi_{uc})$. As mentioned before, the phase transformation, liquefaction, quasi-steady, and critical states are also marked in Figure 5.4.

The definitions of stress tensors and fabric components within the methodology of DEM has been discussed in Chapter 2. Hence the major principal stress (σ_1) and minor principal stress (σ_3) are thus given by:

$$\sigma_1 = \frac{\sigma_{11} + \sigma_{33}}{2} + \sqrt{\left(\frac{\sigma_{11} - \sigma_{33}}{2}\right)^2 + (\sigma_{13})^2} \quad (5.8a)$$

$$\sigma_3 = \frac{\sigma_{11} + \sigma_{33}}{2} - \sqrt{\left(\frac{\sigma_{11} - \sigma_{33}}{2}\right)^2 + (\sigma_{13})^2} \quad (5.8b)$$

The deviatoric stress, effective mean stress can be found in Eq. (2.2), and pseudo excess pore water pressure can be determined as:

$$u = p_c - p \quad (5.9)$$

5.3 Numerical findings and discussions

5.3.1 Macroscopic mechanical responses

Figure 5.5 shows the systematic macro responses of granular samples with different rolling resistance coefficients under “undrained” conditions, where the micro numerical parameters and boundary conditions are identical for exploring the sensitives of α (Table 5.1 and 3). It can be found that UR0 with a loose packing exhibits an explicit liquefaction phenomenon in Figure 5.5 (a), which is qualitatively similar to previous experimental tests and numerical simulations (Guo and Zhao, 2013; Yang et al., 2012, 2013; Yoshimine, 1999; Yoshimine and Ishihara, 1998; Yoshimine et al., 1998). Moreover, the artificial rolling resistance torques can directly influence the liquefied sample UR0 to possess some level of dilation effects. Among these samples, UR1 and UR2 exist a distinct quasi-steady state as the medium sample in Figure 5.4. The slopes of the critical state lines in p - q space as shown in Figure 5.5 (a) increase steadily with the raised rolling resistance coefficient. This relationship has also been captured by Zhao and Guo (2014) for evaluating the development of “undrained” shear induced anisotropy in granular media with different rolling resistance coefficients. Actually, the value of M cannot increase linearly with the rolling resistance coefficient. As shown in Figure 5.5(b), the variation of M is very small for $\alpha > 0.5$, which is analogous to a threshold. This relationship between M and α is similar to the peak friction angle in drained shear test by Mohamed and Gutierrez (2010). Figure 5.5(c) and (d) show the deviatoric stress vs axial strain for capturing the effects of rolling resistance coefficients. It can be seen that the peak deviatoric stress is steadily increased for $\alpha < 0.5$. Fig. 5 (e) and (f) present the pseudo excess pore water pressure (u), which can be obtained by the difference of constant confining pressure and the mean effective pressure, plotted vs axial strain for all the samples. It can be

found that the rolling resistance coefficient can induce the granular sample to generate negative u , which may prohibit the packing to develop into liquefaction state. Moreover, UR2 with a very small rolling resistance coefficient exhibits a positive u when $\varepsilon_a > 15\%$. As an alternative to the deviatoric stress, Figure 5.5(g) and (h) show the evaluation of the mean effective stress with the axial strain. The variation of p is analogous to q . The evaluation of mobilized friction angle is shown in Figure 5.5(i) and (j). It is noticed that higher rolling resistance coefficient may induce larger macroscopic shear strength. In addition, the differences would become very small when $\alpha > 0.5$.

Figure 5.6 shows the evolution of stress path in p - q space for the three different shape samples in Table 5.2. As shown in Figure 5.6, although the rolling resistance coefficient can enhance the slope of critical state line, the effect is limited (UR7). This may also hint that the rolling resistance model cannot fulfill all the M value for the irregular clumps. In addition, particle shape can influence the peak value of q for the loose samples within the liquefaction stage. An interesting finding is that the disk sample is not standing at the minimum level of peak q . Moreover, the rolling resistance samples cannot easily generate an apparent liquefaction in Figure 5.5. This is another drawback of the rolling resistance model for simulating the undrained shear tests.

Figure 5.7 shows the evolution of deviatoric stress with the axial strain. It can be seen that all the three shapes can qualitatively match well with the mechanical responses of typical monotonic undrained shear of granular materials in Figure 5.4. Moreover, particle shape can influence the peak values of q at the quasi-steady state and critical state. The strain levels for the two characteristic states are also influenced by the particle shape.

Figure 5.8 shows the variation of the pseudo excess pore water pressure against the axial strain for the nine samples. For the medium packings, the disk shape is difficult to generate a negative u even at the critical state. Nevertheless, the irregular geometry would induce the granular packing to develop much more dilating behavior, which may be conducive to form a negative u . This feature is very similar as the rolling resistance effect in Figure 5.5(e).

In the below sections, some statistical quantities upon the micro scale would also be compared for the rolling resistance samples and irregular clumps at the characteristic states.

5.3.2 Microscopic behavior

Figure 5.9 shows the validation of SFF relationship, which is a bridge to connect the micro statistical anisotropic information and macro shear strength of a granular assembly, for both the irregular clump and rolling resistance samples. It can be found that the analytical SFF relationship in Eq. (2.60) can match well with the DEM results for the six samples, except for UR5 which possess a quasi-steady feature in Figure 5.4. In addition, these six samples are considered to primarily investigate the difference between rolling resistance and irregular shape. All the samples except UR5 present a typical hardening behavior, hence the macro mechanical responses are qualitatively similar. The UR5 sample is considered to play as an upper bound rolling resistance effect in Figure 5.5. In addition, the highest value of $\sin \varphi_{uc}$ in Figure 5.5 is still lower than the irregular Elongate or Triangular granular assemblage. This phenomenon is an alternative view to the slope of the critical state line in Figure 5.6.

Figure 5.10 shows the variation of the coordination number $CN = (2C - N_1)/(N - N_0 - N_1)$ (C is the total contact number, N is the total particle number, N_1 is the number of particles with only one contact, and N_0 is the number of particles with no contact) for the aforementioned six samples. It can be found that the value of CN drops initially and then increase to the critical state which is affected by the increasing mean effective stress. The reason for the initial decrease in Figure 5.10 is induced by the contact loss along the principal strain directions (Gong et al., 2011). Moreover, the minimum value of CN corresponds well with the quasi-steady state (Gong et al., 2011; Yang and Dai, 2010). Furthermore, the value of CN for UEM and UTM samples is much higher than the rolling resistance samples at the critical state. This also hints that the structural feature of granular assemblage is highly influenced by the particle shape. In addition, the properties of friction mobilization (I_M) can be considered as a basic index to describe the micro interlocking effect, which would influence

the variation of the shear strength. The descriptor I_M can be determined by $I_M = |f_s^c|/(\mu f_n^c)$ for the individual grain. Figure 5.10(b) presents the evolution of the average friction mobilization (I_{gm}) of the whole assemblage for all the six samples. It can be seen that the initial peak value of I_{gm} is quickly increased at a very small strain. From the comparisons of the six samples, it can be found that the value of I_{gm} for the irregular shapes (UEM, UTM) is significantly larger than the resistance samples. Additionally, the rolling resistance effect can only slightly enhance the value of I_{gm} for the disk shape of granular assemblages.

Figure 5.11 presents the contributing percentages of a , a_n and a_t during the “undrained” shear, which are also explored by Guo and Zhao (2013). It can be found that the anisotropy of contact normal force a_n dominates the macro shear strength for nearly 50% of the total value in UDM and rolling resistance samples. Moreover, the rolling resistance effect can slightly increase the portion of tangential force anisotropy a_t and reduce the weighting of a_n . This trend is analogous to previous studies (Guo and Zhao, 2013; Zhao and Guo, 2014). However, for the UEM and UTM samples, the contact normal anisotropy a plays the major role after the axial strain beyond 6%. While the weighting of a_t increases from approximately 15% to 20%. Additionally, the irregular shape may reduce the portion of a_n for contributing the macro shear strength. As well, this is distinct from the rolling resistance samples.

Figure 5.12 shows the contributions of the weak force network (contact force lower than the average contact force), the strong force network (contact force larger than the average contact force) and the whole force network for the contact normal anisotropy a . In the weak force network, a plays a very minor role. Its trend for UDM, UR1 and UR2 is quickly increasing to a maximum value and then drops to a constant which is nearly 0. However, for the high rolling resistance sample UR5, the weak anisotropy of contact normal a stands at a larger value, which is analogous to UTM. Moreover, the trend of a in the strong force network or the entire force network is nearly the same. Furthermore, the value of a in the whole force network is smaller than the strong force network. This pattern has also been found by Guo and Zhao (2014) using sphere particles. Additionally, the trend of a in the weak force network for UEM and UTM firstly decrease and then increase to a certain level which cannot be ignored.

Moreover, the value of a for UEM in the weak force network plays nearly the same role as the strong force network. This may be induced by the excessive weak contacts between the non-convex shapes in the current study. In addition, the ratio of a between the strong and weak force networks within UEM is lower than 3 times as compared with the rolling resistance samples. Meanwhile, the weights of weak and strong a for UTM and UR5 are similar, but the macro mechanical response are different as shown in Figure 5.5 and Figure 5.7. As mentioned above, although the macro response between the irregular granular assemblages and the rolling resistance sample are qualitatively similar, the evolution of the micro anisotropies is different.

Figure 5.13 shows the rose distributions of contact normal for the quasi-steady state and critical state. The determination of contact normal orientation is normalized as the fraction of all contact normals at an angular interval ten degrees. It can be seen that the contact normal anisotropy is significantly developed within the strong force network, where the contacts are mainly orientated along the major principal direction. For the rolling resistance samples, the difference of contact normal distribution (within the strong force network) between the quasi-steady state (QSS) and critical state (CS) parallel the loading direction is not obvious. Moreover, the distribution of the contact normal perpendicular to the loading direction is slightly decreased even for the high rolling resistance sample UR5, which shows a similar macro response as the dense medium in Figure 5.4. Hence, the quasi-steady state is changed as phase transformation state (PTS) for the UR5. However, the contact normal distribution for the strong force network along the loading direction is clearly enhanced by the irregular particle shape (UEM and UTM). For the weak force network, it can also be seen that the polar histogram of contact normal network is approximately a circular shape (Figure 5.13), which means the number of contacts in each interval is nearly the same. This feature hints that the anisotropy coefficient of contact normal is almost zero, which can also be seen in Figure 5.12. Nevertheless, the contact normal distribution for UEM and UTM within the weak force network is increased along the loading direction from the quasi-steady state to the critical state, and decreased at the perpendicular direction. This variation is analogous to the strong force network. It can be said that the anisotropy of contact normal in the weak network cannot

be ignored for the UEM and UTM, which can also be seen in Figure 5.12. Moreover, by comparing these figures, it is noticed that the strong force network plays a much more important role for the whole loading procedure.

Figure 5.14 shows the probability distribution of the contact normal force, normalised by the mean contact force $\langle f_n^c \rangle$ at the quasi-steady state except for UR5 (PTS) and the critical state in log-linear scale. For all the six samples in this chapter, the normalized contact normal force essentially follows a power decay law which is determined in Eq. (3.24). It can be seen both the values of α and β represented the variation indexes are decreased with increasing rolling resistance in Figure 5.14 (a) and (b). The broad of contact normal force is narrowed from the quasi-steady state to critical state. In addition, the variation of UR5 in Figure 5.14 is analogous to UEM and UTM, especially for the critical state. This finding indicates that the rolling resistance model will give similar probability distribution of contact normal force with the irregular shape model. However, the macro stress-strain behaviours are different in Figure 5.5 and Figure 5.7.

Figure 5.15 shows the probability of I_m for the six samples at the quasi-steady state and critical state. It can be seen that the variation of PDF for the two characteristic states shows a similar pattern. That is to say, the probability of I_m is not a strain dependent index. For the rolling resistance samples, the variation of PDF presents a similar trend, with a nearly linear decreasing feature from $I_m = 0.0$ to $I_m = 0.9$. Meanwhile, this result also indicates that the weight of weakly mobilized contacts is larger than the strongly mobilized contacts even when the rolling resistance coefficient is set to a high level (UR5). However, for the irregular samples, a nearly constant PDF emerges for the whole range of I_m except for $I_m > 0.9$, which means a highly mobilized contact even for sliding. It can also be found that the portion of highly mobilized contacts ($I_m > 0.9$) within the two irregular samples is much larger than the rolling resistance assemblages at the two states.

Figure 5.16 shows the variation of average friction mobilization I_{mf} with the associated contact normal force at the quasi-steady state and critical state. The distribution of I_{mf} is also

a strain independent index. It can also be found that the value of I_{mf} within the weak force networks is higher than the contacts within the strong force networks. Moreover, the distributions of rolling resistance samples covered each other for the whole range ($f_n^c / \langle f_n^c \rangle$), and are lower than the irregular clumps. Furthermore, the value of I_{mf} is sensitively influenced by the irregular clump when $f_n^c / \langle f_n^c \rangle < 3.0$. Hence, it can be said that there possess an obvious difference between the rolling resistance samples and the irregular clumps. Figure 5.17 shows the average magnitude of rotation is increased with the increasing rolling resistance coefficient for the same strain state. This finding is similar as other biaxial drained test for rolling resistance samples at the peak and critical state (Zhou et al., 2013). The difference of the spatial rotation distribution is also indicated that the rolling resistance model cannot realistically reflect the microscopic structure feature of granular materials.

5.4 Conclusions

In this chapter, a traditional rolling resistance model has been adopted to explore and compare with the simplified irregular clumps under the undrained shearing tests through the DEM. A series of DEM simulations have been carried out to identify the differences between the macroscopic and microscopic mechanical responses. It can be found from the numerical results that both the rolling resistance coefficient and the irregular shape can induce some level of dilation effects to enhance the shear strength of the granular assemblage. However, the effect of rolling resistance is limited when $\alpha > 0.5$. Moreover, a very small rolling resistance coefficient can trigger a positive pseudo excessive water pressure at the critical state. Furthermore, the slope value of M for the largest rolling resistance coefficient is still lower than the irregular shape. In addition, the artificial rolling resistance effect cannot easily generate an apparent liquefaction as the loose packing of irregular particle.

The coordination number of irregular clumps is significantly higher than the rolling resistance samples, especially for the critical state. It can also be seen that the variation of CN for the rolling resistance samples is extremely smaller than the irregular clumps. Moreover, the average friction mobilization of rolling resistance samples even for UR5 is still much lower than the irregular assemblages. Additionally, the validation of the analytical expression SFF

for the rolling resistance samples and the irregular clumps is confirmed. It can be found that the weights of contact normal anisotropy a for the UEM and UTM samples play a major role when the axial strain beyond 6%. However, for the rolling resistance samples, the anisotropy of contact normal force dominates the macro shear strength for nearly 50%. From the scope of weak or strong force network, it can be found that the anisotropy of contact normal within the weak force network for UEM and UTM cannot be ignored. Although the proportion of contact normal anisotropy a for both weak and strong force networks are similar for UTM and UR5, the macro mechanical responses are completely different. Moreover, it can also be seen that the rose polar distribution of contact normal a within the weak force network is gradually increased along the loading direction from the quasi-steady state to the critical state, and decreased at the perpendicular direction. This phenomenon is also different from the rolling resistance samples. Although the probability distribution of the normalized contact normal force for the rolling resistance sample is analogous to the irregular clumps, the macro stress-strain behaviors are distinct. Moreover, the patterns of the probability distribution of I_m and I_{mf} for the rolling resistance samples and irregular assemblages at the quasi-static and the critical state are obviously different. It can also be found that the portion of highly mobilized contacts for the irregular samples is significant higher than the rolling resistance packings. In addition, the variations of probability distributions of I_m and I_{mf} are insensitive to the rolling resistance coefficient. As discussed above, the rolling resistance model cannot fully replace the irregular particle shape to capture the realistic macroscopic and microscopic responses.

Tables

Table 5.1: Samples to be sheared for the rolling resistance model under undrained condition.

Samples	Void ratio	Particle rolling resistance α
UR0	0.243	0.0 (free rolling)
UR1	0.243	0.01
UR2	0.243	0.025
UR3	0.243	0.05
UR4	0.243	0.1
UR5	0.243	0.5
UR6	0.243	0.25
UR7	0.243	1.0

Table 5.2: Samples for disks and irregular clumps from loose to dense.

Particle shape	Sample	Void ratio	Description
Disk	UDL	0.244	Loose sample
	UDM	0.236	Medium sample
	UDD	0.220	Dense sample
Elongate	UEL	0.227	Loose sample
	UEM	0.220	Medium sample
	UED	0.203	Dense sample
Triangular	UTL	0.230	Loose sample
	UTM	0.214	Medium sample
	UTD	0.201	Dense sample

Table 5.3: Model parameter values used in the DEM simulations.

Model parameters		Values
Sample dimensions (mm)		Height: 200; Width: 100
Particle sizes (mm)		1.0-2.0 (9127) $C_u = 1.47$; $d_{50} = 1.62$
Density (kg/m^3)		2600
Sand particles	Normal/shear contact stiffness (N/m)	1×10^8
	Inter-particle friction coefficient	0.5
	Local non-viscous damping	0.45
Confining boundaries	Normal contact stiffness (N/m)	1×10^7
	Frictional coefficient	0.0

Figures

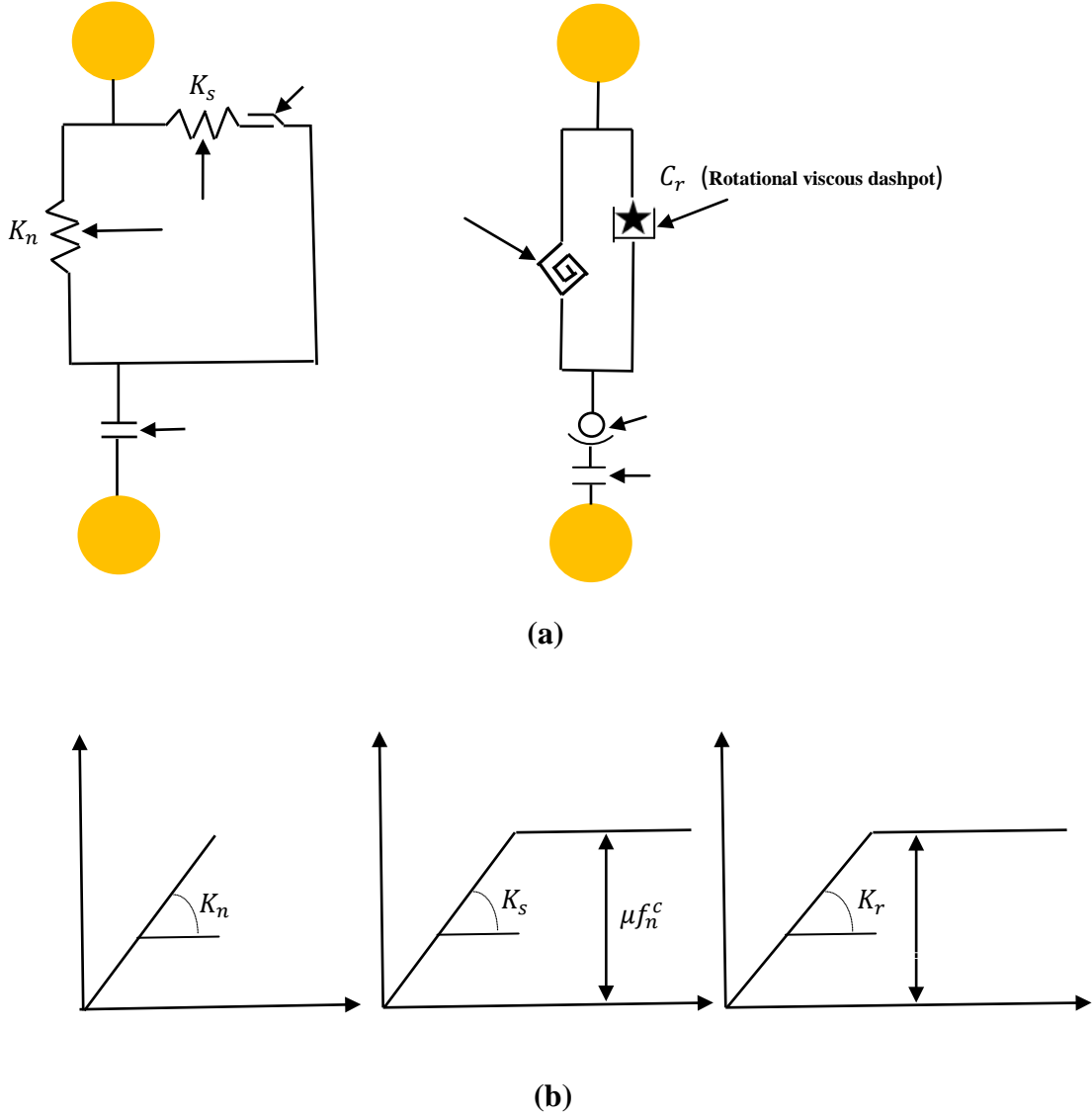


Figure 5.1: (a) The illustration of contact rolling resistance model proposed by Iwashita and Oda (1998, 2000); (b) mechanical responses at contact points.

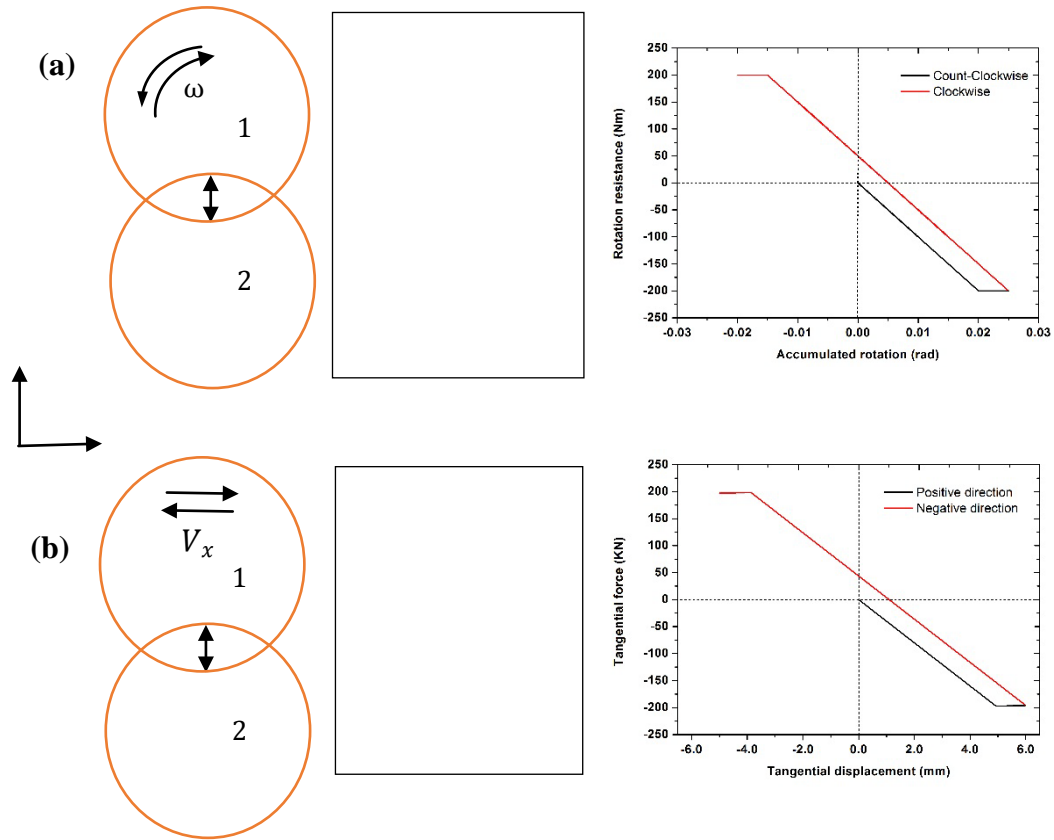


Figure 5.2: Verified the rolling resistance model (a) pure rolling test; (b) pure shearing test.

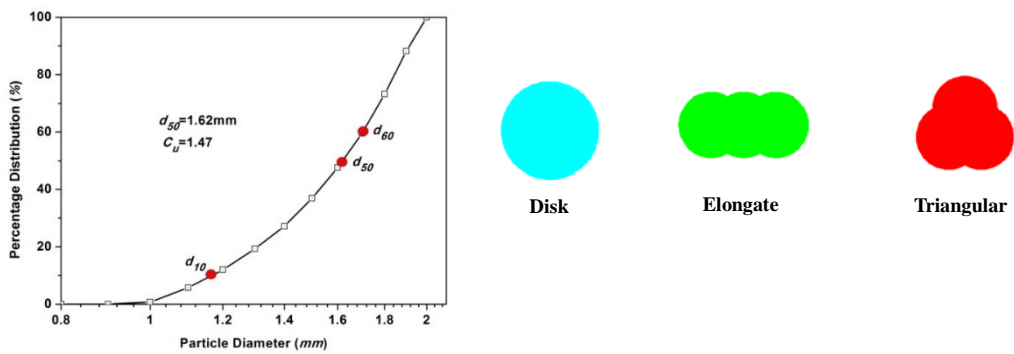


Figure 5.3: Schematic of PSD and particle morphology.

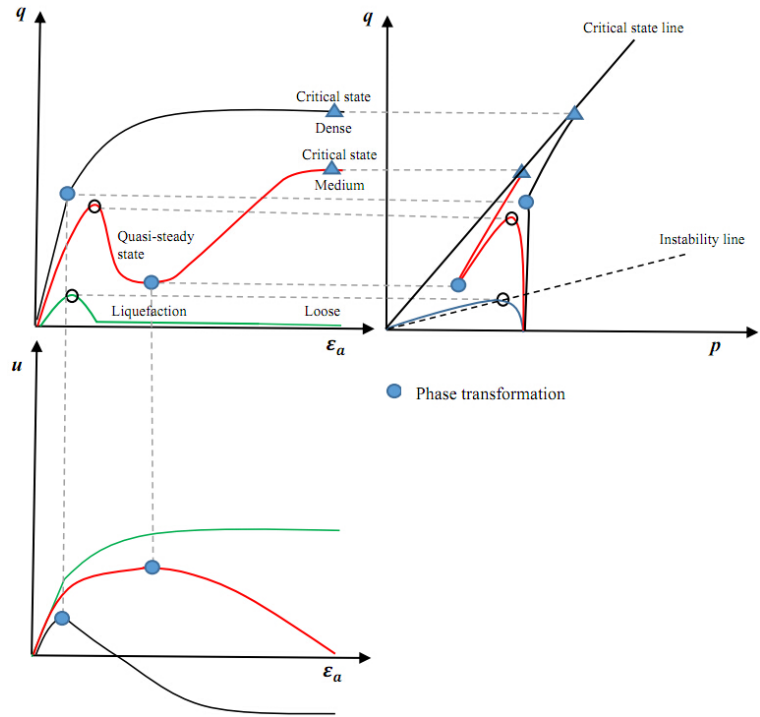
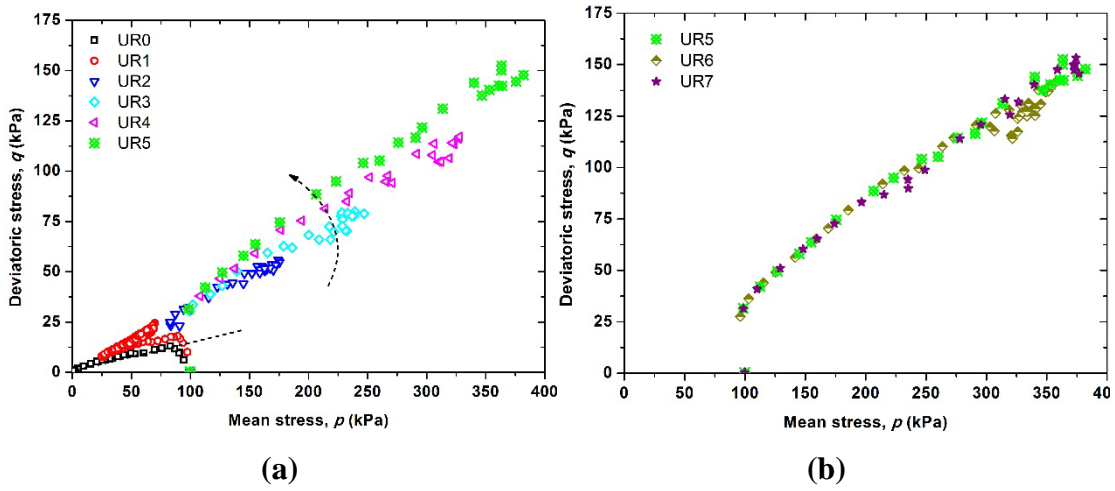
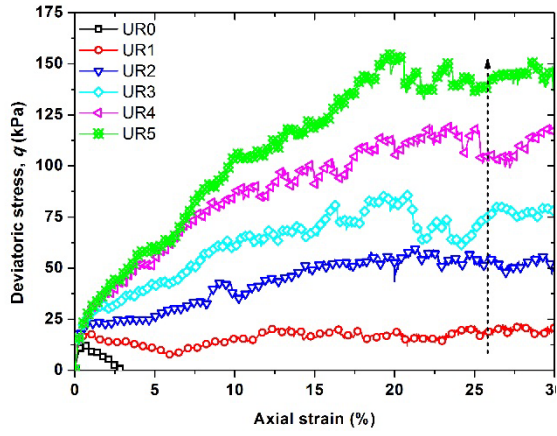
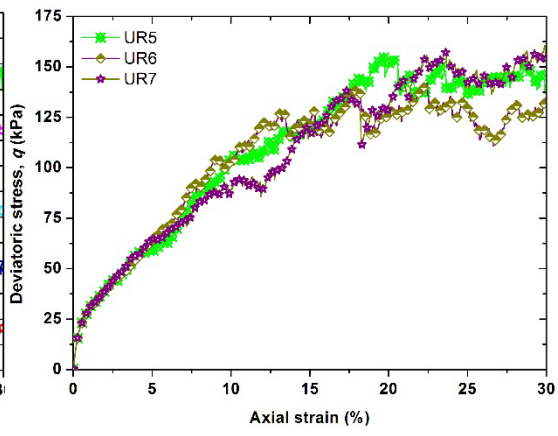


Figure 5.4: Schematic of typical monotonic undrained behavior of granular materials (Gu et al., 2014; Yimsiri and Soga, 2010).

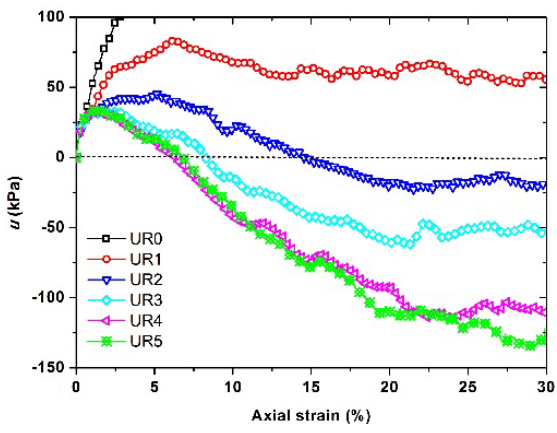




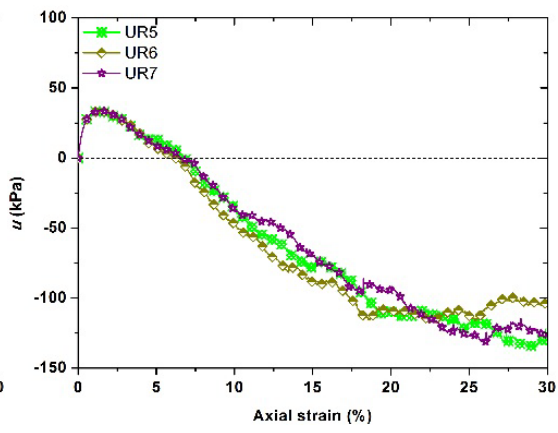
(c)



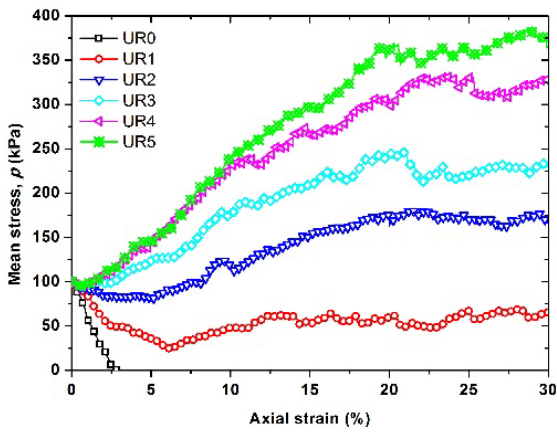
(d)



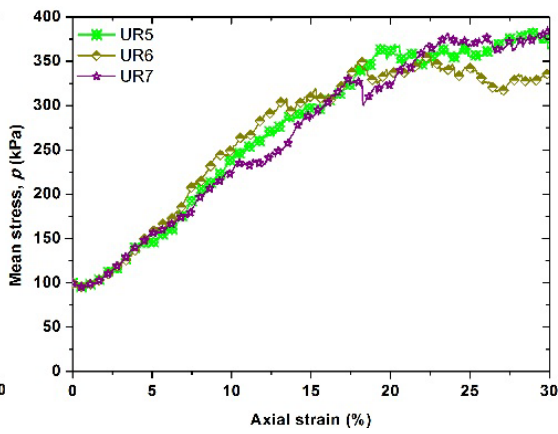
(e)



(f)



(g)



(h)

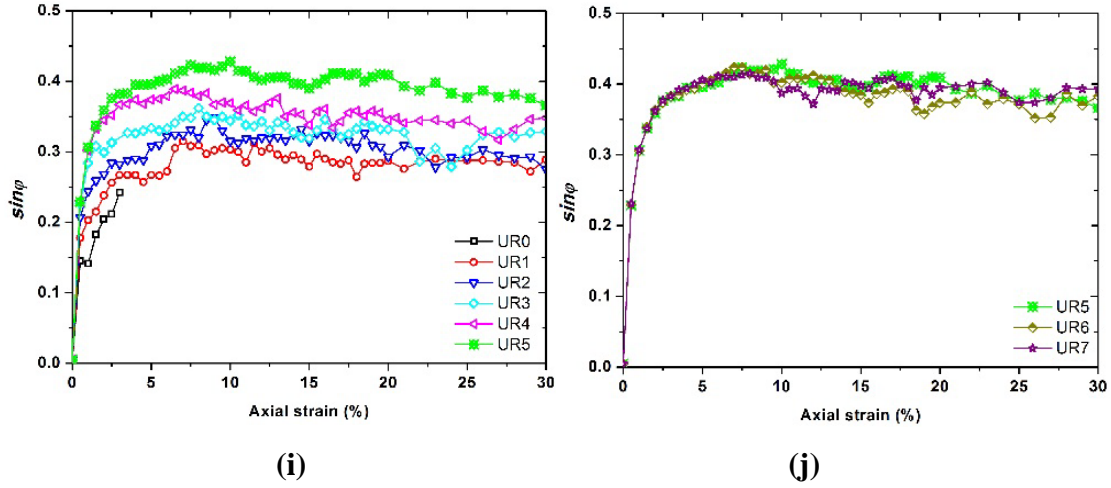


Figure 5.5: Undrained macro responses of biaxial shear tests with different rolling resistance coefficients: (a) (b) stress paths; (c) (d) deviatoric stress versus axial strain; (e) (f) pseudo excess pore water pressure versus axial strain; (g) (h) effective mean stress versus axial strain; (i) (j) the mobilized friction angle versus axial strain.

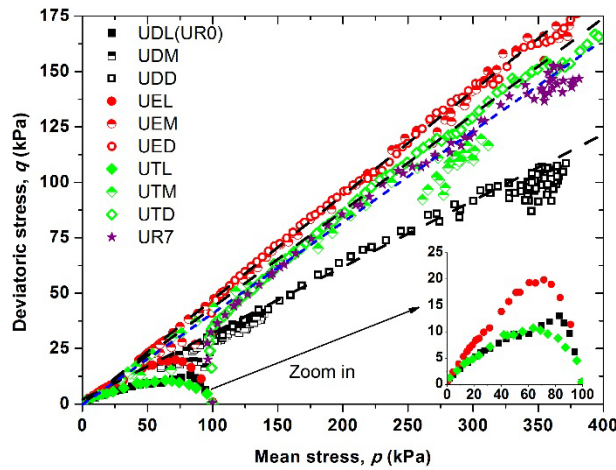
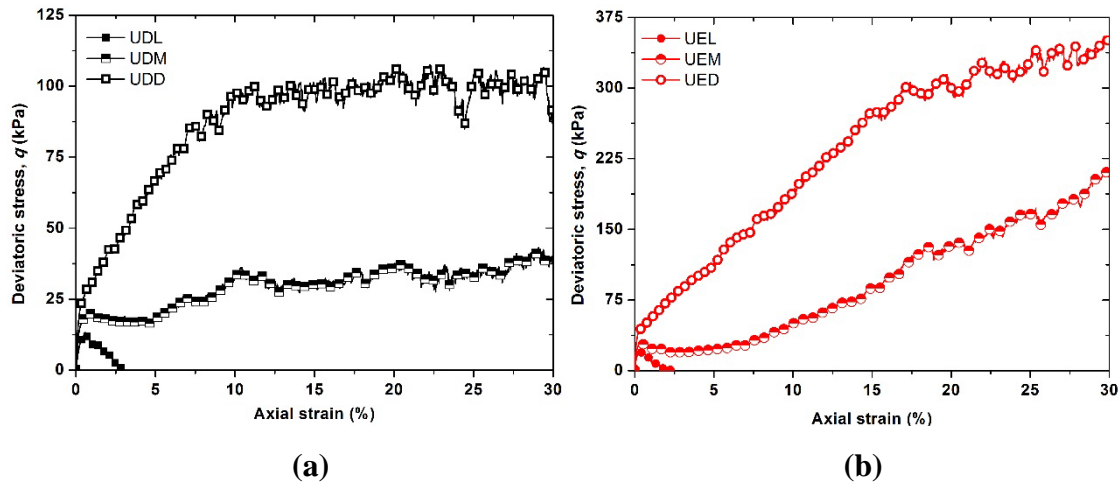
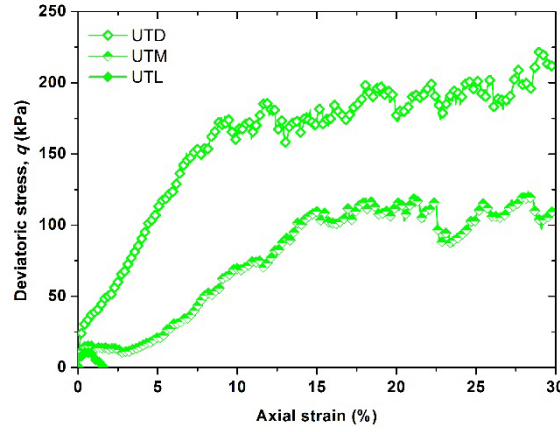


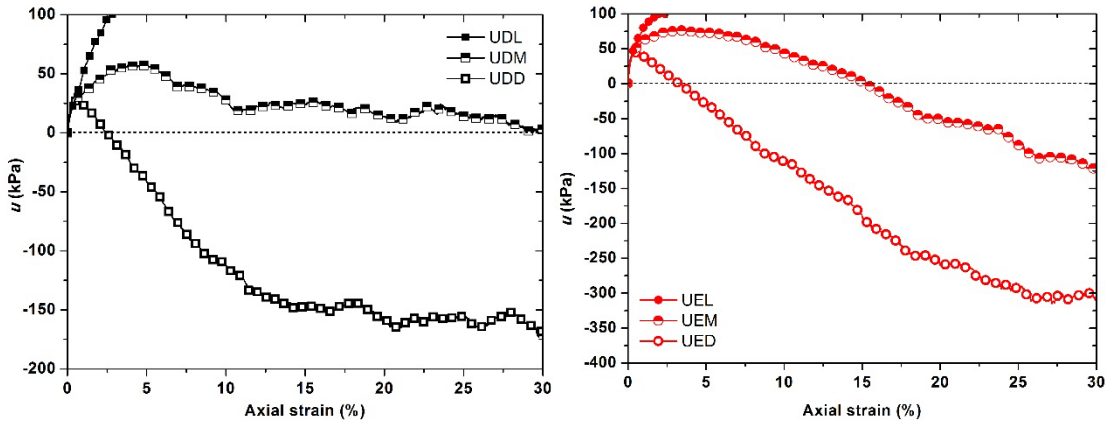
Figure 5.6: Evaluation of stress paths for the granular assemblies with various initial densities and shapes.





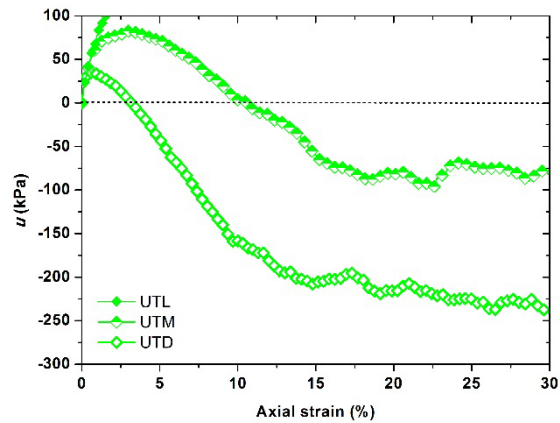
(c)

Figure 5.7: Evolution of deviatoric stress with different initial densities: (a) Disk; (b) Elongate; (c) Triangular.



(a)

(b)



(c)

Figure 5.8: Evolution of pseudo excess pore water pressure with different initial densities: (a) Circle; (b) Elongate; (c) Triangular.

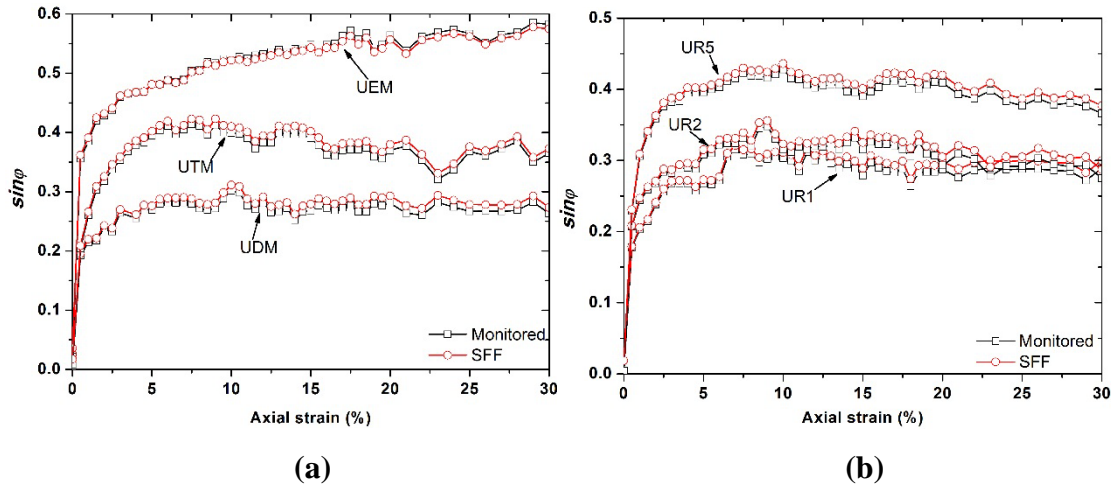


Figure 5.9: Illustration of the SFF relationship in Eq. (2.59) with the collected DEM data: (a) the medium packing for the three shapes; (b) two rolling resistance samples.

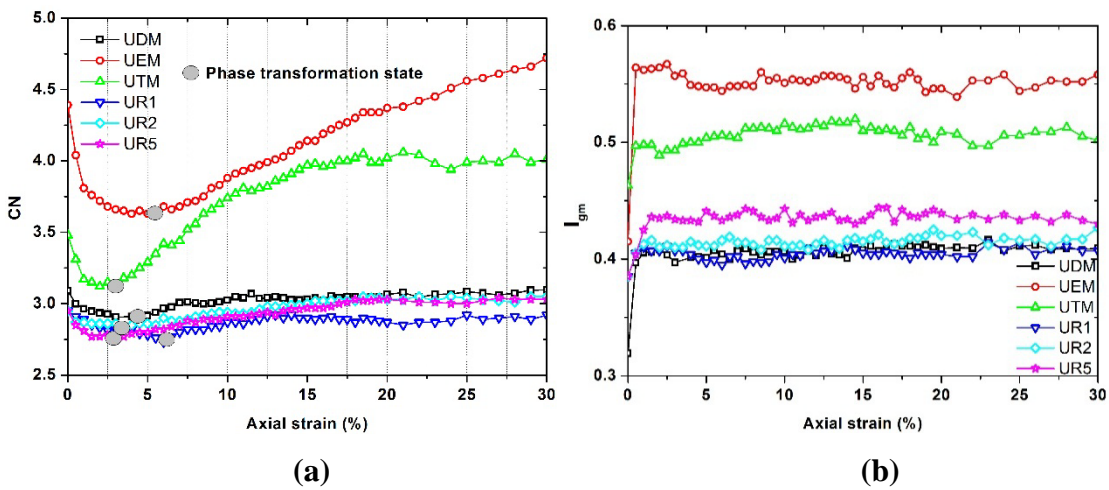


Figure 5.10: Evolution of average coordination number and mobilization index.

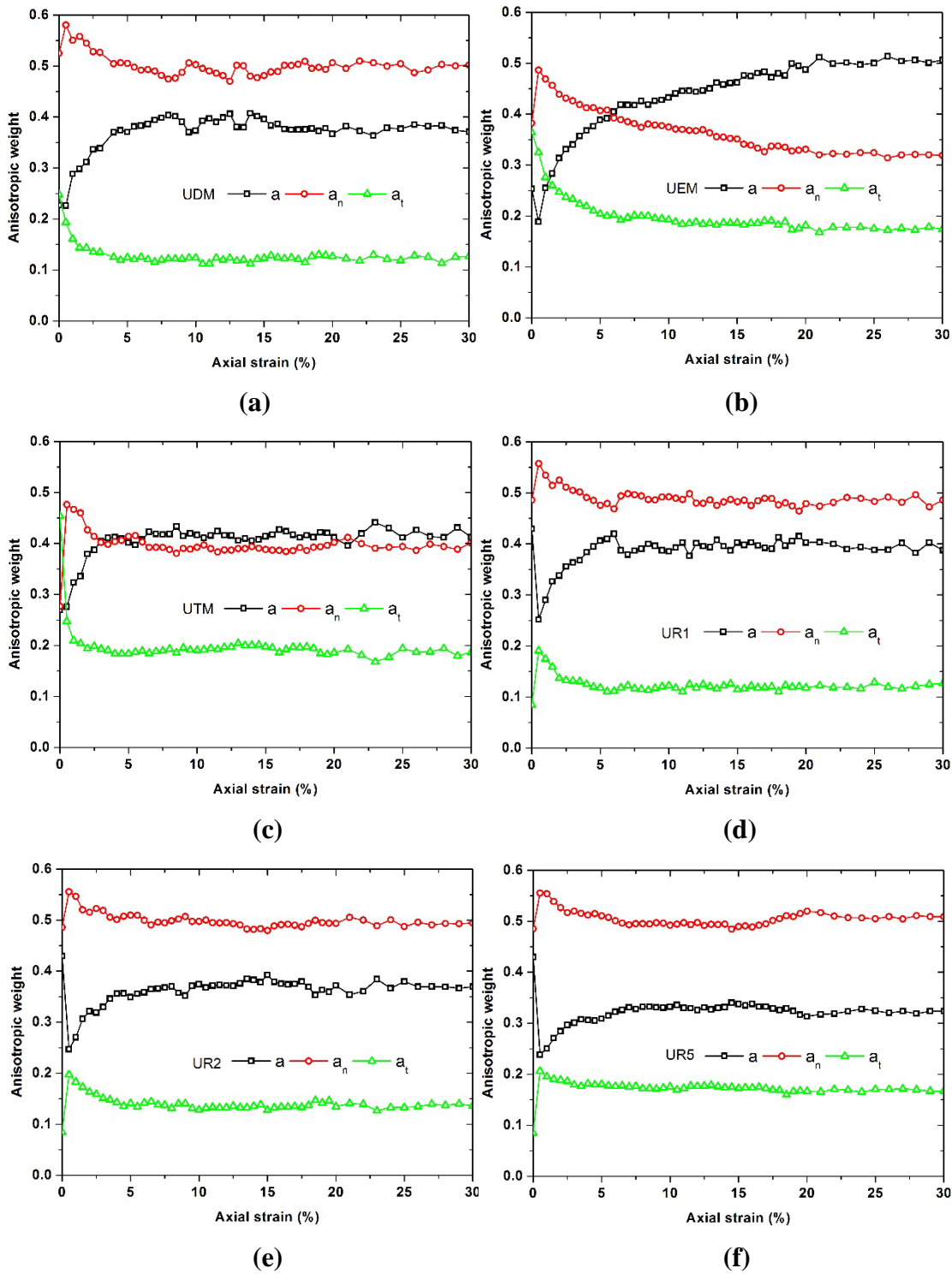
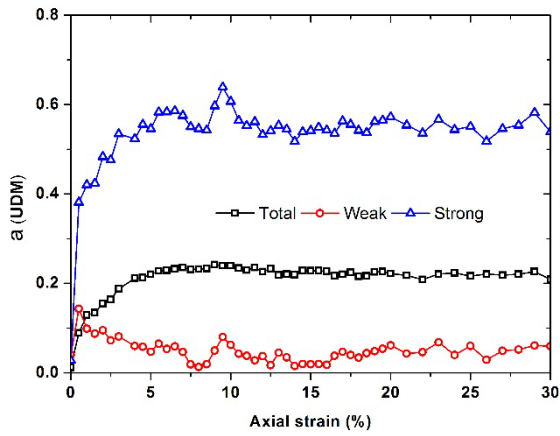
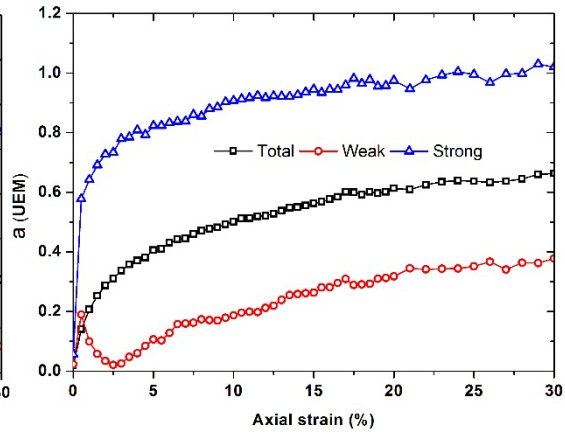


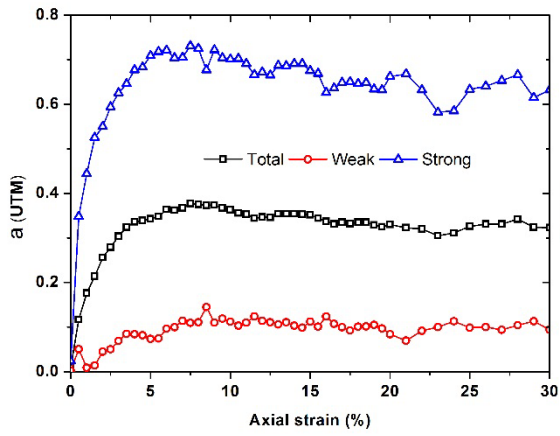
Figure 5.11: Contributing percentages of the three anisotropic coefficients to the undrained shear strength of samples.



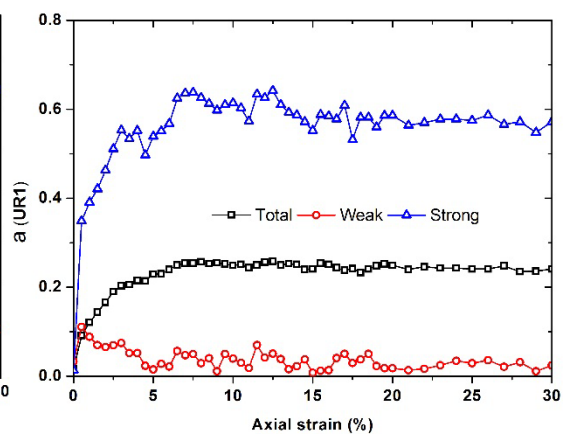
(a)



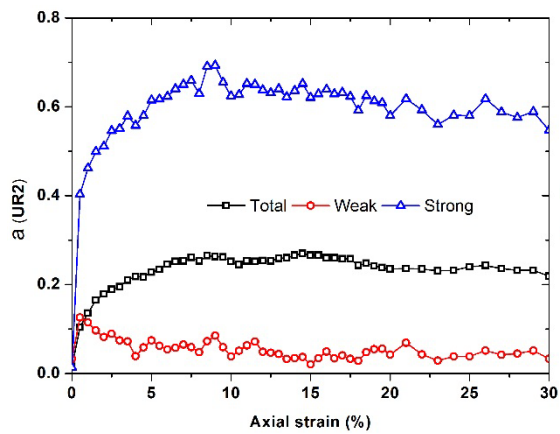
(b)



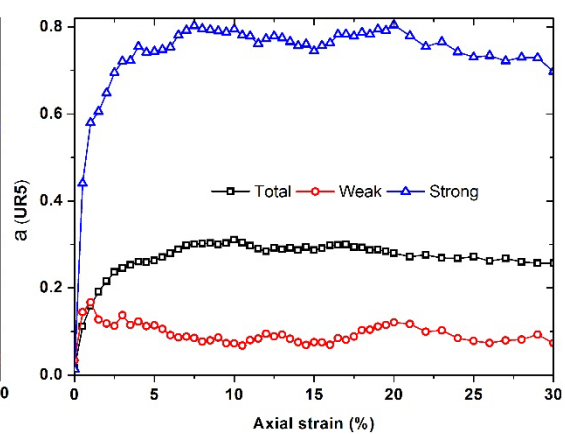
(c)



(d)

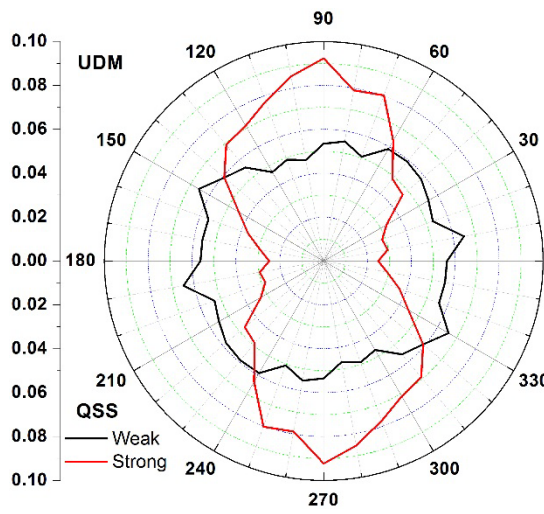


(e)

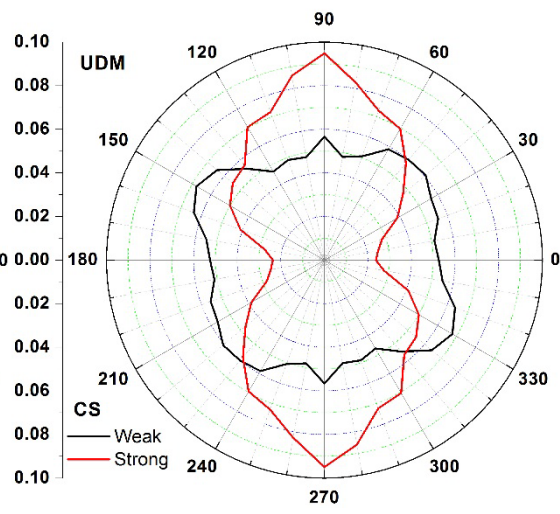


(f)

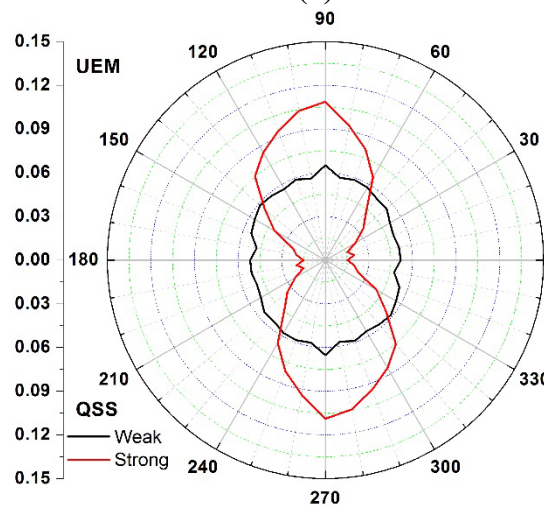
Figure 5.12: Evolution of the anisotropic coefficient of contact normal a .



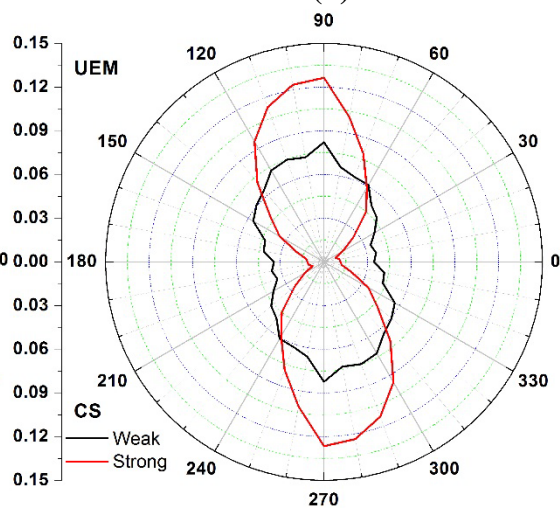
(a)



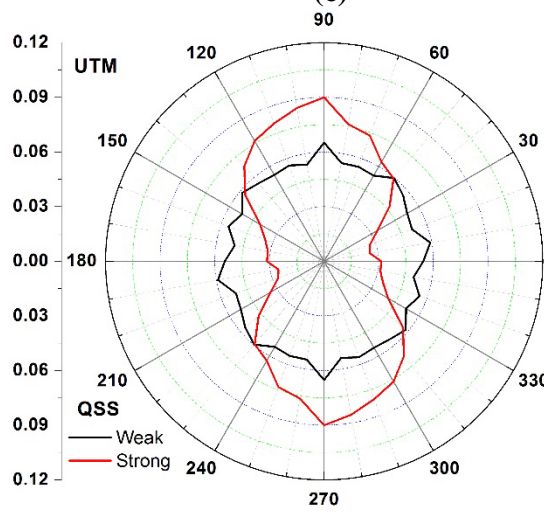
(b)



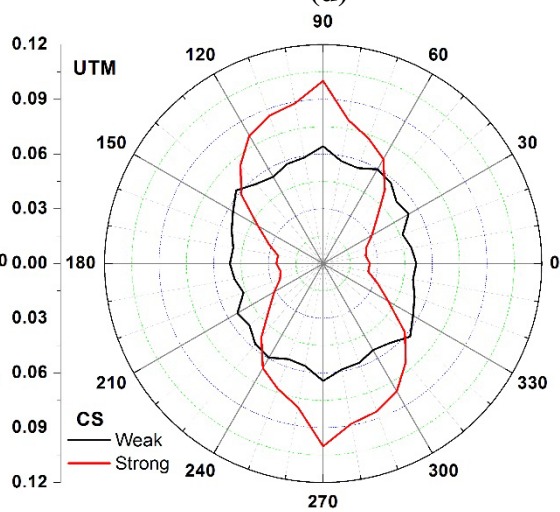
(c)



(d)



(e)



(f)

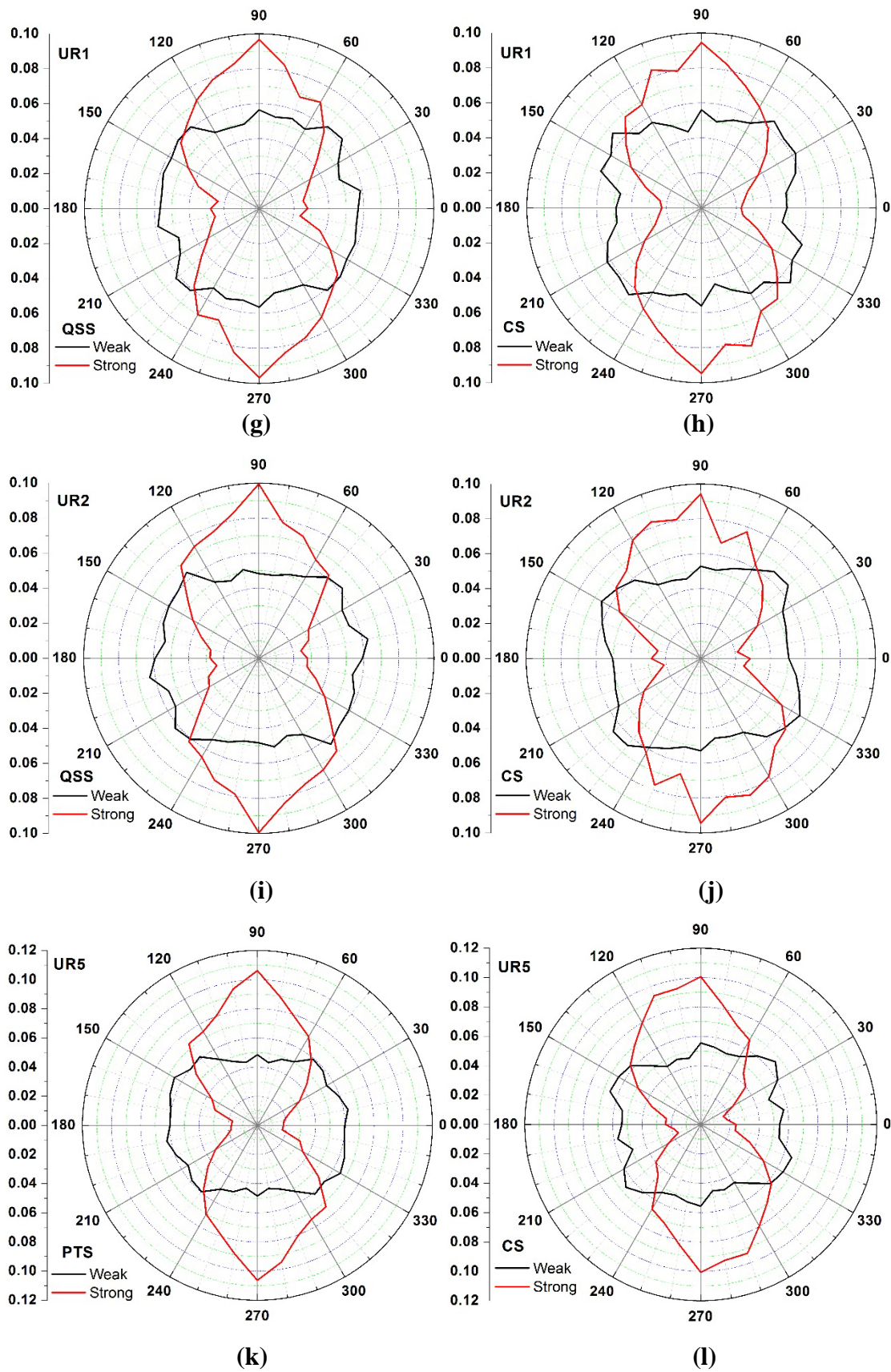
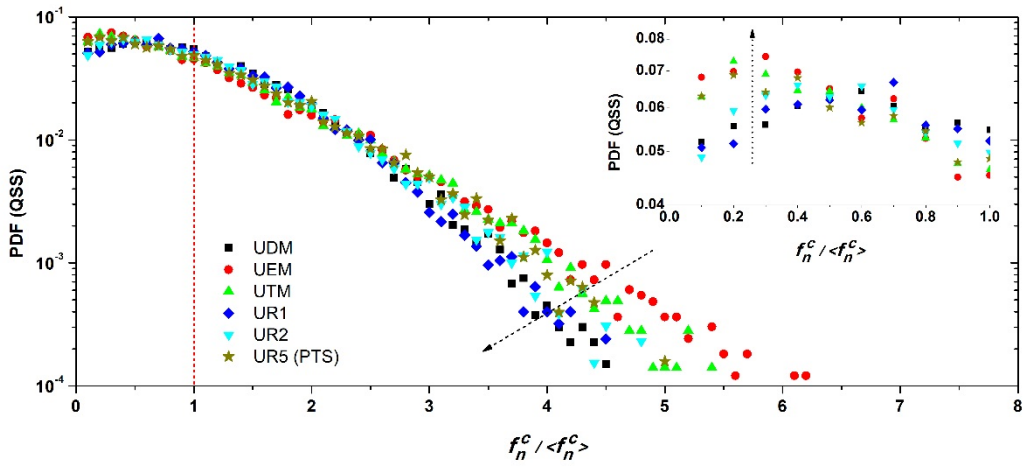
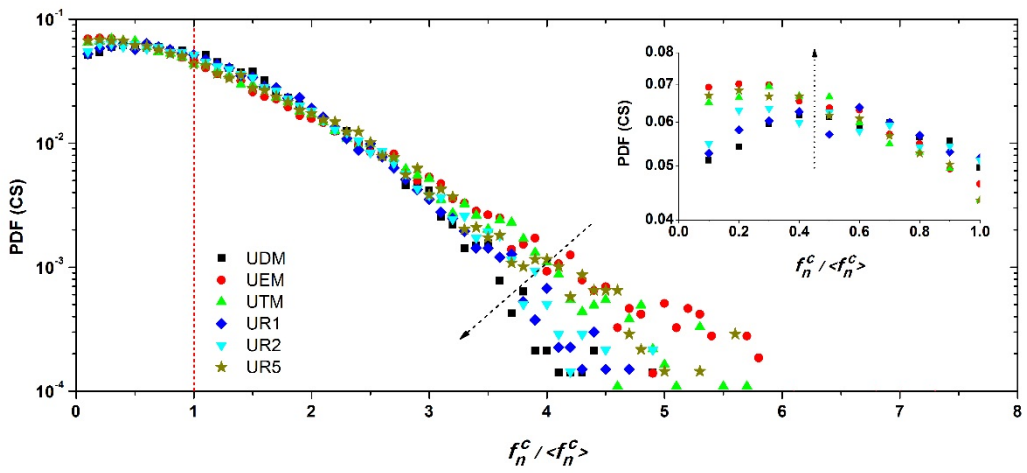


Figure 5.13: Polar distribution of contact normal at quasi-steady state and critical state for the five samples.

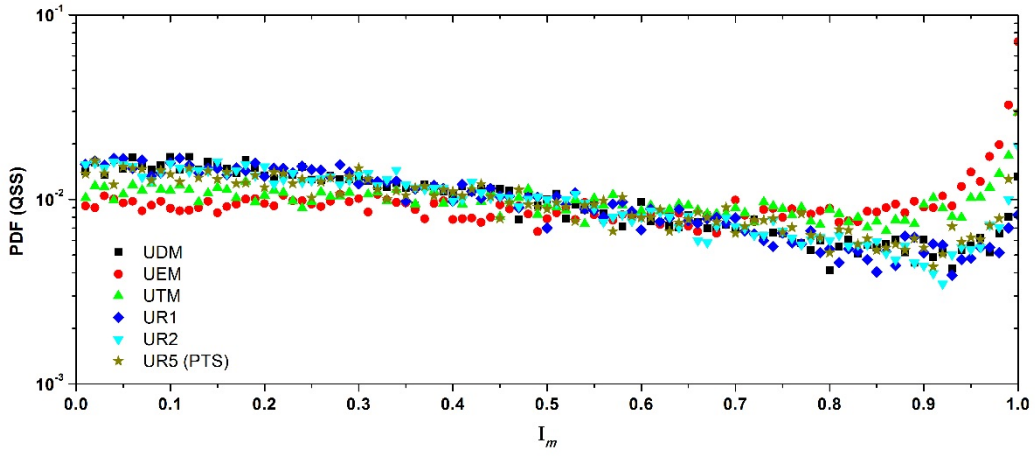


(a)

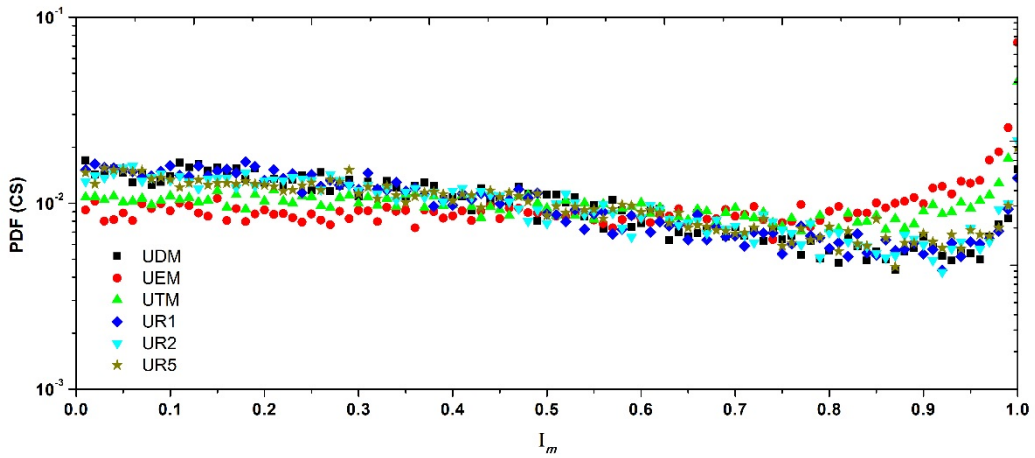


(b)

Figure 5.14: Probability distribution of normalized contact normal force at the quasi-steady state and the critical state (30%) for the six samples.

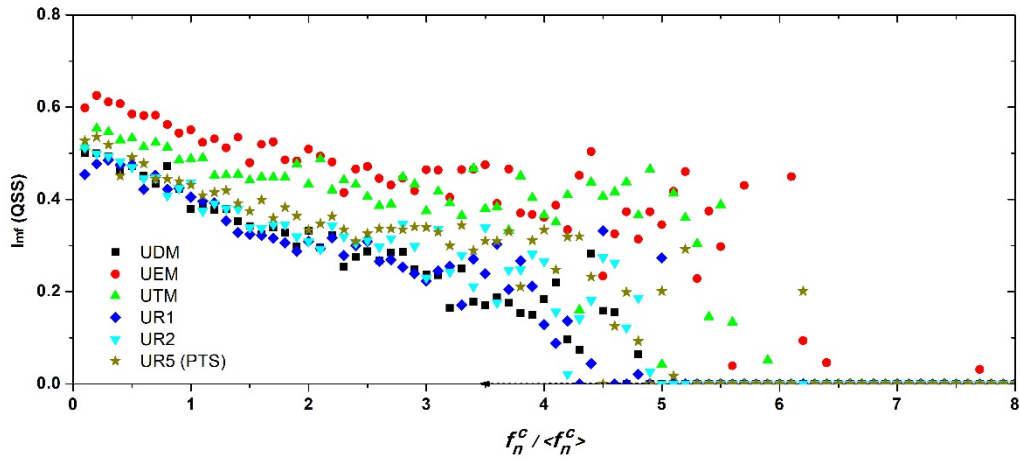


(a)

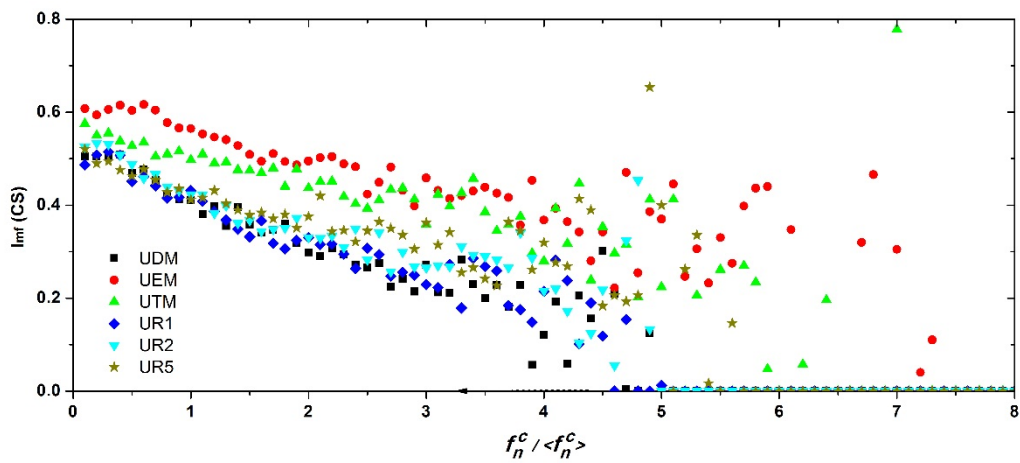


(b)

Figure 5.15: Probability distribution of the friction mobilization index I_m at the quasi-steady state and the critical state (30%).

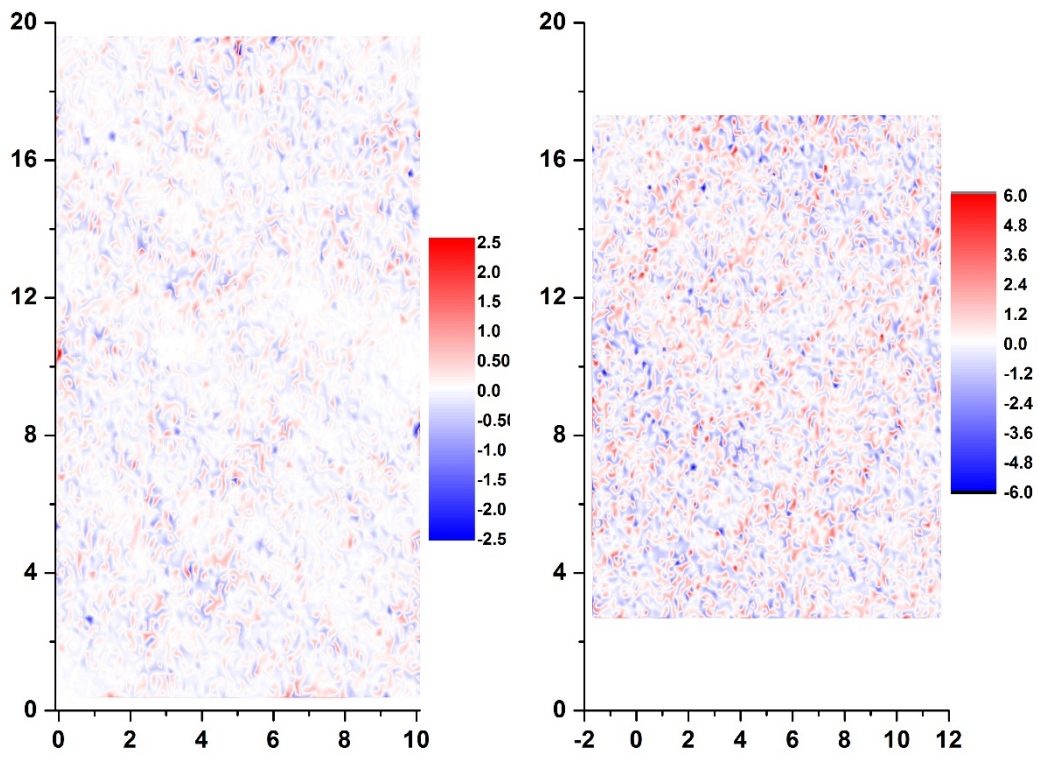


(a)

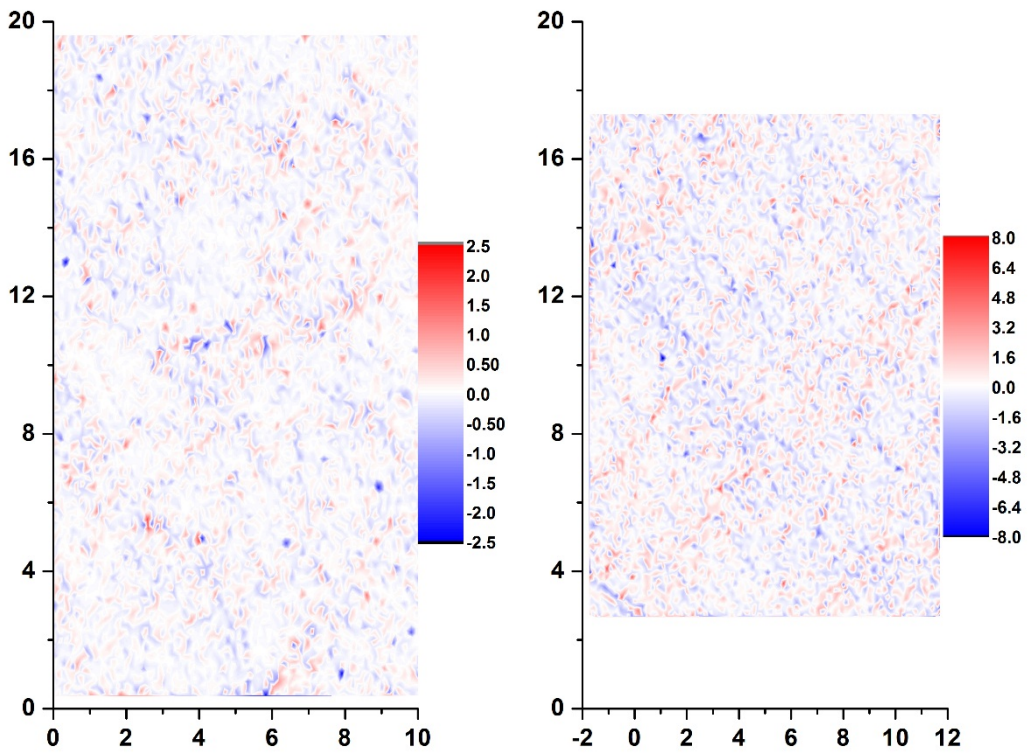


(b)

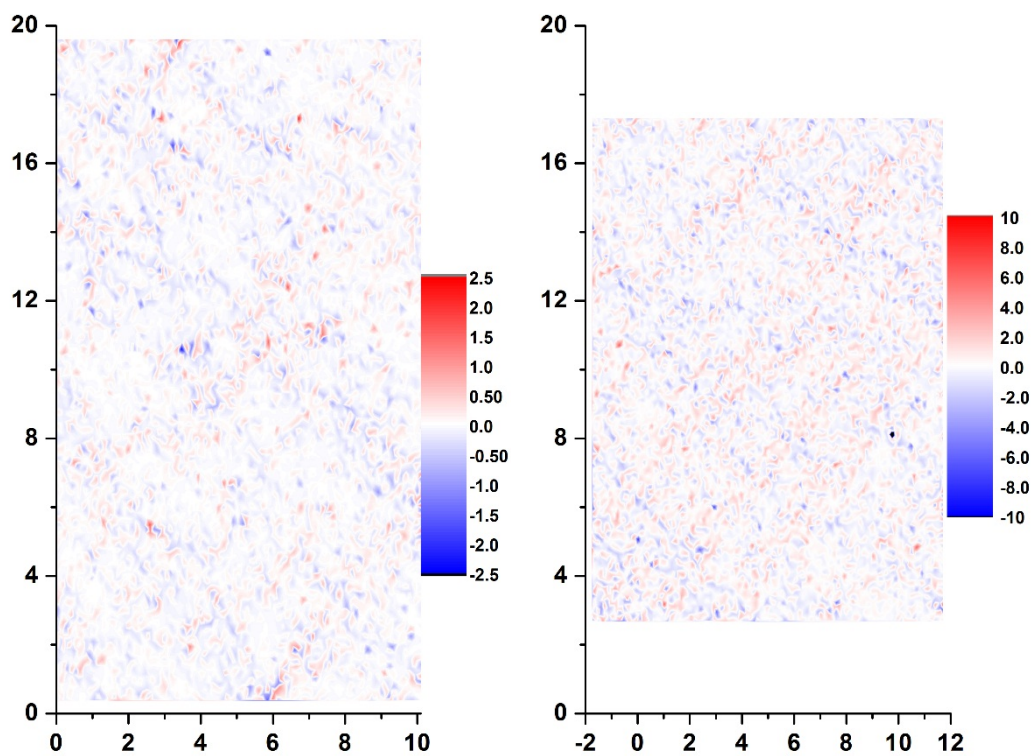
Figure 5.16: Average friction mobilization I_{mf} with the associated normalised contact normal force at the quasi-steady state (UR5 PTS) and the critical state (30%).



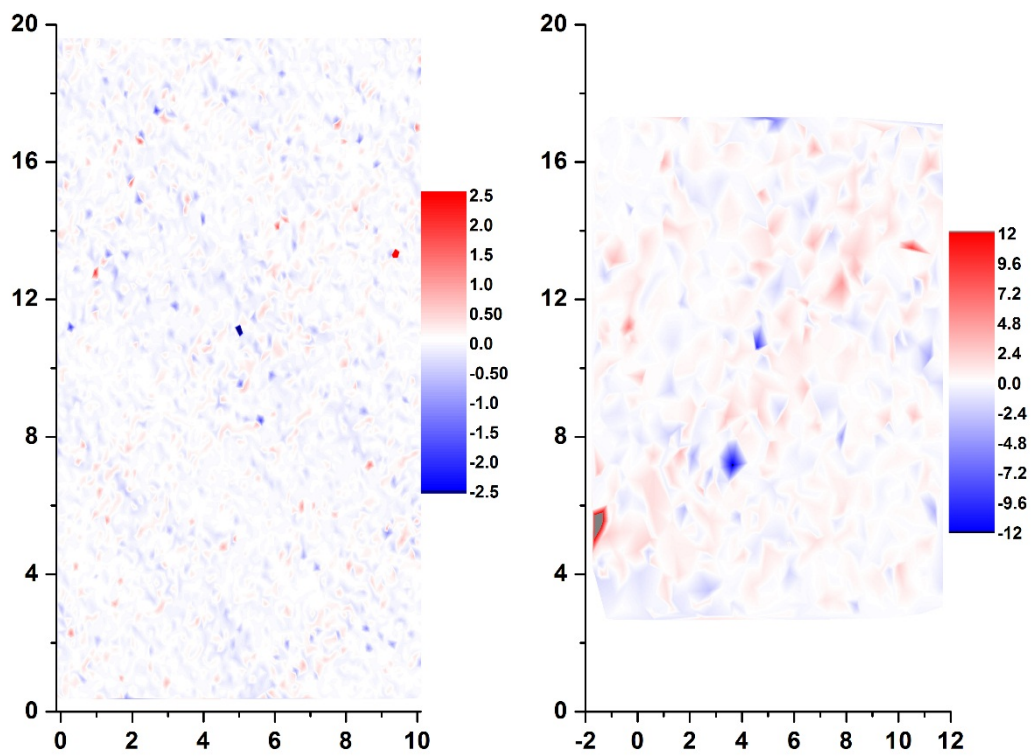
(a) Left QSS and right 30% axial strain of UDM



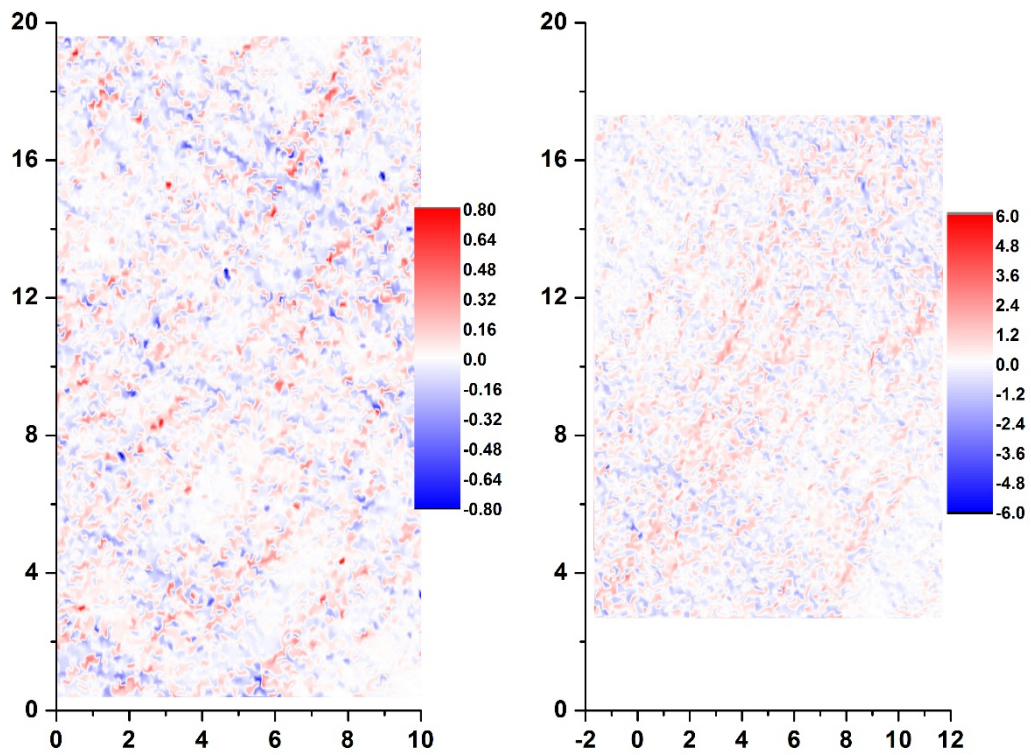
(b) Left QSS and right 30% axial strain of UR1



(c) Left QSS and right 30% axial strain of UR2



(d) Left 3% and right 30% axial strain of UR5



(e) Left QSS and right 30% axial strain of UEM

Figure 5.17: Spatial distribution of accumulated rotation for rolling resistance samples and irregular assemblages.

CHAPTER 6

A fractal model of contact force distribution and the unified coordination distribution for crushable granular materials under confined compression

6.1 Introduction

Particles in the granular system transfers force via the inter-particle contacts to resist external stresses; hence, the inter-particle force networks have striking features to determine the mechanical properties of the granular mass. However, even a homogeneous granular assemblage under uniform loading shows a complex and heterogenous distribution. These non-uniform force chains and particle spatial distributions have been captured in photoelastic experimental studies (Drescher and De Josselin de Jong, 1972; Liu et al., 1995; Majmudar and Behringer, 2005) through stress-induced birefringence. Hence, the probability density function (PDF) is normally considered to suitably characterize the contact force distribution, and the target is to construct a quantitative physical model for it. Coppersmith et al. (Coppersmith et al., 1996) and Liu et al. (1995) proposed the original “q model” with an exponential decay for the strong forces (greater than the average force) and a power law distribution for the weak forces (less than the average force). Afterwards, experimental studies have observed that similar results are consistent with the q-model (Howell et al., 1999). Using numerical simulated approaches, Radjai et al. (1996) investigated the contact force distribution within a two-dimensional confined packing of circular rigid disks and presented a different physical model. This model also shows that the probability of the contact normal force for the weak force follows a power law, whereas the strong-force distribution exponentially decays. In addition, the power exponent of the weak force can be negative, which is different from the q-model (Mueth et al., 1998). For the three-dimensional spherical granular assemblages, the trend of the contact force distribution has also been captured in many investigations with a similar feature as the two-dimensional condition (Antony, 2000, 2007; Radjai and Wolf, 1998; Richefeu et al., 2009; Thornton, 1997; Thornton and Antony, 1998). These physical models can moderately predict the contact force distribution within

jammed static granular assemblies under statically confined states (Ben-Nun, 2011). However, for highly compressed granular assemblages, many investigations have found that the strong-force decay curve is not similar to the “exponential asymptote” relation. For example, a Gaussian distribution (Makse et al., 2000; Tighe et al., 2010) and a steeper downward relation than the exponential asymptote relation (Corwin et al., 2005; van Eerd et al., 2007) have been reported. Recently, Ben-Nun et al. (2010) considered the particle-crushing effect for the polydispersity brittle granular materials during confined comminution, where the ultimate distribution of contact force decays as a clear log-normal distribution. These studies demonstrate that the contact force distribution in granular media is complex and inconsistent among different studies.

In recent years, some advanced high-resolution 3D X-ray diffraction and micro-tomography techniques have been considered to characterize particulate assemblies (Andò et al., 2012; Jia et al., 2007; Moreno et al., 2010). Some researchers have attempted to represent the inter-particle contact forces through the inter-particle strain fields and spatial contact distributions (Andrade and Avila, 2012; Hall et al., 2011; Hurley et al., 2014). However, it remains difficult to directly obtain the accurate inter-particle contact forces within the granular system, particularly when particle crushing is considered.

As an alternative method, the discrete element method (DEM), which was originally developed by Cundall and Strack (1979), can be used to capture more information about the microscopic behaviors for a crushable granular system. A systematic review of the DEM applications and findings is presented in Chapter 2 and will not be repeated here. The DEM is a more robust tool to capture the contact intensity and visualize the contact network for an individual particle (Antony, 2000, 2007; Azéma and Radjai, 2012; Guo and Zhao, 2013, 2014; Kondic et al., 2012; Minh et al., 2014; Peters et al., 2005; Sun et al., 2010; Thornton, 1997; Thornton and Antony, 1998), particularly when the fracture process is considered (Antony et al., 2008; Ben-Nun et al., 2010b; Moreno et al., 2003; Thornton et al., 2004; Walker et al., 2011). In addition, particle crushing makes a more complicated and heterogeneous contact system than a simple system under loading. For example, the topologies of colored grains and

force networks in Figure 6.1 illustrate the response to effective crushing during confined uniaxial compression in our study using the DEM. Over the past two decades, DEM has been used to investigate crushable particles through two alternative approaches: replacing the breaking particles with new smaller fragments or using a bonded agglomerate, which has been reviewed in Chapter 2. In the current chapter, we directly adopt a model that was systematically presented by Ben-Nun and Einav (2010a). This model follows a physical conservation law to replace the pre-crushed particles with new fragments. They noted that the ultimate fractal dimension was independent of the failure criteria (tensile or shear), initial packing porosity and initial particle size distribution (PSD) using the DEM. Later, they found a new force attractor for the brittle sand during confined comminution (Ben-Nun et al., 2010b). Then, they continued to capture a stable 4-cycle loop during the comminution process through the energy scope (Walker et al., 2011). Although some recent investigations on the contact force networks in crushable granular systems were developed, many development mechanisms of fractal fragments in brittle granular materials remain unknown. Additionally, the characteristics of the fabrics of contact forces during one-dimensional compression test are beyond the scope of this chapter (Antony, 2007; Satake, 1993). This study mainly aims to identify the features of the contact force distribution in detail using a fractal model, which is developed to analyze the normal contact force, shear contact force and total contact force in the granular packing (Itasca, 2005). This fractal model can also be used to explain the development of the fractal size distribution. Another core aim is to find the development of coordination number for each particle during the comminution process. Extensive numerical experiments are performed to model two-dimensional crushable granular assemblages, which are subjected to confined uniaxial compression. It is found that the development of the contact force distribution (including the normal contact force, shear contact force, and total contact force) and coordination distribution are strongly affected by the Weibull modulus, inter-particle frictional coefficient and permitted tensile stress for the initial largest particle. The attractor for the distribution of contact forces gradually emerges when the granular assemblage displays a fractal PSD. Interestingly, the distribution of the coordination numbers within the ultimate fractal granular system has a unique relation that is independent of the above variables. In addition, the size ratio between the initial maximum size and the minimum

crushable size can also affect the contact forces to form a fractal distribution. In the numerical analysis, a suitable size ratio gives an acceptable result with a balance between computing efficiency and accuracy. However, this ratio is essentially an artificial factor, which appears to have no physical meaning in nature but is useful in practical computation.

This chapter is organized as follows. First, we introduce the numerical DEM model for this confined comminution analysis. Then, the evolution of the contact forces and coordination number during the crushing process are described by comparing different conditions. Additionally, detailed discussions on the force intensity, force probability and particle fractal size distributions are presented in this section. Finally, a conclusion about the main findings from this study is provided.

6.2 Investigation scheme

6.2.1 Grain breakage criteria

In the current study, the linear contact model in PFC 2D (Itasca, 2005) is adopted to evaluate the confined comminution tests of granular assemblages. The linear contact model has been considered by many previous researchers to investigate the mechanical feature of a crushable granular system under the confined compression or shear test, which have been discussed in Chapter 2. A previous model that was presented by Ben-Nun and Einav (2010a) is used to analyze the grain crushing in the present study. Using this model, the stress-induced grain crushing can be considered by computing multiple contact forces around each individual particle. For the breakage analysis, we must first capture the average stress tensor σ_{ij} that acts on a given particle, which can be calculated by Eq. (2.13). Meanwhile, the major and minor principal stress can be obtained by Eq. (5.8). Because grain crush is strongly associated with the tensile strength, the modified Brazilian criterion (Ben-Nun and Einav, 2010a; Tsoungui et al., 1999), which is given by the followed in this study:

$$\sigma_t = \frac{(\sigma_1 - 3\sigma_3)}{2} \geq \sigma_{crit} \quad (6.1)$$

where σ_t is the particle's maximum tensile stress and σ_{crit} denotes the tensile stress in failure for the given particle. From Weibull's Survival Probability theory (Weibull, 1951), the

size effect of the particle tensile strength can be described as (McDowell and de Bono, 2013; Nakata et al., 1999):

$$\sigma_{crit} = \left(\frac{d}{d_m}\right)^{-2/m} \sigma_m \quad (6.2)$$

where d is the particle size, m is the Weibull modulus, and σ_m is the tensile stress in failure for the initial biggest particle with size d_m .

6.2.2 DEM simulation details

The particles that split during the crushing process are modelled in the present study in an identical manner to that in Ben and Einav (2010a). In their paper, the modelling method was provided in details; hence, we will only provide the key features of this fragment model. Moreover, the modelling procedure of particle crushing is reviewed in chapter 2. A particle breaks when its stresses exceed the failure criterion (Eq. 6.2). Three inscribed smaller particles will replace the pre-crushed particle. Random rotation and linear expansion are subsequently performed by a rapid numerical step to conserve the mass and ignore artificial overlapping. The numerical samples in this study are initially composed of more than 300 particles with a uniform size distribution, where the largest size d_m is 6 mm and the size ratio between the largest and smallest particles is 2.0. The normal and shear stiffness values of the particles are set to 1×10^9 N/m (per 1 m thickness unit). The normal and shear stiffness values of two lateral fixed walls and two vertical loaded walls are 1×10^{11} N/m. The particle density is set to 2600 kg/m^3 . In addition, the initial particles are randomly filled into a rectangular loading box with known dimensions. Moreover, the initial frictional coefficient is set to zero to achieve a target void ratio of 0.24, where the granular system generation is continued until the unbalance forces diminish to a state with negligible global kinematic energy. After this stage, the internal frictional coefficient is assigned a new value, and the isotropic compression is executed to achieve a jamming transition from the fluid phase to the solid phase. The particle property coefficients in the current work are similar to those in previous investigations (Ben-Nun, 2011; Ben-Nun and Einav, 2010a; Ben-Nun et al., 2010b), which are motivated by the experiments of comminuting brittle granular materials (sand or

fault gouge). Vertical stress monitoring from the loading wall is increased by moving the upper and lower walls inwards with a notably slow velocity of 2.5 mm/s. In addition, the two lateral walls are fixed during the comminution procedure. The loading speed in the current study is less than that in Ben-Nun et al. (2010b), which can much more efficiently prevent non-dissipating dynamic effects. The Weibull coefficient m is set to 2.0, 4.0, and 8.0; the inter-particle frictional coefficient is set as 0.1, 0.5, and 1.0; and the tensile stress σ_m is set to 4.0 MPa, 5.0 MPa and 8.0 MPa. The simulation is continued until the attractors of contact forces and coordination appear. Interesting numerical findings are presented in the next section.

6.3 Numerical findings and discussions

6.3.1 Typical typology

In our crushing numerical tests, we first introduce the appearance of the self-organization of the particle arrangement and force chain networks in the fractal crushable conglomeration (Figure 6.1). Because the samples are continuously compressed and the vertical stress increases, the particles in the confined system rearrange and break. This process sometime induces a self-similar pattern in granular packing. Some researchers have investigated this phenomenon and have shown that the topology of particle size and force chain networks has a fractal feature at the ultimate state of the DEM comminution process (Ben-Nun et al., 2010b; Walker et al., 2011). In this section, we first assume a Weibull coefficient of $m = 4.0$ and frictional coefficient of 0.5; σ_m is set to 5.0 MPa; and the minimum broken size is assumed to be 0.2 mm. These parameters form the basis for the benchmark numerical sample. Sensitivity tests are shown in the later parts of this chapter.

The PSD and probability density of normalized normal contact forces for the simulation results are shown in Figure 6.2. The fractal dimension of PSD can be determined based on the number and particle size, which is presented by Turcotte (Turcotte, 1986) as: $N(D > d) = kd^{-D_F}$, where N is the grain number, k is a normalization constant, and D_F is the fractal dimension. Interestingly, the ultimate power law for the broken parts is significantly higher than the entire packing (Figures. 6.2 (a) and (b)). The broken parts only consider the failure

particles and their fragments. However, experimental tests are notably difficult to capture the information for broken particles, which cannot be easily categorized. DEM simulations can obtain all of the internal information of broken particles, even for the individual grain progressing failure. During the comminution process, the normalized contact forces asymptotically achieved the attractor in Figure 6.2(c). Moreover, the comparison between the current numerical simulation at the ultimate state and the physical models of the normal contact force distribution is shown in Figures 6.2(d) and (e). Most of the referred physical models are not consistent with the present confined crushing test, particularly for the later part of the results, but the log-normal distribution that was proposed by Ben-Nun et al. (2010b) is notably close to the DEM data. The differences in Figures 6.2(d) and (e) are induced by the initial assumption that exponential or Gaussian distributions (Liu et al., 1995; Makse et al., 2000; Mueth et al., 1998; Radjai et al., 1996; van Eerd et al., 2007) are constructed without considering the crushing effect within the granular assemblies. Hence, they are not suitable to predict the pattern of the normal contact force distribution under crushing, where the granular system strongly depends on the dispersion of particles and low porosity.

6.3.2 Contact force and coordination number distribution

Here, the author develop a simple fractal model to evaluate the normal, shear and total contact forces. This model is calculated as follows using the cumulated contact number (N_c) of contact force with an intensity F^c that is greater than f^c .

$$N_c(F_n^c > f_n^c) = k_1 (f_n^c)^{-D_F} \quad (6.3a)$$

$$N_c(F_s^c > f_s^c) = k_2 (f_s^c)^{-D_F} \quad (6.3b)$$

$$N_c(F_T^c > f_T^c) = k_3 (f_T^c)^{-D_F} \quad (6.3c)$$

where f_n^c is the normal contact force, f_s^c is the shear contact force, and f_T^c is the total contact force.

Figure 6.3 presents the contact force distribution by number on a log-log scale. It is easily found that an asymptotical feature will emerge at the ultimate state of this numerical study.

All three force components show a power-law relation (Eq. 6.3), which hints that these systems are organized in a self-similar pattern. The fractal dimensions for f_n^c , f_s^c and f_T^c are 1.51, 1.50 and 1.51, respectively, which may be useful to explain the development of the fractal PSD. Additionally, the contact force distribution by number during the comminution procedure can be considered to predict the state of the crushing dynamic behavior of the granular assemblage.

The coordination number for each grain is another important quantity to predict the system stability. Figure 6.4 shows the PDF of coordination number in the benchmark sample in log-linear and log-log scales during the crushing process. The attractor of the coordination number distribution (Figure 6.4(a)) also appears at the ultimate state with a similar curve as the ultimate distribution of the normalized contact normal force in Figure 6.2(c). The peak portion of the coordination gradually forms at number 4 with increasing vertical stress. However, the trend of development is opposite to that of the normalized normal contact force. In this comminution procedure, the probability of a coordination number lower than 4 decreases (see the green arrows in Figure 6.4) and the larger coordination probability increases. This result is reasonable because during the continuous compression, larger particles are surrounded by smaller particles, which will generate a stable system to protect the larger particles. The smaller particles will continuously break to bring in new contacts. Additionally, this phenomenon can induce a decrease in the probability of a larger contact force (Figure 6.2(c)) within the entire granular assemblage.

6.3.3 Parameter sensitive study

Repeating the former benchmark numerical sample, we continue to study the size ratio between the initial maximum particle and the smallest permitted crushing particle. Figure 6.5 shows that the crushing limit size can significantly affect the contact force distribution at the ultimate state. A small particle size threshold (0.2 mm), where the size ratio is 30, may induce the crushable assemblage to develop a fractal contact force distributions. Obviously, the lower particle limit (0.05 mm) is more suitable to generate the fractal distribution. However, the numerical computing time will dramatically increase, and the computation time can be

extremely long. For the scope of numerical research, a ratio of 30 is suggested for the numerical analysis to maintain a balance between the computing efficiency and accuracy.

Figure 6.6 shows the sensitivity analysis results of the contact force distribution at the ultimate compression state (vertical stress = 100 MPa) using Eq. (6.3). The effects of the Weibull modulus, inter-particle frictional coefficient and tensile strength of the largest particle are examined and compared. Figure 6.6 shows that the shear contact force (Figure 6.6(b)) is much lower than the normal contact force (Figures 6.6(a) and (c)), but the shear contact force is much more sensitive to these parameters. In Figure 6.6(a), the granular assemblage with a notably small Weibull modulus and inter-particle frictional coefficient or extremely large tensile strength cannot generate a fractal distribution of normal contact force at the ultimate state. These parameters can also affect the ultimate fractal dimension. In general, the crushable particle assemblage under these circumstances cannot form a fractal fragment distribution during one-dimensional compression. Hence, the descriptors of the contact force distribution in Eq. 6.3, which are simplified and effective, can be used to predict the granular packing whether a fractal distribution is achieved.

Figure 6.7 shows the coordination distribution in log-linear and log-log scales at the ultimate state, where the Weibull modulus, inter-particle frictional coefficient and tensile strength of the largest particle are also considered. We observe that granular packing without the fractal distribution of contact forces (Figure 6.6) shows a concussive variation. After the contact force attains a fractal distribution, the coordination distribution will emerge as a unified distribution, which is independent of the fractal dimension of the contact forces or PSD.

Figure 6.8 presents the PSD of the broken particles and visualization of the contact force network at the ultimate state (vertical stress = 100 MPa). It is observed that the large Weibull modulus can only affect the smallest particles to fracture with increasing stress. Additionally, the inter-particle frictional coefficient and tensile strength for the initial largest particle can induce granular packing to generate a wide range, which can affect the final fractal dimension.

Furthermore, the ultimate contact forces network (Figure 6.8), which can also be used to explain the ultimate fractal fragments through the uniaxial compression (Walker et al., 2011), highly depends on the initial parameters. This result is similar to the contact forces by number in Figure 6.6.

6.4 Conclusions

In this study, we investigated the contact forces and coordination number distribution in a crushable granular assemblage. Extensive numerical tests were performed to validate the developed fractal model and analyze the sensitivity of the parameters. When the distribution of normalized contact normal force shows a pronounced log-normal relation at the ultimate state, a power-law fractal pattern of contact forces emerges. The fractal contact force distribution can also be considered to explain the development of PSD, which also has a power law relation. Additionally, the fractal dimension of the broken particles is much higher than the statistical index of global packing. Furthermore, we demonstrated that the size ratio, Weibull modulus, inter-particle frictional coefficient and permitted tensile stress can affect the development of contact forces to attain an asymptotical power law. In this study, the suggested size ratio is 30 for a balance between computation efficiency and accuracy. Notably, a small Weibull modulus and inter-particle frictional coefficient or large permitted tensile stress are unsuitable to generate a fractal pattern of contact forces. The shear contact forces are much more sensitive to these variables from the present study. The current manuscript also shows that the coordination number distribution has an opposite trend from the normalized normal contact force during the comminution procedure. For the fractal PSD granular assemblage, the coordination number distribution is unified, which is independent of the above parameters. The fractal dimensions of the broken particles are directly affected by the inter-particle frictional coefficient and permitted tensile stress.

Figures

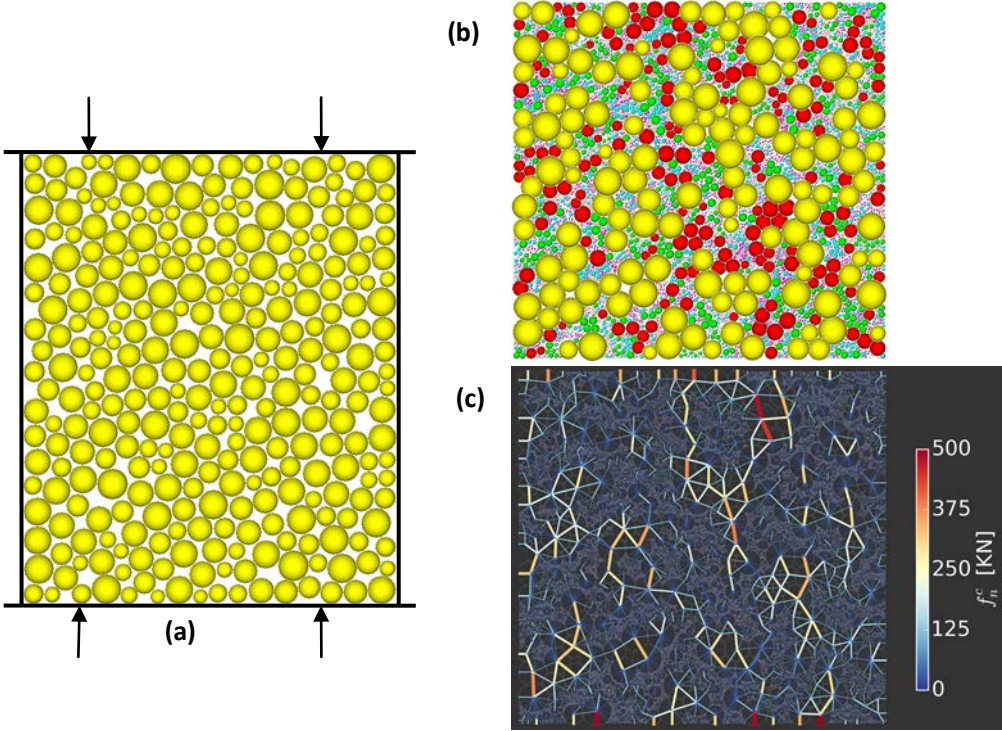
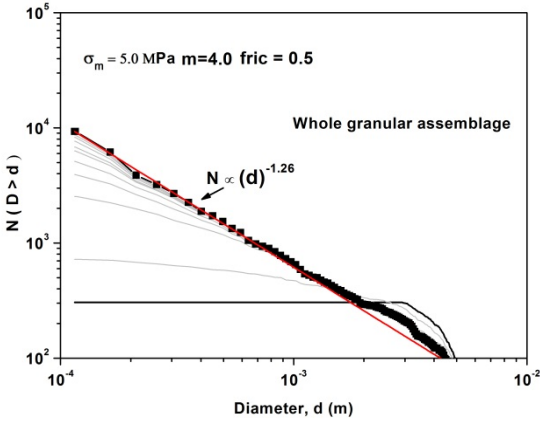
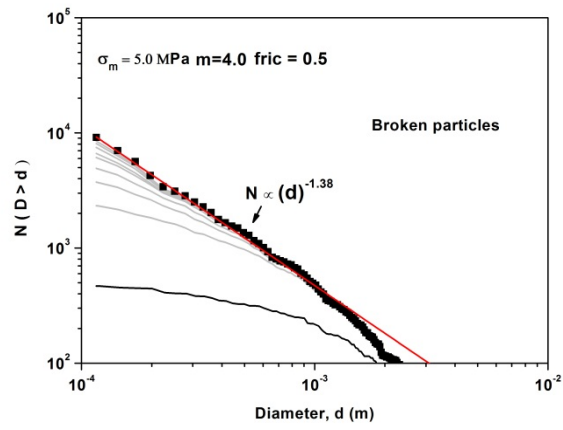


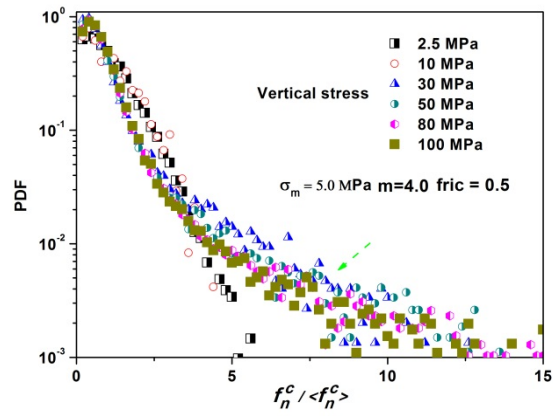
Figure 6.1: Configuration of the crushable granular assemblage (a) initial DEM sample; (b) final grains topology (vertical stress 100 MPa); (c) final contact force network (vertical stress 100 MPa).



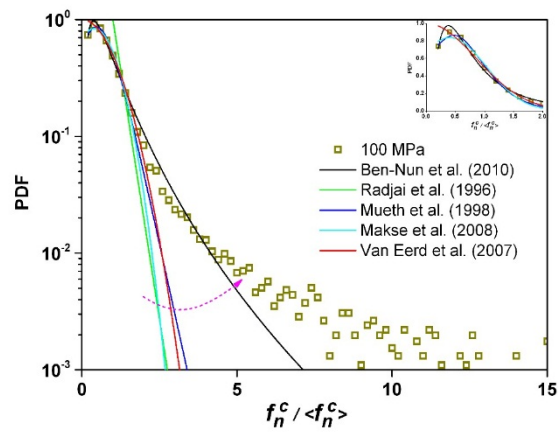
(a)



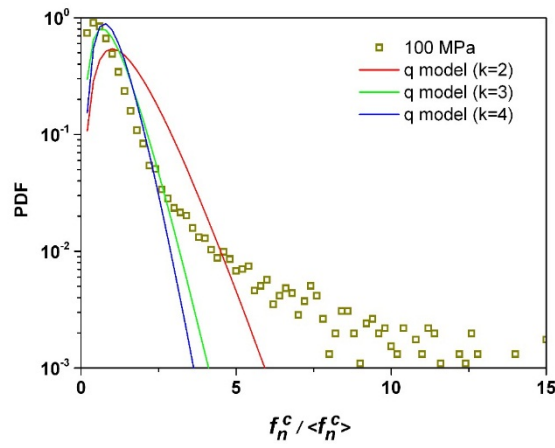
(b)



(c)

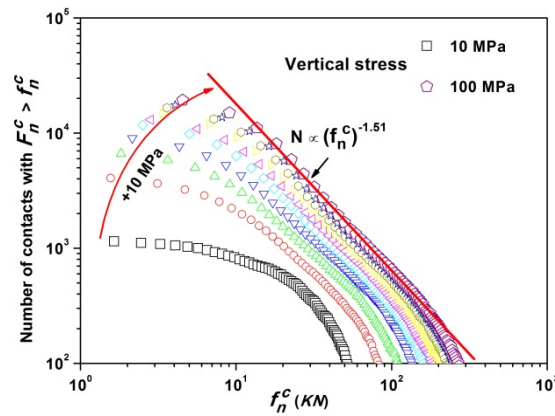


(d)

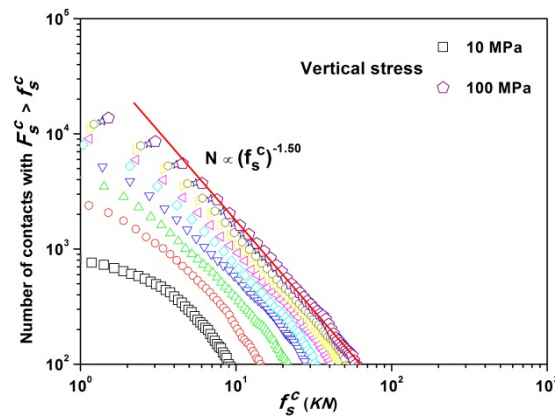


(e)

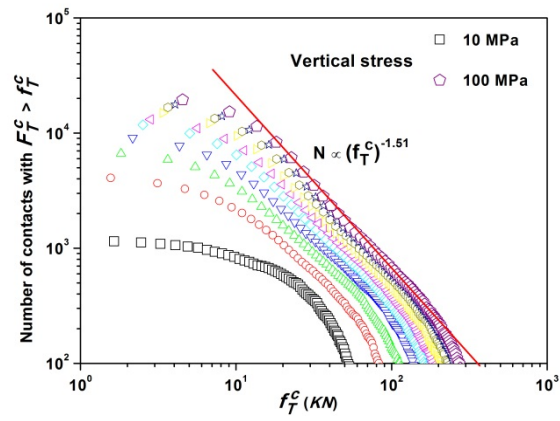
Figure 6.2: (a) Evolution of the PSD in the entire assembly by number; (b) evolution of the PSD within the broken particles by number; (c) probability distribution function of the normalized normal contact force by the average normal contact force in log-linear scale; (d) Comparison of previous physical models with the present crushable DEM simulations at the ultimate state. (e) Comparison with the q model at the ultimate state.



(a)

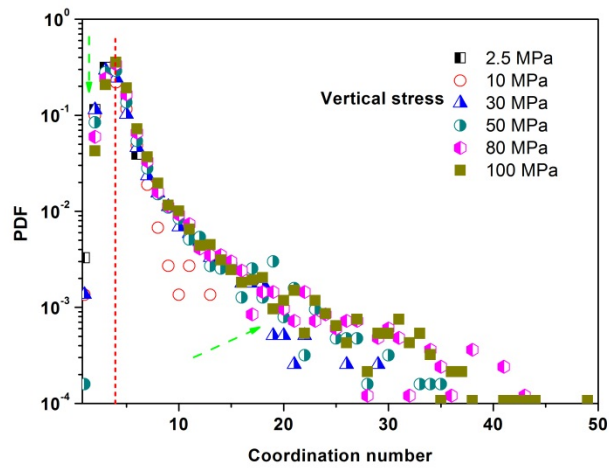


(b)

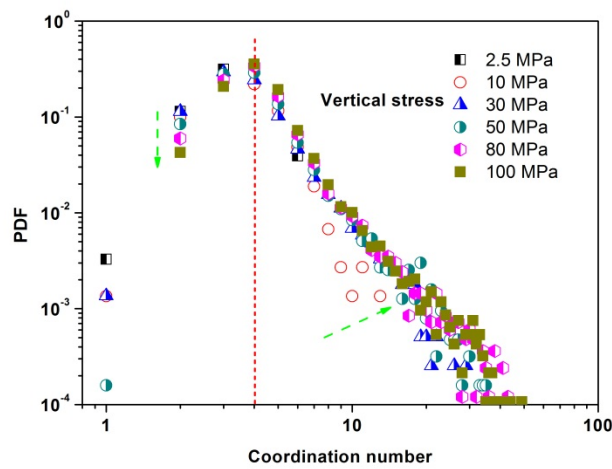


(c)

Figure 6.3: Evolution of the contact force magnitudes: (a) normal contact force by number; (b) shear contact force by number; (c) total contact force by number.

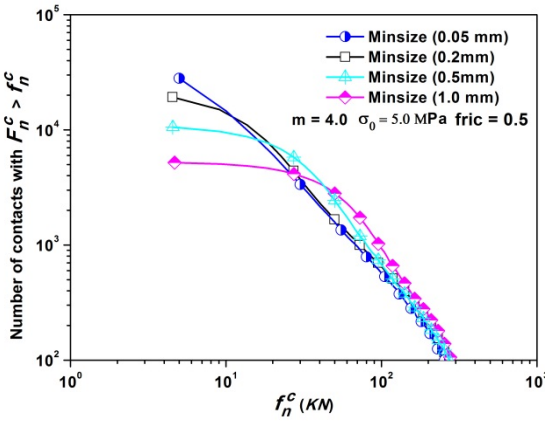


(a)

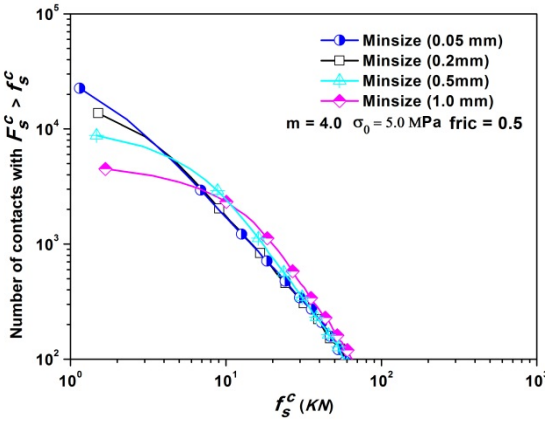


(b)

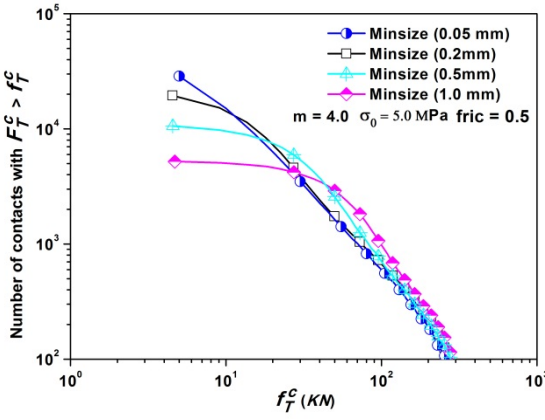
Figure 6.4: Probability distribution function of the coordination number in the (a) log-log scale and (b) log-linear scale.



(a)

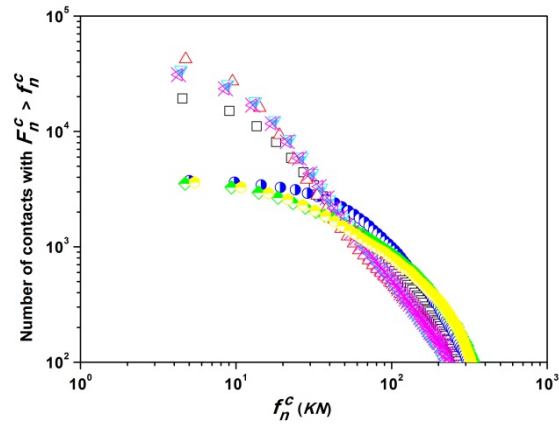


(b)

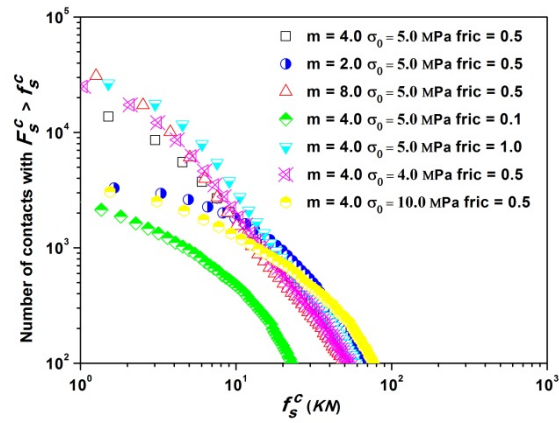


(c)

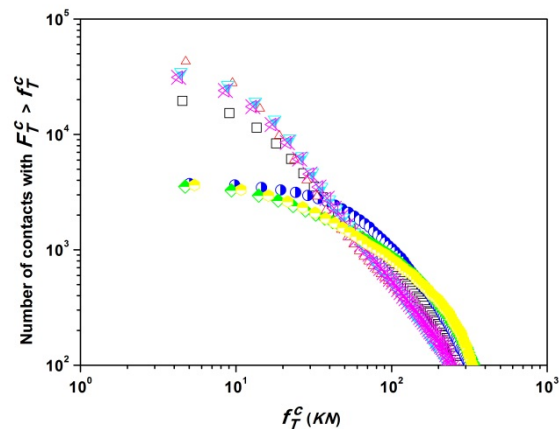
Figure 6.5: Effect of the size of the minimum permitted crushing particle: (a) normal contact force by number; (b) shear contact force by number; (c) total contact force by number.



(a)

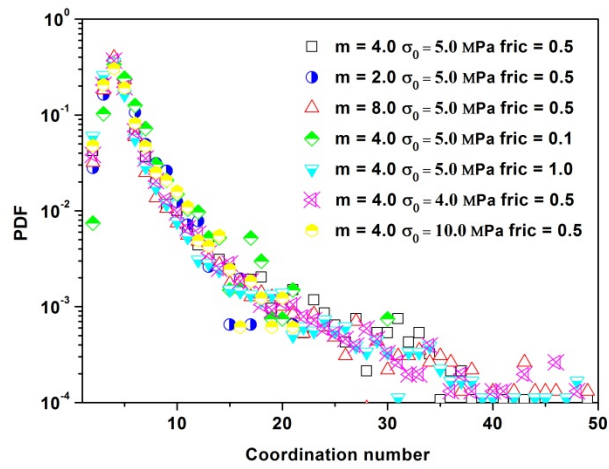


(b)

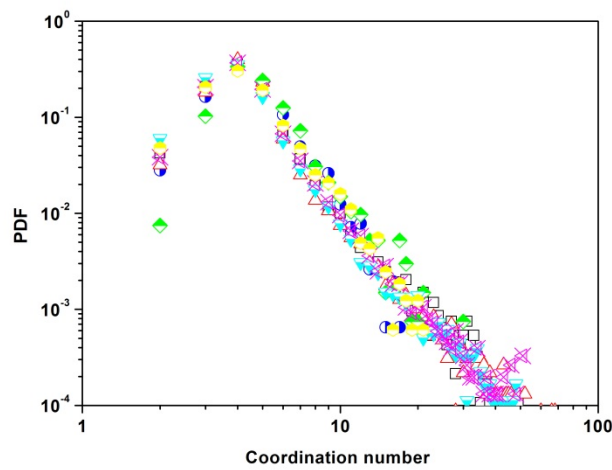


(c)

Figure 6.6: Sensitivity analysis of the Weibull modulus, inter-particle frictional coefficient, and tensile strength of the largest particle for the contact forces: (a) normal contact force by number; (b) shear contact force by number; (c) total contact force by number.



(a)



(b)

Figure 6.7: Sensitivity analysis of the Weibull modulus, inter-particle frictional coefficient, and tensile strength of the largest particle for the PDE of the coordination number in (a) log-log scale and (b) log-linear scale.

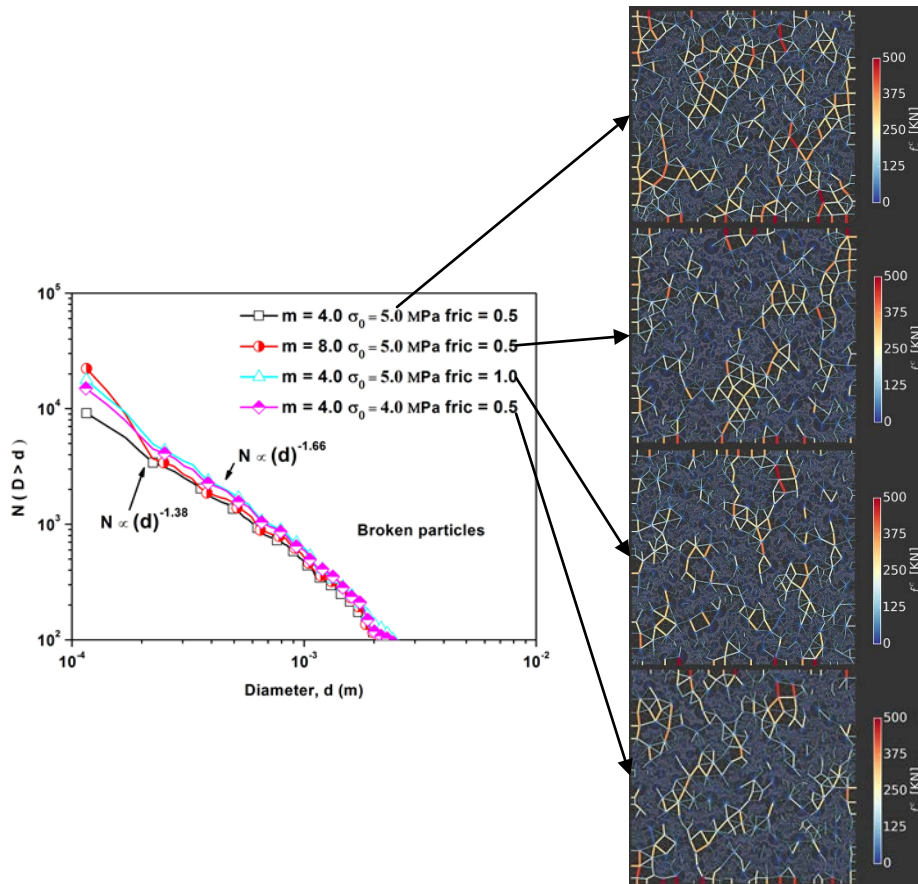


Figure 6.8: Evolution of PSD of the broken particles by number and visualization of the ultimate contact force network (vertical stress 100 MPa).

CHAPTER 7

Different particle size distribution of the crushable granular material within the confined compression throughout the repetitive loading

7.1 Introduction

Particle crushability is a crucial feature for the brittle granular media. It can considerably influence the mechanical properties of soil during loading or deformation (Einav, 2007a, b; Hardin, 1985; Indraratna et al., 2014a). For practical engineering purpose, grain breakage effect can induce variations of many macro indexes such as friction angle, dilation angle and compression slope and others (Coop et al., 2004; Indraratna et al., 2014a; Jiang et al., 2014c; Jiang et al., 2011; Nakata et al., 1999; Nakata et al., 2001a; Uygur and Doven, 2006; Wang and Yan, 2011; Xiao et al., 2014a; Zhao, 2013; Zhao et al., 2012). The particle crushing behavior can be influenced by many factors, and the more crucial factors include the micro contact properties, initial relative density, state of effective stress and effective stress paths (Hardin, 1985). Additionally, many breakage indexes have been developed to quantify the degree of relative crushing (Einav, 2007a; Hardin, 1985; Indraratna et al., 2014a; Russell and Khalili, 2004; Salim and Indraratna, 2004; Varadarajan et al., 2006; Xiao et al., 2014b). However, these constitutive models are suitable only for reproducing the macro responses, and not for the development of internal micro-structural properties. In addition, many experimental investigations are carried out to explore the particle crushing effect through different apparatuses (Coop et al., 2004; Indraratna et al., 2014a; Miao and Airey, 2013; Nakata et al., 2001a; Uygur and Doven, 2006; Xiao et al., 2014a). However, there still exist some conflicts among different investigations, especially for the critical friction angle (Coop et al., 2004; Indraratna et al., 2014a). Moreover, the testing apparatuses can also influence the steady-state properties of sand (Miao and Airey, 2013), hence grain breakage is extremely crucial and complicated within the granular system. There are many uncertain phenomenon associated with the crushing procedure in the granular assemblages, especially for interpreting the micro-structure features. With the developing of computer technology, many numerical

simulations approaches are proposed to evaluate the granular materials such as lattice solid model (LSM) (Mora and Place, 1994) Molecular Dynamic (MD) and DEM, which have been discussed in Chapter 2. These numerical methods are very powerful to visualize the progressing behavior on the micro scale. Moreover, they can capture the internal contact information, which can be used to quantify the granular property and to explore the development of micro structure, even under complicated boundary conditions. Many previous investigations applied DEM to explore the crushing behavior of granular soils under various boundary conditions. However, even for the confined system, the relation between yielding and comminution with the consideration of particle size degradation is still an open challenge (Einav and Valdes, 2008). Recently, Minh and Cheng (2013) used the DEM to explore the relationship between particle size distribution (PSD) and compressibility under the one dimension compression. The PSD in their study is mimicked various power-law distributions. Later, they carried out series of DEM simulations to investigate the force transmission within the binary mixtures (Minh et al., 2014). The particle breakage effect is however not considered in their one dimensional simulations (Minh and Cheng, 2013; Minh et al., 2014). The literatures of particle crushing and related modelling methodologies during one dimensional compression can be found in Chapter 2.

Although many investigations have been performed with respective concentration, the particle size effect within the confined compression system is still not fully understood on the micro structural scale. Hence DEM is also adopted to explore the crushing procedure within the odometer test in this study, with the focuses on the effect of PSDs within the first cycle, which is an intermediate state but not the ultimate steady state. There are two main reasons for choosing the first cycle in this study. One aspect is that the greatest change in PSD appears at the first cycle, and differences are decreasing with the increasing cycles of loading (Miao and Airey). The macro response during the first cycle also has a practical meaning, as the compression curves can also be changed after the first cycle (Uygar and Doven, 2006). The other aspect is for the simplification of the numerical simulations, as considerable amount of computer time is required for the analysis. The approach to model the broken grain in this

study is the adoption of small particles to replace the crushed mother particle when it is beyond the failure criterion (Ben-Nun and Einav, 2010a; Ben-Nun et al., 2010b; De Bono and McDowell, 2014; McDowell and de Bono, 2013). Three initial PSDs, which include the uniform distribution, binary distribution and fractal distribution, are considered to explore the PSD effect in the crushable granular assemblage. Miao and Airey (2013) have performed similar experimental study for capturing the ultimate breakage feature of carbonate sand, but the reloading procedure is ignored. Additionally, only macro investigations are presented to demonstrate the initial grading effect in their investigation. In current study, we will present many micro findings to explore the variations of macro response. For easily understanding of the relationship between coordination and force chains, a new index C_{FC} is presented to interpret the granular structural feature at the micro findings section.

In the following, we first give a brief introduction to the basic information about samples preparations. Then, some macro simulation results are presented during the first cycle loading. Additionally, the micro contact normal force distribution (CNF), stress distribution, coordination number distribution for the individual particle (CNP), force chain visualization, and C_{FC} are explored for the effects of PSDs and loading paths. Finally, the main conclusions of this investigation are presented.

7.2 DEM simulation procedures

Three specified initial gradings, which include a uniform grading, a bimodal grading, and a fractal grading, are selected to perform the simulation tests, where the initial porosity is fixed to 0.18 for the three groups within the mimicked Odemeter tank. The methodology for the grading selection is similar as the experimental study by Miao and Airey (2013). The uniform sample initially composes nearly 300 grains with associated size distribution from 3.0 mm to 6.0 mm (Ben-Nun and Einav, 2010a; Ben-Nun et al., 2010b). The bimodal packing contains more than 1500 grains with the feature of gap graded, where two distributed ranges are random 1.0 mm – 2.0 mm (50%) and 3.0 mm – 6.0 mm (50%). Additionally, the fractal sample with the initial artificial fractal dimension 1.0 includes almost 1000 particles and covers the uniform and bimodal ranges (1.0 mm – 6.0 mm). These gradings are shown in

Figure 6.1. For the sake of simplicity, the normal and shear stiffness of all the grains are set to $1 \times 10^9 \text{N/m}$ with the same inter frictional coefficient (0.5). The confined and loading boundaries are fixed as 100 times of particle stiffness. Particle density is 2600 kg/m^3 . Vertical stress monitoring from the loading wall is increased or decreased by moving the upper and lower walls inwards or outwards with a very slow velocity of 2.5 mm/s throughout the loading, unloading and reloading procedures.

Many of the previous researchers have used DEM to model the crushing process of granular medium through different ways with their respective features, which has been discussed in Chapter 2. Previous model proposed by Ben-Nun and Einav (2010a) is directly applied to determine the grain crushing in the present study. Detailed information on the grain breakage criteria can be seen in Chapter 6. Since the focus of this study is to address the effects of PSDs within the first cyclic loading condition, for the sake of simplification, m is fixed to 4.0 and σ_m is set as 5.0 MPa ($d_m = 6.0 \text{ mm}$).

7.3 Numerical findings and discussions

7.3.1 Macroscopic mechanical responses

The three numerical samples are primarily servo-controlled to achieve the target consolidated state ($\sigma_v = 100 \text{ kPa}$). Then one dimensional compression is applied for the cyclic loading procedure. It can be found that the bimodal and fractal gradings will generate denser initial consolidated packings that are similar to the experimental finding by Miao and Airey (2013) at the initial state. Figure 7.2 (a) and (b) show the compressibility and stress-strain behavior during the cyclic loading procedure. It can be seen that the uniform distribution has a steeper $e\text{-log}\sigma_v$ curve at the initial stage with a larger compression index (C_c). The curves for the three PSDs would merge into a single unique line as the vertical effective stress increases. These findings from Figure 7.2(a) in the loading procedure are similar to the ring shear test of the three PSDs by Miao and Airey (2013). Ben-Nun and Einav (2010a) have obtained analogous results for the crushable samples with different coefficients of uniformity. Another interesting result is that the uniform grading sample shows the largest expansion index (C_e),

which may be induced by the different initial void ratio of the three PSDs. The value of C_e in this study is greater than the traditional granular material by Mitchell and Soga (2005). The higher C_e also hinted that the status after the first cyclic loading in this study is in an intermediate state which is also observed by previous experimental tests (Miao and Airey, 2013; Uygur and Doven, 2006). Another possible reason may be due the restricted plane strain condition (McDowell and de Bono, 2013). However, for the qualitative study in this study, the trend of results is good enough to assess the macro response. It also has an advantage to clearly identify the difference of the three PSDs. Moreover, Uygur and Doven (2006) performed cyclic oedometer tests on crushable sand at high stress levels with different initial relative density and obtained similar variation of C_e as in our numerical tests. The void ratio is reduced as the cycles are progressed (Uygur and Doven, 2006), which is due to the grain degradation. During the reloading procedure, the uniform grading still possess larger C_c than the other two groups. In addition, the merge point for the reloading compression curve stands at the larger vertical effective stress than the initial loading procedure.

It can be seen that uniform grading is more compressible than bimodal grading and fractal grading during the loading and reloading stages in Figure 7.2(b). In addition, the plastic volumetric strain is not sensitive for the gradings, which can be found at the end part of the unloading stage. Moreover, the binary and fractal packings with nearly initial void ratio show the similar compression pattern.

Figure 7.3 (a) and (b) show the variation of the coefficient of lateral pressure K_0 during the cyclic loading procedure. The determination of K_0 from DEM simulations can be get as follow:

$$K_0 = \sigma_h / \sigma_v \quad (7.1)$$

Where the σ_h is the effective horizontal pressure, σ_v is the effective vertical pressure. As the water is not considered in the one dimensional compression test, the above two pressures can be obtained by Eq. (2.85). It is noticeable that the value of K_0 for the three grading is the same, which can also be obtained by the Jaky's equation. At the initial part of the loading

procedure ($\sigma_v < 20$ MPa), the relation of K_0 is a nonlinear curve which is induced by a large number mother particles breakage, hence the system is unstable at this stage. Yamamura and Lade (1996) have obtained similar curve by the high pressure compression test of Cambria sand (stiff property like quartz), but they explained the initial nonlinear curve by the resolution capability of the strain gauges at low pressures. For the unloading and procedure, K_0 gradually increases to nearly 2.0, where the variation gradient is slight different for the three PSDs. It is induced by the locked horizontal stress within the confined boundaries. Similar phenomenon is also found under low vertical stress for the investigation of secondary compression in soil sample by Gao and Wang (Gao and Wang, 2014). For the reloading procedure, K_0 decreases quickly to a stable value which is nearly the same as that for the loading procedure. It is noticed that DEM can handle the compression test of crushable granular media during the cyclic loading procedure. However, the performance of K_0 throughout the numerical test is insensitive to the PSDs. Deeper interpretation on the micro scale would be considered to explore the variation of K_0 in the later part of this study.

Figure 7.4 shows the evaluation of PSDs at the final state of loading and reloading procedures. Intuitively, cyclic loading would enhance the fine contents compared with that for monotonic loading. For the initial uniform and fractal gradings, the PSDs tend toward a fractal distribution in Figure 7.4(a) and (c). However, there exists a pivot or knee point for the bimodal group in Figure 7.4 (b), which has also been obtained by Zhang and Baudet (Zhang and Baudet, 2013) through one dimensional compression tests to a very high stress level. This suggests that the initial PSD can influence the PSD development during the first cyclic loading.

7.3.2 Microscopic findings

The growth of the crushing mass ratio, which is determined by the ratio between the mass of broken mother particles and global mass during the loading and reloading processes for the three gradings are shown in Figure 7.5. The uniform graded packing with a larger initial void ratio (Figure 7.2 (a)) shows the higher crushing mass ratio than the other two categories. This

micro statistical information can also be used to explain the stress-strain curves in Figure 7.2 (b). It is noticeable that the more compressible behavior is associated with the breakage amplitude. Additionally, the breakage processes of the mother grains mainly appear at low stress level, which would influence the variation of K_0 in Figure 7.3. Moreover, the feature of packing and force chain distributions in Figure 7.5 shows that the big particles in the binary packing and fractal packing have massive neighbor small particles, which would hinder the development of particle crushing. Hence the micro structure feature for the three PSDs can induce the macro responses in Figure 7.2.

The fractal dimension of PSD can be determined by the number and particle size, which is proposed by Turcotte (1986) The relationship can be expressed as $N(D > d) = kd^{-D_F}$, where N is grain number; k is a normalization constant; and D_F is the fractal dimension. Figure 7.6 shows that the uniform graded and fractal graded samples exhibit linear distributions on the double logarithmic axes at the ultimate state in loading and reloading stages, where the fractal dimension is larger for the uniform graded assemblage. The bimodal packing in Figure 7.6(b) shows a knee point while the PSD relationship in Figure 7.4(b) behaves in a different manner. This result is different with the cumulative number distribution of gap graded soil by Zhang and Baudet (2013). This micro statistical information reviews that the initial grading can influence the ultimate distribution and fractal dimension throughout the first cyclic loading.

During the comminution procedure, the distribution of normalized contact normal force (CNF) shift from a decay power law with a steeper end (Radjai et al., 1996; Tighe et al., 2010) to a clear log normal distribution (Ben-Nun et al., 2010b) in Figure 7.7(a), (b) and (c). The distribution of CNF for the uniform graded sample in Figure 7.7 can be reconsidered to explain the variation of K_0 (Gao and Wang, 2014). Additionally, the cyclic loading would induce the distribution of CNF tends toward exponential at the end again in Figure 7.7(b), (c) and (d). This is resulted by the development of crushing under the reloading stage which turns toward a weaken level. It can also be found that the knee points in Figure 7.7(d) can matched

with the development of PSD in Figure 7.4(b) and Figure 7.6 (b). Moreover, the range of normalized contact normal force in the bimodal packing is much narrower than other gradings. From Figure 7.7(e), the differences of the strong force chains induced different K_0 during the unloading procedure. Additionally, the pattern of CNF for the three graded sample in Figure 7.7(f) is similar in the reloading stage. It hints that K_0 is not sensitive to the PSDs in Fig. 3 during loading and reloading procedures. It is also suggested that the micro CNF in the different packing can indirectly influence the evaluation of PSD. Figure 7.7(g) describes the locking effect of horizontal stress during the unloading procedure, which has resulted in higher K_0 .

Figure 7.8 demonstrates the coordination distribution of individual particle (CNP), which can be considered to evaluate the structure feature of granular media throughout the cyclic loading procedure. It can be found that CNP is only influenced by the loading paths in the low stress level (Figure 7.8 (a), (b) and (c)). The CNP is partially related to CNF in Figure 7.7 (a), (b) and Figure 7.8 (a), (b). The results suggest that the geometry topology and force topology is not always fully related. That is to say, CNP is less sensitive than CNF when the crushing mass ratio towards to stable level in Figure 7.5. In addition, CNP is also insensitive to the PSDs beyond the loading procedure upon a certain stress level.

A new index C_{FC} is proposed by the author to interpret the relationship between the force chains and the composed particles. C_{FC} can be determined as follow:

$$C_{FC} = \frac{\sum_{i=1}^{N_{fc}} (N_1 + N_2)_i}{2N_{fc}} \quad (7.2)$$

where N_1 and N_2 are the coordination number of the two composed elements for each force chain; N_{fc} is the number of force chain in the related interval of the normalized contact normal force $f_n^c / \langle f_n^c \rangle$.

Figure 7.9 shows the variation of C_{FC} throughout the loading procedure for the three PSDs. It can be seen that C_{FC} is gradually increased with the increasing stress from loading to reloading for the whole CNF. This can effectively explain the macro curves of void ratio and strain with the related stress in Figure 7.2 (b) and (c). C_{FC} has the largest value in the unloading stage for the same stress state. Below the medium force chain, C_{FC} is much greater in the loading procedure, particularly for the weak force zone. Additionally, its value is decreased with the increasing intensity of force chain. However, this trend will turn to a stable value after the reloading stage. It can be found that C_{FC} for the bimodal packing in the unloading stage shows an obviously declined trend within the medium force regions, and inversely increased within the strong force regions in Figure 7.9 (b), (e) and (h). Although the macro curves for the bimodal and fractal packings are almost the same, the stable range of C_{FC} at the end of the reloading stage is larger than the initial fractal grade.

7.4 Conclusions

The current investigation has considered the DEM to simulate one dimensional compression test for the crushable granular media, particularly for exploring the PSD effect during the first cyclic loading. The stress governed the grain fracture, and the replacing mother particle with small particles can effectively and qualitatively evaluate the macro responses of one dimensional comminution tests. The initial compressibility and expansibility can be influenced by the initial PSD. Additionally, the evaluation of PSD at the intermediate state is mainly governed by the initial grade. However, the variations of K_0 are insensitive to the PSDs. Many interesting post-processing results have been investigated to explore the macro responses. In addition to particle space arrangement, the particle crushing mass ratio can directly influence the compressibility of the packing. The knee points would emerge for the bimodal assemblage at the end of the intermediate crushing state, where the mass and number cumulated results are unified. The variation of CNF and its visualized graphs can be considered

to explain the variation of K_0 . The pattern of CNF throughout the loading procedure would shift with a deeper end. Moreover, CNP is found to be not sensitive to the initial PSDs. Furthermore, the proposed index C_{FC} can be considered to explore the structural feature of the granular media by combining the geometrical topology and force chain. It can be found that C_{FC} is gradually increased with the increasing stress. However, the value at the reloading stage is the lowest within the medium force zone. These curves are reasonable for the repetitive compression test. Hence, the C_{FC} is suggested to be considered for the related investigations.

Figures

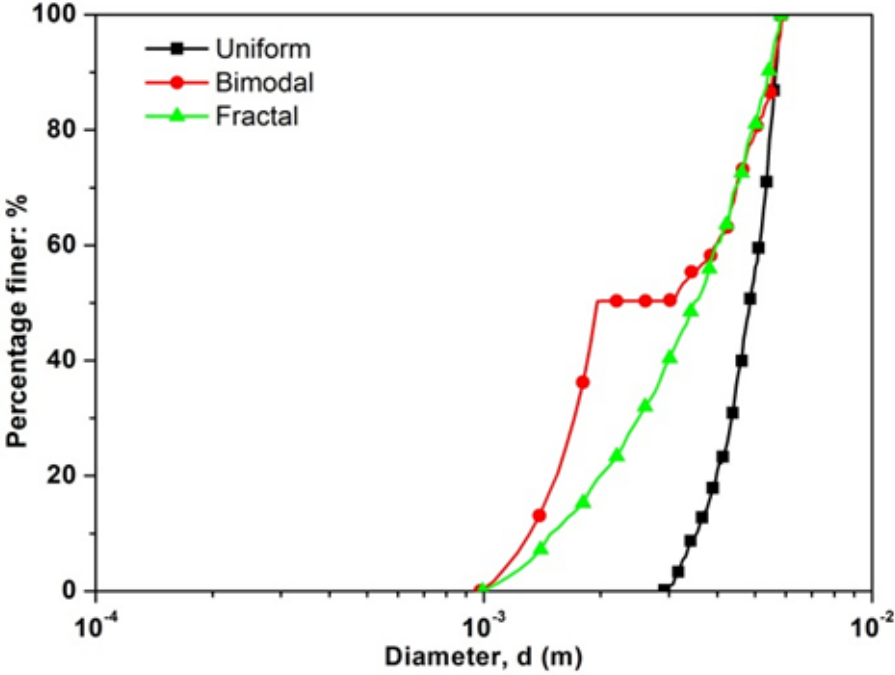
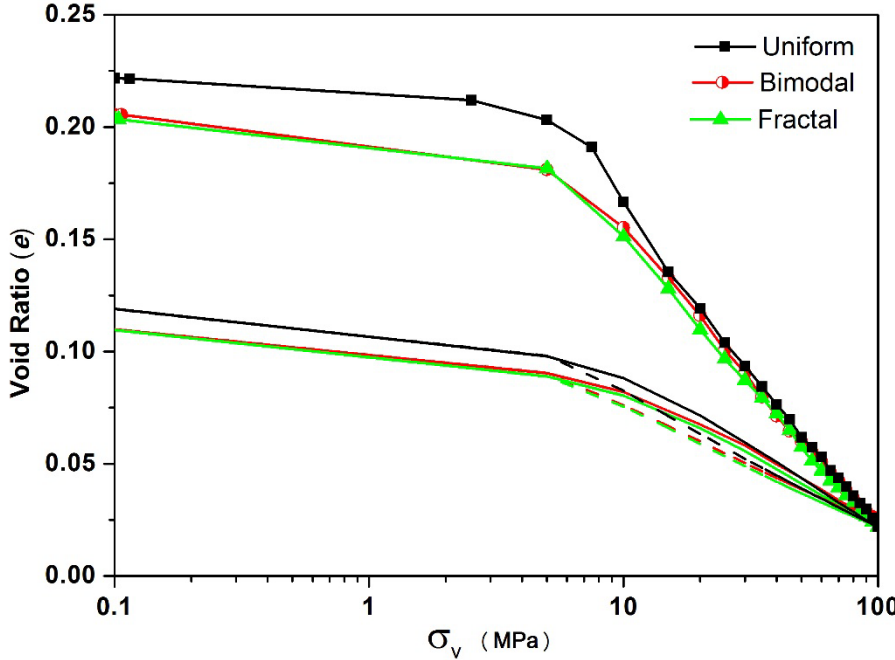
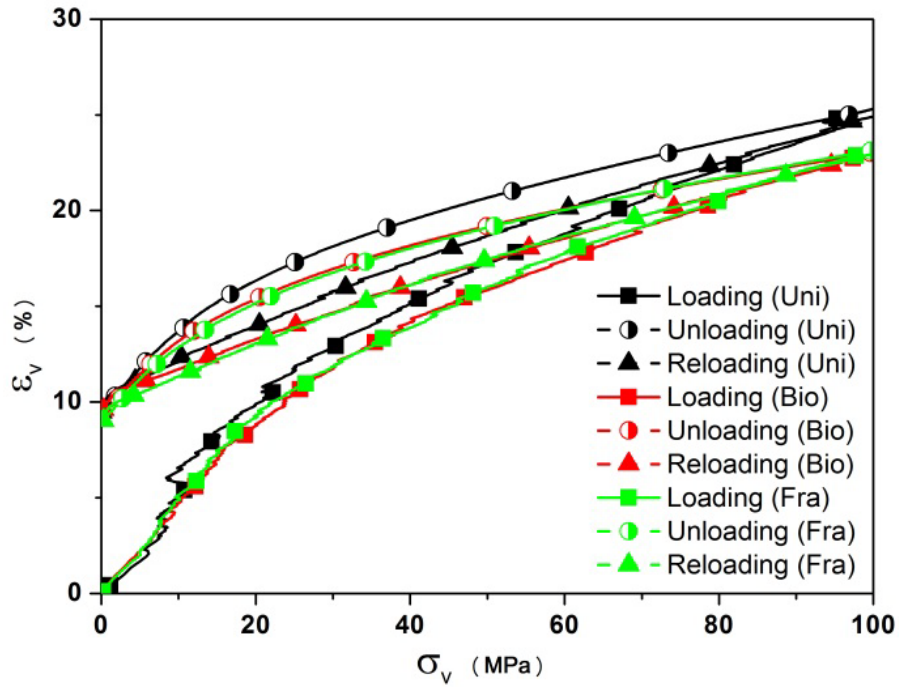


Figure 7.1: The three initial PSDs.

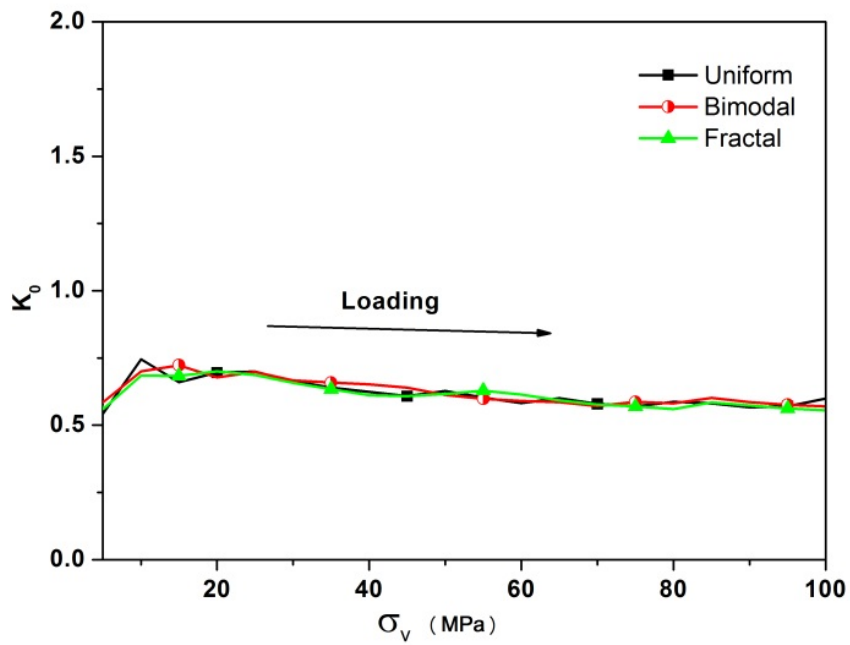


(a)

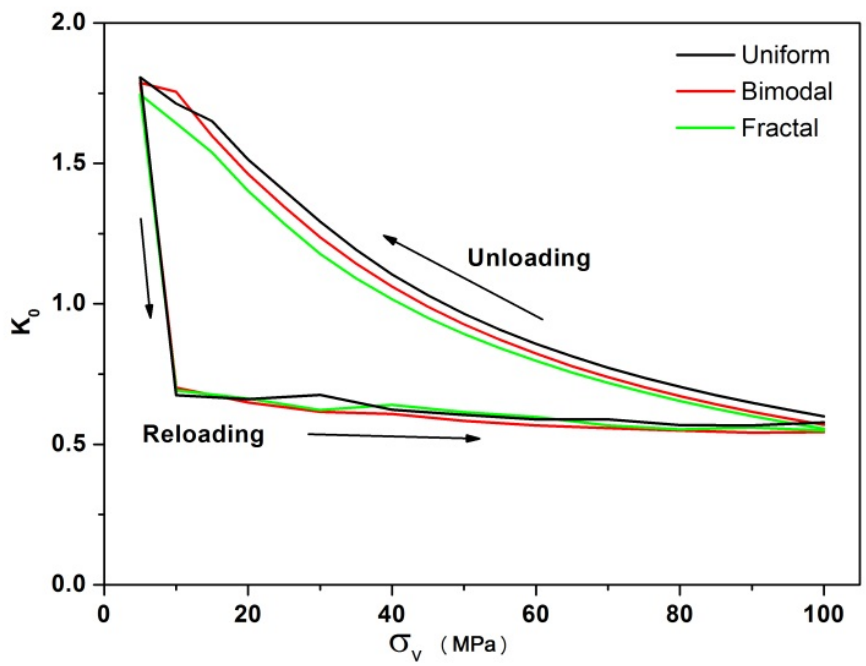


(b)

Figure 7.2: One dimensional compression for three PSDs under cyclic loading (a) compression curves; (b) stress-strain curves.

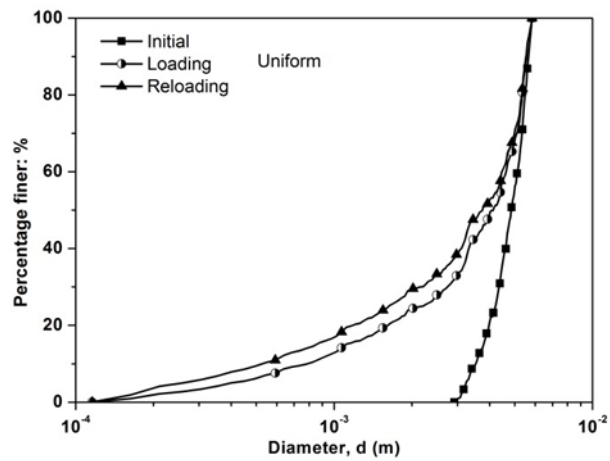


(a)

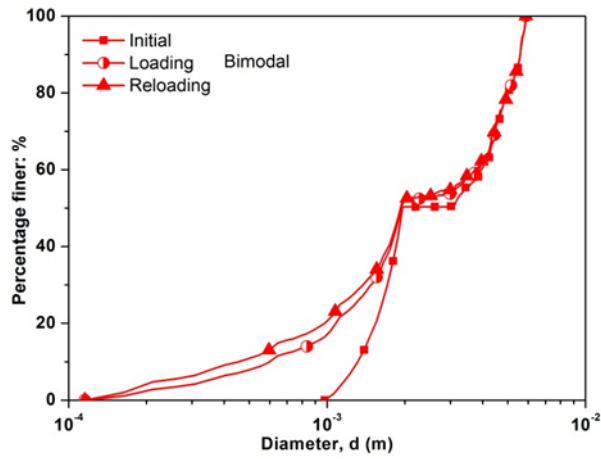


(b)

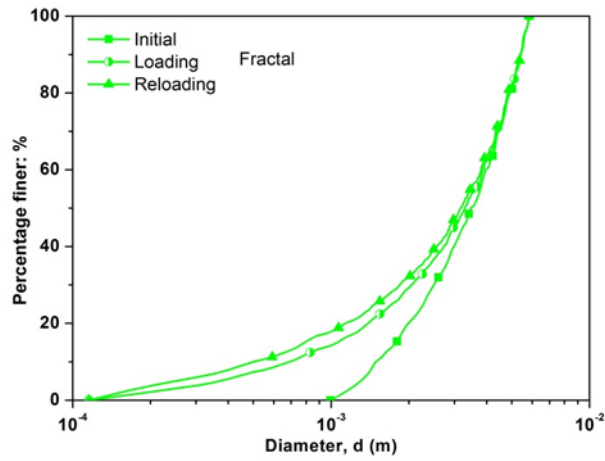
Figure 7.3: The variation of K_0 for the three PSDs during 1st cyclic loading condition (a) Loading stage; (b) Unloading and Reloading stages.



(a)

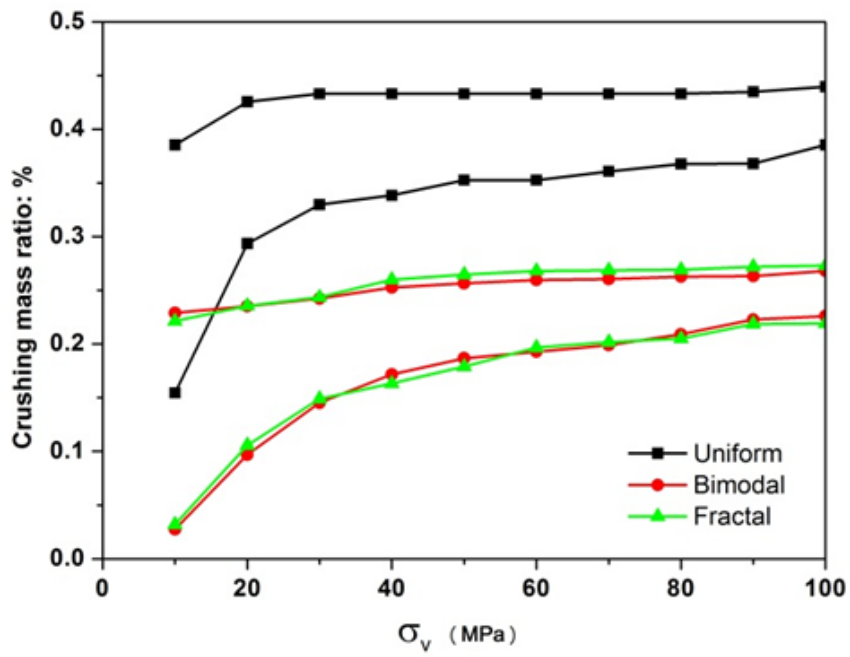


(b)

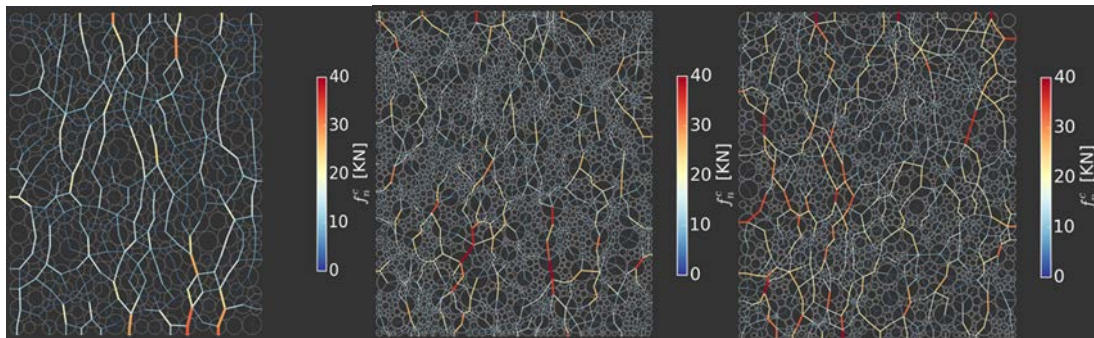


(c)

Figure 7.4: Evaluation of PSD for the three samples at the final state (a) the uniformly graded packing; (b) the binary mixture packing; (c) the fractal graded packing.



(a)



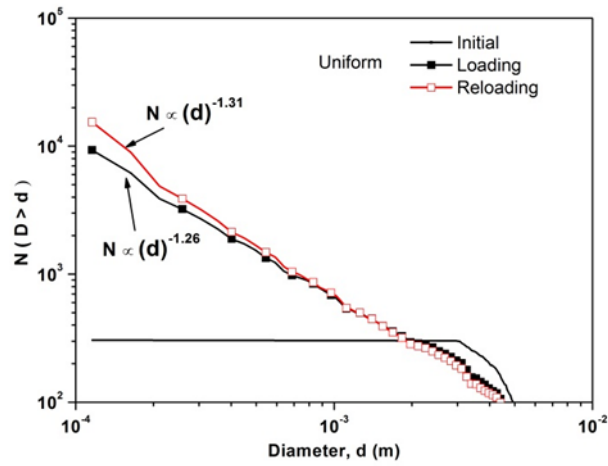
Uniform

Bimodal

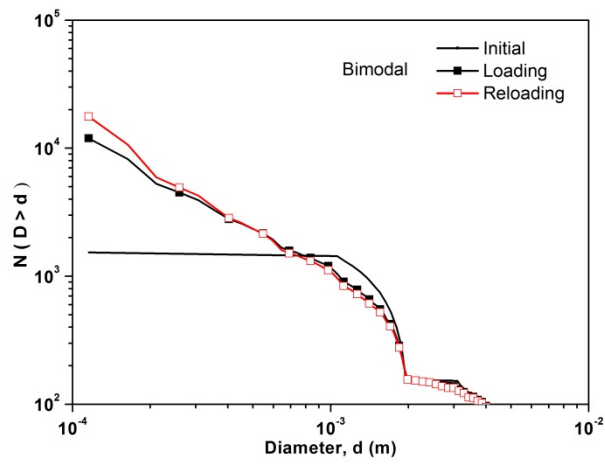
Fractal

(b)

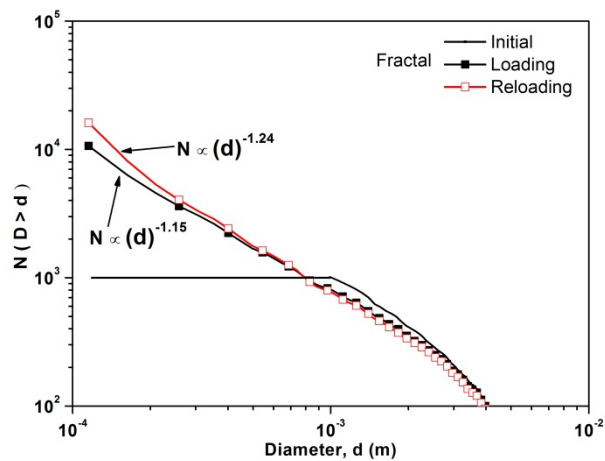
Figure 7.5: (a) the variations of crushing mass ratio during loading and reloading stages; (b) the visualization of force chain at the initial stage.



(a)

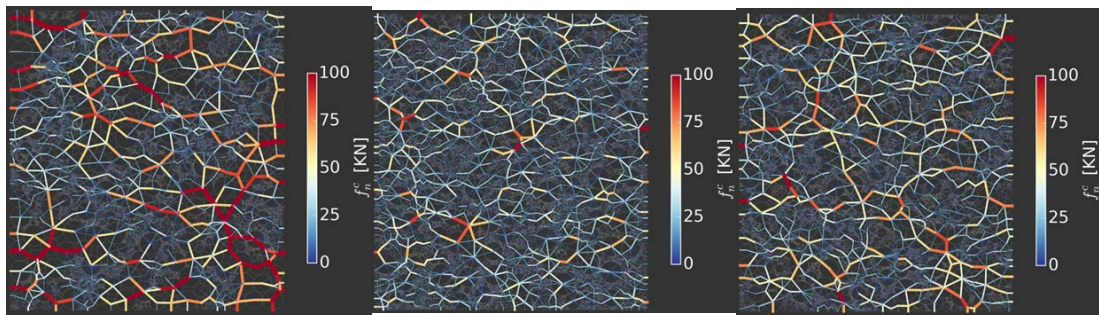
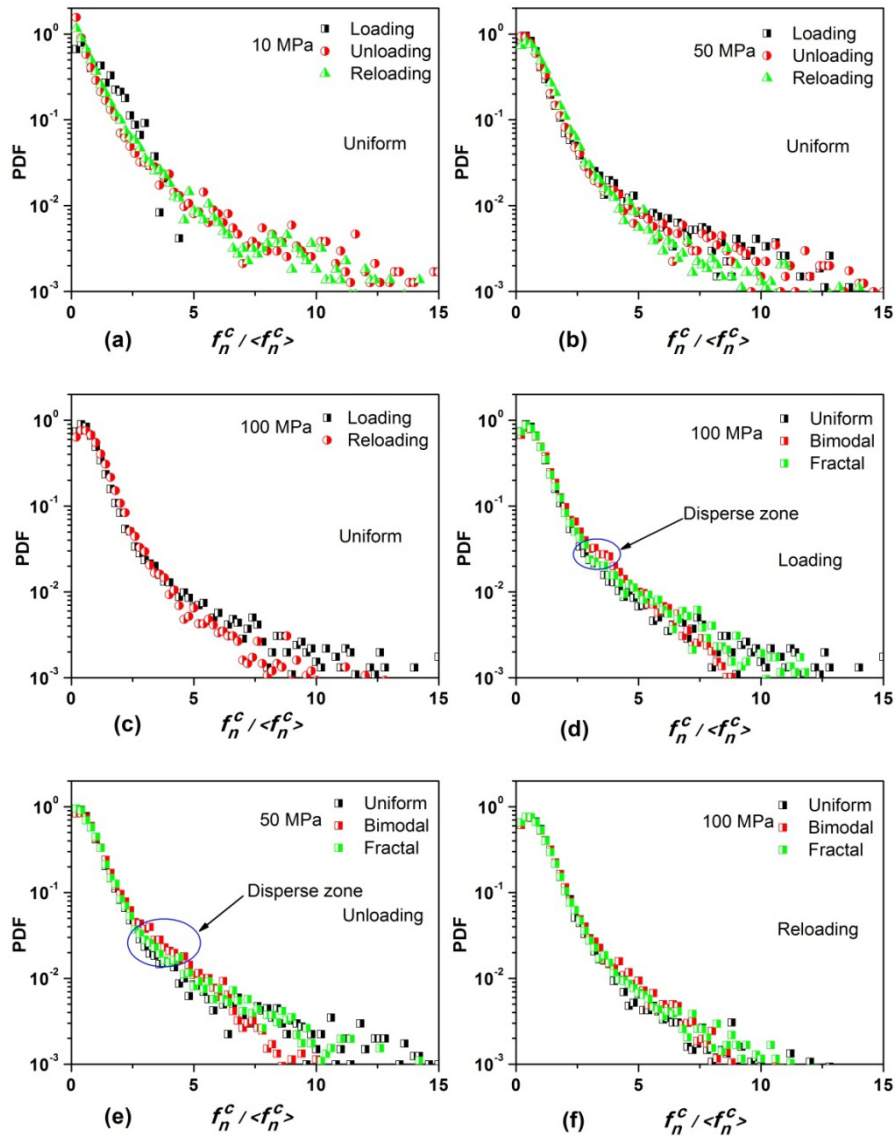


(b)



(c)

Figure 7.6: Evolution of PSDs in the whole assembly by number (a) the uniform graded packing; (b) the bimodal graded packing; (c) the fractal graded packing.



(g)

Figure 7.7: Probability distribution of normalized contact normal force (a) uniform graded 10 MPa; (b) uniform graded 50 MPa; (c) uniform graded 100 MPa; (d) three PSDs 100 MPa (Loading stage); (e) three PSDs 50MPa (Unloading stage); (f) three PSDs 100 MPa (Reloading stage); (g) visualization of contact force chain in unloading stage 10 MPa.

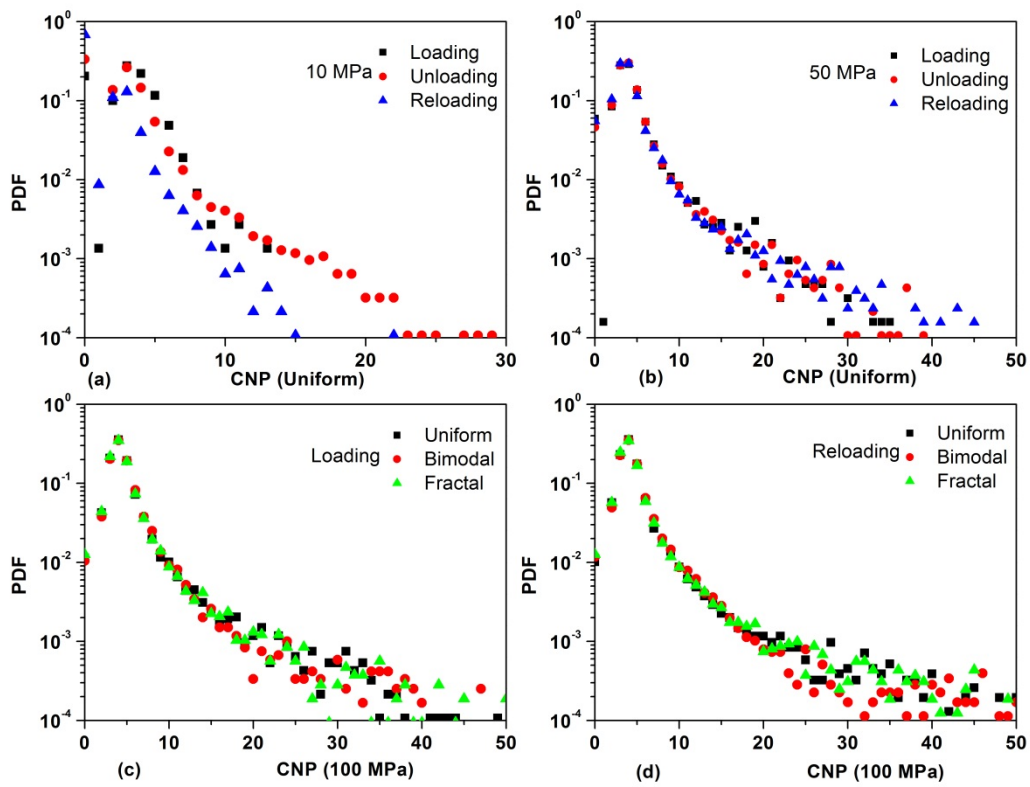


Figure 7.8: Probability distribution of coordination number (a) uniform graded 10 MPa; (b) uniform graded 50 MPa; (c) three PSDs at loading stage; (d) three PSDs at reloading stage.

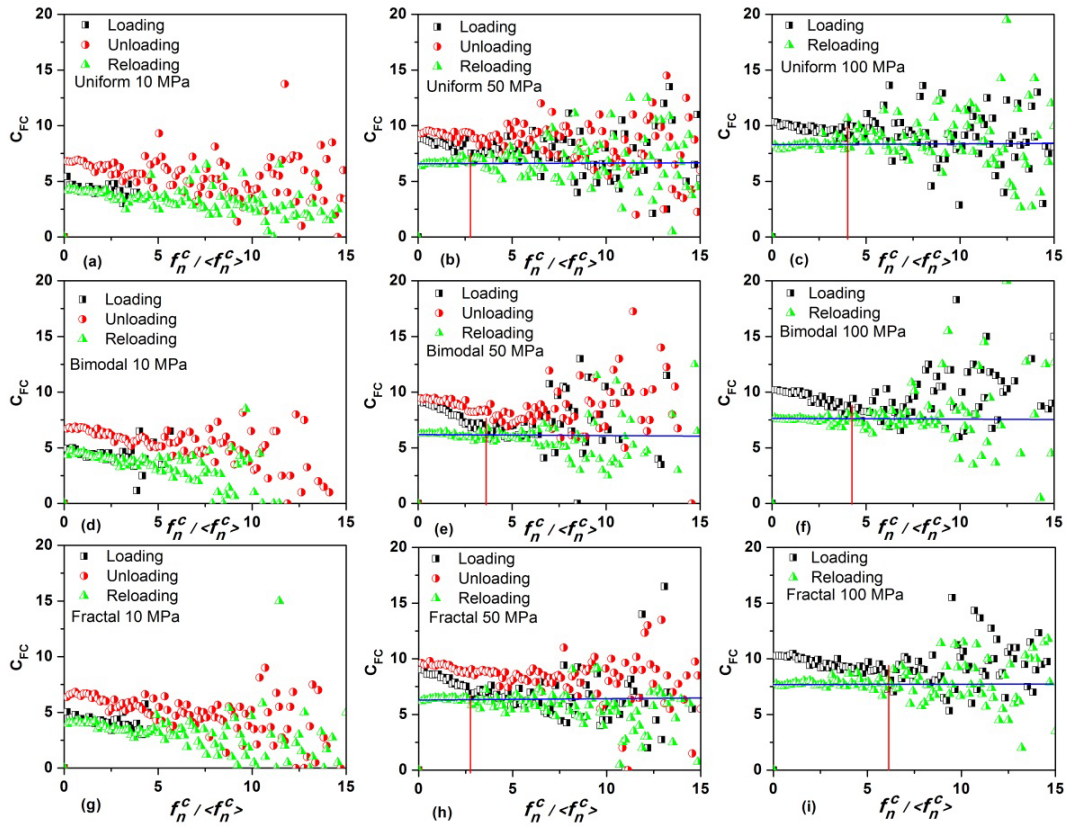


Figure 7.9: evaluation of the C_{FC} during the 1st cyclic loading (a) uniform graded 10 MPa; (b) uniform graded 50 MPa; (c) uniform graded 100 MPa; (d) bimodal graded 10 MPa; (e) bimodal graded 50 MPa; (f) bimodal graded 100 MPa; (g) fractal graded 10 MPa; (h) fractal graded 50 MPa; (i) fractal graded 100 MPa.

CHAPTER 8

Conclusions and future work

8.1 Conclusions

Generally, the mechanical behavior of a granular media is extremely complicated. This thesis is concentrated on the effects of particle shape, inducing anisotropic, particle crushability and loading paths for a granular assemblage by using DEM. By means of systematic numerical investigations, the connections between the macroscopic mechanical responses and the microscopic structural features are deeply explored. In this chapter, the major conclusions are presented in the following.

The results as mentioned in Chapter 3 are successful to quantitatively analyze the particle shape effect of non-convex irregular particles during quasi-static shearing. A practical and effective shape descriptor SF is suggested to quantitatively evaluate the macro strength indexes and micro statistics parameters of non-convex grain packings. The variation of peak friction and dilation angles shows a nonlinear correlation with SF . The patterns of strain localization and rose distribution of contact forces are found to be highly dependent on the composite grain shape of a granular assemblage. Furthermore, the strong force exponents decrease with the increasing magnitude of SF and confining pressure. In addition, the accuracy of SFF can be influenced by the manner of average contact normal force and the anisotropic parameter of the contact vectors for these non-convex granular packings.

The results presented in Chapter 4 capture a reasonable development of four determined contact types within the shape mixtures during the quasi-static shearing. Hence, the macroscopic mechanical responses of these shape mixture packings can be explored into a deeper scale by the contact information of the four contact types. From a macroscopic, the subtle points in the variation of the void ratio are emerged at the little percent of round or irregular grain. Moreover, the ratio value of the four contacts and the related mobilization

indexes can be considered to explain the variation of strength indexes especially at the inverse regions. The probability of the CC contact is approximately the same within the strong force chains. However, the pdf curves of the normalised contact forces of EE1 and EEm show a nearly linear increasing relationship with an increasing η_m . The main trend of I_{fm} for the four contacts can explain the separated global I_{fm} with increasing η_m . It is also notable that the anisotropic coefficient of a_c is not sensitive to the contact portions of EE1 and EEm. For the regime of $\eta_m < 0.7$, the CE contacts play an important part in the three fabric parameters.

A traditional rolling resistance model is installed in Chapter 5 to compare with the irregular clumps on the differences between the artificial and geometrical interlocking effects. DEM is adopted to perform a series of undrained shear tests. Both the rolling resistance coefficient and the irregular shape can induce some level of dilation effects to enhance the shear strength. However, simulated results show that the rolling resistance coefficient is limited when $\alpha > 0.5$. Moreover, a very small rolling resistance coefficient can trigger a positive pseudo excessive water pressure at the critical state. Furthermore, the slope value of M for the largest rolling resistance coefficient is still lower than the irregular shape. In addition, the rolling resistance effect cannot easily generate an apparent liquefaction as the loose packing of irregular particle. Detailed microscopic statistical indexes have been compared for both the rolling resistance model and the selected irregular clumps. It has been found that the average friction mobilization of rolling resistance samples, even for UR5, is still much lower than the irregular assemblages. Although the probability distribution of the normalized contact normal force for the rolling resistance sample is analogous to the irregular clumps, the macro stress-strain behaviors are distinct.

DEM is adopted in Chapter 6 to explore the contact force and coordination distribution within a crushable granular media during one dimensional compression. Extensive numerical tests are carried out to validate the proposed fractal model and analyze the sensitive of the input parameters. When the contact normal force distribution shows a log-normal features, a power-law fractal pattern of contact force emerges. Meanwhile, the fractal contact force

distribution is accompanied with the development of PSD, which also has a power-law relation. In addition, the coordination number distribution has an opposite trend as compared with the normalized normal contact force. For a fractal PSD granular assemblage, the coordination number distribution is unified.

In Chapter 7 the initial PSD effect is explored for the crushable granular materials within the one dimensional compression throughout the unloading-reloading procedure. It is found that the initial compressibility and expansibility can be influenced by the initial PSD. Moreover, the fractal dimension of PSD and contact normal forces will gradually increase during the reloading procedure. Furthermore, the pattern of CNF throughout the loading-reloading procedure would shift with a deeper end. In addition, the coordination distribution at the ultimate state is not sensitive to the initial PSD and reloading effects.

8.2 Recommendations for the future work

This dissertation has explored the initial work of the fundamental feature of granular materials. Although some original results have been presented to enhance the understanding of mechanical behavior of granular materials from micro to macro, there still possess many limitations, and the present work can pave the way to the future study. Few topics are suggested as follow to deeply explore the mechanisms of granular materials.

- (1) All the numerical investigations are performed on two dimensional basis for the study of the particle shape factor of granular materials. On the other hand, the nature of a granular material is always three dimensional, hence three dimensional simulations are suggested to evaluate the geometry effect with a practical meaning. However, the efficiency and accuracy of three dimensional DEM computation is still a challenge to fulfill in the near future, as the required computations are extremely demanding. Faster computer and parallel computation algorithms can help the three dimensional study in the future.
- (2) The qualitative analysis of particle shape should be constructed as a bridge to connect the actual sand grain shape and the DEM modelling approaches. A potential way is to

correlate the numerical modelling grains from realistic CT data. In addition, some sophisticated shape descriptors should be added and compared to evaluate the effect of particle shape.

- (3) The accuracy of SFF relationship for the inherent anisotropic packings should be verified for both two dimension and three dimension.
- (4) The structure feature of granular contact system should be deeply analyzed by the newly developed research tools such as contact types, contact cyclic loops, localized stiffness and energy partition under various boundaries conditions.
- (5) The mechanism of instability of granular materials should be deeply explored to enhance both the microscopic and macroscopic understandings. In addition, the realistic undrained test should be replaced the constant volume or area test. A potential way is to couple the fluid solvers with DEM (CFD) in the future study.
- (6) The strain calculation method in this study can also be suggested to extend from two dimension to three dimension in the future study.
- (7) Larger scale one dimensional compression test should be performed to enhance the present ideal modelling. Moreover, the relationship between PSD and contact force distribution during the confined comminution system is suggested to be study in greater depth.
- (8) Other boundary conditions such as the biaxial shearing test are suggested to study the evaluation of contact force and coordination distribution of crushable granular materials. Meanwhile, the bonded agglomerate is also suggested to study the relationship between particle shape, inherent anisotropic and the crushability.
- (9) Advance micro experimental studies and DEM modelling should be constructed as a coupled method to dynamic update modelling information.

REFERENCES

- Abbiaredo, C., and Clayton, C., 2010, Varying initial void ratios for DEM simulations: *Geotechnique*, v. 60, p. 497-502.
- Abedi, S., and Mirghasemi, A.A., 2011, Particle shape consideration in numerical simulation of assemblies of irregularly shaped particles: *Particuology*, v. 9, p. 387-397.
- Ai, J., Chen, J.F., Rotter, J.M., and Ooi, J.Y., 2011, Assessment of rolling resistance models in discrete element simulations: *Powder Technology*, v. 206, p. 269-282.
- Alarcon-Guzman, A., Leonards, G., and Chameau, J., 1988, Undrained monotonic and cyclic strength of sands: *Journal of Geotechnical Engineering*, v. 114, p. 1089-1109.
- Alonso-Marroquín, F., and Wang, Y., 2009, An efficient algorithm for granular dynamics simulations with complex-shaped objects: *Granular Matter*, v. 11, p. 317-329.
- Altuhafi, F., and Coop, M.R., 2010, Changes to particle characteristics associated with the compression of sands: *Geotechnique*, v. 61, p. 459-471.
- Andò, E., Hall, S.A., Viggiani, G., Desrues, J., and Bésuelle, P., 2012, Grain-scale experimental investigation of localised deformation in sand: a discrete particle tracking approach: *Acta Geotechnica*, v. 7, p. 1-13.
- Andrade, J.E., and Avila, C.F., 2012, Granular element method (GEM): linking inter-particle forces with macroscopic loading: *Granular Matter*, v. 14, p. 51-61.
- Antony, S.J., 2000, Evolution of force distribution in three-dimensional granular media: *Physical Review E*, v. 63, p. 011302.
- Antony, S.J., 2007, Link between single-particle properties and macroscopic properties in particulate assemblies: role of structures within structures: *Philosophical Transactions of the Royal Society A: Mathematical, Physical and Engineering Sciences*, v. 365, p. 2879-2891.
- Antony, S.J., and Kuhn, M.R., 2004, Influence of particle shape on granular contact signatures and shear strength: new insights from simulations: *International Journal of Solids and Structures*, v. 41, p. 5863-5870.
- Antony, S.J., Moreno-Atanasio, R., Musadaidzwa, J., and Williams, R.A., 2008, Impact fracture of composite and homogeneous nanoagglomerates: *Journal of Nanomaterials*, v. 2008, p. 7.
- Arthur, J., Chua, K., and Dunstan, T., 1977, Induced anisotropy in a sand: *Geotechnique*, v. 27, p. 13-30.
- Arthur, J., and Menzies, B., 1972, Inherent anisotropy in a sand: *Geotechnique*, v. 22, p. 115-128.
- Åström, J., and Herrmann, H., 1998, Fragmentation of grains in a two-dimensional packing: *The European Physical Journal B-Condensed Matter and Complex Systems*, v. 5, p. 551-554.
- Azami, A., Pietruszczak, S., and Guo, P., 2010, Bearing capacity of shallow foundations in transversely isotropic granular media: *International Journal for Numerical and Analytical Methods in Geomechanics*, v. 34, p. 771-793.
- Azéma, E., and Radjai, F., 2010, Stress-strain behavior and geometrical properties of packings of elongated particles: *Physical Review E*, v. 81, p. 051304.
- Azéma, E., and Radjai, F., 2012, Force chains and contact network topology in sheared packings of elongated particles: *Physical Review E*, v. 85, p. 031303.
- Azéma, E., Radjai, F., Peyroux, R., and Saussine, G., 2007, Force transmission in a packing of pentagonal particles: *Physical Review E*, v. 76, p. 011301.
- Bagi, K., 1996, Stress and strain in granular assemblies: *Mechanics of Materials*, v. 22, p. 165-177.

- Bandini, V., and Coop, M.R., 2011, The influence of particle breakage on the location of the critical state line of sands: *Soils and Foundations*, v. 51, p. 591-600.
- Banton, J., Villard, P., Jongmans, D., and Scavia, C., 2009, Two - dimensional discrete element models of debris avalanches: Parameterization and the reproducibility of experimental results: *Journal of Geophysical Research: Earth Surface (2003–2012)*, v. 114, p. 04013
- Bardet, J., and Huang, Q., 1993, Rotational stiffness of cylindrical particle contacts: *Powders and Grains*, v. 93, p. 39-43.
- Bardet, J., and Proubet, J., 1991, A numerical investigation of the structure of persistent shear bands in granular media: *Geotechnique*, v. 41, p. 599-613.
- Bardet, J., and Proubet, J., 1992, Shear-band analysis in idealized granular material: *Journal of Engineering Mechanics*, v. 118, p. 397-415.
- Barrett, P., 1980, The shape of rock particles, a critical review: *Sedimentology*, v. 27, p. 291-303.
- Bathurst, R.J., and Rothenburg, L., 1992, Investigation of micromechanical features of idealized granular assemblies using DEM: *Engineering Computations*, v. 9, p. 199-210.
- Been, K., Jefferies, M., and Hachey, J., 1991, The critical state of sands: *Geotechnique*, v. 41, p. 365-381.
- Been, K., and Jefferies, M.G., 1985, A state parameter for sands: *Geotechnique*, v. 35, p. 99-112.
- Belheine, N., Plassiard, J.-P., Donzé, F.-V., Darve, F., and Seridi, A., 2009, Numerical simulation of drained triaxial test using 3D discrete element modeling: *Computers and Geotechnics*, v. 36, p. 320-331.
- Ben-Nun, O., 2011, *Confined Comminution of Granular Materials: Self-organisation, Attractors and Patterns*, University of Sydney.
- Ben-Nun, O., and Einav, I., 2010a, The role of self-organization during confined comminution of granular materials: *Philosophical Transactions of the Royal Society A: Mathematical, Physical and Engineering Sciences*, v. 368, p. 231-247.
- Ben-Nun, O., Einav, I., and Tordesillas, A., 2010b, Force attractor in confined comminution of granular materials: *Physical Review Letters*, v. 104, p. 108001.
- Biarez, J., and Hicher, P.Y., 1994, *Elementary mechanics of soil behaviour: saturated remoulded soils*. AA Balkema.
- Blott, S.J., and Pye, K., 2008, Particle shape: a review and new methods of characterization and classification: *Sedimentology*, v. 55, p. 31-63.
- Bolton, M.D., 1986, The strength and dilatancy of sands: *Geotechnique*, v. 36, p. 65-78.
- Bolton, M.D., Nakata, Y., and Cheng, Y.P., 2008, Micro-and macro-mechanical behaviour of DEM crushable materials: *Geotechnique*, v. 58, p. 471-480.
- Bowman, E.T., Soga, K., and Drummond, W., 2001, Particle shape characterisation using Fourier descriptor analysis: *Geotechnique*, v. 51, p. 545-554.
- Calvetti, F., 2008, Discrete modelling of granular materials and geotechnical problems: *European Journal of Environmental and Civil Engineering*, v. 12, p. 951-965.
- Cambou, B., Chaze, M., and Dedecker, F., 2000, Change of scale in granular materials: *European Journal of Mechanics-A/Solids*, v. 19, p. 999-1014.
- Casagrande, A., and Carillo, N., 1944, Shear failure of anisotropic materials: *Journal of Boston Society of Civil Engineers*, v. 31, p. 74-81.
- Chang, C.S., and Yin, Z.Y., 2010, Modeling stress-dilatancy for sand under compression and extension loading conditions: *Journal of Engineering Mechanics*, v. 136, p. 777-786.

- Cheng, Y.M., Chau, K.T., Xiao, L.J., and Li, N., 2010, Flow pattern for a silo with two layers of materials with single or double openings: *Journal of Geotechnical and Geoenvironmental Engineering*, v. 136, p. 1278-1286.
- Cheng, Y.M., Liu, Z.N., Song, W.D., and Au, S.K., 2009, Laboratory test and particle flow simulation of silos problem with nonhomogeneous materials: *Journal of Geotechnical and Geoenvironmental Engineering*, v. 135, p. 1754-1761.
- Cheng, Y.P., Nakata, Y., and Bolton, M.D., 2003, Discrete element simulation of crushable soil: *Geotechnique*, v. 53, p. 633-641.
- Cheung, G., and O'Sullivan, C., 2008, Effective simulation of flexible lateral boundaries in two-and three-dimensional DEM simulations: *Particulate*, v. 6, p. 483-500.
- Cho, G.C., Dodds, J., and Santamarina, J.C., 2006, Particle shape effects on packing density, stiffness, and strength: natural and crushed sands: *Journal of Geotechnical and Geoenvironmental Engineering*, v. 132, p. 591-602.
- Christoffersen, J., Mehrabadi, M.M., and Nemat-Nasser, S., 1981, A micromechanical description of granular material behavior: *Journal of Applied Mechanics*, v. 48, p. 339-344.
- Cil, M.B., and Alshibli, K.A., 2014, 3D evolution of sand fracture under 1D compression: *Geotechnique*, v. 64, p. 351-364.
- Coop, M.R., and Lee, I.K., 1993, The behaviour of granular soils at elevated stresses, *Predictive Soil Mechanics, Proc., Wroth Memorial Symp.*, p. 186-198.
- Coop, M.R., Sorensen, K., Freitas, T.B., and Georgoutsos, G., 2004, Particle breakage during shearing of a carbonate sand: *Geotechnique*, v. 54, p. 157-163.
- Coppersmith, S.N., Liu, C.H., Majumdar, S., Narayan, O., and Witten, T.A., 1996, Model for force fluctuations in bead packs: *Physical Review E*, v. 53, p. 4673.
- Corwin, E.I., Jaeger, H.M., and Nagel, S.R., 2005, Structural signature of jamming in granular media: *Nature*, v. 435, p. 1075-1078.
- Coulomb, C.A., 1773, Sur une application des règles de maximis et minimis à quelques problèmes de statique relatifs à l'architecture: *Mémoires de mathématiques et de Physique, Académie Royale des Sciences*, v. 7, p. 343-382.
- Cowin, S.C., 1985, The relationship between the elasticity tensor and the fabric tensor: *Mechanics of Materials*, v. 4, p. 137-147.
- Cox, M.R.B., 2008, The influence of grain shape on dilatancy, University of Arizona.
- Cundall, P.A., 1987, Distinct element models of rock and soil structure: *Analytical and computational methods in engineering rock mechanics*, v. 4, p. 129-163.
- Cundall, P.A., 2001, A discontinuous future for numerical modelling in geomechanics?: *Proceedings of the ICE-Geotechnical Engineering*, v. 149, p. 41-47.
- Cundall, P., and Strack, O., 1978, BALL-A program to model granular media using the distinct element method: *Technical note, Advanced Technology Group*.
- Cundall, P.A., 1971, A computer model for simulating progressive large scale movements in blocky rock systems, *Proc. Symp. Rock Fracture (ISRM)*, Nancy, v. 1, p. 8-11.
- Cundall, P.A., 1989, Numerical experiments on localization in frictional materials: *Ingenieur-archiv*, v. 59, p. 148-159.
- Cundall, P.A., and Strack, O.D., 1979, A discrete numerical model for granular assemblies: *Geotechnique*, v. 29, p. 47-65.
- Dafalias, Y.F., and Popov, E.P., 1975, A model of nonlinearly hardening materials for complex loading:

- Acta Mechanica, v. 21, p. 173-192.
- Dafalias, Y.F., and Manzari, M.T., 2004, Simple plasticity sand model accounting for fabric change effects: *Journal of Engineering Mechanics*, v. 130, p. 622-634.
- Dai, B.B., 2010, Micromechanical investigation of the behavior of granular materials: The University of Hong Kong, PhD Thesis.
- Das, B.M., 2008, *Advanced soil mechanics*, CRC Press.
- De Bono, J.P., and McDowell, G.R., 2014, Discrete element modelling of one-dimensional compression of cemented sand: *Granular Matter*, v. 16, p. 79-90.
- Dedecker, F., Chaze, M., Dubujet, P., and Cambou, B., 2000, Specific features of strain in granular materials: *Mechanics of Cohesive - frictional Materials*, v. 5, p. 173-193.
- Desrues, J., and Viggiani, G., 2004, Strain localization in sand: an overview of the experimental results obtained in Grenoble using stereophotogrammetry: *International Journal for Numerical and Analytical Methods in Geomechanics*, v. 28, p. 279-321.
- Drescher, A., and De Jong, G.D.J., 1972, Photoelastic verification of a mechanical model for the flow of a granular material: *Journal of the Mechanics and Physics of Solids*, v. 20, p. 337-340.
- Ehrlich, R., and Weinberg, B., 1970, An exact method for characterization of grain shape: *Journal of Sedimentary Research*, v. 40, p. 205-212.
- Einav, I., 2007a, Breakage mechanics—part I: theory: *Journal of the Mechanics and Physics of Solids*, v. 55, p. 1274-1297.
- Einav, I., 2007b, Breakage mechanics—Part II: Modelling granular materials: *Journal of the Mechanics and Physics of Solids*, v. 55, p. 1298-1320.
- Einav, I., and Valdes, J.R., 2008, On comminution and yield in brittle granular mixtures: *Journal of the Mechanics and Physics of Solids*, v. 56, p. 2136-2148.
- Estrada, N., Azéma, E., Radjai, F., and Taboada, A., 2011, Identification of rolling resistance as a shape parameter in sheared granular media: *Physical Review E*, v. 84, p. 011306.
- Estrada, N., Taboada, A., and Radjai, F., 2008, Shear strength and force transmission in granular media with rolling resistance: *Physical Review E*, v. 78, p. 021301.
- Feda, J., 1982, *Mechanics of Particulate Materials. Development of Geotechnical Engineering*, vol. 30, Elsevier, Amsterdam.
- Ferrellec, J., and McDowell, G.R., 2010, Modelling realistic shape and particle inertia in DEM: *Geotechnique*, v. 60, p. 227-232.
- Fu, P., Walton, O.R., and Harvey, J.T., 2012, Polyarc discrete element for efficiently simulating arbitrarily shaped 2D particles: *International Journal for Numerical Methods in Engineering*, v. 89, p. 599-617.
- Fu, X., Dutt, M., Bentham, A.C., Hancock, B.C., Cameron, R.E., and Elliott, J.A., 2006, Investigation of particle packing in model pharmaceutical powders using X-ray microtomography and discrete element method: *Powder Technology*, v. 167, p. 134-140.
- Gajo, A., and Wood, M., 1999, Severn–Trent sand: a kinematic-hardening constitutive model: the q–p formulation: *Geotechnique*, v. 49, p. 595-614.
- Gao, Y., and Wang, Y.H., 2014, Experimental and DEM Examinations of K₀ in Sand under Different Loading Conditions: *Journal of Geotechnical and Geoenvironmental Engineering*, v. 140, p. 04014012.
- Gao, Z.W., and Zhao, J.D., 2013, Strain localization and fabric evolution in sand: *International Journal of Solids and Structures*, v. 50, p. 3634-3648.

- Gong, G., Thornton, C., and Chan, A.H., 2011, DEM simulations of undrained triaxial behavior of granular material: *Journal of Engineering Mechanics*, v. 138, p. 560-566.
- Graham, J., Alfaro, M., and Ferris, G., 2004, Compression and strength of dense sand at high pressures and elevated temperatures: *Canadian Geotechnical Journal*, v. 41, p. 1206-1212.
- Gu, X.Q., Huang, M.S., and Qian, J.G., 2014, DEM investigation on the evolution of microstructure in granular soils under shearing: *Granular Matter*, v. 16, p. 91-106.
- Guo, N., and Zhao, J.D., 2013, The signature of shear-induced anisotropy in granular media: *Computers and Geotechnics*, v. 47, p. 1-15.
- Guo, N., and Zhao, J.D., 2014, A coupled FEM/DEM approach for hierarchical multiscale modelling of granular media: *International Journal for Numerical Methods in Engineering*, v. 99, p. 789-818.
- Guo, P., 2008, Modified direct shear test for anisotropic strength of sand: *Journal of Geotechnical and Geoenvironmental Engineering*, v. 134, p. 1311-1318.
- Härtl, J., and Ooi, J.Y., 2011, Numerical investigation of particle shape and particle friction on limiting bulk friction in direct shear tests and comparison with experiments: *Powder Technology*, v. 212, p. 231-239.
- Hagerty, M.M., Hite, D.R., Ullrich, C.R., and Hagerty, D.J., 1993, One-dimensional high-pressure compression of granular media: *Journal of Geotechnical Engineering*, v. 119, p. 1-18.
- Hall, S.A., Bornert, M., Desrues, J., Pannier, Y., Lenoir, N., Viggiani, G., and Bésuelle, P., 2010, Discrete and continuum analysis of localised deformation in sand using X-ray μ CT and volumetric digital image correlation: *Geotechnique*, v. 60, p. 315-322.
- Hall, S.A., Wright, J., Pirling, T., Andò, E., Hughes, D.J., and Viggiani, G., 2011, Can intergranular force transmission be identified in sand?: *Granular Matter*, v. 13, p. 251-254.
- Hardin, B.O., 1985, Crushing of soil particles: *Journal of Geotechnical Engineering*, v. 111, p. 1177-1192.
- Houlsby, G.T., 1991, How the dilatancy of soils affects their behaviour, University of Oxford, Department of Engineering Science, Report, n. 121/91.
- Howell, D., Behringer, R.P., and Veje, C., 1999, Stress fluctuations in a 2D granular Couette experiment: a continuous transition: *Physical Review Letters*, v. 82, p. 5241.
- Huang, X., 2014, Exploring critical-state behaviour using DEM, The University of Hong Kong, PhD Thesis.
- Hurley, R., Marteau, E., Ravichandran, G., and Andrade, J.E., 2014, Extracting inter-particle forces in opaque granular materials: Beyond photoelasticity: *Journal of the Mechanics and Physics of Solids*, v. 63, p. 154-166.
- Indraratna, B., Sun, Q.D., and Nimbalkar, S., 2014, Observed and predicted behaviour of rail ballast under monotonic loading capturing particle breakage: *Canadian geotechnical journal*, v. 52, p. 73-86.
- Ishihara, K., 1993, Liquefaction and flow failure during earthquakes: *Geotechnique*, v. 43, p. 351-451.
- Ishihara, K., Tatsuoka, F., and Yasuda, S., 1975, Undrained deformation and liquefaction of sand under cyclic stresses: *Soils and Foundations*, v. 15, p. 29-44.
- Itasca, 2000, User's manual for PFC2D/PFC3D, Minneapolis, USA: Itasca Consulting Group, Inc.
- Itasca, 2005, User's manual for PFC2D/PFC3D, Minneapolis, USA: Itasca Consulting Group, Inc.
- Iwashita, K., and Oda, M., 1998, Rolling resistance at contacts in simulation of shear band development by DEM: *Journal of Engineering Mechanics*, v. 124, p. 285-292.

- Iwashita, K., and Oda, M., 2000, Micro-deformation mechanism of shear banding process based on modified distinct element method: *Powder Technology*, v. 109, p. 192-205.
- Jaeger, H.M., Nagel, S.R., and Behringer, R.P., 1996, *Granular solids, liquids, and gases: Reviews of Modern Physics*, v. 68, p. 1259.
- Jean, M., 1999, The non-smooth contact dynamics method: *Computer Methods in Applied Mechanics and Engineering*, v. 177, p. 235-257.
- Jensen, R.P., Bosscher, P.J., Plesha, M.E., and Edil, T.B., 1999, DEM simulation of granular media—structure interface: effects of surface roughness and particle shape: *International Journal for Numerical and Analytical Methods in Geomechanics*, v. 23, p. 531-547.
- Jensen, R.P., Plesha, M.E., Edil, T.B., Bosscher, P.J., and Kahla, N.B., 2001, DEM simulation of particle damage in granular media-structure interfaces: *International Journal of Geomechanics*, v. 1, p. 21-39.
- Jia, X., Gan, M., Williams, R., and Rhodes, D., 2007, Validation of a digital packing algorithm in predicting powder packing densities: *Powder Technology*, v. 174, p. 10-13.
- Jia, X., and Williams, R., 2001, A packing algorithm for particles of arbitrary shapes: *Powder Technology*, v. 120, p. 175-186.
- Jiang, M.J., Chen, H., Tapias, M., Arroyo, M., and Fang, R., 2014, Study of mechanical behavior and strain localization of methane hydrate bearing sediments with different saturations by a new DEM model: *Computers and Geotechnics*, v. 57, p. 122-138.
- Jiang, M.J., He, J., Wang, J.F., Liu, F., and Zhang, W.C., 2014, Distinct simulation of earth pressure against a rigid retaining wall considering inter-particle rolling resistance in sandy backfill: *Granular Matter*, v. 16, p. 797-874.
- Jiang, M.J., Leroueil, S., Zhu, H.H., Yu, H.S., and Konrad, J.M., 2009, Two-dimensional discrete element theory for rough particles: *International Journal of Geomechanics*, v. 9, p. 20-33.
- Jiang, M.J., Li, T., Hu, H.J., and Thornton, C., 2014, DEM analyses of one-dimensional compression and collapse behaviour of unsaturated structural loess: *Computers and Geotechnics*, v. 60, p. 47-60.
- Jiang, M.J., Yan, H.B., Zhu, H.H., and Uti, S., 2011, Modeling shear behavior and strain localization in cemented sands by two-dimensional distinct element method analyses: *Computers and Geotechnics*, v. 38, p. 14-29.
- Jiang, M.J., Yu, H.S., and Harris, D., 2005, A novel discrete model for granular material incorporating rolling resistance: *Computers and Geotechnics*, v. 32, p. 340-357.
- Jiang, M., Yu, H.S., and Harris, D., 2006, Discrete element modelling of deep penetration in granular soils: *International Journal for Numerical and Analytical Methods in Geomechanics*, v. 30, p. 335-361.
- Jiang, M.J., Zhang, W.C., Sun, Y.G., and Uti, S., 2013, An investigation on loose cemented granular materials via DEM analyses: *Granular Matter*, v. 15, p. 65-84.
- Jing, L., and Stephansson, O., 2007, *Fundamentals of Discrete Element Methods for Rock Engineering: Theory and Applications: Theory and Applications*, Elsevier.
- Karstunen, M., and Yin, Z.Y., 2010, Modelling time-dependent behaviour of Murro test embankment: *Geotechnique*, v. 60, p. 735-749.
- Kennedy, S.K., and Lin, W.H., 1992, A comparison of Fourier and fractal techniques in the analysis of closed forms: *Journal of Sedimentary Research*, v. 62, p. 842-848.
- Kondic, L., 1999, Dynamics of spherical particles on a surface: collision-induced sliding and other

- effects: *Physical Review E*, v. 60, p. 751.
- Kondic, L., Goulet, A., O'Hern, C., Kramar, M., Mischaikow, K., and Behringer, R., 2012, Topology of force networks in compressed granular media: *EPL*, v. 97, p. 54001.
- Kozicki, J., and Donzé, F., 2008, A new open-source software developed for numerical simulations using discrete modeling methods: *Computer Methods in Applied Mechanics and Engineering*, v. 197, p. 4429-4443.
- Krumbein, W.C., and Sloss, L.L., 1951, Stratigraphy and sedimentation: *Soil Science*, v. 71, p. 401.
- Kruyt, N.P., and Rothenburg, L., 1996, Micromechanical definition of the strain tensor for granular materials: *Journal of Applied Mechanics*, v. 63, p. 706-711.
- Kuhn, M.R., 1999, Structured deformation in granular materials: *Mechanics of Materials*, v. 31, p. 407-429.
- Kuhn, M.R., 2006, OVAL and OVALPLOT: Programs for analyzing dense particle assemblies with the discrete element method.
- Kuhn, M.R., Renken, H.E., Mixsell, A.D., and Kramer, S.L., 2014, Investigation of cyclic liquefaction with discrete element simulations: *Journal of Geotechnical and Geoenvironmental Engineering*, v. 140, p. 04014075.
- Kumar, N., Imole, O.I., Magnanimo, V., and Luding, S., 2014, Effects of polydispersity on the micro-macro behavior of granular assemblies under different deformation paths: *Particuology*, v. 12, p. 64-79.
- Lade, P.V., Nam, J., and Hong, W.P., 2008, Shear banding and cross-anisotropic behavior observed in laboratory sand tests with stress rotation: *Canadian Geotechnical Journal*, v. 45, p. 74-84.
- Langston, P., Tüzün, U., and Heyes, D., 1996, Distinct element simulation of interstitial air effects in axially symmetric granular flows in hoppers: *Chemical Engineering Science*, v. 51, p. 873-891.
- Li, F., Pan, J., and Sinka, C., 2011, Modelling brittle impact failure of disc particles using material point method: *International Journal of Impact Engineering*, v. 38, p. 653-660.
- Li, X., 2006, Micro-scale investigation on the quasi-static behavior of granular material: The Hong Kong University of Science and Technology, PhD Thesis.
- Li, X.S., and Dafalias, Y.F., 2000, Dilatancy for cohesionless soils: *Geotechnique*, v. 50, p. 449-460.
- Li, X., and Li, X.S., 2009, Micro-macro quantification of the internal structure of granular materials: *Journal of Engineering Mechanics*, v. 135, p. 641-656.
- Li, X., and Yu, H.S., 2013, On the stress-force-fabric relationship for granular materials: *International Journal of Solids and Structures*, v. 50, p. 1285-1302.
- Li, X.S., and Dafalias, Y.F., 2002, Constitutive modeling of inherently anisotropic sand behavior: *Journal of Geotechnical and Geoenvironmental Engineering*, v. 128, p. 868-880.
- Li, X.S., and Dafalias, Y.F., 2012, Anisotropic critical state theory: role of fabric: *Journal of Engineering Mechanics*, v. 138, p. 263-275.
- Liao, C.L., Chang, T.P., Young, D.H., and Chang, C.S., 1997, Stress-strain relationship for granular materials based on the hypothesis of best fit: *International Journal of Solids and Structures*, v. 34, p. 4087-4100.
- Lim, W., and McDowell, G.R., 2005, Discrete element modelling of railway ballast: *Granular Matter*, v. 7, p. 19-29.
- Lin, X., and Ng, T.T., 1995, Contact detection algorithms for three - dimensional ellipsoids in discrete element modelling: *International Journal for Numerical and Analytical Methods in*

- Geomechanics, v. 19, p. 653-659.
- Liu, C., Nagel, S.R., Schecter, D., Coppersmith, S., Majumdar, S., Narayan, O., and Witten, T., 1995, Force fluctuations in bead packs: *Science*, v. 269, p. 513-513.
- Liu, H., Kou, S., and Lindqvist, P.A., 2005, Numerical studies on the inter-particle breakage of a confined particle assembly in rock crushing: *Mechanics of Materials*, v. 37, p. 935-954.
- Liu, R., Yin, X., Li, H., Shao, Q., York, P., He, Y., Xiao, T., and Zhang, J., 2013, Visualization and quantitative profiling of mixing and segregation of granules using synchrotron radiation X-ray microtomography and three dimensional reconstruction: *International Journal of Pharmaceutics*, v. 445, p. 125-133.
- Lobo-Guerrero, S., and Vallejo, L.E., 2005, Discrete element method evaluation of granular crushing under direct shear test conditions: *Journal of Geotechnical and Geoenvironmental Engineering*, v. 131, p. 1295-1300.
- Lobo-Guerrero, S., Vallejo, L.E., and Vesga, L.F., 2006, Visualization of crushing evolution in granular materials under compression using DEM: *International Journal of Geomechanics*, v. 6, p. 195-200.
- Lu, M., and McDowell, G.R., 2007, The importance of modelling ballast particle shape in the discrete element method: *Granular Matter*, v. 9, p. 69-80.
- Luding, S., 2005, Anisotropy in cohesive, frictional granular media: *Journal of Physics: Condensed Matter*, v. 17, p. S2623.
- Majmudar, T.S., and Behringer, R.P., 2005, Contact force measurements and stress-induced anisotropy in granular materials: *Nature*, v. 435, p. 1079-1082.
- Makse, H.A., Johnson, D.L., and Schwartz, L.M., 2000, Packing of compressible granular materials: *Physical Review Letters*, v. 84, p. 4160.
- Matsushima, T., and Chang, C.S., 2011, Quantitative evaluation of the effect of irregularly shaped particles in sheared granular assemblies: *Granular Matter*, v. 13, p. 269-276.
- McDowell, G.R., and Bolton, M.D., 1998, On the micromechanics of crushable aggregates: *Geotechnique*, v. 48, p. 667-679.
- McDowell, G.R., Bolton, M.D., and Robertson, D., 1996, The fractal crushing of granular materials: *Journal of the Mechanics and Physics of Solids*, v. 44, p. 2079-2101.
- McDowell, G., and Harireche, O., 2002, Discrete element modelling of soil particle fracture: *Geotechnique*, v. 52, p. 131-135.
- McDowell, G.R., and Humphreys, A., 2002, Yielding of granular materials: *Granular Matter*, v. 4, p. 1-8.
- McDowell, G.R., and de Bono, J.P., 2013, On the micro mechanics of one-dimensional normal compression: *Geotechnique*, v. 63, p. 895-908.
- Mesri, G., and Vardhanabhuti, B., 2009, Compression of granular materials: *Canadian geotechnical journal*, v. 46, p. 369-392.
- Miao, G., and Airey, D., in Chau, K.T., and Zhao, J., eds., *Advances in Bifurcation and Degradation in Geomaterials, Proceedings of the 10th International Workshop on Bifurcation and Degradation in Geomaterials (IWBDG2014)*: Hong Kong, China.
- Miao, G., and Airey, D., 2013, Breakage and ultimate states for a carbonate sand: *Geotechnique*, v. 63, p. 1221-1229.
- Minh, N.H., and Cheng, Y.P., 2013, A DEM investigation of the effect of particle size distribution on one-dimensional compression: *Geotechnique*, v. 63, p. 44-53.

- Minh, N.H., Cheng, Y.P., and Thornton, C., 2014, Strong force networks in granular mixtures: *Granular Matter*, v. 16, p. 69-78.
- Mirghasemi, A., Rothenburg, L., and Matyas, E., 1997, Numerical simulations of assemblies of two-dimensional polygon-shaped particles and effects of confining pressure on shear strength: *Soils and Foundations*, v. 37, p. 43-52.
- Mirghasemi, A., Rothenburg, L., and Matyas, E., 2002, Influence of particle shape on engineering properties of assemblies of two-dimensional polygon-shaped particles: *Geotechnique*, v. 52, p. 209-217.
- Mitchell, J.K., and Soga, K., 2005, *Fundamentals of soil behavior*, 3rd edition. : John Wiley & Sons.
- Mohamed, A., and Gutierrez, M., 2010, Comprehensive study of the effects of rolling resistance on the stress-strain and strain localization behavior of granular materials: *Granular Matter*, v. 12, p. 527-541.
- Mollon, G., and Zhao, J.D., 2012, Fourier-Voronoi-based generation of realistic samples for discrete modelling of granular materials: *Granular Matter*, v. 14, p. 621-638.
- Mollon, G., and Zhao, J.D., 2013, Generating realistic 3D sand particles using Fourier descriptors: *Granular Matter*, v. 15, p. 95-108.
- Mollon, G., and Zhao, J.D., 2014, 3D generation of realistic granular samples based on random fields theory and Fourier shape descriptors: *Computer Methods in Applied Mechanics and Engineering*, v. 279, p. 46-65.
- Mora, P., and Place, D., 1994, Simulation of the frictional stick-slip instability: *Pure and Applied Geophysics*, v. 143, p. 61-87.
- Moreno, R., Ghadiri, M., and Antony, S.J., 2003, Effect of the impact angle on the breakage of agglomerates: a numerical study using DEM: *Powder Technology*, v. 130, p. 132-137.
- Moreno, R., Williams, R.A., and Jia, X., 2010, Combining X-ray microtomography with computer simulation for analysis of granular and porous materials: *Particuology*, v. 8, p. 81-99.
- Mueth, D.M., Jaeger, H.M., and Nagel, S.R., 1998, Force distribution in a granular medium: *Physical Review E*, v. 57, p. 3164.
- Munjiza, A., 2004, *The combined finite-discrete element methods*, Wiley Online Library.
- Nakata, A., Hyde, M., and Hyodo, H., 1999, A probabilistic approach to sand particle crushing in the triaxial test: *Geotechnique*, v. 49, p. 567-583.
- Nakata, Y., Hyodo, M., Hyde, A.F., Kato, Y., and Murata, H., 2001a, Microscopic particle crushing of sand subjected to high pressure one-dimensional compression: *Soils and Foundations*, v. 41, p. 69-82.
- Nakata, Y., Hyodo, M., Murata, H., and Yasufuku, N., 1998, Flow deformation of sands subjected to principal stress rotation: *Soils and Foundations*, v. 38, p. 115-128.
- Nakata, Y., Kato, Y., Hydo, M., Hyde, A.F., and Murata, H., 2001b, One-dimensional compression behaviour of uniformly graded sand related to single particle crushing strength: *Soils and Foundations*, v. 41, p. 39-51.
- Ng, T.T., 1994, Numerical simulations of granular soil using elliptical particles: *Computers and Geotechnics*, v. 16, p. 153-169.
- Ng, T.T., 2004, Macro-and micro-behaviors of granular materials under different sample preparation methods and stress paths: *International Journal of Solids and Structures*, v. 41, p. 5871-5884.
- O'Sullivan, C., 2011, *Particulate discrete element modelling*, Taylor & Francis.
- O'Sullivan, C., D Bray, J., and Li, S., 2003, A new approach for calculating strain for particulate media:

- International Journal for Numerical and Analytical Methods in Geomechanics, v. 27, p. 859-877.
- Ochiai, H., and Lade, P.V., 1983, Three-dimensional behavior of sand with anisotropic fabric: Journal of Geotechnical Engineering, v. 109, p. 1313-1328.
- Oda, M., and Iwashita, K., 1999, Mechanics of granular materials: an introduction, CRC Press.
- Oda, M., and Nakayama, H., 1989, Yield function for soil with anisotropic fabric: Journal of Engineering Mechanics, v. 115, p. 89-104.
- Oda, M., Nemat-Nasser, S., and Konishi, J., 1985, Stress-induced anisotropy in granular masses: Soils and Foundation, v. 25, p. 85-97.
- Orford, J., and Whalley, W., 1983, The use of the fractal dimension to quantify the morphology of irregular - shaped particles: Sedimentology, v. 30, p. 655-668.
- Pena, A., Garcia-Rojo, R., and Herrmann, H., 2007, Influence of particle shape on sheared dense granular media: Granular Matter, v. 9, p. 279-291.
- Peters, J., Muthuswamy, M., Wibowo, J., and Tordesillas, A., 2005, Characterization of force chains in granular material: Physical Review E, v. 72, p. 041307.
- Plimpton, S., Crozier, P., and Thompson, A., 2007, LAMMPS-large-scale atomic/molecular massively parallel simulator: Sandia National Laboratories. Report.
- Pourghahramani, P., and Forssberg, E., 2005, Review of applied particle shape descriptors and produced particle shapes in grinding environments. Part I: Particle shape descriptors: Mineral Processing & Extractive Metall. Rev., v. 26, p. 145-166.
- Powers, M.C., 1953, A new roundness scale for sedimentary particles: Journal of Sedimentary Research, v. 23.
- Pradhan, B.S., Tatsuoka, F., and Horii, N., 1979, Simple shear testing on sand in a torsional shear apparatus: Soils and foundations, v. 28, p. 95-112.
- Radjai, F., Jean, M., Moreau, J.-J., and Roux, S., 1996, Force distributions in dense two-dimensional granular systems: Physical Review Letters, v. 77, p. 274.
- Radjai, F., and Wolf, D.E., 1998, Features of static pressure in dense granular media: Granular Matter, v. 1, p. 3-8.
- Richefeu, V., El Youssoufi, M.S., Azéma, E., and Radjaï, F., 2009, Force transmission in dry and wet granular media: Powder Technology, v. 190, p. 258-263.
- Rothenburg, L., and Bathurst, R., 1989, Analytical study of induced anisotropy in idealized granular materials: Geotechnique, v. 39, p. 601-614.
- Rothenburg, L., and Bathurst, R., 1992, Micromechanical features of granular assemblies with planar elliptical particles: Geotechnique, v. 42, p. 79-95.
- Rothenburg, L., and Selvadurai, A., 1981, A micromechanical definition of the Cauchy stress tensor for particulate media, In Mechanics of Structured Media, p. 469-486.
- Rowe, P.W., 1971, Theoretical meaning and observed values of deformation parameters for soil, Proc. Roscoe Mem. Symp, v. 18, p. 143-194.
- Rowe, P.W., 1962, The stress-dilatancy relation for static equilibrium of an assembly of particles in contact, Proceedings of the Royal Society of London A: Mathematical, Physical and Engineering Sciences, v. 269, p. 500-527.
- Russell, A.R., and Khalili, N., 2004, A bounding surface plasticity model for sands exhibiting particle crushing: Canadian Geotechnical Journal, v. 41, p. 1179-1192.
- Sadrekarami, A., and Olson, S., 2011, Critical state friction angle of sands: Geotechnique, v. 61, p.

771-783.

- Saint-Cyr, B., Delenne, J.Y., Voivret, C., Radjai, F., and Sornay, P., 2011, Rheology of granular materials composed of nonconvex particles: *Physical Review E*, v. 84, p. 041302.
- Sakaguchi, H., Ozaki, E., and Igarashi, T., 1993, Plugging of the flow of granular materials during the discharge from a silo: *International Journal of Modern Physics B*, v. 7, p. 1949-1963.
- Salami, M., and Banks, D., 1996, Discontinuous deformation analysis (DDA) and simulations of discontinuous media, *Proc. of the First International Forum on Discontinuous Deformation Analysis (DDA) and Simulations of Discontinuous Media*, Berkeley, CA, p. 415-431.
- Salim, W., and Indraratna, B., 2004, A new elastoplastic constitutive model for coarse granular aggregates incorporating particle breakage: *Canadian Geotechnical Journal*, v. 41, p. 657-671.
- Sallam, A.M., 2004, Studies on modeling angular soil particles using the discrete element method, University of South Florida, PhD Thesis.
- Salot, C., Gotteland, P., and Villard, P., 2009, Influence of relative density on granular materials behavior: DEM simulations of triaxial tests: *Granular Matter*, v. 11, p. 221-236.
- Satake, M., 1993, A theory on the stress-induced anisotropy in granular assemblies, *Geotechnical Management of Waste and Contamination: Proceedings of the conference, Sydney, NSW, 22-23 March 1993, Volume 2*, CRC Press, p. 155.
- Satake, M., 2004, Tensorial form definitions of discrete-mechanical quantities for granular assemblies: *International Journal of Solids and Structures*, v. 41, p. 5775-5791.
- Schanz, T., and Vermeer, P., 1996, Angles of friction and dilatancy of sand: *Geotechnique*, v. 46, p. 145-152.
- Schofield, A., and Worth, C., 1968, *Critical state soil mechanics*. London: McGraw-Hill.
- Seyedi Hosseininia, E., 2012, Discrete element modeling of inherently anisotropic granular assemblies with polygonal particles: *Particuology*, v. 10, p. 542-552.
- Seyedi Hosseininia, E., 2013, Stress–force–fabric relationship for planar granular materials: *Geotechnique*, v. 63, p. 830-841.
- Shi, G.H., 1992, Discontinuous deformation analysis: a new numerical model for the statics and dynamics of deformable block structures: *Engineering computations*, v. 9, p. 157-168.
- Shin, H., and Santamarina, J., 2012, Role of Particle Angularity on the Mechanical Behavior of Granular Mixtures: *Journal of Geotechnical and Geoenvironmental Engineering*, v. 139, p. 353-355.
- Strack, O., and Cundall, P.A., 1984, Fundamental studies of fabric in granular materials, Department of Civil and Mineral Engineering, University of Minnesota. Report.
- Sukumaran, B., and Ashmawy, A., 2001, Quantitative characterisation of the geometry of discrete particles: *Geotechnique*, v. 51, p. 619-627.
- Sulsky, D., and Schreyer, L., 2004, MPM simulation of dynamic material failure with a decohesion constitutive model: *European Journal of Mechanics-A/Solids*, v. 23, p. 423-445.
- Sun, Q.C., Jin, F., Liu, J., and Zhang, G.D., 2010, Understanding force chains in dense granular materials: *International Journal of Modern Physics B*, v. 24, p. 5743-5759.
- Szarf, K., Combe, G., and Villard, P., 2011, Polygons vs. clumps of discs: A numerical study of the influence of grain shape on the mechanical behaviour of granular materials: *Powder Technology*, v. 208, p. 279-288.
- Tang, C.A., 1997, Numerical simulation of progressive rock failure and associated seismicity: *International Journal of Rock Mechanics and Mining Sciences*, v. 34, p. 249-261.

- Tang, C.A., Xu, X.H., Kou, S.Q., Lindqvist, P.A., and Liu, H.Y., 2001, Numerical investigation of particle breakage as applied to mechanical crushing—part I: single-particle breakage: *International Journal of Rock Mechanics and Mining Sciences*, v. 38, p. 1147-1162.
- Taylor, D.W., 1948, *Fundamentals of soil mechanics*: Soil Science, v. 66, p. 161.
- Tejchman, J., Bauer, E., and Wu, W., 2007, Effect of fabric anisotropy on shear localization in sand during plane strain compression: *Acta Mechanica*, v. 189, p. 23-51.
- Thomas, P.A., 1997, *Discontinuous deformation analysis of particulate media*, University of California, Berkeley, PhD Thesis.
- Thornton, C., 1997, Force transmission in granular media: *Kona Powder and Particle Journal*, v. 15, p. 81-90.
- Thornton, C., 2000, Numerical simulations of deviatoric shear deformation of granular media: *Geotechnique*, v. 50, p. 43-53.
- Thornton, C., and Antony, S.J., 1998, Quasi-static deformation of particulate media: *Philosophical Transactions of the Royal Society A: Mathematical, Physical and Engineering Sciences*, v. 356, p. 2763-2782.
- Thornton, C., and Antony, S.J., 2000, Quasi-static shear deformation of a soft particle system: *Powder Technology*, v. 109, p. 179-191.
- Thornton, C., Ciomocos, M., and Adams, M., 2004, Numerical simulations of diametrical compression tests on agglomerates: *Powder Technology*, v. 140, p. 258-267.
- Tighe, B.P., Snoeijer, J.H., Vlugt, T.J., and van Hecke, M., 2010, The force network ensemble for granular packings: *Soft Matter*, v. 6, p. 2908-2917.
- Tobita, Y., and Yanagisawa, E., 1992, Modified stress tensors for anisotropic behavior of granular materials: *Soils and Foundations*, v. 32, p. 84-99.
- Tordesillas, A., Lin, Q., Zhang, J., Behringer, R., and Shi, J., 2011, Structural stability and jamming of self-organized cluster conformations in dense granular materials: *Journal of the Mechanics and Physics of Solids*, v. 59, p. 265-296.
- Tordesillas, A., and Walsh, D.S., 2002, Incorporating rolling resistance and contact anisotropy in micromechanical models of granular media: *Powder Technology*, v. 124, p. 106-111.
- Tsoungui, O., Vallet, D., and Charmet, J.C., 1999, Numerical model of crushing of grains inside two-dimensional granular materials: *Powder Technology*, v. 105, p. 190-198.
- Turcotte, D., 1986, A fractal model for crustal deformation: *Tectonophysics*, v. 132, p. 261-269.
- Uygar, E., and Doven, A.G., 2006, Monotonic and cyclic oedometer tests on sand at high stress levels: *Granular Matter*, v. 8, p. 19-26.
- Vaid, Y., and Chern, J., 1985, Cyclic and monotonic undrained response of saturated sands, *Advances in the art of testing soils under cyclic conditions*, ASCE, p. 120-147.
- Vaid, Y., Chung, E., and Kuerbis, R., 1990, Stress path and steady state: *Canadian Geotechnical Journal*, v. 27, p. 1-7.
- Vaid, Y., Eliadorani, A., Sivathayalan, S., and Uthayakumar, M., 1999, Quasi-steady state: a real behaviour?: Discussion: *Canadian Geotechnical Journal*, v. 36, p. 182-183.
- Valentino, R., Barla, G., and Montrasio, L., 2008, Experimental analysis and micromechanical modelling of dry granular flow and impacts in laboratory flume tests: *Rock Mechanics and Rock Engineering*, v. 41, p. 153-177.
- Vallejo, L.E., 1995, Fractal analysis of granular materials: *Geotechnique*, v. 45, p. 159-163.
- van Eerd, A.R., Ellenbroek, W.G., van Hecke, M., Snoeijer, J.H., and Vlugt, T.J., 2007, Tail of the

- contact force distribution in static granular materials: *Physical Review E*, v. 75, p. 060302.
- Varadarajan, A., Sharma, K., Abbas, S., and Dhawan, A., 2006, Constitutive model for rockfill materials and determination of material constants: *International Journal of Geomechanics*, v. 6, p. 226-237.
- Voivret, C., Radjai, F., Delenne, J.-Y., and El Youssoufi, M.S., 2009, Multiscale force networks in highly polydisperse granular media: *Physical review letters*, v. 102, p. 178001.
- Wadell, H., 1932, Volume, shape, and roundness of rock particles: *The Journal of Geology*, v. 40, p. 443-451.
- Walker, D.M., and Tordesillas, A., 2010, Topological evolution in dense granular materials: a complex networks perspective: *International Journal of Solids and Structures*, v. 47, p. 624-639.
- Walker, D.M., Tordesillas, A., Einav, I., and Small, M., 2011, Complex networks in confined comminution: *Physical Review E*, v. 84, p. 021301.
- Wang, J.F., Dove, J.E., and Gutierrez, M.S., 2007b, Discrete-continuum analysis of shear banding in the direct shear test: *Geotechnique*, v. 57, p. 513-526.
- Wang, J.F., Gutierrez, M.S., and Dove, J.E., 2007a, Numerical studies of shear banding in interface shear tests using a new strain calculation method: *International Journal for Numerical and Analytical Methods in Geomechanics*, v. 31, p. 1349-1366.
- Wang, J.F., and Jiang, M.J., 2011, Unified soil behavior of interface shear test and direct shear test under the influence of lower moving boundaries: *Granular Matter*, v. 13, p. 631-641.
- Wang, J.F., and Yan, H.B., 2011, On the role of particle breakage in the shear failure behavior of granular soils by DEM: *International Journal for Numerical and Analytical Methods in Geomechanics*, v. 37(8), p. 832-854.
- Wang, L., Park, J.Y., and Fu, Y., 2007, Representation of real particles for DEM simulation using X-ray tomography: *Construction and Building Materials*, v. 21, p. 338-346.
- Wang, Y., and Leung, S., 2008, Characterization of cemented sand by experimental and numerical investigations: *Journal of Geotechnical and Geoenvironmental Engineering*, v. 134, p. 992-1004.
- Wei, L.M., and Yang, J., 2014, On the role of grain shape in static liquefaction of sand–fines mixtures, *Geotechnique*, v. 64, p. 740-745.
- Weibull, W., 1951, Wide applicability: *Journal of Applied Mechanics*.
- Wensrich, C., and Katterfeld, A., 2012, Rolling friction as a technique for modelling particle shape in DEM: *Powder Technology*, v. 217, p. 409-417.
- Williams, K.C., Chen, W., Weeger, S., and Donohue, T.J., 2014, Particle shape characterisation and its application to discrete element modelling: *Particuology*, v. 12, p. 80-89.
- Wood, D.M., 1990, *Soil behaviour and critical state soil mechanics*, Cambridge university press.
- Wroth, C., and Bassett, R., 1965, A stress–strain relationship for the shearing behaviour of a sand: *Geotechnique*, v. 15, p. 32-56.
- Xiao, Y., and Liao, J., 2014, Discussion of “Role of Particle Angularity on the Mechanical Behavior of Granular Mixtures” by H. Shin and JC Santamarina: *Journal of Geotechnical and Geoenvironmental Engineering*, v. 140, p. 07014009.
- Xiao, Y., Liu, H., Chen, Y., and Jiang, J., 2014a, Strength and deformation of rockfill material based on large-scale triaxial compression tests. II: Influence of particle breakage: *Journal of Geotechnical and Geoenvironmental Engineering*, v. 140, p. 04014071.
- Xiao, Y., Liu, H., Chen, Y., Jiang, J., and Zhang, W., 2014b, State dependent constitutive model for

- rockfill materials: *International Journal of Geomechanics*, p. 04014075.
- Yamada, Y., and Ishihara, K., 1979, Anisotropic deformation characteristics of sand under three dimensional stress conditions: *Soils and Foundations*, v. 19, p. 79-94.
- Yamada, Y., and Ishihara, K., 1982, Yielding of loose sand in three-dimensional stress conditions: *Soils and Foundations*, v. 22, p. 15-31.
- Yamamoto, J.A., Bopp, P.A., and Lade, P.V., 1996, One-dimensional compression of sands at high pressures: *Journal of Geotechnical Engineering*, v. 122, p. 147-154.
- Yang, D., 2014, Microscopic study of granular material behaviours under general stress paths, University of Nottingham, PhD Thesis.
- Yang, J., and Dai, B.B., 2010, Is the quasi-steady state a real behaviour? A micromechanical perspective: *Geotechnique*, v. 61, p. 175-183.
- Yang, J., and Li, X.S., 2004, State-dependent strength of sands from the perspective of unified modeling: *Journal of Geotechnical and Geoenvironmental Engineering*, v. 130, p. 186-198.
- Yang, J., and Wei, L.M., 2012, Collapse of loose sand with the addition of fines: the role of particle shape: *Geotechnique*, v. 62, p. 1111-1125.
- Yang, Y., and Cheng, Y.M., 2015, A fractal model of contact force distribution and the unified coordination distribution for crushable granular materials under confined compression: *Powder Technology*, v. 279, p. 1-9.
- Yang, Z.X., Yang, J., and Wang, L.M., 2012, On the influence of inter-particle friction and dilatancy in granular materials: a numerical analysis: *Granular Matter*, v. 14, p. 433-447.
- Yang, Z.X., Yang, J., and Wang, L.M., 2013, Micro-scale modeling of anisotropy effects on undrained behavior of granular soils: *Granular Matter*, v. 15, p. 557-572.
- Yimsiri, S., and Soga, K., 2010, DEM analysis of soil fabric effects on behaviour of sand: *Geotechnique*, v. 60, p. 483-495.
- Yin, Z.Y., Chang, C.S., and Hicher, P.Y., 2010a, Micromechanical modelling for effect of inherent anisotropy on cyclic behaviour of sand: *International Journal of Solids and Structures*, v. 47, p. 1933-1951.
- Yin, Z.Y., Chang, C.S., Karstunen, M., and Hicher, P.Y., 2010b, An anisotropic elastic–viscoplastic model for soft clays: *International Journal of Solids and Structures*, v. 47, p. 665-677.
- Yin, Z.Y., and Chang, C.S., 2013, Stress–dilatancy behavior for sand under loading and unloading conditions. *International Journal for Numerical and Analytical Methods in Geomechanics*, v. 37, p. 855-870.
- Yoshimine, M., 1999, Quasi-steady state: a real behavior?: Discussion: *Canadian Geotechnical Journal*, v. 36, p. 186-187.
- Yoshimine, M., and Ishihara, K., 1998, Flow potential of sand during liquefaction: *Soils and foundations*, v. 38, p. 189-198.
- Yoshimine, M., Ishihara, K., and Vargas, W., 1998, Effects of principal stress direction and intermediate principal stress on undrained shear behavior of sand: *Soils and Foundations*, v. 38, p. 179-188.
- Zhang, C., Nguyen, G., and Einav, I., 2012, The end-bearing capacity of piles penetrating into crushable soils: *Geotechnique*, v. 63, p. 341-354.
- Zhang, H., and Garga, V.K., 1997, Quasi-steady state: a real behaviour?: *Canadian Geotechnical Journal*, v. 34, p. 749-761.
- Zhang, W.C., Wang, J.F., and Jiang, M.J., 2013, DEM-aided discovery of the relationship between

- energy dissipation and shear band formation considering the effects of particle rolling resistance: *Journal of Geotechnical and Geoenvironmental Engineering*, v. 139, p. 1512-1527.
- Zhang, X., and Baudet, B., 2013, Particle breakage in gap-graded soil: *Géotechnique Letters*, v. 3, p. 72-77.
- Zhao, J.D., and Guo, N., 2014, Rotational resistance and shear-induced anisotropy in granular media: *Acta Mechanica Solida Sinica*, v. 27, p. 1-14.
- Zhao, Z.H., 2013, Gouge particle evolution in a rock fracture undergoing shear: a microscopic DEM study: *Rock Mechanics and Rock Engineering*, v. 46, p. 1461-1479.
- Zhao, Z.H., Jing, L., and Neretnieks, I., 2012, Particle mechanics model for the effects of shear on solute retardation coefficient in rock fractures: *International Journal of Rock Mechanics and Mining Sciences*, v. 52, p. 92-102.
- Zhou, B., Huang, R., Wang, H., and Wang, J., 2013, DEM investigation of particle anti-rotation effects on the micromechanical response of granular materials: *Granular Matter*, v. 15, p. 315-326.
- Zhou, Y., Wright, B., Yang, R., Xu, B., and Yu, A., 1999, Rolling friction in the dynamic simulation of sandpile formation: *Physica A: Statistical Mechanics and its Applications*, v. 269, p. 536-553.
- Zhu, H., Zhou, Z., Yang, R., and Yu, A.B., 2008, Discrete particle simulation of particulate systems: a review of major applications and findings: *Chemical Engineering Science*, v. 63, p. 5728-5770.